Continuous biomolecular sensing with single-molecule resolution

Continuous biomolecular sensing with single-molecule resolution

Explorations of bioanalytical functionalities

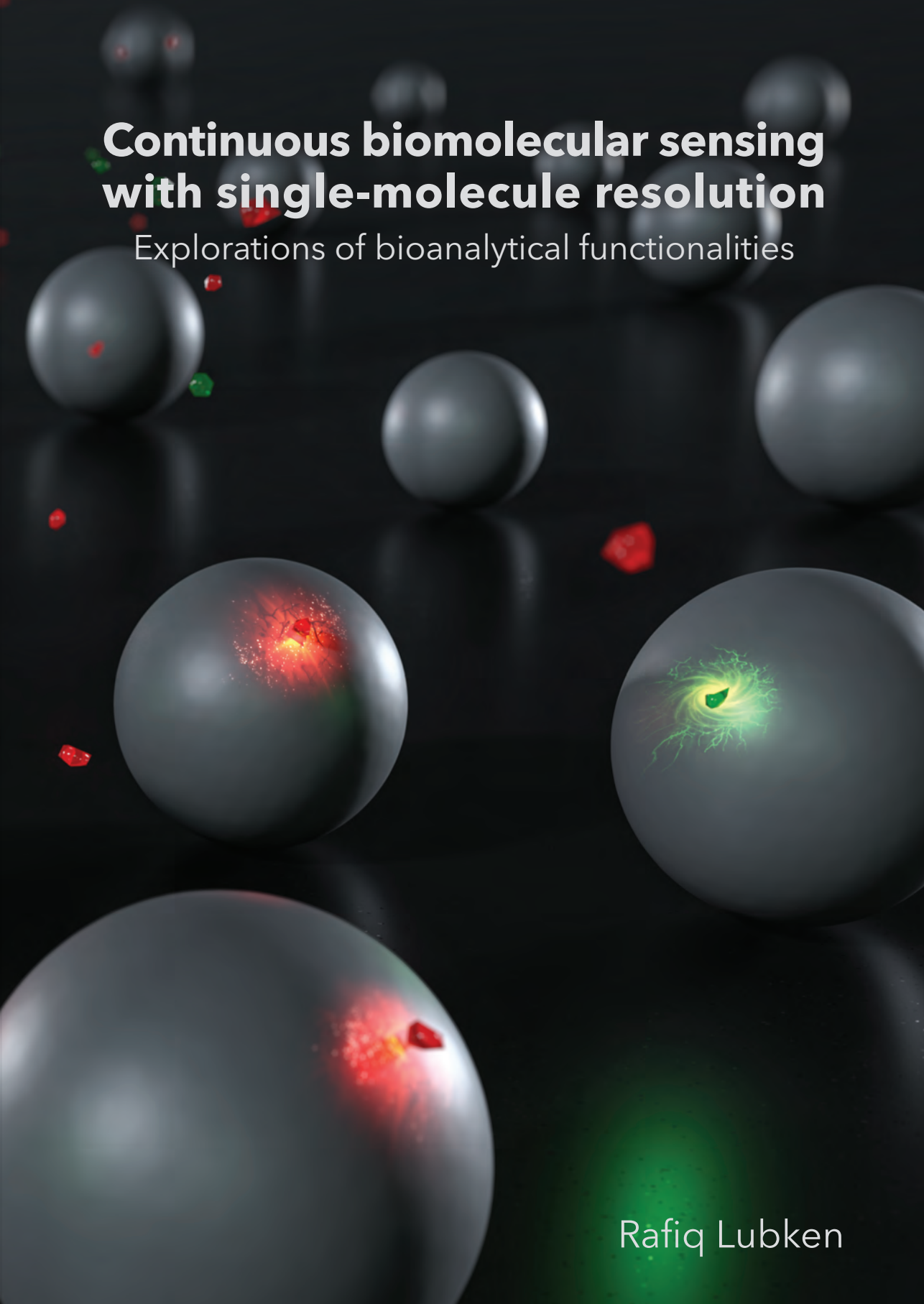

Rafiq Lubken

CONTINUOUS BIOMOLECULAR SENSING WITH SINGLE-MOLECULE RESOLUTION

Explorations of bioanalytical functionalities

PROEFSCHRIFT

ter verkrijging van de graad van doctor aan de Technische Universiteit Eindhoven, op gezag van de rector magnificus prof.dr.ir. F.P.T. Baaijens, voor een commissie aangewezen door het College van Promoties, in het openbaar te verdedigen op vrijdag 14 januari 2022 om 16:00 uur

door

Rafiq Milan Lubken

geboren te Son en Breugel

Dit proefschrift is goedgekeurd door de promotoren en de samenstelling van de promotiecommissie is als volgt:

voorzitter:	prof.dr. J. Pluim
1e promotor:	prof.dr.ir. M.W.J. Prins
copromotor:	dr.ir. A.M. de Jong
leden:	prof.dr. M. Merkx
	prof.dr.ir. T.F.A. de Greef
	prof.dr.ir. J.M.J. den Toonder
	prof.dr.ir. A. van den Berg (Universiteit Twente)
	prof.dr.ir. S.J.T. van Noort (Universiteit Leiden)

Het onderzoek of ontwerp dat in dit proefschrift wordt beschreven is uitgevoerd in overeenstemming met de TU/e Gedragscode Wetenschapsbeoefening.

Opgedragen aan mijn familie, in het bijzonder aan diegenen
tegen wie deze woorden niet meer gezegd kunnen worden.

COLOPHON

Cover design by ICMS Animation Studio and R.M. Lubken. Printed by ADC Dereumaux, 's-Hertogenbosch, the Netherlands.

This document was typeset using the typographical look-and-feel `classicthesis` developed by André Miede and Ivo Pletikosić.

A catalogue record is available from the Eindhoven University of Technology Library.
ISBN: 978–90–386–5438–6

SUMMARY

Studies on the dynamics of biological systems and biotechnological processes require biomolecular sensors that can reveal time-dependencies of concentrations of specific biomolecules. Such sensors are important for fundamental research on biological dynamics, for the development of patient monitoring strategies, and for the development of closed loop control strategies. However, the applicability of such sensors depends on their analytical performance, *e. g.*, sensitivity, molecular specificity, and degree of parallelization. Single-molecule techniques proved to be impactful for increasing the performance of bioanalytical methods, but in the upcoming field of sensors for continuous biomolecular monitoring the advantages are yet to be discovered. This thesis explores the opportunities of sensors for continuous biomolecular monitoring with a single-molecule resolution and quantifies potential enhancements enabled by single-molecule techniques.

Firstly, in Chapter 1, an introduction is given to the field of sensors for continuous biomolecular monitoring and state-of-the-art single-molecule approaches. Here we specifically focus on how single-molecule approaches can be used to enhance the performance of biomolecular recognition strategies.

In Chapter 2 we demonstrate a new multiplexing method by means of single-molecule kinetic identification of single particles. Here, multiplexing is enabled by an analyte-sensitive, single-molecular nanoswitch with a particle as a reporter. We demonstrate by experiments and simulations, using biosensing by particle mobility (BPM) as an example monitoring technique, multiplexed continuous monitoring of oligonucleotides at picomolar concentrations.

In Chapter 3 we present a framework to study the influence of heterogeneities, focused on particle-based sensing applications. Using single-molecule techniques (DNA-PAINT, qPAINT and BPM), the variability in particle reactivity is quantified by counting and spatially mapping individual binder molecules on particles, and by measuring the resulting reactivity of single particles. By combining experimental results and simulations, the influence of various heterogeneities and the collective effect of all heterogeneities on the reactivity of particles is studied as a function of system parameters, such as particle interaction area, targeting moiety density, particle size and number of particles.

In Chapter 4 we present a sensing methodology that enables rapid monitoring of low-concentration biomolecules. We demonstrate using simulations and experiments that this sensing methodology is suitable for monitoring picomolar and sub-picomolar concentrations, for measurement intervals of a few minutes, and in principle for sensing over an endless time span.

In Chapter 5 we investigate continuous biomolecular analyte exchange between a dynamic system of interest and the measurement chamber of a sensor. For this, we simulate mass transport and surface reactions, where an oscillating concentration-time profile is used as input. Subsequently, we quantify the time lag of the measured concentration and the sensitivity of the sensor as a function of system parameters, such as measurement chamber geometry and flow rate. This enables researchers to rationally design a biomolecular monitoring system with a desired sensor performance for specific applications.

Lastly, Chapter 6 discusses the main findings in this thesis and sketches the outlines of further research in the field of continuous monitoring applications and the added value of single-molecule techniques to enhance the performance of sensors for continuous biomolecular monitoring.

CONTENTS

LIST OF ABBREVIATIONS

APD	avalanche photodiode
BPM	biosensing by particle mobility
CCR	concentration change rate
CDF	cumulative distribution function
CE test	Clark-Evans test
CRP	C-reactive protein
CSR	complete spatial randomness
CV	coefficient of variation
DNA	deoxyribonucleic acid
DNA-PAINT	DNA points accumulation in nanoscale topography
dsDNA	double-stranded DNA
EC_{50}	effective concentration 50, *i. e.*, concentration with 50% effect
ELISA	enzyme-linked immunosorbent assay
FOV	field-of-view
IL-6	interleukin-6
LoCCR	limit of quantification of the concentration change rate
LoD	limit of detection
LoQ	limit of quantification
MSD	mean-squared displacement
MW	molecular weight
NN	nearest-neighbor
PBS	phosphate buffered saline
PCR	polymerase chain reaction

PCT	procalcitonin
PEG	polyethylene-glycol
POC	point-of-care
qPAINT	quantitative points accumulation in nanoscale topography
ROI	region of interest
SEM	scanning electron microscope
Simoa	single-molecule array
SMC	single-molecule counting
ssDNA	single-stranded DNA
TIR	total internal reflection

1 INTRODUCTION

The goal of this thesis is to investigate bioanalytical functionalities that can be achieved with continuous affinity-based biomolecular sensors using single-molecule resolution. This chapter describes a general introduction into the field of biosensors, with particular focus on biosensors for continuous monitoring. Subsequently, a short overview is given of the development of bioanalytical single-molecule techniques and how these techniques are used in the field of biosensing. Then, we focus on the promises of continuous monitoring biosensors with single-molecule resolution by comparing the theoretical limits for biosensor sensitivity with an ensemble read out *versus* a single-molecule read out. Finally, the main research question and the outline of the thesis are given.

1.1 STATE-OF-THE-ART BIOSENSORS

Biosensors are compact devices that are used to quantify the concentration of a chemical substance of interest, referred to as biomarker, analyte, or target molecule. Figure 1.1 shows three components of a generic biosensor design: (1) receptors, also referred to as binder molecules, capture molecules, probes, or targeting moieties; (2) a transduction method; and (3) signal processing and concentration display.[1–5] The very heart of a biosensor is formed by a bioanalytical assay to recognize the biomarker molecules using the receptors that bind specifically to these biomarker molecules, forming biomarker-receptor complexes. A biosensor integrates this recognition reaction between the biomarker molecule and the receptor *via* a transduction method to a signal that relates to the biomarker concentration in the sample.

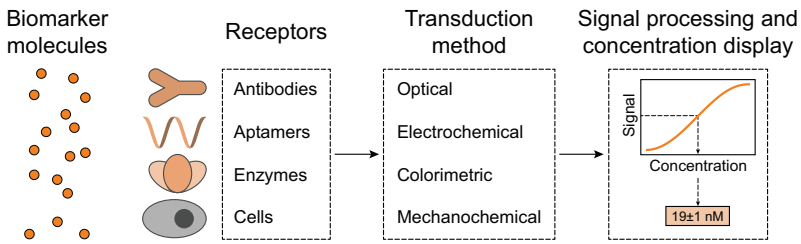

FIGURE 1.1: SCHEMATIC OVERVIEW OF A GENERIC BIOSENSOR DESIGN. Biomarker molecules are recognized using (biological) receptors. Subsequently, the formed biomarker-receptor complexes are detected *via* a transduction method. The measured signal is converted *via* a predetermined calibration curve into a biomarker concentration which reflects the biomarker concentration present in the analyzed sample.

1.1.1 *Rapid biosensors*

Laboratory-based *in vitro* tests are the prevailing methods for biomarker concentration quantification. These tests require transportation of samples to a laboratory and as a consequence the test results are not directly available. For example in health care applications, due to the demand for more effective and efficient patient care, faster and easy-to-use diagnostic methods are being developed.[6–12] These rapid biosensors for health care are known as point-of-care (POC) biosensors, which are handheld devices that test at or near the site of the patient, to facilitate immediate and well-considered decisions improving patient outcomes. Currently developed POC biosensors are able to measure the concentration of various biomarkers such as glucose, CRP, and cardiac troponin.[10–14]

1.1.2 *Continuous biomolecular monitoring*

When a biosensor is able to measure a biomarker concentration continuously, the applicability of biosensors expands even further. Especially for rapidly fluctuating biomarker concentrations, small changes in trends become useful parameters, when concentration information is available on a continuous basis.[15–20] An example in health care of such a biosensor is the continuous glucose biosensor, which can be worn in or on the skin, or can be connected to a catheter.[21,22] The sensor records how the glucose concentration fluctuates over time in order to provide optimal treatment for the patient. Commercial biosensors are currently available for glucose and lactate[21–23] and research is ongoing for the monitoring of for example antibiotics.[24] These biomarkers are present in relatively high concentrations (millimolar and micromolar) and therefore these studies mainly focus on electrochemical detection methods. For biomarkers with lower concentrations, more sensitive and more specific sensing methods have to be developed. In the search for highly sensitive and highly specific transduction methods suitable for continuous biomolecular monitoring, the field of single-molecule biophysics forms a source of inspiration.

1.2 COMBINING SINGLE-MOLECULE TECHNIQUES AND BIOSENSING

1.2.1 *Single-molecule techniques*

In the early 90's of the last century, in the research field of biophysics the first single-molecule measurements were developed, based on absorption[25] and fluorescence.[26] These methods enabled researchers to reveal phenomena that were previously concealed in traditional ensemble-based methods, as these record averages over many molecules. Single-molecule fluorescence measurement techniques[27–29] are nowadays part of the standard research arsenal in biochemical and biophysical laboratories. Other single-molecule measurement methods[30] are for instance force-based techniques, such as tethered particle motion,[31–33] magnetic and optical tweezers,[34–36] and single-molecule atomic force microscopy,[37] which are primarily applied for studies of enzyme activity, DNA interactions, and DNA properties.

1.2.2 *Single-molecule detection in endpoint assays*

Single-molecule biophysical techniques penetrated into the field of biosensing for achieving high sensitivities. Here, sensitivity is defined as the signal change for a given concentration change, where a high

sensitivity refers to a biosensor in which a small concentration change results in a large signal change. Biosensors with a high sensitivity are therefore able to quantify low biomarker concentrations with a high precision. A high sensitivity is important for many applications,[17,18] *e. g.*, the measurement of inflammatory markers.[38–40] The majority of the approaches described in literature to increase the sensitivity of a biosensor assay are focused on reducing the background of the signal[41,42] or changing assay components and formats.[43] Single-molecule detection poses the ability to count individual molecules and therefore get digital read out signals. In principle, discrete counting of molecules results in an infinitely high precision of the actual number of counted molecules; the sensitivity of the biosensor itself is then only determined by counting statistics.

Figure 1.2 shows two examples of endpoint assays with single-molecule detection: single-molecule arrays (Simoa®, commercialized by Quanterix)[44] and single-molecule counting (SMC™, commercialized by Singulex).[45,46] Figure 1.2a shows a general sandwich type assay using micrometer-sized particles. These particles are functionalized with capture molecules, such as antibodies or aptamers, which are able to specifically bind to the biomarker molecule of interest. Upon binding of the biomarker molecule from the bulk solution to the capture molecule on the particle, biomarker-capture molecule complexes are formed. Subsequently, these complexes are detected using labeled detection molecules, by forming sandwich complexes.

Figure 1.2b schematically shows a single-molecule biosensing technique using Simoa®, illustrated for a sandwich assay. The particle concentration during incubation is chosen in such a way that the majority of the particles do not bind a biomarker molecule from solution, and that only a few percent of the particles capture a single or more biomarker molecules following a Poisson distribution. This method provides the opportunity to achieve both a small, micrometer-sized (~fL) detection space in which a single particle can be isolated and subsequently observed, as well as a high degree of parallelization (~50,000 particles in a single concentration determination). Therefore, the presence of a luminescence signal per well corresponds to a single particle that captured a biomarker molecule. If the number of particles with a single biomarker molecule is much larger than the number of particles with two or more biomarker molecules, the number of particles that show a luminescence signal scales directly with the biomarker concentration.

Figure 1.2c schematically shows a single-molecule biosensing tech-

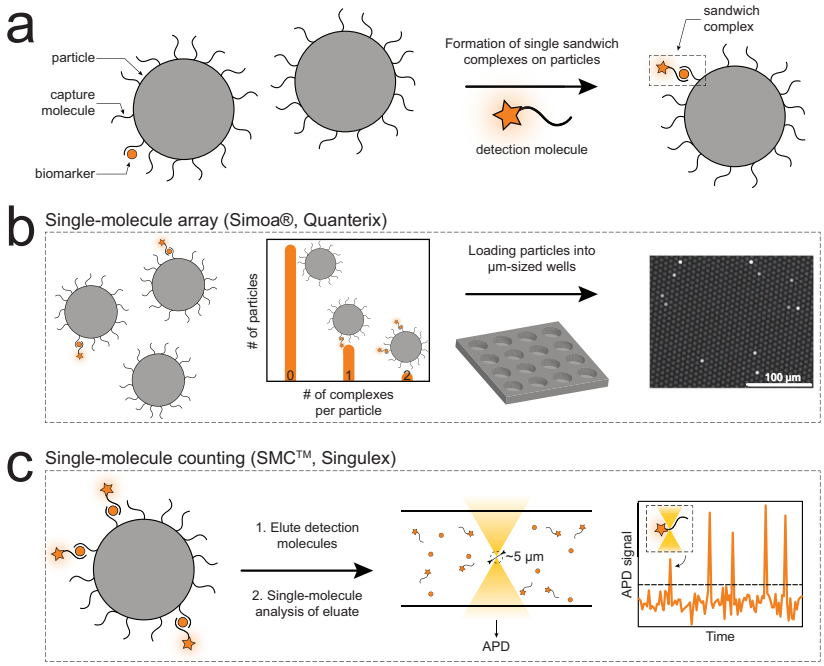

Figure 1.2: single-molecule biosensing methods for biomolecular concentration quantification with a high sensitivity. (a) General sandwich type assay on micrometer-sized particles which are functionalized with capture molecules. The particles are incubated with the biomarker of interest, which results in biomarker-capture molecule complexes on the particles. Since an excess of particles is used, the equilibrium is towards the biomarker-capture molecule complexes. Subsequently, sandwich complexes are formed by adding labeled detection molecules specific for the biomarker of interest. (b) Single-molecule array (Simoa®) technology used to read out the luminescence signal of the detection molecules. The probability that a particle contains zero, one, or more sandwich complexes, follows a Poisson distribution. The signal is proportional to the biomarker concentration when the average number of sandwich complexes per particle is low. By loading the particles into micrometer-sized (~fL) wells, the luminescence signal of a single particle can be measured as a digital "on" and "off" signal. Due to the fact that a femtoliter detection space and a high degree of parallelization (~50,000 particles) are possible, a concentration quantification with a limit of detection down to ~1 fg mL^{-1} for various markers could be reached.[47] Panel adapted from Rissin *et al.*[44] (c) Single-molecule counting (SMC™) technology used to read out a fluorescence signal of the detection molecules. The formed sandwich complex on the particle is eluted after which the eluate, containing the detection molecules and biomarker molecules, is separated from the particles. Subsequently, the eluate is analyzed using a confocal laser beam with an excitation volume of roughly 5 µm (~fL).[48] To obtain high counting statistics, a static confocal laser beam and capillary flow, or a scanning confocal laser beam is used. The fluorescence signal of a detection molecule passing through the excitation volume measured using an avalanche photodiode (APD), results in a sharp peak in the APD signal. Due to the small excitation volume and the fast sequential measurements, a concentration quantification with a limit of detection down to ~10 fg mL^{-1} for various markers could be reached.[47]

nique using SMC™, again illustrated for a sandwich assay. After eluting the detection molecules from the sandwich complexes formed on the particle, single detection molecules are observed using a focused laser beam in combination with an avalanche photodiode (APD) detector. The passing of detection molecules through the excitation volume of the focused laser beam results in sharp peaks in the APD signal. To

achieve subdiffusional times before a detection molecule is observed, a capillary flow[45,46] or a scanning confocal laser beam[48] is used.

1.2.3 *Continuous biomolecular monitoring with single-molecule resolution*

A continuous biomolecular monitoring method with single-molecule resolution, developed at Eindhoven University of Technology, is biosensing by particle mobility (BPM).[49–51] In Figure 1.3, the sensing principle is schematically visualized. In a BPM assay, the particles are tethered to a surface by a flexible molecular tether, causing every particle to move due to thermal motion within a confined space which is restricted by the tether. The sensing capability of the particles is derived from binder molecules on the particle (*cf.* Figure 1.2a, capture molecules) and multiple binder molecules on the planar substrate (*cf.* Figure 1.2a, detection molecules), see Figure 1.3a,[49,50] or a single binder molecule on the molecular tether (not shown here).[51] Biomarker molecules in solution can bind to the particle binder molecules and subsequently to the substrate binder molecules. When such a compact molecular

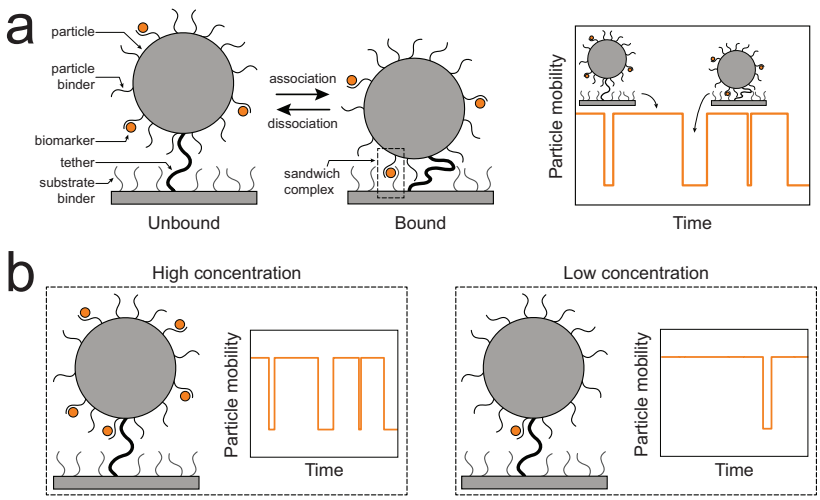

FIGURE 1.3: MOLECULAR DESIGN AND MEASUREMENT PRINCIPLE OF BIOSENSING BY PARTICLE MOBILITY (BPM). (a) Micrometer-sized particles (gray) are tethered to a substrate using a flexible molecular tether (black). The particle is functionalized with particle binder molecules (black lines) and multiple substrate binder molecules (gray lines) on the planar surface. Both particle binder and substrate binder molecules can reversibly bind to single biomarker molecules (orange) present in solution. Biomarker molecules binding to the binder molecules on the particle and subsequently binding and unbinding to the binder molecules on the substrate cause the particle to exhibit either of two concentric Brownian motion patterns, corresponding to the unbound state (high mobility) and bound state (low mobility). (b) Digital binding and unbinding events are identified by following the mobility of the hundreds of particles over time and subsequently used for concentration determination. For a high or low target concentration in solution, the microparticle shows a high or a low switching frequency respectively.

sandwich complex is formed (*cf.* Figure 1.2a, sandwich complex), the motion of the particle is strongly restricted. The molecular interactions between the particle binder molecule, biomarker molecule, and the substrate binder molecule are designed to be reversible, causing unbound and bound particle states to be observed over time. In the particular design visualized in Figure 1.3a, for a high biomarker concentration, the mean unbound state lifetime of a particle decreases when the number of captured biomarker molecules on the particle increases, see Figure 1.3b. Therefore, the average switching frequency of particles between unbound and bound states increases with an increasing biomarker concentration. For a low biomarker concentration, the number of biomarker molecules bound to the particle is small, resulting in a low switching frequency.

Figure 1.4 shows a matrix scheme that illustrates the developments in the field of biosensing. The scheme highlights the development toward single-molecule resolution on the x-axis (to achieve a higher sensitivity) and developments toward continuous monitoring on the y-axis (to obtain real time insight). The BPM technology is being developed to realize the monitoring functionality for biomolecules at low concentrations (orange arrow).

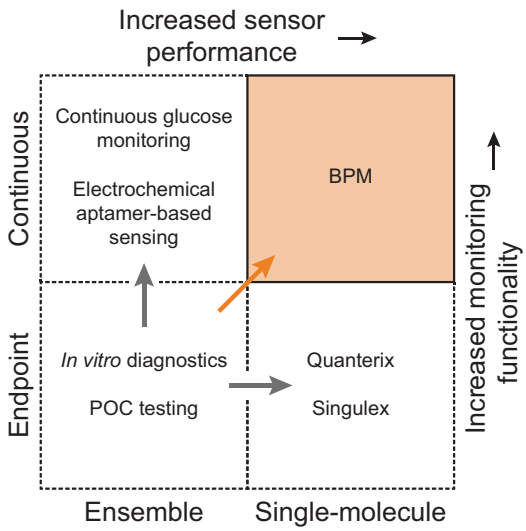

Figure 1.4: Conceptual overview of the developments in the field of biosensing. With *in vitro* diagnostics and POC testing as starting points, continuous monitoring biosensors are being developed (vertical gray arrow) as well as biosensing systems with single-molecule resolution for measuring biomarkers at low concentrations (horizontal gray arrow). The BPM technology is being developed to realize both aspects: continuous monitoring functionality with single-molecule resolution, for the monitoring of biomolecules at low concentrations (orange arrow).

1.3 CHALLENGES IN CONCENTRATION DETERMINATION USING SINGLE-MOLECULE QUANTITATION

Applying single-molecule techniques to biosensing, poses three main challenges which have to be overcome to be able to quantify biomarker concentrations accurately and precisely. These challenges are dictated by (1) the biomarker concentration, (2) diffusion of the biomarker molecule, and (3) by the free-energy landscape of the biomarker molecule with its corresponding receptor molecule.

First, the detection volume needs to be small enough so that single molecules can be detected reliably. This is achieved by reducing the detection space (*cf.* Figure 1.2), *e. g.*, by using small detection volumes (compartmentalization)[44–46] or surfaces (surface immobilization).[52,53]

Second, molecules need to travel into the detection volume, which takes time. At low concentrations, the intermolecular distance is so large that the typical diffusion time from one molecule to the other is long. This diffusion time results in prolonged times before molecules of interest diffuse into the detection volume where detection is possible. Example calculations to quantify this challenge using a typical diffusion time[52,54] are given in Figure 1.5, assuming a protein molecule with a molecular weight of 50 kDa and a corresponding diffusion coefficient $D = 10^{-10}$ m² s⁻¹, detected in a detection volume of 1 fL, *i. e.*, 1 µm³ (note that a molecular binding process is not included in these calculations). With these conditions, concentrations of a femtomolar and lower result in a typical diffusion time of several minutes before a single molecule enters the detection volume, and thus resulting in a long assay time. Besides this long assay time, the occurrence of stochastic events itself form an intrinsic problem for single-molecule quantitation: first, the number of sampled molecules in the detection volume should reflect the concentration in the bulk, and second, the precision of the concentration determination needs to be high. To achieve both, enough molecules have to be detected in order to accurately and precisely determine the bulk concentration. Solutions to detect many molecules within a short period of time are a high degree of parallelization (*cf.* Figure 1.2b and Figure 1.3)[44,49–51] or decreasing the time for a molecule to enter the detection volume and therefore enabling fast sequential measurements (*cf.* Figure 1.2c).[45,46,48]

Third, the binding of biomarkers to specific receptors requires time, determined by kinetic and thermodynamic properties of the molecules. Here, reaction mechanisms of association and dissociation of molecules determine the response time of the signals. Binder molecules, such as

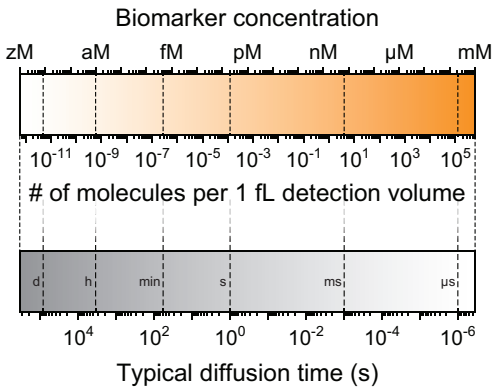

FIGURE 1.5: CHALLENGES IN SINGLE-MOLECULE BIOSENSING. Top: biomarker concentration (orange gradient) and the number of molecules for a detection volume of 1 fL. Bottom: typical diffusion time (gray gradient) for molecules to enter the detection volume, assuming a protein of 50 kDa with a diffusion coefficient $D = 10^{-10}$ m² s⁻¹.

antibodies, can have equilibrium dissociation constants down to a few picomolar resulting in slow reaction kinetics at low concentrations.[55,56] Here, the kinetic properties and concentrations of biomarkers and binder molecules need to be taken into account in order to determine the time-dependence of the observed signals.

1.4 BIOSENSOR SENSITIVITY: ENSEMBLE *versus* SINGLE-MOLECULE READ OUT

In this section, we want to address the question how the sensitivity of a biomolecular assay is improved using a single-molecule read out compared to an ensemble read out. Assume a particle-based assay where each particle has roughly 10^5 binder molecules that are specific for the biomarker of interest, hereafter referred to as analyte, and where 10^4 particles generate the observed signal. In case of first-order affinity binding under equilibrium conditions and infinite supply of analyte molecules, the fraction f_b^a of binder molecules that captured an analyte molecule can be calculated by:

$$f_b^a = \frac{C_{a,0}}{C_{a,0} + K_d} \tag{1.1}$$

with $C_{a,0}$ being the analyte concentration and K_d the equilibrium dissociation constant. We assume that the observed signal S scales directly with f_b^a (*i. e.*, we can directly observe the analyte-binder complexes), which yields the dose-response curve described by:

$$S = S_{bg} + (1 - S_{bg})\frac{C_{a,0}}{C_{a,0} + K_d} \tag{1.2}$$

with S_{bg} being the background signal. Figure 1.6 shows how the shape of the dose-response curve, described by Equation 1.2, and the error of the measured signal influence the precision of the concentration determination. In Figure 1.6a, two dose-response curves are given for an assay without any background (orange solid line) and with 10% background signal (orange dashed line). The background signal changes the slope of the dose-response curve in particular at low concentrations (see inset). The error of the observed signal σ_S can be calculated by including a stochastic error σ_{stoch} due to the discrete nature of binder and analyte molecules, a background error σ_{bg}, and an error σ_{other} that is caused by other sources of variability than stochastics and the background signal:

$$\sigma_S^2 = \sigma_{\text{stoch}}^2 + \sigma_{bg}^2 + \sigma_{\text{other}}^2 \tag{1.3}$$

The background error σ_{bg} can be measured directly and is used in the definition of the limit of detection (LoD, gray dashed line) which is the concentration at which the signal is equal to $S_{bg} + 3\sigma_{bg}$. The error σ_{other} can be estimated based on heterogeneities in the measurement system, such as heterogeneity in particle size, *i. e.*, $\sigma_{\text{other}} = S \cdot CV_{\text{other}}$ where CV_{other} is the coefficient of variation of the heterogeneity present in the assay, *e. g.*, heterogeneity in particle size. The stochastic error σ_{stoch} can be calculated using the number of binder molecules that have captured an analyte molecule:

$$\sigma_{\text{stoch}} = \frac{1}{\sqrt{f_a^b A_s \Gamma_b}} = \frac{1}{\sqrt{f_a^b N_p N_b^{\text{particle}}}} \tag{1.4}$$

with A_s being the sensor area over which the signal is collected, Γ_b is the total binder density, N_p the number of observed particles, N_b^{particle} the number of binder molecules per particle. To determine how precise a concentration determination is, the concentration error σ_C needs to be calculated by projecting the signal error σ_S that results from Equation 1.3 on the dose-response curve, using the slope of the dose-response curve (see Figure 1.6b). In the absence of background, this slope is approximately linear at low concentrations, while this slope becomes sublinear at high concentrations, resulting in increased concentration errors.

In Figure 1.7 the influence of the error contributors, as defined in Equations 1.3 and 1.4, on the coefficient of variation CV_C of the

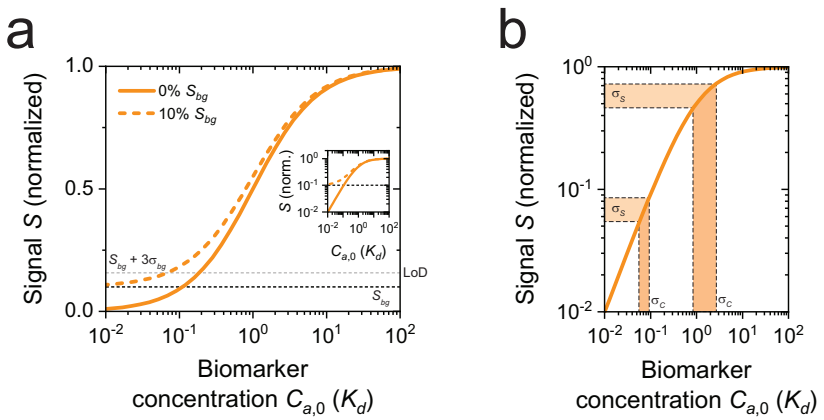

FIGURE 1.6: PROPAGATION OF AN ERROR OF THE SIGNAL TO A PRECISION OF THE CONCENTRATION DETERMINATION. (a) Dose-response curves with the normalized signal S as a function of analyte concentration $C_{a,0}$, in case of equilibrium conditions and infinite supply of analyte molecules, in absence of any background (solid orange line) or with a 10% background signal S_{bg} (dashed orange line). The inset shows the same data on a logarithmic-logarithmic scale. A background signal S_{bg} (dashed black line) changes the slope of the dose-response curve at low analyte concentrations while the background error σ_{bg} induces an imprecision in the slope of the dose-response curve. The limit of detection (LoD, dashed gray line) is defined as $S_{bg} + 3\sigma_{bg}$. (b) Estimating the concentration error σ_C using the signal error σ_S and the slope of the dose-response curve. At low concentrations, the slope of the dose-response curve is approximately linear (in absence of background signal). At high concentrations, the slope of the dose-response curve is sublinear which results in an increased concentration error σ_C.

concentration, as a measure of precision, defined as $CV_C = \sigma_C / C_{a,0}$, is shown. The CV_C is given as a function of the analyte concentration $C_{a,0}$ for a background signal S_{bg} (left), a corresponding background error σ_{bg} (middle) and error σ_{other} (right). Here the limit of quantification (LoQ, black dashed line) is given, which is the concentration where the concentration determination has a precision of 10%.

Under the assumption that we can determine any background signal infinitely precise, the presence of this background signal induces an increased concentration error σ_C (see left graph) by a change of the shape of the dose-response curve (*cf.* Figure 1.6a). This results in a decreased precision of the concentration determination in particular at low concentrations (*i. e.*, an increased CV_C), since here the signal has to be distinguished from a relatively high background signal. In contrast, at high concentrations, the majority of the observed signal is generated by the analyte-binder complexes and thus the precision is not limited by the background signal.

Let us now assume that the background signal has an error σ_{bg} of 1% (*i. e.*, $\sigma_{bg} = S_{bg}/100$). Since the shape of the dose-response curve is based on the measured background signal, the precision of this

background measurement has a large influence on the precision over the full concentration range (see middle graph). The background error has a slightly larger influence on the precision at low concentrations since here the influence of the background itself is larger (*cf.* left graph).

Lastly, other sources of variabilities present in the system result in additional variations in the concentration determination. Here, we assume an error σ_{other} of 1% (*i. e.*, $\sigma_{\text{other}} = S_{bg}/100$). This total error σ_{other} caused by these sources of variability, mostly influences the higher concentration determinations, since the signal is high and the contributions of the stochastic and background errors are relatively small, *i. e.*, $\sigma_{\text{other}} \gg \sigma_{\text{stoch}}, \sigma_{bg}$ (see right graph).

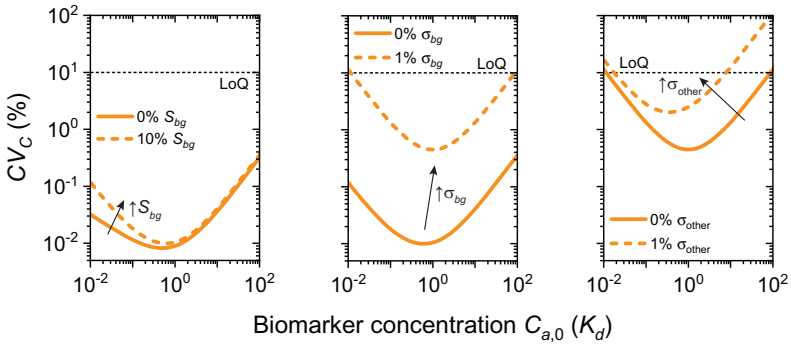

FIGURE 1.7: INFLUENCE OF ERROR CONTRIBUTORS ON THE PRECISION OF A CONCENTRATION DETERMINATION. Left: influence of background signal on the precision of a concentration determination in the absence of background (orange solid line) and with 10% background signal (orange dashed line). Middle: influence of background error on the precision of a concentration determination for no error (orange solid line) and 1% error (orange dashed line). Right: influence of the error caused by other sources of variability for no error (orange solid line) and 1% error (orange dashed line).

Now we can address the question how the precision of a concentration determination depends on the level of read out of a particle-based affinity assay. In Figure 1.8, three read out modes are sketched. First, an ensemble read out mode where the observed signal is generated by a large number of particles. Second, a single-particle read out mode where the observed signal is distinguished per particle. Third, a single-molecule read out mode, where the observed signal is distinguished per molecule resulting in digital quantitation. For the ensemble read out mode, the corresponding dose-response curve is equal to the curve given in Figure 1.6a and Equation 1.1. At low concentrations, the precision is mainly determined by the background signal, while at high concentrations the precision is mainly determined by saturation of the binders. For a single-particle read out where the observed signal is distinguished per particle, the detection sensitivity needs to be higher

compared to the ensemble read out mode. The concentration precision at high concentrations is determined by either saturation of the binders, or signal saturation of the reader and/or transduction method. Here, an EC_{50}, *i. e.*, the concentration at which the signal is 50%, was assumed to be 1% of the K_d, effectively shifting the dose-response curve to lower concentrations. For a single-molecule read out, we assumed that the observed signal is the fraction of particles that show a signal (*e. g.*, a luminescence or fluorescence signal, *cf.* Figure 1.2). At low concentrations the precision of the concentration determination is determined by the number of observed molecules (*i. e.*, the precision is limited by stochastics), while at high concentrations the precision is determined by saturation since no distinction between one, two, three molecules can be made. The shift of the dose-response curve in the direction of the negative x-axis depends on the number of particles and the number of binder molecules per particle.

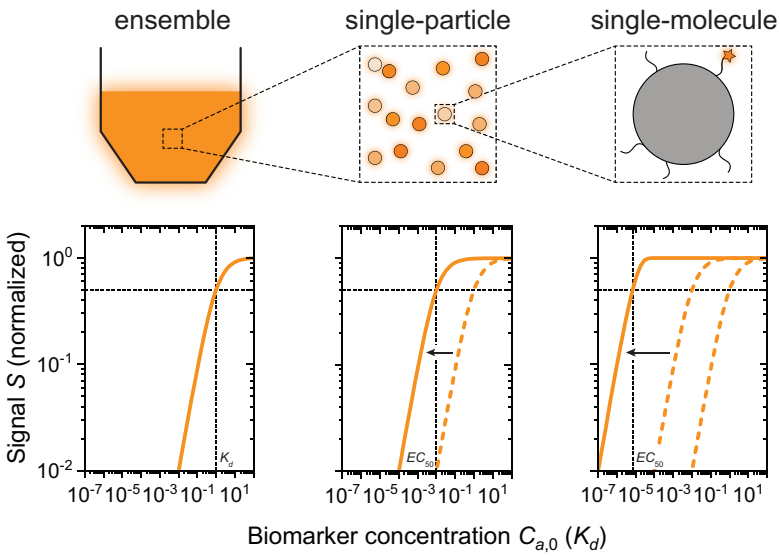

FIGURE 1.8: THREE READ OUT MODES OF A BIOMOLECULAR PARTICLE-BASED AFFINITY ASSAY WITH THEIR CORRESPONDING DOSE-RESPONSE CURVE. Left: ensemble read out mode yields a dose-response curve which is located around the K_d value. Middle: single-particle read out mode results in an EC_{50} which can be several orders of magnitude lower than the K_d value of the binders on the particle. Right: single-molecule read out yields a high precision at the lowest concentration since the signal generated by single-molecules can be distinguished, resulting in digital quantitation. The EC_{50} with respect to the K_d value depends on the number of observed particles and the number of binder molecules per particle. Here the number of particles $N_p = 10^4$ and number of binder molecules per particle $N_b = 10^5$.

Figures 1.6-1.8 show quantitatively with simple calculations the potential increase in sensitivity by designing an assay with a single-particle or single-molecule read out mode instead of an ensemble read

out mode. The precision of the assay can be increased, where an EC_{50} of more than five orders of magnitude below the K_d value can be achieved. Besides, assays with multiple read out modes, such as Simoa®,[44] have the potential of using these multiple read out modes to increase the dynamic concentration range over which concentration determinations with a high precision can be performed. For both advantages, the key challenge in assay development is to design an assay which yields a highly precise signal generated by only a limited number of analyte-binder complexes, using specific chemistries and efficient receptor molecules and transduction methods.

1.5 OUTLINE OF THE THESIS

The goal of this thesis is to study analytical functionalities that can be achieved in continuous biomolecular sensing with single-molecule resolution. The thesis focuses on two main topics. First, Chapters 2 and 3 describe new applications of single-molecule information within the field of biosensing. It has been shown that a single-molecule resolution can be used to enable multiplexing functionalities and to quantify heterogeneities and their consequences. Second, Chapters 4 and 5 focus on the speed, sensitivity and precision functionalities of continuous biomolecular monitoring sensors in the limit of single-molecule resolution.

In Chapter 2 we demonstrate a new application of single-molecule detection in continuous monitoring, namely multiplexing by means of single-molecule kinetic identification of single particles. Here, multiplexing is enabled by an analyte-sensitive, single-molecular nanoswitch with a particle as a reporter. We demonstrate by experiments and simulations, using BPM as an example, multiplexed continuous monitoring of oligonucleotides at picomolar concentrations.

In Chapter 3 we present a framework to study the influence of heterogeneities, focused on particle-based biosensing applications. Using single-molecule techniques (DNA-PAINT, qPAINT and BPM), the underlying distributions in particle reactivity are quantified by counting and spatially mapping individual binder molecules on particles, and by measuring the resulting reactivity of single particles. By combining experimental results and simulations, the influence of various heterogeneities and the collective effect of all heterogeneities on the reactivity of particles is studied as a function of biosensor system parameters, such as particle interaction area, binder molecule density, particle size and number of particles.

In Chapter 4 we present a sensing methodology that enables rapid monitoring of low-concentration biomolecules. We demonstrate using simulations and experiments that this sensing methodology is suitable for monitoring picomolar and sub-picomolar concentrations, with measurement intervals of a few minutes, and in principle for sensing over an endless time span, where continuous monitoring biosensors with a single-molecule resolution are advantageous for obtaining a high sensitivity.

In Chapter 5 we investigate continuous biomolecular analyte exchange between a dynamic system of interest and the measurement chamber of a biosensor. For this, we simulate mass transport and surface reactions, where an oscillating concentration-time profile is used as input. Subsequently we quantify the time lag of the measured concentration and the precision of the biosensor as a function of system parameters, such as measurement chamber geometries and flow rates. This enables researchers to rationally design a biomolecular monitoring system with a desired biosensor performance for specific applications such as monitoring low-concentration biomarkers.

Lastly, Chapter 6 summarizes the main findings in this thesis and sketches the outlines of further research in the field of continuous monitoring applications and the added value of single-molecule techniques to enhance sensing performance.

1.6 REFERENCES

1. Turner, A. P. F., Karube, I. & Wilson, G. S. *Biosensors: Fundamentals and Applications* (Oxford University Press, 1989).
2. Sadana, A. & Sadana, N. *Handbook of Biosensors and Biosensor Kinetics* (Elsevier, 2011).
3. Zourob, M. *Recognition Receptors in Biosensors* (Springer, 2010).
4. Turner, A. P. F. Biosensors: Sense and Sensibility. *Chemical Society Reviews* **42,** 3184–3196 (2013).
5. Turner, A. P. F. Biosensors - Sense and Sensitivity. *Science* **290,** 1315–1317 (2000).
6. Vandenberg, O., Martiny, D., Rochas, O., Belkum, A. V. & Kozlakidis, Z. Considerations for Diagnostic COVID-19 Tests. *Nature Reviews Microbiology* **19,** 171–183 (2021).
7. Everitt, M. L., Tillery, A., David, M. G., Singh, N., Borison, A. & White, I. M. A Critical Review of Point-of-Care Diagnostic Technologies to Combat Viral Pandemics. *Analytica Chimica Acta* **1146,** 184–199 (2021).
8. Nayak, S., Blumenfeld, N. R., Laksanasopin, T. & Sia, S. K. Point-of-Care Diagnostics: Recent Developments in a Connected Age. *Analytical Chemistry* **89,** 102–123 (2017).
9. Dincer, C., Bruch, R., Kling, A., Dittrich, P. S. & Urban, G. A. Multiplexed Point-of-Care Testing – xPOCT. *Trends in Biotechnology* **35,** 728–742 (2017).
10. St. John, A. & Price, C. P. Existing and Emerging Technologies for Point-of-Care Testing. *The Clinical Biochemist Reviews* **35,** 155–167 (2014).
11. Vashist, S. K., Luppa, P. B., Yeo, L. Y., Ozcan, A. & Luong, J. H. Emerging Technologies for Next-Generation Point-of-Care Testing. *Trends in Biotechnology* **33,** 692–705 (2015).
12. Zarei, M. Portable Biosensing Devices for Point-of-Care Diagnostics: Recent Developments and Applications. *Trends in Analytical Chemistry* **91,** 26–41 (2017).
13. Vashist, S. K., Venkatesh, A., Schneider, E. M., Beaudoin, C., Luppa, P. B. & Luong, J. H. Bioanalytical Advances in Assays for C-Reactive Protein. *Biotechnology Advances* **34,** 272–290 (2016).
14. Bruls, D. M. *et al.* Rapid Integrated Biosensor for Multiplexed Immunoassays Based on Actuated Magnetic Nanoparticles. *Lab on a Chip* **9,** 3504–3510 (2009).
15. Ates, H. C., Brunauer, A., Stetten, F., Urban, G. A., Güder, F., Merkoçi, A., Früh, S. M. & Dincer, C. Integrated Devices for Non-Invasive Diagnostics. *Advanced Functional Materials* **31,** 2010388 (2021).
16. Li, J., Liang, J. Y., Laken, S. J., Langer, R. & Traverso, G. Clinical Opportunities for Continuous Biosensing and Closed-Loop Therapies. *Trends in Chemistry* **2,** 319–340 (2020).

17. Heikenfeld, J., Jajack, A., Feldman, B., Granger, S. W., Gaitonde, S., Begtrup, G. & Katchman, B. A. Accessing Analytes in Biofluids for Peripheral Biochemical Monitoring. *Nature Biotechnology* **37,** 407–419 (2019).

18. Kim, J., Campbell, A. S., Esteban-Fernández de Ávila, B. & Wang, J. Wearable Biosensors for Healthcare Monitoring. *Nature Biotechnology* **37,** 389–406 (2019).

19. Heikenfeld, J., Jajack, A., Rogers, J., Gutruf, P., Tian, L., Pan, T., Li, R., Khine, M., Kim, J. & Wang, J. Wearable Sensors: Modalities, Challenges, and Prospects. *Lab on a Chip* **18,** 217–248 (2018).

20. Christodouleas, D. C., Kaur, B. & Chorti, P. From Point-of-Care Testing to eHealth Diagnostic Devices (eDiagnostics). *ACS Central Science* **4,** 1600–1616 (2018).

21. Rodbard, D. Continuous Glucose Monitoring: A Review of Successes, Challenges, and Opportunities. *Diabetes Technology & Therapeutics* **18,** S3–S13 (2016).

22. Umpierrez, G. E. & Klonoff, D. C. Diabetes Technology Update: Use of Insulin Pumps and Continuous Glucose Monitoring in the Hospital. *Diabetes Care* **41,** 1579–1589 (2018).

23. Rassaei, L., Olthuis, W., Tsujimura, S., Sudhölter, E. J. R. & van den Berg, A. Lactate Biosensors: Current Status and Outlook. *Analytical and Bioanalytical Chemistry* **406,** 123–137 (2014).

24. Ferguson, B. S. *et al.* Real-Time, Aptamer-Based Tracking of Circulating Therapeutic Agents in Living Animals. *Science Translational Medicine* **5,** 213ra165 (2013).

25. Moerner, W. E. & Kador, L. Optical Detection and Spectroscopy of Single Molecules in a Solid. *Physical Review Letters* **62,** 2535–2538 (1989).

26. Orrit, M. & Bernard, J. Single Pentacene Molecules Detected by Fluorescence Excitation in a p-Terphenyl Crystal. *Physical Review Letters* **65,** 2716–2719 (1990).

27. Gell, C., Brockwell, D. & Smith, A. *Handbook of Single Molecule Fluorescence Spectroscopy* (Oxford University Press, 2006).

28. Van den Wildenberg, S. M. J. L., Prevo, B. & Peterman, E. J. G. in *Single Molecule Analysis: Methods and Protocols* chap. A Brief Introduction to Single-Molecule Fluorescence Methods (Springer, 2011).

29. Walter, N. G., Huang, C.-Y., Manzo, A. J. & Sobhy, M. A. Do-It-Yourself Guide: How to Use the Modern Single-Molecule Toolkit. *Nature Methods* **5,** 475–489 (2008).

30. Hinterdorfer, P. & van Oijen, A. *Handbook of Single-Molecule Biophysics* (Springer, 2009).

31. Schafer, D. A., Gelles, J., Sheetz, M. P. & Landick, R. Transcription by Single Molecules of RNA Polymerase Observed by Light Microscopy. *Nature* **352,** 444–448 (1991).

32. Yin, H., Landick, R. & Gelles, J. Tethered Particle Motion Method for Studying Transcript Rlongation by a Single RNA Polymerase Molecule. *Biophysical Journal* **67,** 2468–2478 (1994).

33. Finzi, L. & Gelles, J. Measurement of Lactose Repressor-Mediated Loop Formation and Breakdown in Single DNA Molecules. *Science* **267,** 378–380 (1995).

34. Smith, S. B., Finzi, L. & Bustamante, C. Direct Mechanical Measurements of the Elasticity of Single DNA Molecules by Using Magnetic Beads. *Science* **258,** 1122–1126 (1992).

35. Strick, T. R., Allemand, J. F., Bensimon, D., Bensimon, A. & Croquette, V. The Elasticity of a Single Supercoiled DNA Molecule. *Science* **271,** 1835–1837 (1996).

36. Smith, S. B., Cui, Y. & Bustamante, C. Overstretching B-DNA: The Elastic Response of Individual Double-Stranded and Single-Stranded DNA Molecules. *Science* **271,** 795–799 (1996).

37. Zlatanova, J., Lindsay, S. M. & Leuba, S. H. Single Molecule Force Spectroscopy in Biology Using the Stomic Force Microscope. *Progress in Biophysics and Molecular Biology* **74,** 37–61 (2000).

38. Buszko, M., Nita-Lazar, A., Park, J.-H., Schwartzberg, P. L., Verthelyi, D., Young, H. A. & Rosenberg, A. S. Lessons Learned: New Insights on the Role of Cytokines in COVID-19. *Nature Immunology* **22,** 404–411 (2021).

39. Fajgenbaum, D. C. & June, C. H. Cytokine Storm. *New England Journal of Medicine* **383,** 2255–2273 (2020).

40. Chen, P., Huang, N.-T., Chung, M.-T., Cornell, T. T. & Kurabayashi, K. Label-Free Cytokine Micro- and Nano-Biosensing towards Personalized Medicine of Systemic Inflammatory Disorders. *Advanced Drug Delivery Reviews* **95,** 90–103 (2015).

41. Duffy, D. Standardized Immunomonitoring: Separating the Signals from the Noise. *Trends in Biotechnology* **36,** 1107–1115 (2018).

42. Wilson, B. D. & Soh, H. T. Re-Evaluating the Conventional Wisdom about Binding Assays. *Trends in Biochemical Sciences* **45,** 639–649 (2020).

43. Ricci, F., Vallée-Bélisle, A., Simon, A. J., Porchetta, A. & Plaxco, K. W. Using Nature's "Tricks" To Rationally Tune the Binding Properties of Biomolecular Receptors. *Accounts of Chemical Research* **49,** 1884–1892 (2016).

44. Rissin, D. M. *et al.* Single-Molecule Enzyme-Linked Immunosorbent Assay Detects Serum Proteins at Subfemtomolar Concentrations. *Nature Biotechnology* **28,** 595–599 (2010).

45. Wu, A. H., Fukushima, N., Puskas, R., Todd, J. & Goix, P. Development and Preliminary Clinical Validation of a High Sensitivity Assay for Cardiac Troponin Using a Capillary Flow (Single Molecule) Fluorescence Detector. *Clinical Chemistry* **52,** 2157–2159 (2006).

46. Todd, J., Freese, B., Lu, A., Held, D., Morey, J., Livingston, R. & Goix, P. Ultrasensitive Flow-Based Immunoassays Using Single-Molecule Counting. *Clinical Chemistry* **53,** 1990–1995 (2007).

47. Marin, M. & Van Wijk, X. in *Biomarkers for Traumatic Brain Injury* chap. Sensitive Immunoassay Testing Platforms (2020).

48. *Single Molecule Counting (SMC™) Technology,* accessed on 11 October 2021. https://www.sigmaaldrich.com/NL/en/products/protein-biology/immunoassay-platform-solutions/single-molecule-counting-technology.

49. Visser, E. W. A., Yan, J., van IJzendoorn, L. J. & Prins, M. W. J. Continuous Biomarker Monitoring by Particle Mobility Sensing with Single Molecule Resolution. *Nature Communications* **9,** 2541 (2018).

50. Yan, J., van Smeden, L., Merkx, M., Zijlstra, P. & Prins, M. W. J. Continuous Small-Molecule Monitoring with a Digital Single-Particle Switch. *ACS Sensors* **5,** 1168–1176 (2020).

51. Lubken, R. M., de Jong, A. M. & Prins, M. W. J. Multiplexed Continuous Biosensing by Single-Molecule Encoded Nanoswitches. *Nano Letters* **4,** 2296–2302 (2020).

52. Gooding, J. J. & Gaus, K. Single-Molecule Sensors: Challenges and Opportunities for Quantitative Analysis. *Angewandte Chemie International Edition* **55,** 11354–11366 (2016).

53. Jungmann, R., Avendaño, M. S., Dai, M., Woehrstein, J. B., Agasti, S. S., Feiger, Z., Rodal, A. & Yin, P. Quantitative Super-Resolution Imaging with qPAINT. *Nature Methods* **13,** 439–442 (2016).

54. Holzmeister, P., Acuna, G. P., Grohmann, D. & Tinnefeld, P. Breaking the Concentration Limit of Optical Single-Molecule Detection. *Chemical Society Reviews* **43,** 1014–1028 (2014).

55. Kamat, V., Rafique, A., Huang, T., Olsen, O. & Olson, W. The Impact of Different Juman IgG Capture Molecules on the Kinetics Analysis of Antibody-Antigen Interaction. *Analytical Biochemistry* **593,** 113580 (2020).

56. Yang, D., Singh, A., Wu, H. & Kroe-Barrett, R. Dataset of the Binding Kinetic Rate Constants of Anti-PCSK9 Antibodies Obtained Using the Biacore T100, ProteOn XPR36, Octet RED384, and IBIS MX96 Biosensor Platforms. *Data in Brief* **8,** 1173–1183 (2016).

2

MULTIPLEXED CONTINUOUS BIOSENSING BY SINGLE-MOLECULE ENCODED NANOSWITCHES

ABSTRACT: Single-molecule techniques have become impactful in the bioanalytical sciences, though the advantages for continuous biosensing are yet to be discovered. In this chapter, we present a multiplexed, continuous biosensing method, enabled by an analyte-sensitive, single-molecular nanoswitch with a particle as a reporter. The nanoswitch opens and closes under the influence of single target molecules. This reversible switching yields binary transitions between two highly reproducible states, enabling reliable quantification of the single-molecule kinetics. The multiplexing functionality is encoded per particle *via* the dissociation characteristics of the nanoswitch, while the target concentration is revealed by the association characteristics. We demonstrate by experiments and simulations the multiplexed, continuous monitoring of oligonucleotide targets, at picomolar concentrations in buffer and in filtered human blood plasma.

Parts of this chapter have been published as: Lubken, R. M. *et al.* Multiplexed Continuous Biosensing by Single-Molecule Encoded Nanoswitches. *Nano Letters* **4,** 2296–2302 (2020).

2.1 INTRODUCTION

Single-molecule techniques have become impactful in the bioanalytical sciences because of their high detection sensitivity and digital quantitation.[1–3] However, in the upcoming field of sensors for continuous biomolecular monitoring,[4–8] the advantages of single-molecule methodologies are yet to be discovered. Multiplexing refers in the bioanalysis to the ability to measure multiple specific molecules in parallel. This is used to obtain comprehensive knowledge about biological systems and optimal diagnostic power in medical applications. Well-known methods for multiplexing are, for example, bead arrays,[9,10] real time PCR,[11] and DNA microarrays.[12] Here, samples are processed with mixtures of reagents and thereafter analyte-specific signals are measured in separate spectral channels or distinct positions. Such reagent-based multiplexing assays involve taking distinct samples and passing these through sequential processing steps. However, an ideal multiplexing methodology for real time monitoring does not require reagents nor complicated sample processing. Such a methodology would allow the generation of a continuous and uninterrupted stream of measurement data, over a prolonged period of time, in a simple and cost-effective manner.

In this chapter, we describe a novel methodology to achieve reagentless, multiplexed, continuous biomolecular sensing by single-molecule encoded binary nanoswitches. The molecular design and measurement principle are sketched in Figure 2.1, exemplified with a DNA model system. Figure 2.1a shows a micrometer-sized particle bound to a substrate by a single nanoswitch. The nanoswitch comprises three components: (1) a single double-stranded DNA (dsDNA) stem tethering the particle to the substrate; (2) a single probe attached to the dsDNA stem; and (3) multiple probes attached to the particle surface. The probe on the stem binds reversibly to target molecules that are captured from solution by the probes on the particle. The probe on the stem encodes the nanoswitch, because the interaction between this stem probe and the target molecules is designed to have a characteristic dissociation rate, which is the basis of the multiplexing functionality. In previous work, we studied sensor designs with less controlled numbers and orientations of probes on the substrate,[13] giving variable responses within and between particles. In the nanoswitch design of Figure 2.1, every particle has only a single probe, in a well-defined orientation on the central stem. Combined with the smooth spherical particle, unambiguous concentric Brownian motion patterns are obtained (see Figure 2.1b).

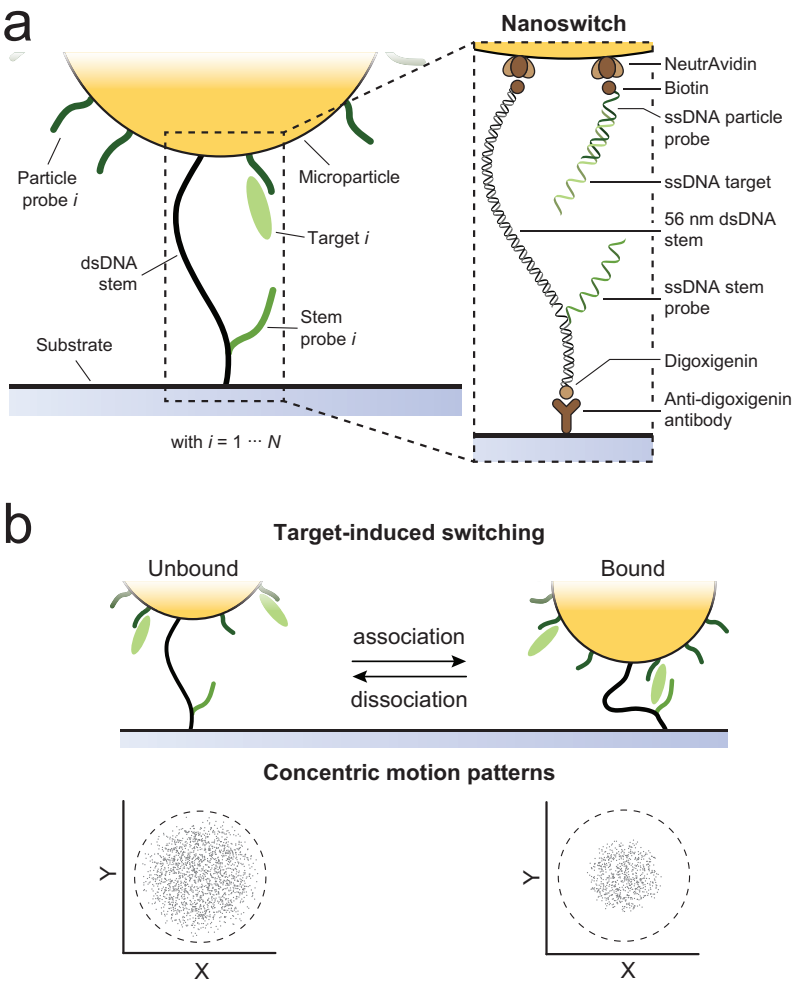

Figure 2.1: sensor concept with a single-molecule encoded binary nanoswitch. (a) Micrometer-sized particles (yellow) are tethered to a substrate using a 56 nm dsDNA stem (black). The particle is functionalized with particle probes of type *i* (dark green) and a single stem probe of type *i* (green). Both probes bind reversibly to a single target molecule of type *i* (light green) present in solution. The inset shows schematically the DNA-based nanoswitch conjugated to the particle by a NeutrAvidin–biotin interaction and to the substrate by an antibody–antigen (digoxigenin) interaction. A detailed overview of the DNA sequences is given in Supplementary note 2.5.1. (b) Target molecule binding to the nanoswitch causes the particle to exhibit either of two concentric motion patterns corresponding to the unbound (high mobility) and bound state (low mobility).

The Brownian motion patterns translate into time traces with binary transitions, from which unbound and bound state lifetimes, and therefore association and dissociation kinetic rates, are extracted at the single-particle level. The dissociation kinetics of each particle are a unique signature that identifies to which kinetic subpopulation the

particle belongs (index i or j, see Figure 2.2a). Hundreds of particles are measured simultaneously, each kinetically identified, and assigned to their specific subpopulation. In each subpopulation, the association rates are continuously measured. The effective association rate depends on the amount of target molecules captured on the particle. Thus, by using a differently kinetic encoded nanoswitch per particle subpopulation, the concentration of multiple specific analyte molecules can be recorded over time simultaneously (see Figure 2.2b).

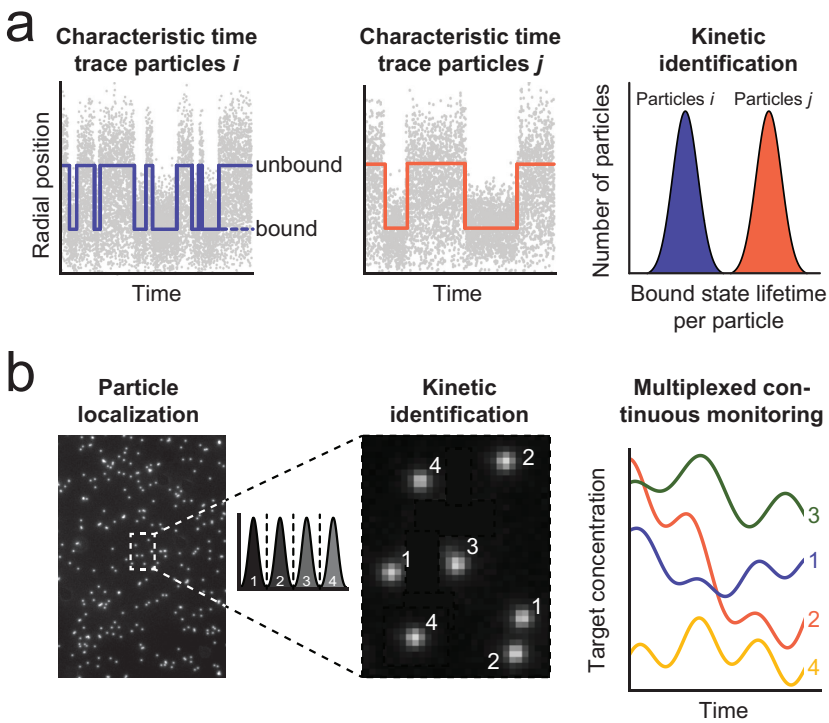

FIGURE 2.2: KINETIC IDENTIFICATION FOR MULTIPLEXED CONTINUOUS BIOMOLECULAR MONITORING. (a) Radial position of a particle over time shows binary transitions caused by single-molecule binding and unbinding events. The distribution of observed bound state lifetimes per particle can be used to distinguish between, *e.g.*, low-affinity (particles i, blue) and high-affinity (particles j, red) target-specific particle subpopulations, referred to as kinetic identification. Examples of raw data traces are shown in Supplementary note 2.5.2. (b) Hundreds of particles, each functionalized with an encoded binary nanoswitch, are observed simultaneously. By kinetic identification based on the dissociation kinetics, each particle can be assigned to a target-specific particle subpopulation. For each particle subpopulation, the respective target concentration can be determined over time using the measured association kinetics.

2.2 RESULTS AND DISCUSSION

Figure 2.3 illustrates the analytical performance and tunability of the stem probe sensor of Figure 2.1a. Figures 2.3a,b show the association

and dissociation rates measured in both buffer (a) and filtered blood plasma (b) for a single-stranded DNA target with a mid affinity to the particle probe. The mean bound state lifetime τ_B (red), determined by fitting all observed bound state lifetimes by a single-exponential distribution (see Supplementary note 2.5.3), is independent of the target concentration and of the matrix, which is the basis for the kinetic encoding strategy. In contrast, the mean unbound state lifetime τ_U shows a clear concentration dependency (blue); an increasing target concentration in solution results in a shorter τ_U as more target molecules are bound to the particle and therefore accessible for hybridization to the stem probe. In contrast to the dissociation kinetics, the association kinetics per particle show a broad distribution, indicating particle-to-particle variability. The mean unbound state lifetime τ_U could be determined by fitting all observed unbound state lifetimes by a lognormal multiexponential distribution (see Supplementary note 2.5.4). This method gives large errors at low statistics, which is particularly visible at low concentrations (see inset of Figure 2.3b). Figure 2.3c shows dose–response curves for DNA targets with different affinities. The signal plotted on the y-axis is the switching activity, the average number of binding and unbinding events per particle per time interval.[13] The dose–response curves exhibit an S-shape on a linear-logarithmic scale, which is characteristic for first-order affinity binding. The curves are fitted by the Hill equation:[14]

$$A = A_b + A_a \frac{[C]}{EC_{50} + [C]} \tag{2.1}$$

with A being the activity, A_b the background signal, A_a the activity amplitude (difference between the maximum signal and the background signal), EC_{50} the half maximal effective concentration, and $[C]$ the target concentration in solution. The curves shift to lower concentrations for an increasing affinity between target and particle probes, showing the tunability of the system. Figure 2.3d shows a dose–response curve measured for the mid-affinity target in blood plasma filtered with a 50 kDa molecular weight cutoff. Here, a similar EC_{50} was found, but a higher background activity and larger uncertainty were found, compared to its counterpart in buffer. The higher background activity and larger uncertainty are caused by more nonspecific interactions and lower statistics, respectively.

The response to dynamic changes in target concentration is quantified in Figure 2.4 for the low- and mid-affinity targets in buffer (a, b) and the mid-affinity target in blood plasma (c). The response to a sudden drop in target concentration can be described with a single-exponential

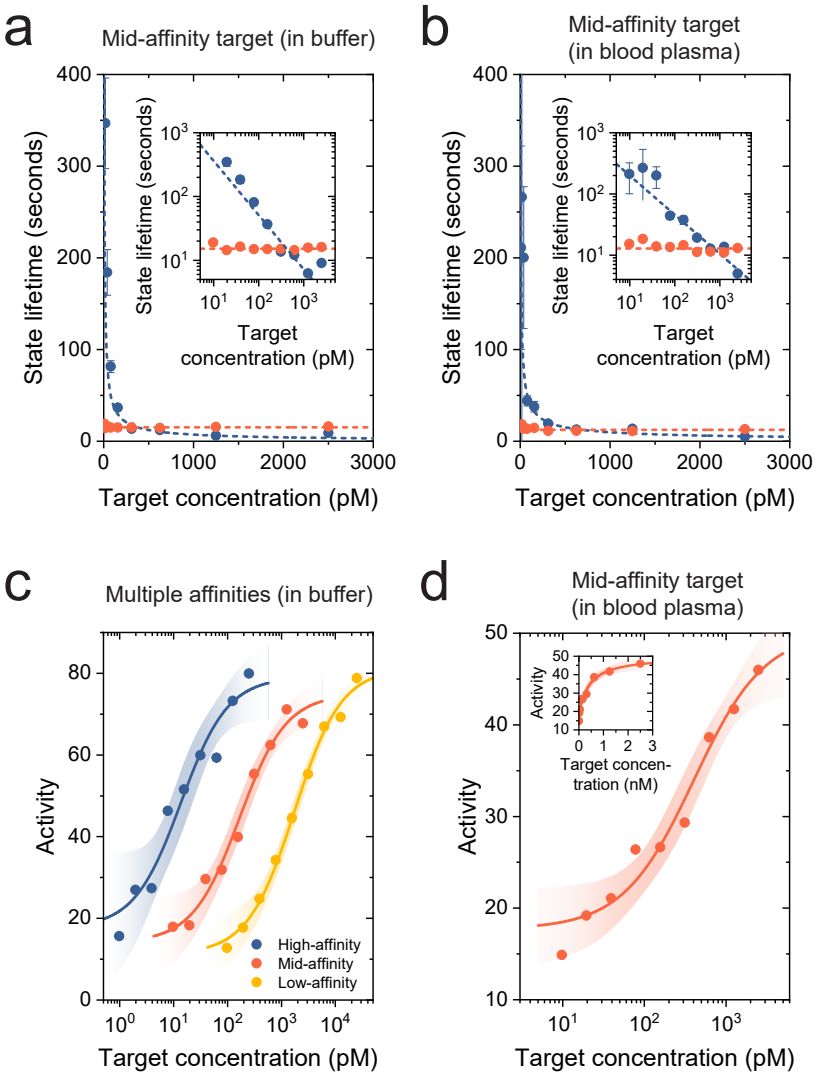

FIGURE 2.3: PERFORMANCE OF THE SENSOR CONCEPT WITH A SINGLE-MOLECULE ENCODED NANOSWITCH IN BUFFER AND BLOOD PLASMA. (a-b) Mid-affinity target concentration dependencies of the bound state lifetime τ_B (red) and the unbound state lifetime τ_U (blue). We observed that $\tau_B = 15.2 \pm 0.3$ s and $\tau_B = 12.5 \pm 0.5$ s, and τ_U scales approximately as $\tau_U \propto [T]^{-0.8\pm0.1}$ and $[T]^{-0.64\pm0.09}$ for buffer and blood plasma conditions respectively. (c) Dose-response curves of ssDNA targets in buffer, with a high-, mid- and low-affinity to the particle probe. Hill equation fits according to Equation 2.1 (solid lines) yield EC_{50} values of 14 ± 6 pM, 0.17 ± 0.05 nM and 1.7 ± 0.3 nM respectively. (d) Dose-response curve in blood plasma of the mid-affinity ssDNA target. Hill equation fit (solid line) yields EC_{50} of 0.4 ± 0.1 nM. The inset shows the data on a double linear scale. Reported errors are the standard errors of the fit. The error bars in the activity graphs are the stochastic errors and mostly smaller than the symbol size. The shading in the figures indicates the 95% confidence interval of the Hill equation fit according to Equation 2.1. The number of particles per data point was between 15 and 100, measured in two microscopic fields-of-view.

relaxation of the observed activity, with characteristic relaxation times of approximately 10 min for the low-affinity target and 40 min for the mid-affinity target. For the mid-affinity target, the single-exponential relaxation profiles in buffer and in blood plasma show comparable time scales within their uncertainty interval (see Figures 2.4b,c).

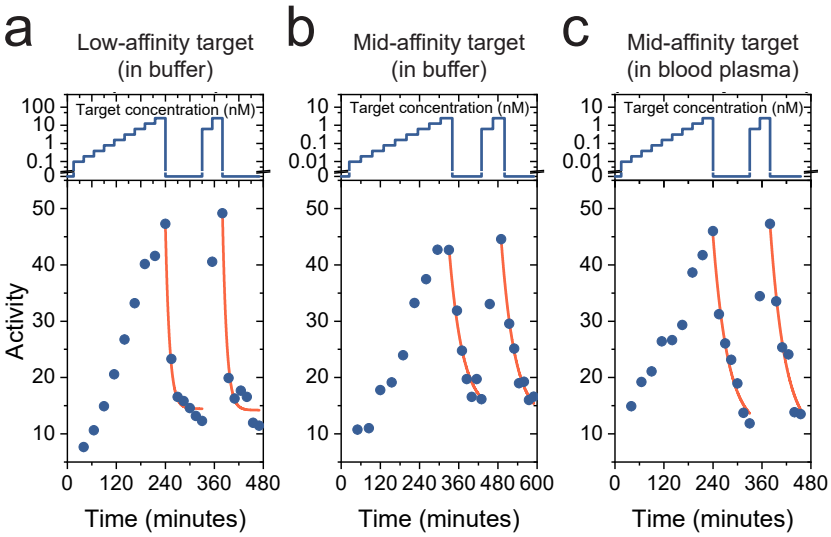

Figure 2.4: concentration response of the sensor concept with a single-molecule encoded nanoswitch in buffer and blood plasma. Concentration response traces for low- and mid-affinity ssDNA target in buffer (a, b), and mid-affinity ssDNA target in blood plasma (c) with $\tau_R = 10 \pm 1$ min, $\tau_R = 41 \pm 6$ min, and $\tau_R = 37 \pm 8$ min respectively. Reported errors are the standard errors of the fit. The error bars in the activity graphs are the stochastic errors and mostly smaller than the symbol size. The number of particles per data point was between 15 and 100, measured in two microscopic fields-of-view.

The multiplexing functionality is shown in Figure 2.5, using two particle populations having different particle probes and equal stem probes, and two targets with comparable affinities to the particle probes and different affinities to the stem probes (see Supplementary note 2.5.1). For this, separate flow cells were used to determine the multiplexing specificity and sensitivity. Figure 2.5a shows the measured average bound state lifetimes for the two cases, that are clearly different and that are independent of target concentration, confirming that particle populations can be identified on the basis of kinetic dissociation rates. Each particle can in fact be considered as a single sensing entity. The distribution of the bound state lifetimes of all individual particles shows clearly two populations, as depicted in Figure 2.5b. The two populations can be separated by a combination of thresholding (indicated by the black line) and discarding the overlap of the distributions (indicated by the shaded area). The bound state lifetime distributions

correspond to the distribution found using simulations (see inset Figure 2.5b and Material and methods 2.4). Due to the finite duration of the measurement, long bound state lifetimes are underestimated, causing the mean of the distribution of the longer lifetimes to be smaller than the ensemble bound state lifetime (*cf.* Figure 2.5a). Increasing the measurement time from 10 to 30 min reduces this underestimation. Longer measurement times result in narrower distributions, which increases the ability to discriminate between the two populations. Figure 2.5c quantifies the performance of the kinetic identification by its sensitivity and specificity for the low-affinity target. The sensitivity is defined as the fraction of true positives of the total number of particles below the threshold, and the specificity as the fraction of true negatives of the total number of particles above the threshold. Both the sensitivity and specificity can be increased by discarding overlapping data. This is shown in the inset for the values at the position of the red dot in the graph. In Figure 2.5d, the cross-talk between two particle populations is shown. In this experiment, the low- and high-affinity DNA targets were added to both flow cells sequentially, as indicated in the target concentration profiles. For the mismatched target condition, only a small fraction of switching particles was observed, indicating a negligible cross-talk. For both particle populations, the number of switching particles and the activity per particle increased when the fluid-cell-specific DNA targets were added, confirming the selectivity and sensitivity of the system.

In Figure 2.6a, the kinetic identification is demonstrated using two mixed particle populations in a single flow cell. The combined bound state lifetimes exhibit a double-exponential distribution, caused by the superposition of two single-exponential distributions of low-affinity and high-affinity dissociation reactions. Using the threshold and window determined in Figures 2.5b,c, the two particle populations can be separated, resulting in two single-exponential distributions (see inset Figure 2.6a).

The simulations of Figure 2.6b support the multiplexing potential. Simulated data were generated from measurements of particles with different dissociation rate constants, corresponding to different interaction strengths between target and stem probe. The association rate constants of all six data sets were equal. The graph shows the resulting bound state lifetime distributions per particle, for a 30 min measurement duration. The width of the distributions is mainly determined by the stochastic binding and unbinding processes; increasing the length of the measurement decreases the width of the distribution. Therefore, longer measurements increase the multiplexing capabilities. To sepa-

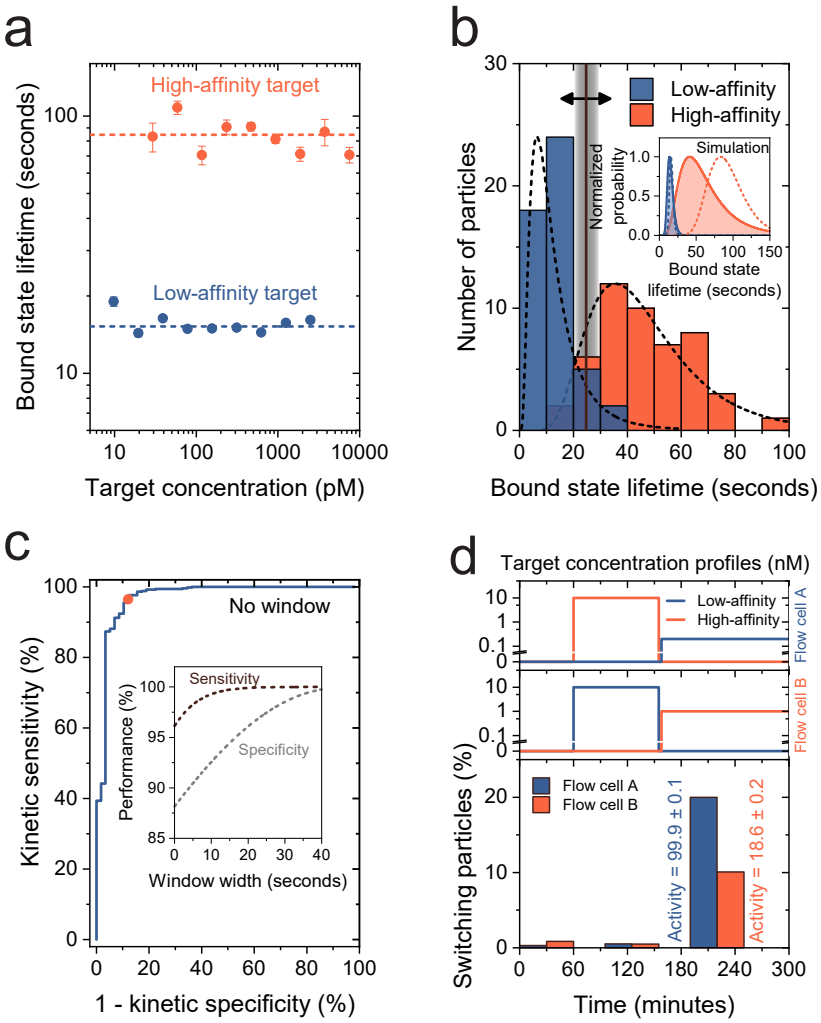

FIGURE 2.5: MULTIPLEXING PERFORMANCE BY KINETIC IDENTIFICATION OF NANOSWITCHES IN SEPARATE FLOW CELLS. (a) Concentration dependencies of the bound state lifetime τ_B for low- and high-affinity target (blue and red respectively). We observed that $\tau_B = 15.4 \pm 0.1$ s and $\tau_B = 86 \pm 2$ s for low- and high-affinity targets respectively. (b) Bound state lifetime distribution per particle for low- and high-affinity target. The threshold and overlap window used for kinetic identification are indicated by the black line and shaded area respectively. The dashed black lines show lognormal distributions. The inset shows simulated bound state lifetime distributions for both affinities, for a 10 minutes (solid lines) and 30 minutes (dashed lines) measurement. (c) Receiver operating curve that quantifies the performance of the kinetic identification. An optimum of a kinetic sensitivity of 97% and a kinetic specificity of 88% was found at a zero window width. The inset shows the approximate trend of the kinetic sensitivity and specificity as a function of the window width. (d) Cross-talk between particle populations in the sensor. Flow cell A contains particles specific for low-affinity target molecules and flow cell B for high-affinity target molecules. The concentration-time profiles show how the targets are applied to each individual flow cell. Both sensors only respond to their specific target.

rate bound state lifetime distributions on a single-particle level, a high

accuracy to determine the mean bound state lifetime per particle is not required when the distributions are distinguishable; *i. e.*, the kinetic sensitivity and specificity should be high. Therefore, kinetic encoding potentially results in six levels of multiplexing within a measurement time of 30 min. The time window suitable for multiplexing can be extended by another decade into shorter time scales, by increasing the particle diffusivity (see the Supplementary note 2.5.5).

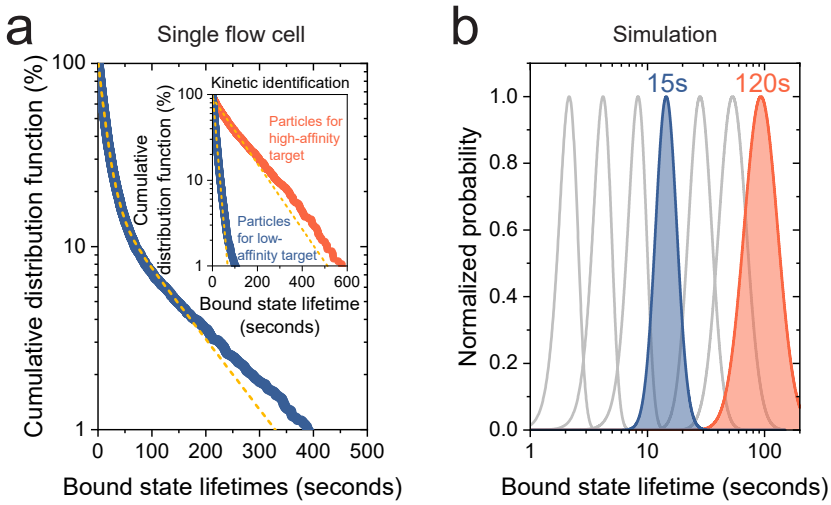

FIGURE 2.6: MULTIPLEXING PERFORMANCE BY KINETIC IDENTIFICATION OF NANOSWITCHES IN A SINGLE FLOW CELL. (a) Cumulative distribution function (CDF) of the bound state lifetimes with $\tau_B^1 = 13.7 \pm 0.1$ s and $\tau_B^2 = 113 \pm 2$ s resulting from a double-exponential fit (yellow). The inset shows the CDFs of the two separate particle populations. The single-exponential fits (yellow) give $\tau_B = 14.4 \pm 0.1$ s and $\tau_B = 113 \pm 2$ s for the low- and high-affinity interaction respectively. (b) Simulated bound state lifetime distributions for a 30 minutes measurement show the multiplexing potential with the current experimental limits. The blue and red distributions have mean bound state lifetimes that are matched with the lifetimes found in panel a. Reported errors are the standard errors of the fit. The number of particles per data point was between 15 and 100.

2.3 CONCLUSION

In this chapter, we presented a sensor design with an encoded binary nanoswitch, enabling continuous sensing of target molecules at picomolar concentrations in human blood plasma, across a broad dynamic range. The ability to create and identify particle subpopulations with distinct dissociation properties allows multiplexed biosensing with high sensitivity and specificity. Multiplexing by single-molecule kinetic encoding does not require any reagents and is therefore suited for continuous sensing and real time biomolecular monitoring, in contrast to multiplexing methods such as bead arrays,[9,10] real time PCR,[11] and DNA microarrays.[12] Kinetic encoding can be supplemented with

orthogonal identification approaches, such as using particles with different colors (optical identification) and patterning of the sensor surface (identification by surface area imaging). Combining three identification approaches, each with six levels of multiplexing, would potentially give in total $6^3 = 216$ levels. In practice, a tradeoff exists between the degree of multiplexing and the analytical performance of the biosensor. To maintain the precision of the concentration determination of multiple target molecules, the number of particles should scale linearly with the degree of multiplexing. Furthermore, while the functionality of kinetically encoded nanoswitches is demonstrated in this chapter using DNA as a model system, other markers may be addressed using affinity binders such as aptamers and antibodies.[13]

In conclusion, single-molecule encoded nanoswitches open the perspective to gain accurate real time insights into live biological systems by continuous monitoring of biomolecules with a high level of multiplexing, high sensitivity, and high specificity using single-molecule information.

2.4 MATERIAL AND METHODS

BINARY NANOSWITCH ASSEMBLY: All ssDNA oligonucleotides (IDT, standard desalting and HPLC purification for chemically modified DNA, stem probe: 5′ - ~TGC GAG AAC TCA GCA TAC ATC TA - 3′) were diluted in TE buffer (10 mM Tris–HCl, 1 mM EDTA at pH 8.0) to a final concentration of 50 µM. The DNA strands were added together in equivalent amounts to a final concentration of 5 µM per strand in TE buffer with 50 mM NaCl. Using a thermal cycler (Bio-Rad, T100 Thermal Cycler), the mixture was heated to 95°C and cooled down to 4°C with a temperature decrease of 1°C every 35 s. Analysis of DNA tethers was performed in a non-denaturing TBE gel (Thermo Fisher Scientific, Novex TBE Gels, 4-20%). The TBE gel was assembled according to the supplier's instructions, loaded with sample DNA mixtures in Nucleic Acid Sample Loading Buffer (Bio-Rad Laboratories) and an O'GeneRuler Ultra Low Range DNA Ladder (Thermo Fisher Scientific), and ran in TBE buffer (89 mM Tris–HCl, 89 mM boric acid, 2 mM EDTA at pH 8.3). Subsequently, the gel was stained with SYBR Gold Nucleic Acid Gel Stain (Thermo Fisher Scientific, 10,000× concentrate in DMSO) in TBE buffer for 30 min. Finally, the TBE gel was visualized using an ImageQuant camera setup (GE Healthcare Life Sciences).

SILICA PARTICLE FUNCTIONALIZATION: Carboxyl-functionalized silica particles (Bangs Laboratories, 1 µm mean diameter) at a concentration of 10 mg mL^{-1} were activated with EDC (Sigma-Aldrich,

final concentration of 4.3 mM) and NHS (Merck, for synthesis, final concentration of 10 mM) in MES buffer (0.1 M MES at pH 5.0) for 30 min at room temperature. After activation, the particles were centrifugally washed at 6,000× g for 5 min using a tabletop spinner (Eppendorf MiniSpin) and resuspended in MES buffer. NeutrAvidin (Thermo Fisher Scientific) was dissolved in Milli-Q (Thermo Fisher Scientific, Pacific AFT 20) at a concentration of 10 mg mL^{-1} and added to the activated particles at a final concentration of 500 µg mL^{-1}. The protein functionalization was performed overnight at room temperature. The NeutrAvidin-functionalized silica particles were twice washed in TBS–Tween-20 buffer (25 mM Tris–HCl, 0.15 mM NaCl, 0.05 vol-% Tween-20) and twice in 0.1 wt-% BSA in PBS–Tween-20 buffer (130 mM NaCl, 7 mM Na_2HPO_4, 3 mM NaH_2PO_4, 0.05 vol-% Tween-20, at pH 7.4). The binding capacity was determined using a fluorescence supernatant assay with Atto655-biotin and was approximately 800 pmol per mg of particles. The NeutrAvidin-functionalized silica particles were stored at 10 mg mL^{-1} in PBS–Tween-20 at 5°C for up to 2 months until use.

FLOW CELL EXPERIMENTS: Glass slides (25 × 75 mm, #5, Menzel-Gläser) were cleaned by 15 min of sonication in methanol (VWR, absolute), isopropanol (VWR, absolute), and methanol (VWR, absolute) baths. After each sonication step, the glass coverslips were dried under nitrogen flow. A custom-made fluid cell sticker (Grace Biolabs) with an approximate volume of 24 µL was attached to the glass slide. A flow cell was made by inserting tubing (Freudenberg Medical, monolumen) into the fluid cell sticker and connecting the tubing to a syringe pump (Harvard Apparatus, Pump 11 Elite). First, the flow cell was prewetted with PBS (130 mM NaCl, 7 mM Na_2HPO_4, 3 mM NaH_2PO_4 at pH 7.4) at a flow speed of 500 µL min^{-1} for 2 min. Functionalization of the glass substrate was performed by physisorption of 83 ng mL^{-1} anti-digoxigenin antibodies (Thermo Fisher Scientific) in PBS for 60 min. Finally, the glass substrate was blocked by incubation with 1.0 wt-% casein (Sigma-Aldrich, casein sodium salt from bovine milk) in PBS for 60 min. After each incubation step, the fluid cells were flushed with PBS (250 µL min^{-1} for 1 min). NeutrAvidin-functionalized silica particles were incubated in bulk with a 10 nM nanoswitch for 10 min. Subsequently, the particles were coated with ssDNA by an incubation with 40 µM biotin-labeled single-stranded oligonucleotide (IDT, standard desalting, 5′ - TAG TCA GGT TGG ATG TCT AC - 3′ - biotin). The particles were thrice centrifugally washed in 1.0 wt-% BSA (Sigma-Aldrich, lyophilized powder, essentially globulin free, low endotoxin, $\geq$ 98%) and 0.05 vol-% Tween-20 (Sigma-Aldrich) in PBS at 6,000× g for 5 min using a tabletop spinner (Eppendorf MiniSpin).

Finally, the particles were resuspended in PBS/BSA/Tween-20 to a final concentration of 0.17 mg mL^{-1} (0.26 pM) and sonicated using an ultrasonic probe (Hielscher). The particles were added to the flow cell at a flow speed of 50 µL min^{-1} for 5 min and incubated for 30 min. After incubation, the fluid cell was reversed and subsequently flushed with PBS/BSA/Tween-20 at a flow speed of 50 µL min^{-1} for 5 min to remove unbound particles. A ssDNA target (IDT, standard desalting, low-affinity: 5′ - AAC CTG ACT AAA AAT AGA TGT ATG - 3′, mid-affinity: 5′ - CAA CCT GAC TAA AAA TAG ATG TAT G - 3′, high-affinity: 5′ - CCA ACC TGA CTA AAA ATA GAT GTA TG - 3′) at the required concentration in PBS/BSA/Tween-20 was added at a flow speed of 50 µL min^{-1} for 5 min and incubated for 20 min to reach equilibrium.

FLOW CELL EXPERIMENTS WITH BLOOD PLASMA: Single-donor human blood plasma (Sanquin, the Netherlands, citrate stabilized, healthy volunteer) was filtered through a 50 kDa molecular weight cutoff centrifugal filter (Merck Millipore, Amicon). The plasma filtrate was collected and spiked with ssDNA at the required concentration. The measurements were then performed as described in the previous section.

PARTICLE IMAGING AND TRACKING: Samples were observed under a white light source using a microscope (Leica DM6000M) using a dark field illumination setup at a total magnification of 20× (Leica objective, N PLAN EPI BD, 20×, NA 0.4). A field-of-view of approximately 400 × 400 μm^2 was imaged using a CMOS camera (Grasshopper 2.3 MP Mono USB3 Vision, Sony Pregius IMX174 CMOS sensor) with an integration time of 10 ms and a sampling frequency of 30 Hz. The silica particles were tracked with a 3 nm accuracy using the center-of-intensity of the bright particles on the dark background. Trajectory parameters were calculated which describe the motion pattern and were used to select single-tethered particles.[13]

STATE LIFETIME ANALYSIS: Particles that showed strong irregularities in their motion pattern (*e.g.*, strongly confined or asymmetrical) or no switching behavior were excluded from further analysis.[13] The measurements were performed in a flow cell setup in which the target concentration was increased sequentially by means of buffer exchange. After 20 min incubation, the measurement was performed. Trajectory analysis was performed only on particles showing a bimodal distribution in the averaged radial position. In order to detect binding and unbinding events, a dual thresholding method was implemented in which the threshold was set on the (local) minimum between the two

peaks of the bimodal distribution. A dual threshold with a 12.5% offset was found to yield accurate event detection with 91% sensitivity and 96% specificity (data not shown here). Based on the detected events, the bound (low mobility) and unbound states (high mobility) could be identified. The lifetimes of the two states were plotted in a cumulative distribution function for different target concentrations to extract the association and dissociation rate constants (see the Supplementary notes 2.5.3 and 2.5.4). This was done for single binding and unbinding events per particle or as an ensemble using the information on single binding and unbinding events of all particles together or of a subset (specific population) of particles after kinetic identification.

SIMULATIONS: Data were simulated using experimental positional data of bound and unbound particles. For each simulation, two single-exponential distributions were generated: one with a given mean bound state lifetime and one with a given mean unbound state lifetime. The particle traces were reconstructed block-by-block with each block length according to the two predefined single-exponential distributions. Non-specific interactions and inter- and intraparticle heterogeneity were neglected. Subsequent time-dependent analysis was performed as if experimental data were analyzed.

2.5 SUPPLEMENTARY NOTES

2.5.1 *DNA sequences*

The DNA sequences for the stem probe, particle probes and target molecules used in this chapter are given in Figure 2.7. In Figure 2.7a the DNA sequences are given that were used to demonstrate the sensitivity for multiple concentration regimes (see Figure 2.3) and the continuous monitoring concept (see Figure 2.4). In order to ensure an activity per particle that depends on the fractional occupancy of the particle probes by target molecules, the molecular system has been designed to have a (relatively) high-affinity particle probe and a low-affinity stem probe. Therefore, the particle probe functions as a capture molecule and the stem probe as a detection molecule. For all three target molecules the interaction with the stem probe has a free energy of $\Delta G = -10.2$ kcal mol^{-1}. The interaction with the particle probe are $\Delta G = -12.3$ kcal mol^{-1}, -14.4 kcal mol^{-1} and -17.0 kcal mol^{-1} for the low-, mid- and high-affinity targets respectively based on their sequence.[15] Therefore, all target molecules have a higher affinity for the particle probes than for the stem probe.

The difference in the found EC_{50} for the three target molecules

can be explained by the exponential relation between the equilibrium dissociation equilibrium constant K_d and the free energy of the affinity reaction ΔG described by:

$$K_d = \frac{k_{\text{off}}}{k_{\text{on}}} = \exp\left(-\frac{\Delta G}{k_b T}\right) \cdot c^{\ominus} \tag{2.2}$$

with k_{off} being the dissociation rate constant, k_{on} the association rate constant, k_b the Boltzmann's constant, T the temperature and $c^{\ominus}$ the standard reference concentration. Under the assumption that there is no target depletion from solution and the number of particle probes occupied by a target molecule scales linearly with the observed signal, we can assume that the EC_{50} is an accurate representation of the dissociation equilibrium constant K_d of the particle probe and target

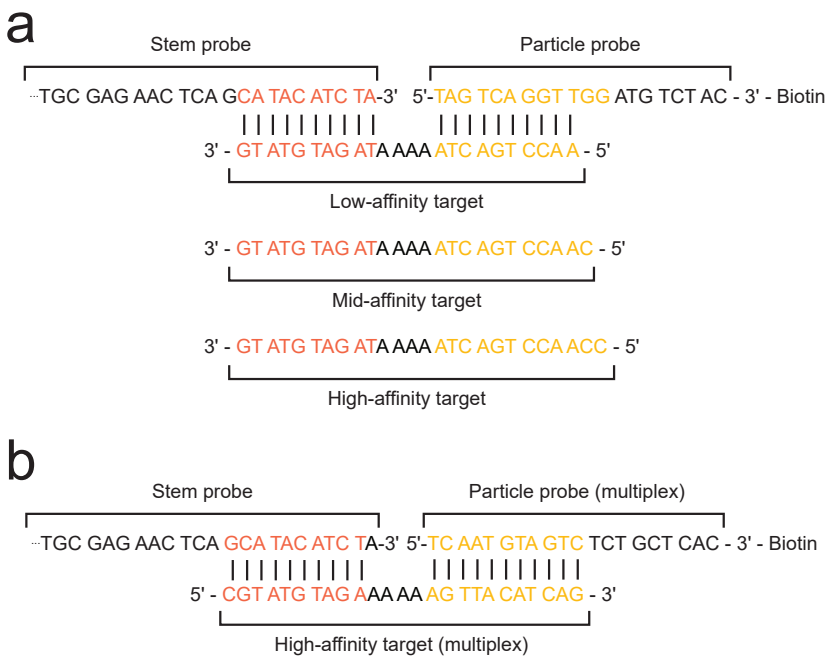

Figure 2.7: Overview of the DNA sequences used in the experiments. (a) DNA sequences of the stem probe, particle probe and three target molecules, used to demonstrate the sensing concept with single stem probe, see Figures 2.3 and 2.4. The complementary DNA sequence for target detection (to the stem probe) is given in red. For all three targets this sequence is equal, resulting in equal dissociation kinetics. The complementary DNA sequence for target capturing (to the particle probe) is given in yellow. The affinity between the target molecule and particle probe is tuned by the number of complementary base pairs; increasing the number of complementary base pairs yields a higher affinity target molecule. (b) DNA sequences of the stem probe, particle probe and target molecule used to demonstrate multiplexing, see Figures 2.5 and 2.6. The complementary DNA sequence for target detection is given in red. The complementary DNA sequences for target capturing is given in yellow.

interaction. The K_d values at 298 K for the three observed interactions, calculated using Equation 2.2, are 0.96 nM, 28 pM, and 0.35 pM for the low-, mid- and high-affinity targets respectively.

In Figure 2.7b the DNA sequences are given that were used to demonstrate multiplexing by kinetic encoding, see Figures 2.5 and 2.6. The same stem probe is used, but the DNA sequence complementary to the target molecule is shifted by a single base in order to introduce a higher affinity. The free energy of the interaction between the high-affinity target and the stem probe is $\Delta G = -11.7$ kcal mol^{-1} indicating a higher affinity compared to the target molecules in Figure 2.7a. The free energy of the interaction between this target and the particle probe with $\Delta G = -13.2$ kcal mol^{-1} is in the range of the three target molecules in Figure 2.7a. Furthermore, the particle probe used for the multiplexing experiment has a different sequence in order to obtain two separate sensing entities with limited cross-talk. The second target for the multiplexing experiments is the mid-affinity target given in Figure 2.7a. All free energies were calculated for the condition of $[Na^+] = 1$ M and pH 7.0.[15] The systems presented in Figures 2.7a,b share the same DNA sequence of the stem probe; this implies that there is a possibility of having cross-talk between the two particle populations. However, since the lifetimes of a bond between the target and the stem probe is relatively short (~15 s and ~100 s) compared to the measurement time (10 minutes), the effect of cross-talk was assumed to be limited and cross-talk was indeed not observed in the measurements.

2.5.2 *Time traces per particle*

In Figure 2.8 three examples are given of accumulated motion patterns and their corresponding radial position as a function of time.

2.5.3 *Quantifying single-molecule affinity kinetics*

Equations to quantitatively interpret single-molecule information have been described in literature.[16] Here, a brief derivation is given of the equations used in this chapter, focusing on the affinity kinetics.

We assume that the system is observed for a total time t in which there are N time intervals of equal length Δt. During a given time interval, the probability P that an event (binding or unbinding) occurs is determined by the reaction rate k and can be described by $P = k\Delta t$. The assumption is that the events are caused by a single molecular process with equal (local) conditions per particle. Since the chance

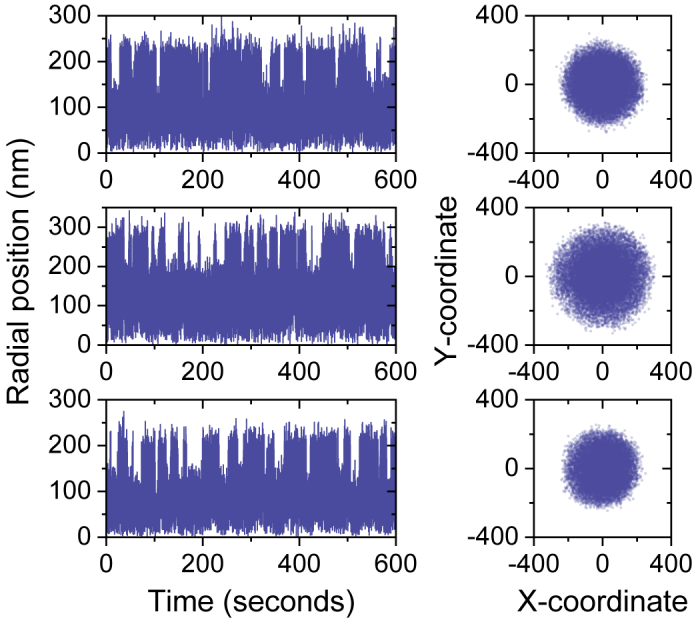

Figure 2.8: examples of accumulated motion patterns, and radial position time traces for three particles. (a) Accumulated motion pattern for three particles. The in-plane x- and y-coordinates of the position of all particles were optically recorded from which the accumulated motion pattern per particle was reconstructed. (b) Radial position over time for three particles. Using the x- and y-coordinates, the radial position per particle was calculated. The radial position over time shows binary transitions caused by single-molecule binding and unbinding events. The length of the primary tether (*i. e.*, the dsDNA stem) determines the radius of the unbound state motion pattern (~250-300 nm). The length of the secondary tether (*i. e.*, stem probe, target, and particle probe) determines the radius of the bound state motion pattern (~150-175 nm). The accumulated motion patterns with their corresponding radial position time trace were measured at a bulk concentration of 63 pM high-affinity target (see Figure 2.3c).

per time interval is independent of the preceding time interval, for each interval the probability that an event occurs equals $k\Delta t$ while the probability that no event occurs equals $1 - k\Delta t$. When considering all time intervals within the total observation time, the number of time intervals in which an event has occurred is x while the number of time intervals in which no events could be observed is equal to $N - x$. The probability of a specific sequence of x events during measurement time t can then be described by:

$$P(x|N) = (k\Delta t)^x (1 - k\Delta t)^{N-x}, \text{ with } x = 0, 1, \ldots, n \tag{2.3}$$

with n being the number of observed events where $n \leq N$. However, since this relates to a specific sequence, all combinations of x events in all N time intervals should be considered. This can be done by implementing a binomial coefficient as given in the following equation:

$$P(x|N) = \frac{N!}{x!(N-x)!}(k\Delta t)^x(1-k\Delta t)^{N-x}, \quad \text{with } x = 0, 1, \ldots, n \tag{2.4}$$

If we assume that the number of time intervals is very large (*i. e.*, $N \to \infty$) and the time interval length very short compared to the reaction rate ($\Delta t < 1/k$, *i. e.*, $\Delta t \to 0$), Equation 2.4 can be simplified to:[16–18]

$$\lim_{N\to\infty} P(x|N) = \lim_{N\to\infty} \frac{N!}{x!(N-x)!}\left(\frac{\lambda}{N}\right)^x\left(1-\frac{\lambda}{N}\right)^{N-x} \quad P(x) = \frac{\lambda^x}{x!}\exp(-\lambda) \tag{2.5}$$

with $\lambda = N(k\Delta t)$. Since the total measurement time t is described by $N\Delta t$, and the cumulative distribution function (CDF) of the observed state lifetimes can be described by the probability that no event has occurred, *i. e.*, $x = 0$, the equation simplifies to:

$$P(x=0) = \exp(-kt) \tag{2.6}$$

Since the time that no events have occurred equals the lifetime of the state (either bound or unbound) of the system, Equation 2.6 can be expressed as follows:

$$F(t) = \frac{n(t)}{n_0} = \exp(-kt) = \exp\left(\frac{-t}{\tau}\right) \tag{2.7}$$

with n_0 being the total number of observed lifetimes, $n(t)$ the number of observed lifetimes with a length larger than t, and τ the mean bound or unbound state lifetime. Using Equation 2.7, the reaction rate constant k has the meaning of a probability per unit time that a binding or unbinding event happens. Therefore, it describes the CDF of the observed state lifetime in a molecular system and can be interpreted as the apparent association rate constant κ (for unbound states) and dissociation rate constant k_{off} (for bound states).

2.5.4 *Heterogeneity in association kinetics*

STATE LIFETIME HETEROGENEITY: In Figure 2.9 the CDFs of both the bound and the unbound states are shown, experimentally determined using the system described in Figures 2.1 and 2.2. The straight

line of Figure 2.9a is in agreement with the assumption of a well-defined, single-molecular process with similar (local) conditions which holds for the bound state lifetimes, since the observed bound state lifetimes are single-exponentially distributed. This indicates that the bound state lifetime distribution can be used to kinetically identify the molecular interaction. In contrast, the observed unbound state lifetimes show a curved line and indicate a multiexponential distribution. We attribute the multiexponential behavior to particle-to-particle variability. This hypothesis is supported by plotting the unbound state lifetimes per particle (Figure 2.9b). The per-particle curves appear approximately as straight lines (with noise due to lower event statistics), which indicates that the association kinetics of every particle are determined by a bimolecular interaction with a single association rate and that different particles exhibit different rates. The particle-to-particle variability causes the curved line in Figure 2.9a, where the data is accumulated for all particles. A large contribution to the heterogeneity is caused by the nonuniformity of the NeutrAvidin coating on the particles, which we visualized using quantitative points accumulation for imaging in nanoscale topography (qPAINT). Hypotheses for the presence of such a multiexponential distribution are variability in (1) NeutrAvidin functionalization on the particle surface; (2) particle probe conjugation to the NeutrAvidin complexes; or (3) target hybridization to the particle probes, such as slow equilibrium of the fractional occupancy of the particle probes whereby the affinity reaction did not reach (local) equilibrium. Besides, only a small fraction of the particle surface area is probed, namely the area close to the stem. This might lead to a small number of accessible particle probes and therefore increase the susceptibility to variability between particles.

In Figure 2.10 the distributions of the mean state lifetime per particle are given. For the dissociation kinetics, the experimentally found width of the distribution is similar to the width that was found using simulated data (see Material and methods 2.4). However, for the association kinetics, a large distribution was observed compared to simulations. Both observations correspond to the findings in Figure 2.9. It was found that the mean unbound state lifetime τ_U is approximately lognormal distributed, as shown in Figure 2.10 (right). Therefore the distribution of τ_U per particle can be described by:

$$f(\tau_U; \mu_{\tau_U}, \sigma_{\tau_U}) = \frac{1}{\tau_U \sigma_{\tau_U} \sqrt{2\pi}} \exp\left(-\frac{(\ln \tau_U - \mu_{\tau_U})^2}{2\sigma_{\tau_U}^2}\right) \tag{2.8}$$

with μ_{τ_U} being the mean and σ_{τ_U} the standard deviation of the natural logarithm of the unbound state lifetime τ_U per particle, respectively.

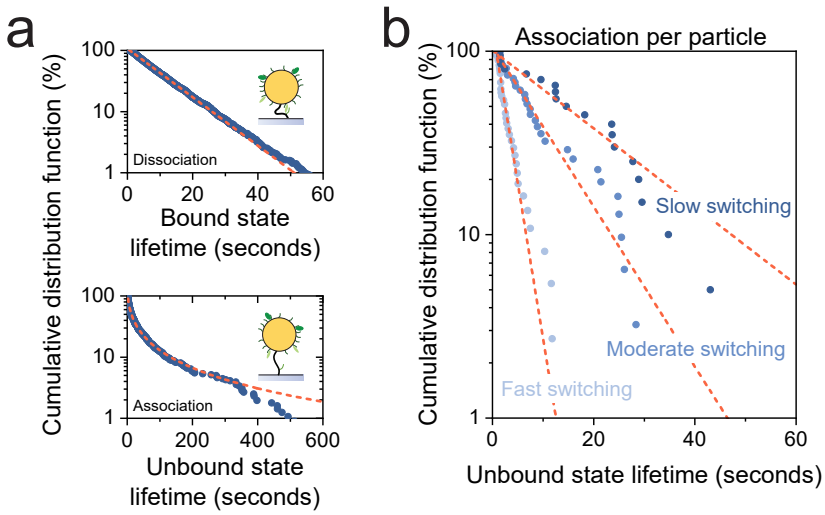

FIGURE 2.9: STATE LIFETIME ANALYSIS OF THE OBSERVED STATE LIFETIMES. (a) Cumulative distribution function (CDF) of observed bound (top) and unbound (bottom) state lifetimes of all particles. Top: the red dashed line shows a single-exponential fit. For longer bound state lifetimes ($>$ 40 seconds, $<$ 3% of the total number of observed bound states) a minor deviation from the fit is observed, caused by merged bound states (missed unbound state lifetime in particular at high target concentrations). Bottom: the red dashed line shows a multiexponential fit according to Equation 2.8. For longer unbound state lifetimes ($>$ 350 seconds, $<$ 4% of the total number of observed unbound states), a deviation of the fit is observed due to a finite measurement time. (b) CDFs of the observed unbound state lifetimes of three individual particles (classified as slow, moderate, fast switching) at equal target concentration. The red dashed lines show a single-exponential distribution fit per particle. All accumulated CDFs are reconstructed using all observed state lifetimes of all particles ($N = 58$) at a fixed target concentration for a single measurement (10 minutes).

FIGURE 2.10: EXPERIMENTAL (BLUE) AND SIMULATED (RED) DISTRIBUTIONS OF THE OBSERVED STATE LIFETIME PER PARTICLE. Left: experimental and simulated lognormal distributed bound state lifetimes per particle show a high similarity. Right: experimental and simulated lognormal distributed unbound state lifetimes per particle. The experimental distribution shows a broad distribution with a coefficient of variation of approximately 80% indicating for a large particle-to-particle heterogeneity.

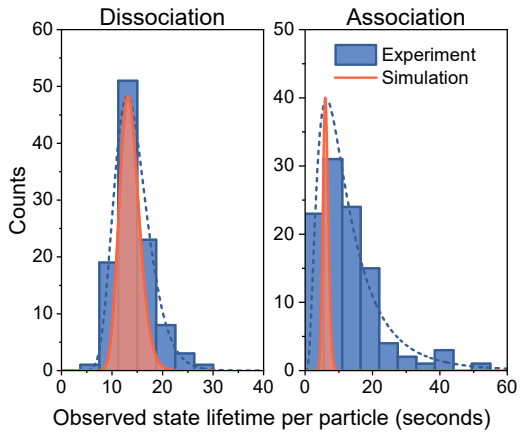

In order to interpret the unbound state lifetime distribution, we first assume that all unbound state lifetimes τ_U can be found during a single measurement. The fraction of observed unbound state lifetimes

F_U, defined in Equation 2.7, can be described by the integral over all positive values of τ_U. By combining Equations 2.7 and 2.8, particles with short unbound state lifetimes have a larger contribution in the CDF. In order to correct for this, a weight factor should be implemented. The CDF of the observed unbound state lifetimes can then be described by:

$$F_U(t) = \int_0^\infty w(\tau_U) f(\tau_U) \exp\left(-\frac{t}{\tau_U}\right) d\tau_U \tag{2.9}$$

with $w(\tau_U) = \frac{T_M}{\tau_U + \tau_B}$, with T_m being the measurement time and τ_B the mean bound state lifetime. By fitting the CDF with this multiexponential distribution, with a lognormal distributed contribution of each exponential component, the concentration dependency can be condensed in a single parameter that describes the lognormal distribution: this single parameter is the median of the lognormal distribution and referred to as the ensemble mean unbound state lifetime τ_{ens}. In order to accurately determine τ_{ens}, the distribution of τ_U per particle should comprise a considerable number of particles and events. It appears that τ_{ens} suffers from missed long state lifetimes due to a finite measurement time and low statistics at low target concentrations, and therefore the mean unbound state lifetime is underestimated and large uncertainty intervals are obtained. In the limit of low target concentrations, the assumption that all unbound state lifetime τ_U can be observed during a single measurement therefore does not hold. Note that the calculated mean unbound state lifetime τ_{ens} is reported as τ_U in this chapter, see Figures 2.3a,b.

VARIABILITY IN NEUTRAVIDIN FUNCTIONALIZATION: To investigate the origin of the broad distribution of association lifetime (see Figures 2.9 and 2.10), we quantified the particle-to-particle variability in NeutrAvidin functionalization using qPAINT.[19] The number of NeutrAvidin-bound, biotinylated ssDNA strands (docking strands) per particle was determined using total internal reflection (TIR) excitation of transiently binding dye-labeled ssDNA strands (imager strands) with a complementary sequence. Here, it was assumed that the number of docking strands represents the number of NeutrAvidin complexes. In order to quantify the particle-to-particle variability, the coefficient of variation (CV) of the distribution of number of docking strands per particle was calculated.

In qPAINT the number of docking strands is calculated using the association kinetics of the transient binding of imager strands to the docking strands, according to the following equation:

$$N_{DS} = \frac{1}{k_{\text{on}} c_i \tau_d} \tag{2.10}$$

with N_{DS} being the number of docking strands, k_{on} the association rate constant (assumed to be $2.3 \cdot 10^6$ M^{-1} s^{-1}),[19,20] c_i the imager strand concentration and τ_d the mean dark time, *i. e.*, the time in which no imager strand is bound to a docking strand. Since this method is prone to underestimating the number of docking strands when multiple binding events occur simultaneously, τ_d should be much larger than the mean bright time τ_b, *i. e.*, the time in which a single imager strand is bound to a docking strand. Furthermore, to ensure comparable statistics for sparsely and densely functionalized particles, the τ_d/τ_b ratio is tuned by decreasing c_i for increasing number of docking strands per particle.

Figure 2.11 shows the results of the qPAINT measurements. For these measurements, the incubated ssDNA concentration consists of 3% docking strands and 97% ssDNA strands with a random sequence and equal length. Using an imager strand complementary to the docking strand, only the docking strands are imaged. Subsequently, the total number of ssDNA strands can be calculated with the known ratio between docking strand and ssDNA strands with a random sequence. The number of ssDNA strands is therefore the sum of the number of docking strands and ssDNA strands with a random sequence. Figure 2.11a shows a concentration series of ssDNA strands incubated with NeutrAvidin-functionalized particles. For the measured concentration range, a linear relationship with the observed number of ssDNA strands was found. The saturation point of 5.5 µM (~350,000 binding sites per particle) was found using a supernatant assay with Atto655-biotin (data not shown here) from which a number of ssDNA strands per particle as a function of ssDNA concentration could be calculated (gray dashed line). Here it was assumed that there exists a linear relationship between number of ssDNA strands per particle and ssDNA strand concentration, that the binding capacity of Atto655-biotin is equal to the binding capacity of biotinylated ssDNA strands, and that approximately 50% of the docking strands could be observed due to TIR excitation. Therefore, the maximum possible number of observable docking strands per particle is approximately 175,000.

Figure 2.11b shows an example of the found distribution of the number of ssDNA strands per particle for particles incubated with a ssDNA concentration of 667 nM. The distribution is fitted with a normal distribution, from which the CV can be calculated. Figure 2.11c shows

the dependency of the observed and expected CV on the incubated ssDNA strand concentration. The expected CV is calculated using the mean observed number of ssDNA strands per particle and the mean number of observed binding events under the assumption of a Poisson distributed ssDNA strand functionalization and probing processes. It appears that for both the observed and expected CVs the CV scales with the incubated ssDNA concentration (dashed blue and red lines) with $CV \propto N_{DS}^{-0.5}$ which is expected based on the previously mentioned assumptions. The difference between the observed CV and the expected CV is approximately 10%; this can only partially explain the broad distribution observed in Figure 2.10, caused by particle-to-particle heterogeneity in NeutrAvidin functionalization. Note that the experimental results presented in this figure were obtained using a preliminary event detection algorithm which suffers from background signals with many false positive events, effectively inflating the CV at low DNA concentrations. In Chapter 3, in particular Figure 3.2, the same data have been analyzed with an improved event detection algorithm. Nevertheless, the data in Figure 2.11 show a clear difference between the observed and expected variability, indicating variability between particles.

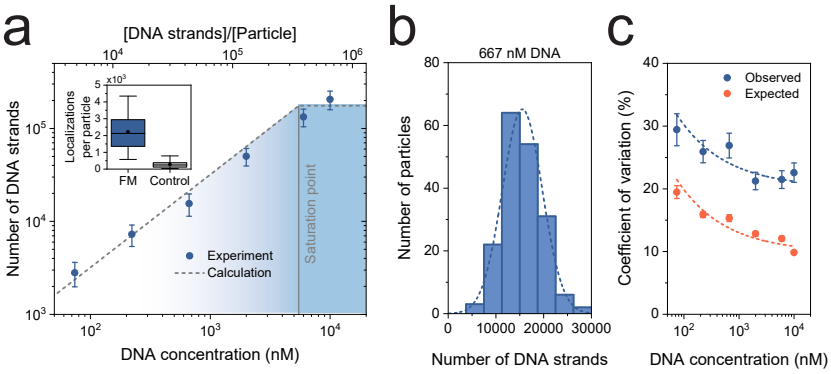

FIGURE 2.11: QUANTIFICATION OF INTERPARTICLE SURFACE FUNCTIONALIZATION VARIABILITY. (a) Experimentally found (blue) number of ssDNA strands as a function of the incubated ssDNA strand concentration. The calculated number of ssDNA strands (gray dashed line) are based on supernatant assay from which the total binding capacity was calculated. The inset shows the specificity of the imager strands for the docking strands; a fully matched docking strand (FM) yields a high number of localizations per particle while a negative control with a fully mismatched docking strand yields a low number of localizations. The box plots show the median, 5%, 25%, 75% and 95% confidence intervals. The error bars in the graphs represent the calculated standard deviation with $N \geq 150$ accumulated over two fields-of-view. (b) Calculated number of binding sites per particle at an incubated docking strand concentration of 25 nM; an approximate normal distribution was found from which the coefficient of variation (CV) was calculated. (c) The experimentally observed (blue) and expected (red) CV as a function of incubated ssDNA strand concentration show a significant difference at each ssDNA strand concentration. The dashed lines show the approximately trend of $CV \propto N_{BS}^{-0.5}$. The error bars in the graphs represent the calculated standard deviation of the fit of the distributions.

QPAINT: All ssDNA oligonucleotides (IDT, HPLC purification) were diluted in Milli-Q water (Thermo Fisher Scientific, Pacific AFT 20) to a final concentration of 20 µM for the docking strand, 10 µM for the ssDNA strand with a random sequence, and 200 nM for the imager strand. Glass slides (25 × 75 mm, #1, Menzel-Gläser) were cleaned by 15 minutes sonication in methanol (VWR, absolute) and thereafter dried under nitrogen flow. A custom-made fluid cell sticker (Grace Biolabs) with an approximate volume of 24 µL was attached to the glass slide. NeutrAvidin-functionalized silica particles were incubated in bulk overnight with docking strands at the required concentration. The particles were thrice centrifugally washed in PBS (130 mM NaCl, 7 mM Na_2HPO_4, 3 mM NaH_2PO_4 at pH 7.4) at 6,000× g for 5 minutes using a tabletop spinner (Eppendorf MiniSpin). Finally, the particles were resuspended in PBS to a final concentration of 0.17 mg mL^{-1} (0.26 pM) and sonicated using an ultrasonic probe (Hielscher). The particles were added to the fluid cell and nonspecifically absorbed to the glass surface for 30 minutes. After incubation, the fluid cell was washed with 200 µL buffer B+ (5 mM Tris-HCl, 10 mM $MgCl_2$, 1 mM EDTA, 0.05 vol.-% Tween-20 at pH 8.0) to remove unbound particles and change the buffer in the fluid cell. Finally, 200 µL imager strand of the required concentration in buffer B+ was added and the fluid cell was closed using sticky tape. Imaging at a 60× magnification (Nanoimager S, ONI) was performed under TIR conditions using a 647 nm laser at 50 mW at a frame rate of 13.3 Hz for 30 minutes. The integrated pixel intensity of the region of interest around each particle was used to determine binding and unbinding events of imager strands. The mean dark time was extracted by fitting all observed dark times to a single-exponential distribution.

2.5.5 *Potential of multiplexing by kinetic encoding and temporal resolution*

The potential of multiplexing by single-molecule kinetic encoding is determined by the temporal resolution of the measurement of the dissociation rate, which is governed by the diffusion coefficient of the tethered particle. The tethered particle moves within a confined volume defined by the molecular tether. At the boundaries of the confinement, the molecular tether is fully stretched and the entropic spring effect forces the particle to move toward the center of the confined space. This confinement effect can be described by the mean squared displacement (MSD) of the position of the particle in a two-dimensional space:[21]

$$\langle r^2(t) \rangle = R_c^2 \cdot (1 - \exp(-t/\tau_c)) \tag{2.11}$$

with R_c being the radial confinement and τ_c a time constant which describes the diffusion time scale on which the particle experiences the confinement of its motion. On small time scales of $t \ll \tau_c$, the diffusion resembles free diffusion. Therefore, by taking the limit of the derivative of Equation 2.11 at $t = 0$, R_c and τ_d can be related to the bulk diffusion coefficient D of the particle:

$$\begin{aligned} \frac{d\langle r^2(t)\rangle}{dt} &= R_c^2 \cdot \frac{\exp\left(-t/\tau_c\right)}{\tau_c} \\ \rightarrow \lim_{t\rightarrow 0} &\left(R_c^2 \cdot \frac{\exp\left(-t/\tau_c\right)}{\tau_c}\right) = \frac{R_c^2}{\tau_c} = 4D \end{aligned} \tag{2.12}$$

In Figure 2.12 normalized MSD curves of four particles are given as an example and the calculated diffusion coefficient D for all particles. In Figure 2.12a, the MSD was fitted with Equation 2.11 for the first 10 data points (~300 ms) since all particles follow the diffusive behavior of a confined particle. From the MSD fits it was found that for NeutrAvidin-functionalized silica particles the observed diffusion coefficient $D = 1.5 \pm 0.2 \cdot 10^{-13}$ m^{-2} s^{-1} (see Figure 2.12b). To account for the hydrodynamic coupling between the particle and the substrate, a correction can be applied according to Faxén's Law.[22] The corrected diffusion coefficient was found to be $D = 3.4 \pm 0.4 \cdot 10^{-13}$ m^{-2} s^{-1} which is close to the theoretical bulk diffusion coefficient calculated using the Stokes-Einstein equation, *i. e.*, $D^{SE} = 4.2 \cdot 10^{-13}$ m^{-2} s^{-1}:

$$D^{SE} = \frac{k_B T}{6\pi\eta a} \tag{2.13}$$

with k_B being the Boltzmann constant, T the temperature, η the viscosity of the fluid, and a the particle radius.

The temporal resolution of kinetic encoding is limited by the particle diffusivity in two ways. First, a slow diffusing particle increases the probability of target rebinding, causing longer bound state lifetimes than would be expected based on the affinity of the molecular interaction alone. Second, the time scale in which the particle exhibits confined diffusion should be smaller than the observed bound and unbound state lifetimes in order to separate the unbound from the bound states, *i. e.*, $\tau_c \ll \tau_U, \tau_B$. We assume that this requirement is met when $\tau_U, \tau_B = 5 \cdot \tau_c$ which corresponds to the time step at which $\langle r^2 \rangle$ equals approximately 99% of the plateau value R_c. Using these values, for the current experimental design the achieved temporal resolution

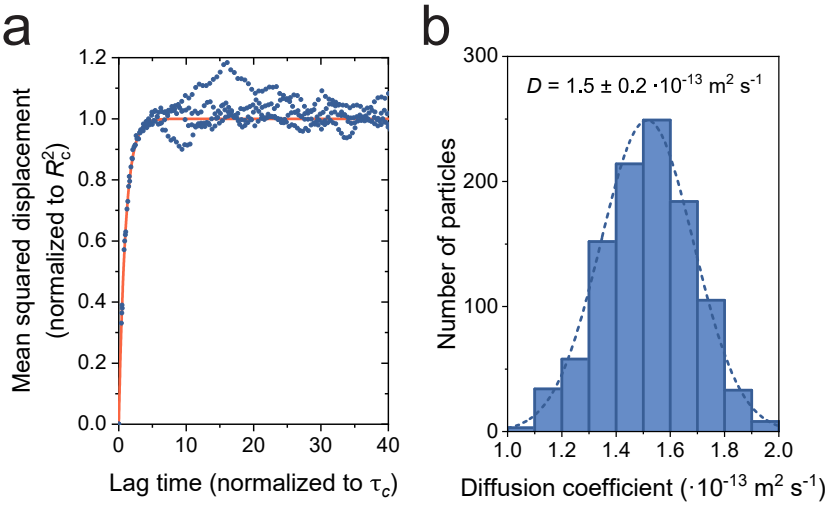

FIGURE 2.12: CHARACTERIZATION OF THE CONFINED DIFFUSION BEHAVIOR OF TETHERED SILICA PARTICLES. (a) Mean squared displacement (MSD), normalized to R_c, as a function of data lag time, normalized to τ_c with a diffusion time $\tau_c = 68 \pm 16$ ms. (b) Calculated bulk diffusion coefficient calculated per particle using Equation 2.12. The mean of the fitted normal distribution is $D = 1.5 \pm 0.2 \cdot 10^{-13}$ m^2 s^{-1}

is 340 ± 80 ms. Since the state lifetimes are exponentially distributed, the mean state lifetime should be longer than this temporal resolution; when $\geq 90\%$ of all state lifetimes are observed the found mean state lifetime is overestimated by less than or equal to 10%. To meet this requirement, it was found that the mean state lifetime τ should be larger than $50 \cdot \tau_c$ which corresponds to approximately ≥ 4 seconds.

When faster kinetics have to be observed, the particle has to diffuse faster in order to meet the stated requirements. By decreasing the radius of the particle, the diffusivity is increased. However, the radial confinement of the tethered particle is decreased as well. According to Equation 2.12 the diffusion time τ_c depends on both the diffusion coefficient of the particle and the radial confinement. The diffusion coefficient scales with the inverse of the radius according to the Stokes-Einstein equation, and the radial confinement with the square root of the radius:

$$R_c = \sqrt{R_{e-e}^2 + 2R_{e-e} \cdot a} \tag{2.14}$$

with R_{e-e} being the end-to-end distance of the tether. Therefore the diffusion time τ_c scales with the radius squared. Decreasing the current particle radius by a factor 3, decreases the diffusion time to approxi-

mately 7 ms. Therefore, decreasing the particle size opens an additional decade of time space (0.35–4 s as a mean bound state lifetime) available for kinetic encoding.

2.6 REFERENCES

1. Rissin, D. M. *et al.* Single-Molecule Enzyme-Linked Immunosorbent Assay Detects Serum Proteins at Subfemtomolar Concentrations. *Nature Biotechnology* **28,** 595–599 (2010).
2. Pinheiro, L. B., Coleman, V. A., Hindson, C. M., Herrmann, J., Hindson, B. J., Bhat, S. & Emslie, K. R. Evaluation of a Droplet Digital Polymerase Chain Reaction Format for DNA Copy Number Quantification. *Analytical Chemistry* **84,** 1003–1011 (2012).
3. Eid, J., Fehr, A., Gray, J., Luong, K., Lyle, J., Otto, G., Peluso, P., Rank, D., Baybayan, P. & Bettman, B. Real-Time DNA Sequencing from Single Polymerase Molecules. *Science* **323,** 133–138 (2009).
4. Lipani, L., Dupont, B. G. R., Doungmene, F., Marken, F., Tyrrell, R. M., Guy, R. H. & Ilie, A. Non-Invasive, Transdermal, Path-Selective and Specific Glucose Monitoring Via a Graphene-Based Platform. *Nature Nanotechnology* **13,** 504–511 (2018).
5. Heikenfeld, J., Jajack, A., Feldman, B., Granger, S. W., Gaitonde, S., Begtrup, G. & Katchman, B. A. Accessing Analytes in Biofluids for Peripheral Biochemical Monitoring. *Nature Biotechnology* **37,** 407–419 (2019).
6. Zhang, B., Korolj, A., Lai, B. F. L. & Radisic, M. Advances in Organ-on-a-Chip Engineering. *Nature Reviews Materials* **3,** 257–278 (2018).
7. Kim, J., Campbell, A. S., Esteban-Fernández de Ávila, B. & Wang, J. Wearable Biosensors for Healthcare Monitoring. *Nature Biotechnology* **37,** 389–406 (2019).
8. Heikenfeld, J., Jajack, A., Rogers, J., Gutruf, P., Tian, L., Pan, T., Li, R., Khine, M., Kim, J. & Wang, J. Wearable Sensors: Modalities, Challenges, and Prospects. *Lab on a Chip* **18,** 217–248 (2018).
9. Rissin, D. M., Kan, C. W., Song, L., Rivnak, A. J., Fishburn, M. W., Shao, Q., Piech, T., Ferrell, E. P., Meyer, R. E. & Campbell, T. G. Multiplexed Single Molecule Immunoassays. *Lab on a Chip* **13,** 2902 (2013).
10. Dunbar, S. A. Applications of Luminex® xMAP™ Technology for Rapid, High-Throughput Multiplexed Nucleic Acid Detection. *Clinica Chimica Acta* **363,** 71–82 (2006).
11. Gurvich, O. L. & Skoblov, M. Real-Time PCR and Multiplex Approaches. *Methods in Molecular Biology Gene Expression Profiling* **784,** 1–13 (2011).
12. DeRisi, J., Penland, L., Brown, P. O., Bittner, M. L., Meltzer, P. S., Ray, M., Chen, Y., Su, Y. A. & Trent, J. M. Use of a cDNA Microarray to Analyse Gene Expression Patterns in Human Cancer. *Nature Genetics* **14,** 457–460 (1996).
13. Visser, E. W. A., Yan, J., van IJzendoorn, L. J. & Prins, M. W. J. Continuous Biomarker Monitoring by Particle Mobility Sensing with Single Molecule Resolution. *Nature Communications* **9,** 2541 (2018).
14. Atkins, P. W. & Paula, J. D. *Physical Chemistry for the Life Sciences* (Oxford University Press, 2010).

15. Sugimoto, N., Nakano, S.-I., Yoneyama, M. & Honda, K.-I. Improved Thermodynamic Parameters and Helix Initiation Factor to Predict Stability of DNA Duplexes. *Nucleic Acids Research* **24,** 4501–4505 (1996).

16. Levitus, M. Chemical Kinetics at the Single-Molecule Level. *Journal of Chemical Education* **88,** 162–166 (2011).

17. Bertsekas, D. P. *Introduction to Probability* (Athena Scientific, 2008).

18. Tijms, H. C. *Understanding Probability: Chance Rules in Everyday Life* (Cambridge University Press, 2007).

19. Jungmann, R., Avendaño, M. S., Dai, M., Woehrstein, J. B., Agasti, S. S., Feiger, Z., Rodal, A. & Yin, P. Quantitative Super-Resolution Imaging with qPAINT. *Nature Methods* **13,** 439–442 (2016).

20. Delcanale, P., Miret-Ontiveros, B., Arista-Romero, M., Pujals, S. & Albertazzi, L. Nanoscale Mapping Functional Sites on Nanoparticles by Points Accumulation for Imaging in Nanoscale Topography (PAINT). *ACS Nano* **12,** 7629–7637 (2018).

21. Saxton, M. J. in *Fundamental Concepts in Biophysics: Volume 1* chap. Single Particle Tracking (Humana Press, 2009).

22. Faxén, H. Der Widerstand gegen die Bewegung einer starren Kugel in einer zähen Flüssigkeit, die zwischen zwei parallelen ebenen Wänden eingeschlossen ist. *Annalen der Physik* **373,** 89–119 (1922).

3

HOW REACTIVITY VARIABILITY OF BIOFUNCTIONALIZED PARTICLES IS DETERMINED BY SUPERPOSITIONAL HETEROGENEITIES

ABSTRACT: The biofunctionalization of particles with specific targeting moieties forms the foundation for molecular recognition in biomedical applications such as targeted nanomedicine and particle-based biosensing. To achieve a high precision of targeting for nanomedicine and high precision of sensing for biosensing, it is important to understand the consequences of heterogeneities of particle properties. In this chapter, we present a comprehensive methodology to study with experiments and simulations the collective consequences of particle heterogeneities on multiple length scales, called superpositional heterogeneities, in generating reactivity variability per particle. Single-molecule techniques are used to quantify stochastic, interparticle, and intraparticle variabilities, in order to show how these variabilities collectively contribute to reactivity variability per particle, and how the influence of each contributor changes as a function of the system parameters such as the particle interaction area, the particle size, the targeting moiety density, and the number of particles. The results give insights into the consequences of superpositional heterogeneities for the reactivity variability in biomedical applications and give guidelines on how the precision can be optimized in the presence of multiple independent sources of variability.

Parts of this chapter have been published as: Lubken, R. M. *et al.* How Reactivity Variability of Biofunctionalized Particles Is Determined by Superpositional Heterogeneities. *ACS Nano* **15,** 1331–1341 (2021).

3.1 INTRODUCTION

The biofunctionalization of micro- and nanoparticles with specific targeting moieties forms the basis of biomedical applications such as particle-based biomolecular assays and targeted nanomedicine.[1–6] The specific targeting moieties are coupled to particles that can have various chemical compositions, *e. g.*, metallic particles, polymer-based particles, and oxide-based particles. To achieve targeting and sensing with high precision, good control is needed of the particles and their biofunctionalization. Therefore, it is important to know the heterogeneities present in the system and understand how these lead to variabilities in the targeting functionality of the particles.[7,8] For example, heterogeneities in the particle surface (*e. g.*, nonuniform chemical composition, surface roughness), heterogeneities in the targeting moieties (*e. g.*, number and location of conjugation sites), and heterogeneities in the coupling processes (*e. g.*, nonuniform reaction conditions) cause variabilities, such as variable densities of targeting moieties, variable orientations of the moieties, and variable functional activities. In that way, the underlying heterogeneities affect the number of molecular interactions that the particles can effectuate.

In this work we ask the question, how do multiple independent heterogeneities collectively determine the reactivity variability of particles? Here, reactivity is defined as the number of particle-coupled targeting moieties that are available for interaction toward a countersurface. The independent particle heterogeneities are referred to as superpositional heterogeneities, as the heterogeneities are superposed onto each other to generate the total observed reactivity variability. We address this question using three experimental techniques with single-molecule resolution and using simulations. Single-molecule techniques are able to count molecules and molecular events, revealing detailed heterogeneities and stochastic properties of biomolecular systems.[9–16] Here, we use two fluorescence-based single-molecule techniques (qPAINT and DNA-PAINT) to identify individual targeting moieties on particles and gain insight in their number and spatial distribution.[9,10] The reactivity variability is studied using a biosensing technique with both single-particle and single-molecule resolution, called biosensing by particle mobility (BPM).[17–19] These techniques jointly cover all relevant length scales of the interactions of the particles. The data quantify the reactivity variability and how this reactivity variability scales as a function of the system parameters, namely, particle interaction area, particle size, targeting moiety density, and number of particles. The results provide insights into the origins of variability and give guidelines how

particle-based biomedical applications can be engineered in such a way that a high precision can be obtained.

3.2 SUPERPOSITIONAL HETEROGENEITY

The concept of superpositional heterogeneity is explained in Figure 3.1, showing the various contributors to reactivity variability and the distributions of reactivity caused by each individual contributor. Figure 3.1a sketches two important applications of biofunctionalized particles, namely, targeted nanomedicine and biosensing. In targeted nanomedicine applications, biofunctionalized particles interact with a biological countersurface such as a vessel wall, a cell membrane, or a tissue. In particle-based biosensing, particles interact with a biosensor substrate. In both cases, biofunctionalized particles form biomolecular bonds with a countersurface. In this chapter, we study how multiple heterogeneities of the particles cause reactivity variability, *i. e.*, variability in the number of particle-coupled targeting moieties that are available for interaction toward a uniformly reactive countersurface. The reactivity variability is analyzed as a function of system parameters, such as particle size and density of targeting moieties on the particles. The reactivity variability can have stochastic and nonstochastic origins. Stochastic heterogeneity relates to the discrete nature of the targeting moieties, causing random placements of targeting moieties on the particle surface and distributions according to Poisson statistics. Nonstochastic heterogeneity refers to physical and chemical differences, such as particle size, surface roughness, and chemical surface heterogeneities. We subdivide the nonstochastic heterogeneity into two parts: heterogeneity between particles, which is called interparticle heterogeneity, and heterogeneity within particles, which is called intraparticle heterogeneity.

Figure 3.1b shows the stochastic heterogeneity of targeting moieties on the particle surface for three different reaction levels: ensemble level, single-particle level, and subparticle level. At ensemble level (left), the interaction is effectuated by a large ensemble of particles, where the total surface area of all particles contributes to this interaction. The total area is large, so many targeting moieties generate molecular interactions, resulting in a small reactivity variability between individual measurements. For a single-particle level (middle), where each particle is an individual effectuator, the total number of targeting moieties is much lower and therefore the distribution of reactivity per single-particle measurement is broader. The distribution is broadened even further when the interaction area is reduced to a fraction of the surface of a single particle (right).

The contributions of interparticle and intraparticle heterogeneity to the superpositional heterogeneity are visualized in Figure 3.1c. When these heterogeneities are present, the reactivity variability is larger than would be expected based on the stochastic contribution alone (gray dashed lines). The collective effect of stochastic, interparticle, and intraparticle heterogeneity results in the observed reactivity variability.

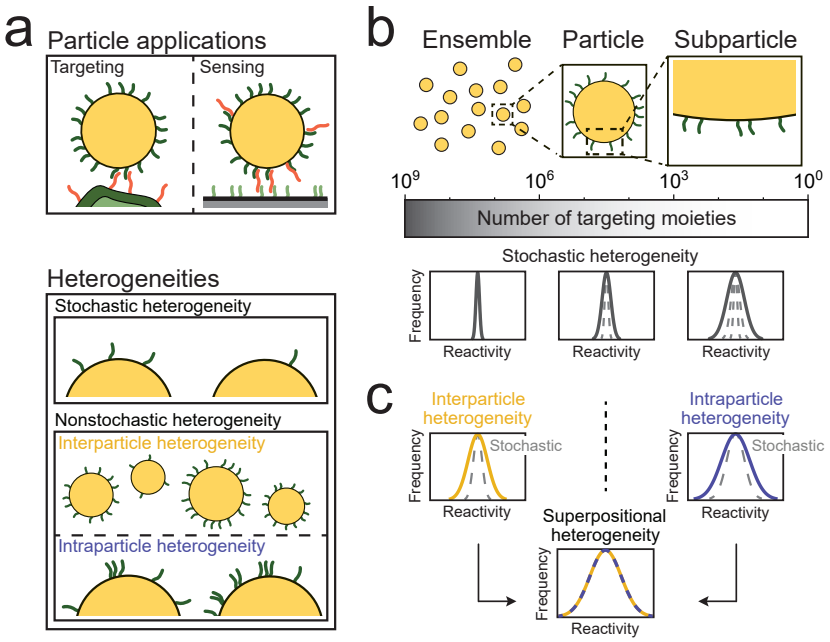

FIGURE 3.1: SUPERPOSITIONAL HETEROGENEITY AND HOW IT INDUCES REACTIVITY VARIABILITY. (a) Sketch of two applications of biofunctionalized particles: targeted drug delivery in nanomedicine (left) and sandwich assay biosensor with a particle as detection label (right). The reactivity variability is determined by the collective sum of stochastic and non-stochastic heterogeneities resulting in varying numbers of targeting moieties on the particle surface. (b) Stochastic heterogeneity, where the width of the reactivity distribution is determined by Poisson statistics. Left: in case the targeting or sensing is effectuated by targeting moieties on the surfaces of many particles, then the total number of involved targeting moieties is large (indicative: 10^6-10^9 targeting moieties) and therefore the width of the reactivity distribution is narrow. Middle: when the targeting or sensing is caused by a single-particle measurement, a lower number of targeting moieties is involved (indicative: 10^3-10^6 targeting moieties), resulting in a larger variability of reactivity. Right: if only a subparticle area is available for interaction to a countersurface, the number of targeting moieties is low (indicative: 10^0-10^3 targeting moieties), resulting in the broadest reactivity distribution. (c) Nonstochastic heterogeneities. Interparticle heterogeneity refers to targeting moiety variability between particles, *e.g.*, due to size dispersion. Intraparticle heterogeneity refers to targeting moiety variability between different subparticle areas, *e.g.*, due to nonuniform targeting moiety density. The observed reactivity distribution is determined by the superposition of stochastic, interparticle and intraparticle heterogeneities, *i.e.*, superpositional heterogeneity.

In the next section we will study how the reactivity variability is influenced by stochastic, interparticle, and intraparticle heterogeneities. The interparticle variability is quantified by measuring the number of

active targeting moieties per particle, and the intraparticle variability is determined by mapping the locations of active targeting moieties on the particle surface. Subsequently, the reactivity variability is studied using BPM. Finally, using simulations the reactivity variability is studied as a function of the system parameters, namely, particle interaction area, targeting moiety density, particle size, and number of particles.

3.3 RESULTS AND DISCUSSION

3.3.1 *Interparticle targeting moiety variability*

The particles used in this work are commercially available silica particles with a diameter of 1 µm, functionalized with single-stranded DNA (ssDNA) molecules as targeting moieties (see Material and methods 3.5). These particles are used in this study because they have a low size dispersion ($CV_{\text{size}} = 5\%$) and a smooth surface (see Supplementary note 3.6.4). For each particle, the number of ssDNA molecules was quantified using a fluorescent imaging method with single-molecule resolution, namely, quantitative points accumulation in nanoscale topography (qPAINT).[10,12,16] qPAINT makes use of the distribution of observed unbound times (*i. e.*, dark times) of imager strands to targeting moieties in a region of interest (ROI), which depends on the number of targeting moieties present in this ROI (see Supplementary note 3.6.1). In Figure 3.2 the interparticle targeting moiety variability is quantified on the silica particles, which were functionalized with NeutrAvidin and subsequently incubated with a dilution series of biotinylated ssDNA molecules. Figure 3.2a shows the dependency of the number of active targeting moieties per particle, quantified using qPAINT, as a function of the ssDNA to particle ratio present in solution during incubation (blue). For an increasing ratio, a linearly increasing number of targeting moieties per particle was observed (gray dashed line). This linear dependency is expected when the solution with biotinylated ssDNA molecules is depleted by the particles and the particles are not saturated. The found number of targeting moieties per particle is approximately a factor 2 lower than the ssDNA to particle ratio; this is in agreement with the fact that only half of the particle surface is observed due to illumination by total internal reflection (see Supplementary note 3.6.2).

Figure 3.2b shows the experimentally found and simulated coefficient of variation (CV) of the number of targeting moieties per particle as a function of the incubated ssDNA concentration. Two CVs are indicated: the observed total CV (blue) and the CV induced by the qPAINT measurement (red). In the simulations it was assumed that the particle

size has a normal distribution (CV_{size} = 5%; see Supplementary note 3.6.4) and that the solution with biotinylated ssDNA molecules is depleted by the particles. The variability in the number of targeting moieties induced by the qPAINT measurement σ_{qPAINT} can be described by:

$$\sigma^2_{\text{qPAINT}} = \sigma^2_{\text{sampling}} + \sigma^2_{\text{stochastic}} \tag{3.1}$$

with σ_{sampling} being the variability in the number of targeting moieties introduced by the finite sampling time, and $\sigma_{\text{stochastic}}$ the variability in the number of targeting moieties introduced by the stochastic placement of ssDNA molecules on the NeutrAvidin-functionalized particles. These two individual variabilities can be further defined as:

$$\begin{aligned} \sigma_{\text{sampling}} &= N_{\text{moiety}} \cdot \left(\frac{T_M}{\tau_b + \tau_d} \right)^{-0.5} \\ \sigma_{\text{stochastic}} &= \sqrt{N_{\text{moiety}}} \end{aligned} \tag{3.2}$$

with N_{moiety} being the average number of targeting moieties per particle, T_M the measurement time, τ_b and τ_d the mean bright and dark times respectively. At low ssDNA concentrations, and thus a low number of targeting moieties per particle, σ_{qPAINT} is dominated by the stochastic contribution, where $\sigma_{\text{sampling}} \propto N_{\text{moiety}}$ and $\sigma_{\text{stochastic}} \propto \sqrt{N_{\text{moiety}}}$.

When comparing the experimental data to the simulated data, it appears that the variability in particle size and the qPAINT measurement variability together (light blue) are not sufficient to explain the CV_{moiety} observed in the experiment. This implies that an additional variability contribution must be present which is not included in the simulation. A possible additional contributor is variability in targeting moiety density per particle; including a targeting moiety density variability per particle in the simulations (with $CV_{\text{density}} = 15\%$, dark blue) matches the simulated results to the experimental results. A variability in targeting moiety density may originate from variations in surface chemistry (*e. g.*, causing variable NeutrAvidin densities and thus variable targeting moiety densities) or other differences between particles on subparticle length scales. Such variability on a smaller length scales, *i. e.*, intraparticle variability, will be discussed in the next section.

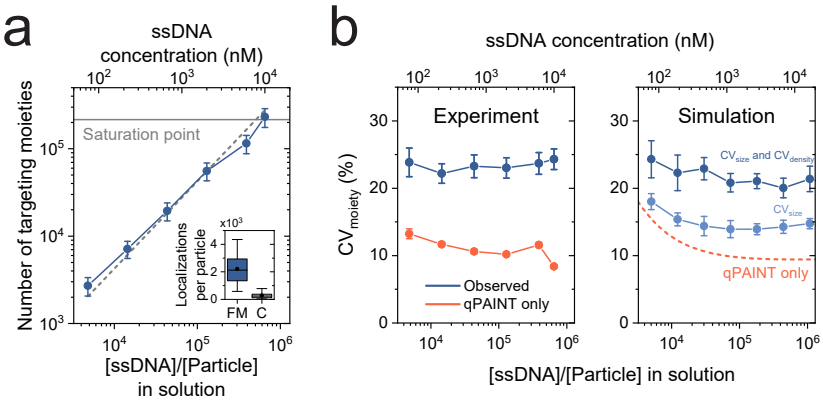

FIGURE 3.2: INTERPARTICLE TARGETING MOIETY VARIABILITY QUANTIFIED USING QPAINT EXPERIMENTS. (a) Number of targeting moieties (blue) as a function of the ssDNA to particle ratio in solution. The saturation point of $(2.0 \pm 0.2) \cdot 10^5$ targeting moieties per particle is determined by a supernatant assay (gray solid line, see Supplementary note 3.6.3). The values on the y-axis are the number of targeting moieties per particle (*i. e.,* corrected for the fractional occupation of the NeutrAvidin by the complementary ssDNA molecules in the qPAINT experiment, see Material and methods 3.5). The gray dashed line indicates a linear relation (slope = 1) between the number ssDNA molecules per particle present in solution and the number of observed targeting moieties in the qPAINT experiment. The top x-axis indicates the total incubated ssDNA concentration (both complementary and non-complementary ssDNA). The reported errors are standard deviations. The inset shows the specificity of the qPAINT experiment by means of the number of localizations per particle for full match (FM) ssDNA and control (C) ssDNA with a random sequence. The boxes show the median, 25th and 75th percentile, and the whiskers show the 5th and 95th percentile. (b) Variability in the number of active targeting moieties per particle. The panels indicate the experimental results (left) and the simulated results (right). Experiment: the observed CV is indicated in blue, the CV caused by the qPAINT measurement only is indicated in red. The CV caused by the qPAINT measurement shows a weak concentration dependency due to stochastics. Simulation: light blue includes only size variability ($CV_{\text{size}} = 5\%$); dark blue includes size as well as targeting moieties density variability ($CV_{\text{density}} = 15\%$). The experimental data was measured in two fields-of-view with approximately 10^2 particles each. The errors are the fitting errors for the experiment, and the standard error for the simulation using 10 simulations with 10^2 particles per simulation.

3.3.2 *Intraparticle targeting moiety variability*

The intraparticle targeting moiety variability was investigated by DNA-PAINT experiments.[9] The imaging data were used to confirm or reject whether the positions of these moieties on the particle surface were spatially randomly distributed. Figure 3.3a shows the positions of (a subset of) targeting moieties obtained in a DNA-PAINT measurement on a single particle (see Supplementary note 3.6.2). Since the targeting moieties are located on the surface of a spherical particle, the 2D localization data need to be projected on a hemisphere (see Supplementary note 3.6.2) to calculate the true distance (great-circle distance) between the localizations. The dashed circle visualizes the projection of the particle on the xy-plane based on the DNA-PAINT localization cloud (see Supplementary note 3.6.4).

Figure 3.3b quantifies the degree of targeting moiety clustering and

the influence of the DNA-PAINT measurement on the observed degree of clustering using clustering parameter z_m, the standardized mean nearest-neighbor (NN) distance, which is a measure for the degree of clustering (negative z_m) or dispersion (positive z_m) (see Supplementary note 3.6.5).[20] Examples are shown of simulated (true) targeting moiety positions (blue) on a particle hemisphere and corresponding simulated DNA-PAINT localizations (red), both projected on the xy-plane. The simulated data are shown for three cases: absence of clustering, superposition of clustered (25% of the localizations) and nonclustered localizations (75% of the localizations), and full clustering (100% of the localizations). For all simulated particles, the z_m values are shown for the true positions (blue) and corresponding DNA-PAINT localizations (red). The data show that the z_m distributions measured with DNA-PAINT data are wider and that the mean is less negative compared to the true positions. In Figure 3.3c, experimental z_m values calculated from DNA-PAINT results (green line) are shown for all particles in a field-of-view as a function of particle coverage by ssDNA. The remainder of the ssDNA consists of noncomplementary ssDNA equal in length. As a reference, DNA-PAINT simulations (red line) are shown for particles without targeting moiety clustering. Both curves show a slight decrease of z_m with decreasing coverage. The lower z_m values at low particle coverage represent a clustering artifact due to repeated localizations of the same targeting moiety in a DNA-PAINT experiment. This artifact is not present at the higher targeting moiety densities. The experimental results systematically show more negative z_m values compared to the simulation over the full particle coverage range, which indicates the presence of clustered true positions of the targeting moieties. The histogram (bottom panel) shows the experimentally found z_m per particle at a NeutrAvidin coverage by complementary ssDNA of 2.9%. The distribution is comparable to the simulated distribution for 25% clustering in both mean and width ($z_m = -1.2 \pm 0.6$ and $z_m = -1.4 \pm 0.6$ for the experiment and simulation respectively, see Figure 3.3b), indicating that a degree of nonrandomness is indeed present in the spatial distribution of targeting moieties on the particle surface. A nonrandomness of targeting moiety positions gives an intraparticle contribution to the reactivity variability that scales with the interaction area of the particle (see Supplementary note 3.6.6). Furthermore, it was found that a comparable distribution of z_m values could be observed for the full range of number of targeting moieties per particle (see Supplementary note 3.6.7), indicating that the typical length scale of intraparticle variability is much smaller than the particle size. The inter- and intraparticle targeting moiety variabilities cause a variability of reactivities of the biofunctionalized particles. This reactivity variability depends in particular on the interaction area of the particle, size of the

particle, targeting moiety density, and number of particles. This topic is explored in the next section, using BPM, a particle-based biosensing method with single-particle and single-molecule resolution.

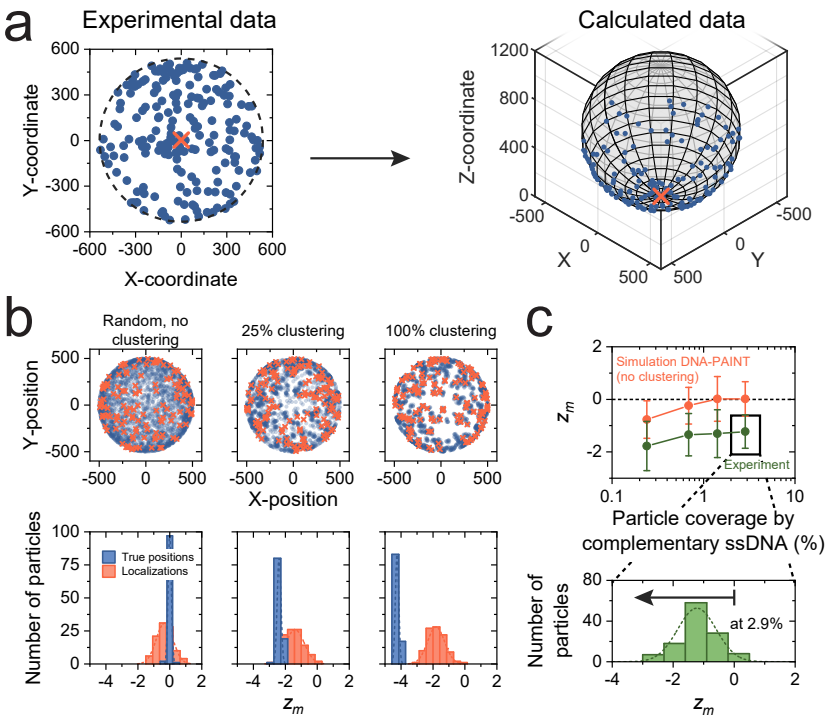

Figure 3.3: intraparticle targeting moiety variability studied using DNA-PAINT experiments. (a) Example of an experimentally measured 2D and calculated 3D localization image of DNA-PAINT localizations with the contours of the particle (black dashed line). Using the x- and y-coordinates of the localizations and the calculated diameter of the localization cloud, a 3D localization image on the lower particle hemisphere can be reconstructed. (b) Examples of simulated true positions of targeting moieties (blue) and simulated DNA-PAINT localizations (red) with corresponding z_m per particle for three cases: randomly distributed targeting moieties, 25% clustering and 75% random, and 100% clustering of targeting moieties. For an increasing degree of clustering, more negative z_m values were found. For this example, a cluster size of 25 nm and an average 10 ssDNA molecules per cluster were used as an example. (c) Experimentally calculated z_m (green) and simulated z_m (red) values as a function of the particle coverage by the complementary ssDNA. Here the particles are incubated with a dilution series of ssDNA comprising 2.9% of complementary ssDNA and the remainder non-complementary ssDNA equal in length. For all data points, a systematic difference could be observed which indicates the presence of clustered targeting moieties. The experimental data were measured in two fields-of-view with approximately 10^2 particles each. The distribution shows z_m per particle for a ssDNA coverage of 2.9%, with $z_m = -1.2 \pm 0.6$ (mean $\pm$ standard deviation). The arrow indicates that a negative z_m corresponds to clustered targeting moieties. The errors indicated in the figure are the standard deviations.

3.3.3 *Reactivity variability*

The reactivity variability was studied using BPM.[19] A detailed description of the BPM technique is given in Supplementary note 3.6.8. Briefly,

particles are tethered to a surface by a flexible double-stranded DNA (dsDNA) stem, causing every particle to move due to thermal motion within a confined space. The sensing capability of the particles results from targeting moieties on the particle and a single targeting moiety on the dsDNA stem. Target molecules in solution can bind to targeting moieties on the particle as well as to the targeting moiety on the stem; when this happens simultaneously, a compact molecular sandwich arrangement is formed, which strongly reduces the motion of the particle. The molecular interactions are designed to be reversible, causing bound and unbound particle states to be observed over time. The mean unbound state lifetime of a particle decreases when the number of captured target molecules increases. Therefore, the average switching frequency of particles between unbound and bound states increases with the target concentration in solution.

The BPM sensor is designed in such a way that the affinity between target molecule and targeting moieties on the particle is much higher than the affinity between target molecule and the single moiety on the stem. Therefore, the sensing mechanism can be described as a two-step process: target molecules bind first to the targeting moieties on the particle and thereafter to the moiety on the stem. This effectively results in target molecules bound to targeting moieties on the particles to function as the reactive component toward the moiety on the stem (see Supplementary note 3.6.8).

Figure 3.4a shows the response of the sensor as a function of the ssDNA target concentration in solution. The left graph shows the measured particle switching frequency, defined as the mean frequency with which a single particle switches between bound and unbound states. The right graph shows the measured mean state lifetimes. The switching frequency as a function of target concentration follows an S-shaped dose-response curve on a linear-logarithmic scale,[19] which is characteristic for a first-order affinity binding process. The mean state lifetime as a function of target concentration shows different behaviors for the mean bound state lifetime τ_B (red) and mean unbound state lifetime τ_U (blue). τ_B is independent of target concentration, because it is determined by the dissociation lifetime of the single-molecular interaction between a ssDNA target molecule and the ssDNA molecule on the stem. In contrast, τ_U shows a clear concentration dependency, which is in agreement with the fact that the occupation of targeting moieties by target molecules depends on the target concentration in solution.

The reactivity variability per particle becomes apparent when ana-

lyzing the distributions of measured lifetimes. Figure 3.4b shows the bound and unbound state lifetimes of all observed particles plotted as cumulative distribution functions (CDFs), for a high target concentration (blue) and a low target concentration (green). The CDFs of the bound state lifetimes show straight lines on a linear-logarithmic scale, equal for both target concentrations. This demonstrates a single-exponential lifetime distribution, which is in agreement with a well-defined single-molecular unbinding process. In contrast, the CDFs of the unbound state lifetimes do not show single-exponential distributions. The data cannot be fitted with straight lines but can be fitted with lognormal distributed mean unbound state lifetime per particle.[19] The fact that the association kinetics do not show a single-exponential distribution suggests the presence of reactivity variability per particle.

Figure 3.4c plots the CDFs of the unbound state lifetimes for two individual particles as an example; these CDFs of individual particles show single-exponential distributions (red dashed lines) in contrast to the ensemble CDFs in Figure 3.4b. The CDFs of the two individual particles show a different τ_U, indicating that the molecular binding process occurs under different local conditions per particle. Experiments show that the observed difference in τ_U per particle is of static nature, *i. e.*, does not change during a measurement. Therefore, we attribute the observed differences between particles to time-independent heterogeneities, such as differences in the number of accessible targeting moieties. For example, if more targeting moieties are present in the interaction area, then more target molecules are captured at a given target concentration, resulting in a shorter τ_U (see the two sketches in Figure 3.4c).

In Figure 3.4d the experimental (blue) and simulated (red) distributions of both τ_B and τ_U per particle are visualized. The simulated distributions were determined using mock data with a measurement duration equal to the experiment; the distribution width reported by the simulations is therefore only caused by the finite measurement time. The observed bound and unbound state lifetimes for all particles were sampled from a single-exponential distribution, with mean bound and mean unbound state lifetimes equal to the peak values of the experimental distributions (blue dashed line). The experimental and simulated distributions for τ_B (panel d, left) per particle show $CV_{\text{exp}} = 24 \pm 3\%$, and $CV_{\text{sim}} = 14 \pm 1\%$, respectively. The slightly larger CV_{exp} compared to CV_{sim} is caused by a relatively long τ_U for the majority of the particles (panel d, right), resulting in lower bound state lifetime statistics per particle compared to the simulation. However, the results for the unbound state lifetime show large differences between

experiment and simulation. The experimental distribution for τ_U per particle shows a much larger variability than would be expected from the simulated results, namely, $CV_{\text{exp}} = 80 \pm 10\%$ in the experiment *versus* $CV_{\text{sim}} = 14 \pm 2\%$ in the simulation. The data in Figure 3.4 show strong differences in the reactivity between individual particles. In the next section, the contribution of each source of variability (stochastic, nonstochastic interparticle, and nonstochastic intraparticle) will be studied. Subsequently, using simulations the reactivity variability will be determined as a function of interaction area, targeting moiety density, particle size, and the number of particles.

3.3.4 *Influence of system parameters on reactivity variability*

In this section we study by simulations the scaling behavior of different contributors to the reactivity variability for different system parameters, namely, particle size, targeting moiety density, interaction area, and number of particles. In the simulations we generate initial distributions (*e.g.*, of particle size and targeting moiety density) with an experimentally found or estimated mean and width, and subsequently perform calculations on these distributions to determine the number of targeting moieties per interaction area, which determines the reactivity per particle. Finally, we determine the mean and width of the distributions for the given number of particles in the system. The results are shown in Figure 3.5a for particle-based biosensing by BPM and are generalized in Figures 3.5b and 3.6 for other particle-based biosensing and targeted nanomedicine applications.

Figure 3.5a shows the reactivity variability in BPM as a function of the particle interaction area, highlighting the contributions of stochastic, interparticle, and intraparticle variability. In the BPM design with a single ssDNA molecule on the stem, the reactivity variability per particle is caused by variability in the number of target molecules captured on the particles that can interact with the ssDNA molecule on the stem. Due to the limited length of the tether between particle and substrate, the stem can reach only a limited area on the particle. Only target molecules captured within this interaction area are able to reach the ssDNA molecule on the stem. It was found that the interparticle variability $\sigma_{\text{interparticle}}$ depends on particle size dispersion and targeting moiety density fluctuations (see Figure 3.2). The intraparticle variability $\sigma_{\text{intraparticle}}$ originates from nonuniform functionalization of targeting moieties (see Figure 3.3) and was found to scale with the inverse square root of a_i (see Supplementary note 3.6.6). The stochastic contribution of the targeting moieties is defined as $\sigma_{\text{stochastic}} = \sqrt{f \cdot N_{\text{moiety}}}$, with f

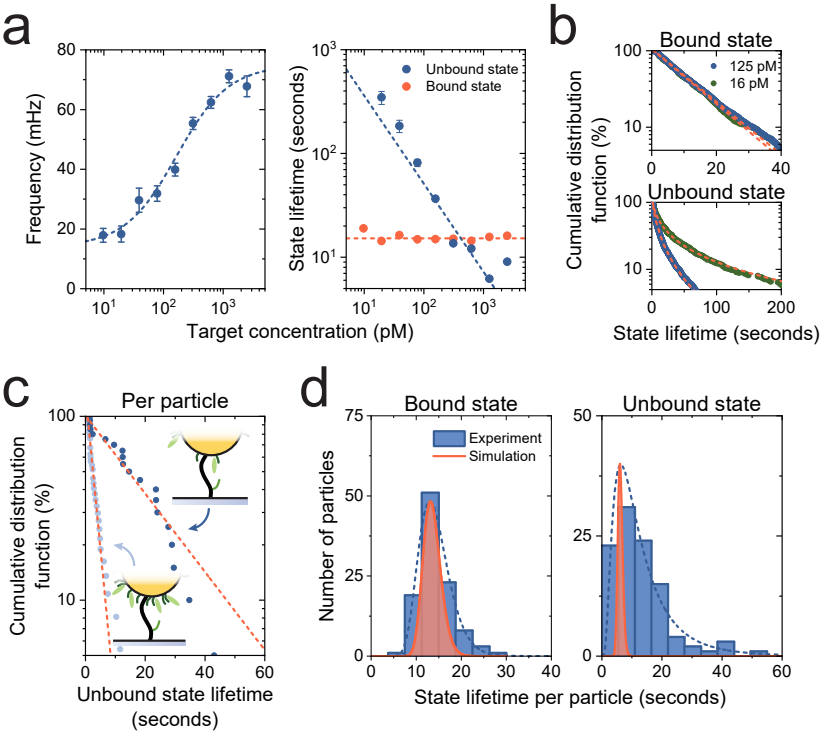

FIGURE 3.4: REACTIVITY VARIABILITY PER PARTICLE QUANTIFIED USING BIOSENSING BY PARTICLE MOBILITY (BPM). (a) Sensing response as a function of ssDNA target concentration. Left: the switching frequency as a function of target concentration. A Hill equation fit[21] (blue dashed line) yields an EC_{50} value of 170 ± 50 pM. Right: the bound and unbound state lifetimes as a function of target concentration, derived from distributions as shown in panel b.[19] The red dashed line represents a constant time; the blue dashed line represents a fitted line with slope $1/[T]$. The errors indicated in this panel are the standard errors for the switching frequency, and fitting errors for the state lifetimes. (b) State lifetime analysis by means of cumulative distribution functions (CDFs) for ssDNA target concentrations of 125 pM (blue) and 16 pM (green). The bound state lifetime shows a single-exponential distribution while the unbound state lifetime shows a multiexponential distribution (red dashed lines). (c) CDFs for two individual particles which show an approximate single-exponential distribution. (d) Distributions of the observed state lifetime per particle for both the bound and unbound states for a target concentration of 125 pM. The width of the experimentally found distribution (blue) is rather close to the simulated distribution (red) for the bound state lifetime per particle ($CV_{\text{exp}} = 24 \pm 3\%$, and $CV_{\text{sim}} = 14 \pm 1\%$). However, for the unbound state lifetime per particle, the experimental and simulated distributions are very different ($CV_{\text{exp}} = 80 \pm 10\%$ and $CV_{\text{sim}} = 14 \pm 2\%$). The errors indicated in the caption are the fitting errors.

being the fraction of targeting moieties occupied by a target molecule and N_{moiety} the average number of targeting moieties in the interaction area. The fractional occupancy is typically less than 1% in the low-concentration regime of a BPM sensor and depends on the target concentration in solution. For Figure 3.4d, f was estimated to be approximately 0.3%. The parameters $\sigma_{\text{interparticle}}$ and $\sigma_{\text{reactivity}}$ were determined experimentally in the previous sections using qPAINT (Figure 3.2b) and BPM data (Figure 3.4d), respectively. On the basis of these

parameters, $\sigma_{\text{intraparticle}}$ could be estimated and therefore the reactivity variability could be calculated as a function of a_i.

The results in Figure 3.5a show that for a small a_i, where the number of targeting moieties N_{moiety} is small, the $CV_{\text{reactivity}}$ is dominated by stochastic and intraparticle variability. For large a_i, where N_{moiety} is large, the contribution of interparticle variability dominates. The stochastic contribution scales as $CV \propto a_i^{-1/2}$, corresponding to Poisson statistics. The intraparticle contribution scales with $CV \propto a_i^{-1/2}$ as well (see Supplementary note 3.6.6), while the superposition of all contributions scales roughly with $CV \propto a_i^{-2/3}$.

The three histograms on the right side of Figure 3.5a show reactivity distributions for different a_i, *i. e.*, distributions of the number of target molecules captured onto a particle interaction area of a given size. This is indicated as $N_{\text{moiety,eff}}$, because these target molecules are the moieties effective for generating a signal. The top histogram applies to the BPM sensor with a single ssDNA molecule on the stem (see Figure 3.4), which has a particle interaction area a_i of about $6 \cdot 10^3$ nm². In this condition, the simulations show that the reactivity variability is dominated by stochastic and intraparticle variabilities of targeting moieties that captured a target molecule on the small interaction area of the particle. The simulations predict a CV of 82%, which is similar to the experimental value for the unbound state lifetime reported in Figure 3.4d. The middle histogram applies to a BPM sensor with the whole substrate coated with ssDNA molecules, as reported in previous work.[17,18] This sensor design has a larger particle interaction area of about $6 \cdot 10^4$ nm² (see Supplementary note 3.6.8). With this larger interaction area, the simulations show that the contributions of stochastic and inter- and intraparticle heterogeneity are approximately equal, giving a CV of 21%. This value is in agreement with the experimentally measured CV for the BPM sensor with the whole substrate coated with ssDNA molecules.[18] The third histogram applies to a sensor that would probe the full area of a particle (*i. e.*, $a_i = 4\pi R_p^2$, with R_p being the particle radius). Here, the CV is dominated by interparticle heterogeneity and the CV is about 19%. This result is in agreement with the experimental value found in the qPAINT experiments when the qPAINT induced contribution is neglected (see Figure 3.2b). Overall, the results show that the stochastic contribution to the reactivity variability in BPM is small with respect to the other sources of variability if the interaction area is at least 5% of the particle surface.

The reactivity variability calculated by simulations in Figure 3.5a and the corresponding experimental values are in good agreement

for different BPM sensor designs, where the particles interact with a biofunctionalized sensing surface. To extrapolate these results toward targeted nanomedicine and particle-based biosensing in general, the calculated reactivity variability is shown in Figures 3.5b and 3.6 for different sizes of interaction area, particle radii, targeting moiety densities, and number of particles.

Figure 3.5b shows the reactivity variability as a function of interaction area for two particle radii R_p (50 and 500 nm) and two targeting moiety densities ρ_{moiety}. A lower $\rho_{\text{moiety}} = 1,600$ µm^{-2} corresponds to an average intermolecular distance of 25 nm and resembles a typical density of a particle surface functionalized with antibodies. A higher $\rho_{\text{moiety}} = 130,000$ µm^{-2} corresponds to an average intermolecular distance of 3 nm and resembles a typical density of a particle surface functionalized with oligonucleotides. The reactivity variability is expressed as a function of the relative interaction area, *i. e.*, the percentage of the total particle surface. Due to stochastics, the reactivity variability is largest for small particles and for a low targeting moiety density.

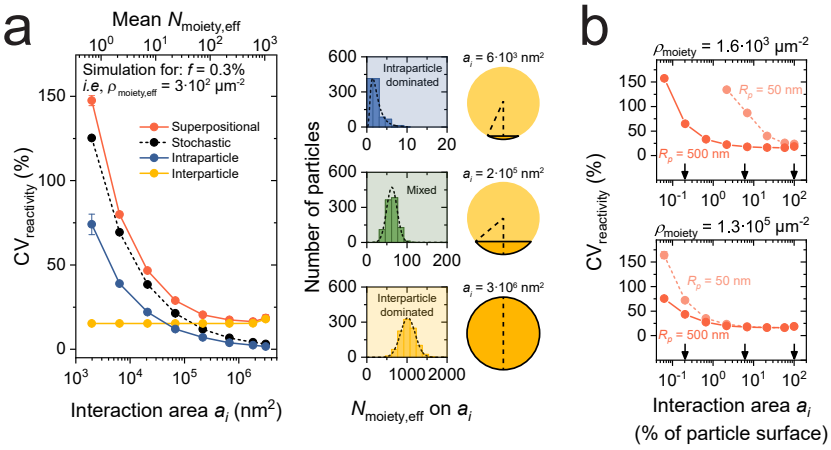

Figure 3.5: Limiting effect of superpositional heterogeneity on the reactivity variability of biofunctionalized particles for various interaction areas. (a) Reactivity variability as a function of the interaction area a_i for BPM. Shown are the stochastic (black), interparticle (yellow), and intraparticle (blue) contributions to the variability as well as the superposed result (red), for a particle with a radius of 500 nm and an effective targeting moiety density $\rho_{\text{moiety,eff}}$ of $3 \cdot 10^2$ µm^{-2}. The errors indicated in the figure are standard errors using 5 simulations with 10^3 particles per simulation; most error bars are smaller than the symbol size. On the right, examples of three distributions of the number of target molecules per interaction area a_i are visualized. Particles are schematically shown with their corresponding a_i indicated in dark orange. The found $CV_{\text{reactivity}}$ are $82 \pm 1\%$, $21.3 \pm 0.3\%$, and $18.9 \pm 0.5\%$ (mean $\pm$ standard error) for intraparticle heterogeneity dominated, mixed, and interparticle heterogeneity dominated examples respectively. (b) The variability of reactivity per particle as a function of the interaction area for two particle radii R_p (50 and 500 nm) and a low targeting moiety density (top, $\rho_{\text{moiety}} = 1.6 \cdot 10^3$ µm^{-2}) and high targeting moiety density (bottom, $\rho_{\text{moiety}} = 1.3 \cdot 10^5$ µm^{-2}). The arrows in the panel indicate three values for the interaction area a_i that are used in Figure 3.6.

For large interaction areas, the reactivity variability converges to about 20%; here the stochastic contribution is small and the variability is dominated by interparticle heterogeneity (see also Figure 3.5a).

Figure 3.6a shows how the reactivity variability depends on particle radius R_p, for two targeting moiety densities, and for three interaction areas (indicated by the arrows in Figure 3.5b). For all conditions, the reactivity variability decreases as a function of particle radius, due to the decreasing contribution of stochastic and intraparticle variability. The particle radius where the stochastic and intraparticle contributions become insignificant depends on the interaction area and the targeting moiety density: a smaller interaction area results in a larger reactivity variability while a higher density of targeting moiety results in a smaller reactivity variability.

Figure 3.6b visualizes the ensemble reactivity variability as a function of the number of particles, shown for two targeting moiety densities, two different particle sizes (solid and dashed lines), and three interaction area percentages (indicated by the three colors). The ensemble reactivity variability is lower (lower CV, better precision) when more particles are used, scaling with the inverse square root of the number of particles. The number of particles required to get a desired CV depends on the particle size, interaction area, and targeting moiety density. The stochastic and intraparticle heterogeneity are large in the case of small particles, low targeting moiety density, and small interaction area. The results show that systems with small particles (< 100 nm), low targeting moiety density (for example particles coated with proteins), and a

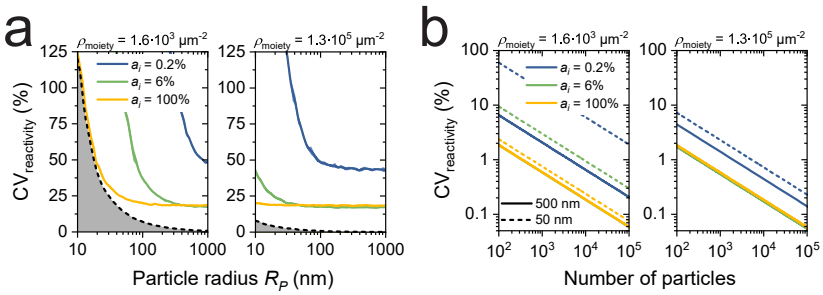

FIGURE 3.6: LIMITING EFFECT OF SUPERPOSITIONAL HETEROGENEITY ON THE REACTIVITY VARIABILITY OF BIOFUNCTIONALIZED PARTICLES. (a) Reactivity variability per particle as a function of particle radius for three interaction areas and for a low and high density of targeting moieties. The experimental limit (black dashed line) indicates the limit with only stochastic heterogeneity and an interaction area that equals the full particle surface. The error indicated by the shading is the standard error using 5 simulations with 10^3 particles per simulation. (b) Ensemble reactivity variability as a function of the number of particles, for particle sizes of 500 nm (solid lines) and 50 nm (dashed lines). Left: the green solid line is behind the yellow solid line. Right: the yellow and green dashed and solid lines are very close to each other.

limited interaction area between particle and countersurface, can have very large reactivity variability. When the targeting at the biological site of interest is effectuated by a limited number of particles (< 1000 particles), then the number of molecular interactions realized by the particles can vary by tens of percent.

3.4 CONCLUSION

The reactivity variability of biofunctionalized particles used in targeted nanomedicine and particle-based biosensing applications depends on heterogeneities of various kinds. We have studied three factors that contribute to a variability in the number of targeting moieties on the particles, namely, stochastic heterogeneity, interparticle heterogeneity, and intraparticle heterogeneity, jointly referred to as superpositional heterogeneity.

In this chapter, we have presented a comprehensive methodology to quantify particle heterogeneities and their consequences. We have experimentally quantified targeting moiety variabilities using microscopy methods with single-molecule resolution, namely, qPAINT and DNA-PAINT, using ssDNA-functionalized silica particles as a model system. The data show that the interparticle heterogeneity originates from particle size dispersion and targeting moiety density fluctuations, and intraparticle heterogeneity is caused by nonuniform functionalization.

The three types of heterogeneities cause biofunctionalized particles to have variable reactivities, where reactivity is defined as the number of particle-coupled targeting moieties that are available for interaction toward a countersurface. The variability was quantified by the coefficient of variation, which depends on the interaction area of the particles, the particle size, the targeting moiety density, and the number of particles. The reactivity variability was studied by experiments and simulations for BPM, a particle-based biosensing technique with single-particle and single-molecule resolution. The results show that the reactivity variability strongly depends on the size of the interaction area. When the contributions of stochastic and inter- and intraparticle heterogeneity are approximately equal, then the reactivity variability stabilizes and is approximately equal to the reactivity variability for a full-particle interaction.

The results were extrapolated toward the fields of targeted nanomedicine and particle-based biosensing in general, where the precision in the available number of particle-coupled targeting moieties depends on the particle size, targeting moiety density, interaction area, and

number of particles. The stochastic and intraparticle heterogeneity are large in the case of small particles, low targeting moiety density, and small interaction area. The results show that large fluctuations (tens of percent) can be expected when targeting effects at a biological site of interest or at a sensor surface are determined by interactions from a limited number of particles.

The methodologies and understanding described in this chapter warrant further studies on variabilities of biofunctionalized particles on multiple length scales. Studies can include various biofunctionalization strategies, different particle materials, sizes, and geometries of particles, different targeting moiety types, and the influence of complex biological matrices (*e. g.*, protein corona). Measured distributions and heterogeneity simulations can be related to the precision of particle-based targeting effects. The developed insights will enable researchers to engineer particles for biomedical applications with high precision, guided by a thorough understanding of heterogeneities and their collective consequences.

3.5 MATERIAL AND METHODS

QPAINT: All ssDNA oligonucleotides (IDT, HPLC purification) were diluted in Milli-Q water (Thermo Fisher Scientific, Pacific AFT 20) to a final concentration of 20 µM for the complementary ssDNA, 10 µM for the ssDNA with a random sequence, and 200 nM for the imager strand. Glass slides (25 × 75 mm, #1, Menzel-Gläser) were cleaned by 15 min sonication in methanol (VWR, absolute) and thereafter dried under nitrogen flow. A custom-made fluid cell sticker (Grace Biolabs) with an approximate volume of 24 µL was attached to the glass slide. NeutrAvidin-functionalized silica particles[19] were incubated in bulk overnight with biotinylated ssDNA at the required concentration. The particles were thrice centrifugally washed in PBS (130 mM NaCl, 7 mM Na_2HPO_4, 3 mM NaH_2PO_4 at pH 7.4) at 6000× g for 5 min using a tabletop spinner (Eppendorf MiniSpin). Finally, the particles were resuspended in PBS to a final concentration of 0.17 mg mL^{-1} (0.26 pM) and sonicated using an ultrasonic probe (Hielscher). Thereafter, the silica particles were added to the fluid cell and nonspecifically absorbed to the glass surface for 30 min (approximately 100 particles per field-of-view). After incubation, the fluid cell was washed with 200 µL of buffer B+ (5 mM Tris-HCl, 10 mM $MgCl_2$, 1 mM EDTA, 0.05 vol-% Tween-20 at pH 8.0) to remove unbound particles and change the buffer in the fluid cell. Finally, 200 µL of imager strand of the required concentration in buffer B+ was added and the fluid cell was closed using sticky tape. Imaging at a 60× magnification (Nanoimager S, ONI)

was performed under TIR conditions using a 647 nm laser at 50 mW at a frame rate of 13.3 Hz for 30 min. Thresholding the integrated pixel intensity of the ROI around each particle was used to determine binding and unbinding events of imager strands. The mean dark time was extracted by fitting all observed dark times to a single-exponential distribution.

DNA-PAINT: Experimental conditions as described under qPAINT. Drift correction was performed by cross-correlation. After drift correction, the positions of the targeting moieties were determined by clustering the DNA-PAINT localizations both in space and time; DNA-PAINT localizations were clustered into a single targeting moiety position if the distance between DNA-PAINT localizations was less than 100 nm in space and less than 15 frames in time. The diameter of the localization cloud was determined using the area of the convex hull; this diameter represents the diameter of the particle (see Supplementary note 3.6.4). Second, the localization cloud was centered by averaging all targeting moiety positions after discarding top and bottom 5% outliers. The centered positions are projected on a sphere with the calculated diameter. The NN-distance is determined for each position by calculating the great-circle distance to the closest position.

BPM ASSAY: Glass slides (25 × 75 mm, #5, Menzel-Gläser) were cleaned by 15 min of sonication in methanol (VWR, absolute), isopropanol (VWR, absolute), and methanol (VWR, absolute) baths. After each sonication step, the glass coverslips were dried under nitrogen flow. A custom-made fluid cell sticker (Grace Biolabs) with an approximate volume of 60 µL was attached to the glass slide. A fluid cell was made by inserting tubing (Freudenberg Medical, monolumen) into the fluid cell sticker and connecting this tubing to a syringe pump (Harvard Apparatus, Pump 11 Elite). First the fluid cell was prewetted with PBS (130 mM NaCl, 7 mM Na_2HPO_4, 3 mM NaH_2PO_4 at pH 7.4) at a flow speed of 500 µL min^{-1} for 2 min. Functionalization of the glass substrate was performed by physisorption of 83 ng mL^{-1} anti-digoxigenin antibodies (Thermo Fisher Scientific) in PBS for 60 min. Finally, the glass substrate was blocked by incubation with 1.0 wt.-% casein (Sigma-Aldrich, casein sodium salt from bovine milk) in PBS for 60 min. After each incubation step, the fluid cells were flushed with PBS (250 µL min^{-1} for 1 min). NeutrAvidin-functionalized silica particles were incubated in bulk with 10 nM nanoswitch for 10 min.[19] Subsequently, the particles were coated with ssDNA by an incubation with 40 µM biotin-labeled single-stranded oligonucleotide. The particles were thrice centrifugally washed in 1.0 wt.-% BSA (Sigma-Aldrich, lyophilized powder, essentially globulin free, low endotoxin, $\geq$ 98%)

and 0.05 vol-% Tween-20 (Sigma-Aldrich) in PBS at 6000× g for 5 min using a tabletop spinner (Eppendorf MiniSpin). Finally, the particles were resuspended in PBS/BSA/Tween-20 to a final concentration of 0.17 mg mL^{-1} (0.26 pM) and sonicated using an ultrasonic probe (Hielscher). The particles were added to the fluid cell at a flow speed of 50 µL min^{-1} for 5 min and incubated for 30 min. After incubation, the fluid cell was turned over and subsequently flushed with PBS/BSA/Tween-20 at a flow speed of 50 µL min^{-1} for 5 min to remove unbound particles. ssDNA target (IDT, standard desalting) at the required concentration in PBS/BSA/Tween-20 was added at a flow speed of 50 µL min^{-1} for 5 min and incubated for 20 min. Samples were observed under a white light source using a microscope (Leica DM6000M) using a darkfield illumination setup at a total magnification of 20× (Leica objective, N PLAN EPI BD, 20×, NA 0.4). A field-of-view of approximately 400 × 400 μm^2 was imaged using a CMOS camera (Grasshopper 2.3 MP Mono USB3 Vision, Sony Pregius IMX174 CMOS sensor) with an integration time of 10 ms and a sampling frequency of 30 Hz. The silica particles were tracked using the center-of-intensity of the bright particles on the dark background. Trajectory parameters were calculated which describe the motion pattern and were used to select single-tethered particles.[17] The state lifetimes were extracted using a previously described method.[19]

SIMULATIONS OF BPM ASSAY: Data were simulated using experimental positional data of bound and unbound particles. For each simulation, two single-exponential distributions were generated: one with a given mean bound state lifetime and one with a given mean unbound state lifetime. The particle traces were reconstructed block-by-block with each block length according to the two predefined single-exponential distributions. Nonspecific interactions and inter- and intraparticle heterogeneity were neglected. Subsequent time-dependent analysis was performed as if experimental data were analyzed.

SIMULATIONS ON REACTIVITY VARIABILITY: Two independent (normal) distributions were generated for the particle diameter ($CV_{\text{size}} = 5\%$) and targeting moiety density ($CV_{\text{density}} = 15\%$); both a particle size and a targeting moiety density were assigned randomly to a particle. The spherical cap area (*i. e.*, the interaction area) was calculated for each particle. Using the assigned particle size and targeting moiety density, the (mean) number of targeting moieties on the spherical cap area was calculated. In the absence of intraparticle heterogeneity, the number of targeting moieties per spherical cap and the number of target molecules per spherical cap are Poisson distributed. To include intraparticle heterogeneity, a lognormal distributed number of targeting moieties per spherical cap was used as well. The variance of the

lognormal distribution of the number of targeting moieties on the interaction area $\sigma^2_{\text{intraparticle}}$ was matched to the experimental value of the reactivity variability found in Figure 3.4d and Supplementary note 3.6.6. Subsequently, the number of targeting moieties per spherical cap was fitted by a lognormal distribution, from which the $CV_{\text{reactivity}}$ was calculated.

3.6 SUPPLEMENTARY NOTES

3.6.1 *Quantitative points accumulation in nanoscale topography*

qPAINT measurement

Quantitative points accumulation in nanoscale topography (qPAINT) is a fluorescence-based measurement technique by which quantitative information on the number of molecules on complexes or surfaces can be obtained.[10] The method exploits the well-defined and controllable binding behavior of dye-labeled ssDNA imager strands to ssDNA docking strands (see Figure 3.7), which are referred to in this chapter as targeting moieties. The number of targeting moieties can be determined via imager strands that transiently bind to the complex- or surface-bound ssDNA docking strands, causing observable binding and unbinding events (see Figure 3.7a). The distribution of the observed unbound times (*i. e.*, dark times) of imager strands to ssDNA docking strands in a ROI, depends on the number of ssDNA docking strands in this ROI for a given imager strand concentration (see Figure 3.7b). Under the assumption that no simultaneous binding events occur in a single ROI at each given time point, the number of targeting moieties per ROI can be calculated using:

$$N_{\text{moiety}} = \frac{1}{k_{\text{on}} c_i \tau_d} \tag{3.3}$$

with N_{moiety} being the number of targeting moieties in the ROI (in this chapter a single particle), k_{on} the association rate constant of the interaction between the imager strand and the docking strand, c_i the imager strand concentration, and τ_d the mean observed dark time. Since k_{on} is a molecularly determined constant,[10,12] and c_i an experimental condition, the observable τ_d reveals the number of targeting moieties per particle. The precision with which N_{moiety} can be determined experimentally depends on the number of observed dark states following Poisson statistics (see Equation 3.2).

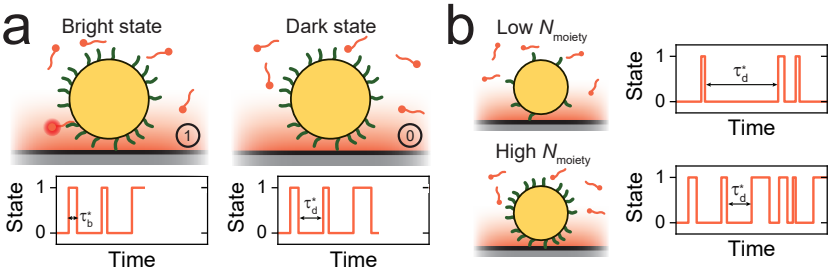

FIGURE 3.7: MEASUREMENT PRINCIPLE OF QUANTITATIVE POINTS ACCUMULATION IN NANOSCALE TOPOGRAPHY (QPAINT) TO QUANTIFY THE NUMBER OF TARGETING MOIETIES ON A SINGLE PARTICLE. (a) Binding and unbinding behavior of dye-labeled ssDNA imager strands (red) to ssDNA docking strands (green) yields observable bright states (state 1) with length τ_b^* and dark states (state 0) with length τ_d^*. Only the associated ssDNA imager strands close to the glass substrate yield a fluorescent signal due to total internal reflection excitation, causing an evanescent field (red gradient). (b) For particles with a low number of targeting moieties N_{moiety}, the observed dark times are on average longer than for particles with a high number of targeting moieties; using the mean observed dark time τ_d, the number of targeting moieties can be determined using Equation 3.3.

Analysis of qPAINT data

In Figure 3.8 the data analysis procedure of experimental qPAINT data is shown. Figure 3.8a visualizes an example of the integrated pixel intensity (blue) of a single ROI (*i. e.*, a single particle) as a function of time. The red dashed line indicates a threshold of $\mu_b + 5\sigma_b$ with μ_b and σ_b the mean and the standard deviation of the background signal respectively. Using this threshold, the bright and dark times can be extracted from the integrated pixel intensity trace. In order to correct for intensity fluctuations in the bright time and blinking, which might lead to falsely detected binding and unbinding events, two filters were used. The first filter removes single frames below the intensity threshold with neighboring frames above the intensity threshold; these events are regarded as false unbinding events and set to a bound state, under the condition that the integrated pixel intensity in this particular frame is above $\mu_b + \sigma_b$. The second filter removes single frames above the intensity threshold with neighboring frames below the intensity threshold; these are regarded as false binding events and set to an unbound state, under the conditions that the integrated pixel intensity in this particular frame is below $\mu_b + 9\sigma_b$. The red solid line (see inset) visualizes the state trace that results from thresholding the integrated pixel intensity profile; a high level indicates a bound state from which the bright time was extracted, and a low level indicates an unbound state from which the dark time was extracted.

Figure 3.8b shows two CDFs, and two histograms of the mean dark and bright times of all observed lifetimes on a single particle. For the CDF of the dark times, a single-exponential distribution (blue

dashed line) with $\tau_d = 12.2 \pm 0.1$ s was observed indicating for a single-molecular binding process. In contrast, the CDF for the bright times only exhibit an approximate single-exponential distribution (red dashed line) with $\tau_b = 830 \pm 29$ ms for 70% of all observed bright times. This effect might be explained by filtering the dark times with a length that equals a single frame; this results in a tail of merged, and thus longer, bright times. However, since 70% of the observed bright times and all observed dark times follow a single-exponential distribution, we neglected the influence of this effect on the quantitation of the number of targeting moieties per particle.

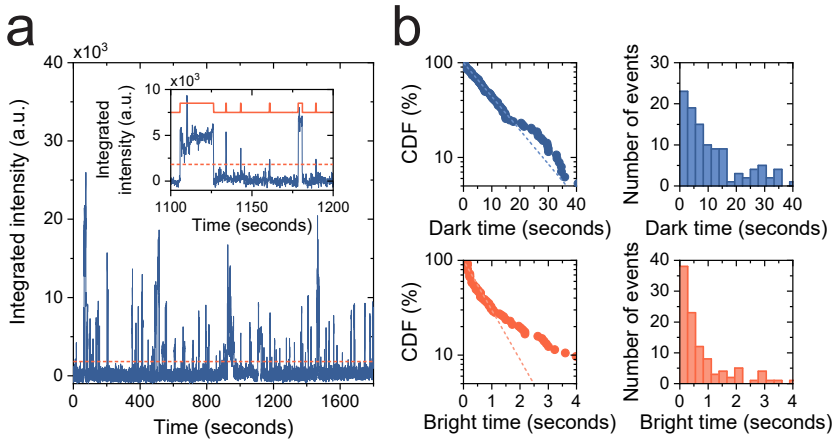

FIGURE 3.8: DATA ANALYSIS PROCEDURE OF EXPERIMENTAL QPAINT DATA. (a) Integrated intensity in a ROI (*i.e.*, a single particle) as a function of time. The threshold (red dashed line) is determined by means of the background signal and has the value of $\mu_b + 5\sigma_b$ with μ_b and σ_b the mean and the standard deviation of the background signal respectively. The inset shows a zoom-in in which individual bright and dark times can be observed after thresholding the integrated intensity (red solid line). (b) Lifetime analysis of the dark and bright times observed in a single particle. The cumulative distribution function (CDF) of all observed dark times shows a single-exponential distribution (blue dashed line) with $\tau_d = 12.2 \pm 0.1$ s. The CDF of all observed bright times shows a single-exponential distribution (red dashed line) for approximately 70% of the observed bright times with $\tau_b = 830 \pm 29$ ms. The errors indicated in the caption are fitting errors.

Mass transport limitation in qPAINT experiments

Since the number of targeting moieties per particle is calculated from the mean dark time τ_d per particle, no more than a single event within a ROI should occur at a point in time per particle. If this condition is not met, the number of targeting moieties per particle is underestimated.[16] However, in order to meet this condition, particles with a large number of targeting moieties (in this chapter ~400,000 moieties per particle) pose an intrinsic imager strand transport problem since low imager strand concentrations are required (~fM) in order to determine the number of targeting moieties per particle. Conventional qPAINT

measurements[10,12,16] are performed at imager strand concentrations of > 100 pM which result in a mean intermolecular distance d_{mol} in solution of < 3 µm with a corresponding characteristic diffusion time τ_{diff} of < 0.03 s where τ_{diff} is defined as the time required for the imager strand to diffuse over distance d_{mol}:

$$\tau_{\text{diff}} = \frac{d_{\text{mol}}^2}{D} \tag{3.4}$$

where $d_{\text{mol}} \cong \frac{1.18 \cdot 10^{-9}}{\sqrt[3]{c_i}}$ and D being the diffusion coefficient of the imager strand. Under the assumption that $\tau_{\text{diff}} \ll \tau_d$, τ_d is indeed inversely proportional to N_{moiety} and c_i according to Equation 3.3. However, when low imager strand concentrations (sub-picomolar range) are used, the assumption that $\tau_{\text{diff}} \ll \tau_d$ does no longer hold; the observed association kinetics are then mass transport limited and the number of docking strands is underestimated.

In Figure 3.9 the results of a qPAINT experiment are given in which the mass transport limitation is clearly visible. Figure 3.9a shows the dependency of the number of active targeting moieties per particle, quantified by qPAINT, as a function of the ssDNA to particle ratio present in solution during incubation (blue). The top x-axis indicates the incubated ssDNA concentration and the y-axis the measured number of ssDNA targeting moieties per particle. For an increasing ratio, a linearly increasing number of targeting moieties per particle was observed at low ssDNA concentrations. This linear relation is similar to the linear relation presented in Figure 3.2a (gray dashed line). However, at high ssDNA concentrations, the experimental data exhibit a deviating behavior from this linear dependency; in this regime, the imager strand concentration is in the low pM concentration range, and thus mass transport limits the observed transient binding behavior.

In Figure 3.9b the experimentally determined number of targeting moieties on a single particle and the characteristic diffusion time is given as a function of imager strand concentration. On the left, two samples, with an incubated ssDNA concentration of 333 nM (dark blue) and 56 nM (light blue), were measured each with three imager strand concentrations. Since no imager strand dependency exists, the conditions of $\tau_{\text{diff}} \ll \tau_d$ is met at lower ssDNA concentrations. However, on the right, the characteristic diffusion time is calculated as a function of imager strand concentration. Since mass transport effects start to appear at a ssDNA concentration of 667 nM (see Figure 3.9a), with a corresponding imager concentration of 4 pM, the gray solid line indicates the threshold below which the condition of $\tau_{\text{diff}} \ll \tau_d$ is met.

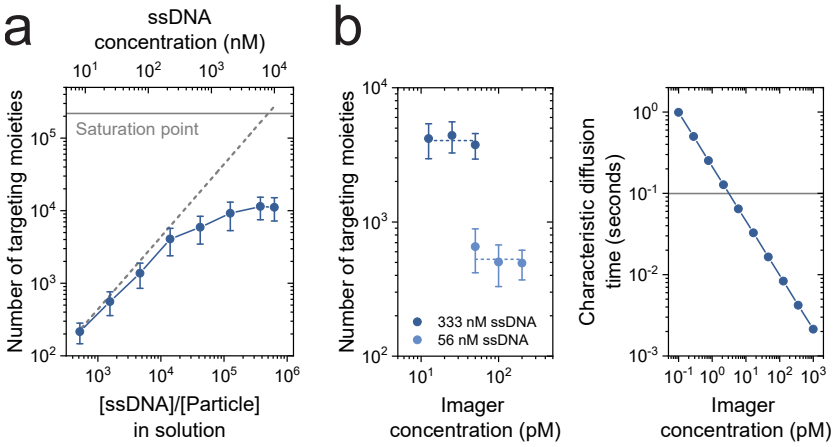

FIGURE 3.9: MASS TRANSPORT LIMITATION IN THE QUANTIFICATION OF THE NUMBER OF TARGETING MOIETIES PER PARTICLE. (a) Number of targeting moieties (blue) as a function of the ssDNA to particle ratio in solution. The saturation point (gray solid line) of $(2.0 \pm 0.2) \cdot 10^5$ targeting moieties per particle is determined by a supernatant assay (see Supplementary note 3.6.3). The gray dashed line indicates the linear relation between the number of targeting moieties per particle present in solution and the number of observed targeting moieties presented in Figure 3.2a. The secondary x-axis reveals the incubated ssDNA concentration. The errors indicated in the panel are the standard deviations. (b) Left: two samples (333 nm and 56 nM ssDNA) which were measured thrice with a different imager strand concentration. Right: calculated characteristic diffusion time as a function of imager strand concentration. The gray line indicates the threshold above which mass transport effects are visible in the quantitation of the number targeting moieties.

To solve this mass transport problem, only a fraction of the ssDNA molecules on the particle (2.9% in this chapter) has a sequence complementary to the used imager strand, which results in imager strand concentrations of > 5 pM. The remainder of the ssDNA molecules have a random, noncomplementary sequence with an equal length. Therefore, the y-axis of Figure 3.2a shows the measured number of ssDNA molecules after correcting from 2.9% to 100%.

3.6.2 *DNA points accumulation in nanoscale topography*

DNA-PAINT measurements

DNA points accumulation in nanoscale topography (DNA-PAINT) is a fluorescence-based measurement technique from which the spatial distribution of molecules on complexes or surfaces can be obtained. Similar to qPAINT, the well-defined and controllable binding behavior of dye-labeled imager strands to ssDNA docking strands is exploited.[9] Hybridization of an imager strand to the ssDNA docking strand results in a fluorescent signal, from which the super-resolved location can be extracted using its diffraction-limited spot (see Figure 3.10). Therefore

DNA-PAINT can be used to map the active targeting moieties on the surface of nanomaterials.

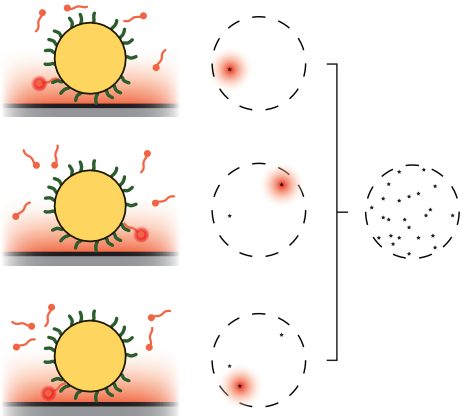

FIGURE 3.10: MEASUREMENT PRINCIPLE OF DNA POINTS ACCUMULATION IN NANOSCALE TOPOGRAPHY (DNA-PAINT) TO MAP THE POSITIONS OF TARGETING MOIETIES ON A SINGLE PARTICLE. Binding of dye-labeled ssDNA image strands (red) to ssDNA docking strands (green) yields an observable fluorescence signal. Only the associated ssDNA imager strands close to the glass substrate yield a fluorescent signal due to total internal reflection excitation, causing an evanescent field (red gradient). Since it concerns an isolated emitter, its diffraction-limited spot can be fitted with a point-spread function, from which the super-resolved position of the emitter can be determined (black star).

3D DNA-PAINT measurements

In Figure 3.11, the results of a 3D DNA-PAINT measurement are shown. Here an astigmatic lens was used in order to obtain the z-position of the targeting moieties. Figure 3.11a shows the 3D positions of the targeting moieties on a single particle; the shape of the lower hemisphere of the particle can be distinguished. The z-coordinates span from approximately 0-1200 nm which suggests that the whole particle is imaged. However, the localization uncertainty in the z-direction is large compared to the uncertainty in the xy-direction, thus the targeting moiety positions were projected on the xy-plane in Figure 3.11b. From panels a and b can be concluded that the localized targeting moieties are mainly located on the lower hemisphere of the particle, and no targeting moieties are found on the top hemisphere of the particle. Therefore, it can be concluded that at least the lower hemisphere of the silica particles is imaged in a DNA-PAINT experiment.

3.6.3 *Supernatant assay*

A supernatant assay with Atto655-biotin was performed to determine the mean binding capacity per particle. Figure 3.12 shows the experimental results of the supernatant assay from which the saturation point was obtained as visualized in Figure 3.2a and Figure 3.9a. Figure 3.12a shows the measured fluorescence intensity of the supernatant as a function of the initial Atto655-biotin concentration. For the calibration curve where no NeutrAvidin-coated particles were incubated (blue dots) a

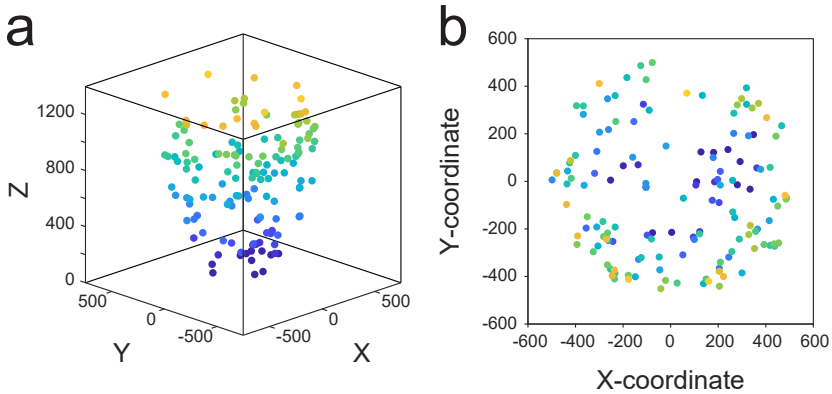

FIGURE 3.11: TARGETING MOIETY POSITIONS IN A 3D DNA-PAINT MEASUREMENT. (a) 3D visualization of the targeting moiety positions. The color is an indication for the height. (b) 2D projection of the targeting moiety positions visualized in panel a. At the edge of the position cloud, the z-coordinates of the positions are larger compared to the positions in the middle of the cloud. The color indicates the z-coordinates, equal to panel a.

linear dependency was observed (blue dashed line). When the Atto655-biotin solution was incubated with the NeutrAvidin-coated particles the dependency was no longer linear, since Atto655-biotin can bind to the NeutrAvidin complexes on the particles. By calculating the remaining Atto655-biotin concentration in the supernatant using the measured fluorescence intensity of the supernatant and the calibration curve, the binding capacity could be calculated. In Figure 3.12b, the amount of protein per particle and the binding capacity of a particle is given for two samples (each measured twice). From an absorbance measurement at 280 nm, the amount of absorbed protein on the particle surface was determined to be $(2.6 \pm 0.4) \cdot 10^5$ (mean $\pm$ standard error, two samples each measured twice). A binding capacity of $(4.0 \pm 0.3) \cdot 10^5$ (mean $\pm$ fitting errors, two samples) Atto655-biotin molecules per particle follows from panel a. This results in $(2.0 \pm 0.2) \cdot 10^5$ targeting moieties per hemisphere which was observed in qPAINT experiments. The parameter n indicates the number of accessible biotin-binding sites on the NeutrAvidin molecules, determined by dividing the total binding capacity by the number of protein complexes. This parameter was found to be $n = 1.5 \pm 0.3$ Atto655-biotin molecules per NeutrAvidin complex.

Based on the supernatant assay, a saturation point is expected for ssDNA concentrations higher than 6.3 µM. In the qPAINT data (see Figure 3.2a), no saturation point was found. This absence of a saturation point in the qPAINT measurement is probably caused by two differences in experimental conditions between qPAINT and supernatant assay experiments. Firstly, the supernatant assay uses an excess

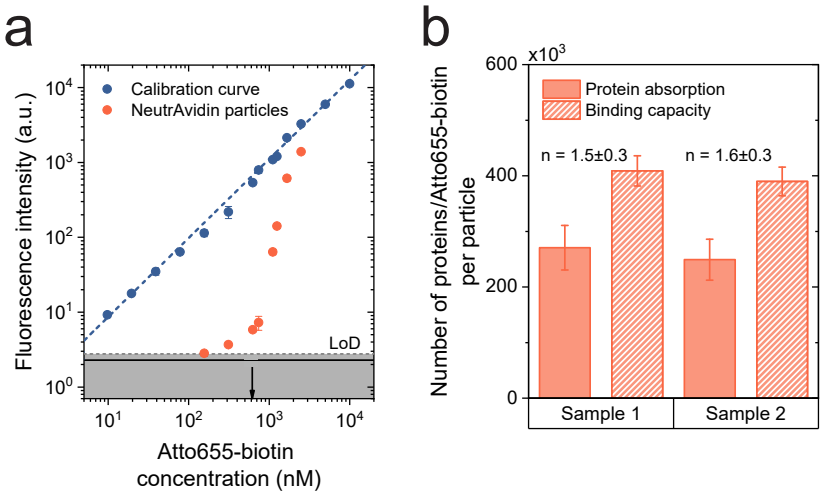

FIGURE 3.12: SUPERNATANT ASSAY TO DETERMINE THE BINDING CAPACITY OF NEUTRAVIDIN-COATED PARTICLES. (a) Supernatant assay with Atto655-biotin to determine the mean binding capacity per particle. The calibration curve (blue dots) shows a linear dependency (blue dashed line) between the measured fluorescence intensity and the Atto655-biotin concentration. When NeutrAvidin-functionalized particles were added to an Atto655-biotin solution (red), no linear dependency could be observed, which shows that Atto655-biotin binds to NeutrAvidin. The black solid line indicates the background signal and the dashed gray line $\mu_b + 3\sigma_b$ (*i.e.*, Limit of Detection, LoD) where μ_b is the background signal and σ_b the standard deviation of the background signal. The arrow on the x-axis indicates the binding capacity in the experiment. (b) The protein absorption using absorption measurements was found to be $(2.7 \pm 0.4) \cdot 10^5$ and $(2.5 \pm 0.4) \cdot 10^5$ (mean $\pm$ standard error) NeutrAvidin complexes per particle for sample 1 and sample 2 respectively, and the binding capacity that results from panel a was found to be $(4.1 \pm 0.3) \cdot 10^5$ and $(3.9 \pm 0.3) \cdot 10^5$ Atto655-biotin molecules per particle (mean $\pm$ fitting errors) for sample 1 and sample 2 respectively. The mean number of Atto655-biotin molecules per NeutrAvidin complex was found to be 1.5 ± 0.3 and 1.6 ± 0.3 for sample 1 and sample 2 respectively.

of Atto655-biotin to quantify the saturation point which precludes depletion of Atto655-biotin. The association of Atto655-biotin to the particle is therefore faster compared to the association of ssDNA to the particle in the qPAINT experiment. Furthermore, Atto655-biotin is a smaller and a less charged molecule compared to ssDNA, causing less steric hindrance and charge repulsion on the particle surface respectively. These differences both cause a slower association of ssDNA to NeutrAvidin and thus a higher saturation point in qPAINT experiments compared to the supernatant assay.

SUPERNATANT ASSAY: 5 µL NeutrAvidin-coated silica particles (1 wt.-%) were added to 195 µL PBS (130 mM NaCl, 7 mM Na_2HPO_4, 3 mM NaH_2PO_4 at pH 7.4). The particles were centrifuged at 6000× g for 5 minutes using a tabletop spinner (Eppendorf MiniSpin) to clear the supernatant. The supernatant was carefully removed and discarded. 100 µL Atto655-biotin (Sigma-Aldrich, $\geq$ 95.0%) in PBS in the required concentration was added to the particles and vortexed to redisperse

the particles. The particles were incubated with the Atto655-biotin for 3 hours on a rotating fin. Again, the particles were centrifuged at 6000× g for 15 minutes to clear the supernatant. The supernatant was separated from the particles and the fluorescence intensity was measured with a plate reader (Fluoroskan Ascent) using a 384 well plate (Corning).

3.6.4 *Size dispersion of silica particles*

In Figure 3.13, the size dispersion of silica particles was determined by scanning electron microscopy (SEM). A circle was fitted through each particle outline. The area of this circle was used to calculate the particle diameter and was found to be 0.97 ± 0.04 µm (mean $\pm$ standard deviation). The size dispersion was quantified with the coefficient of variation (CV) of the particle diameter and was found to be $CV_{\text{size}} = 3.9 \pm 0.5\%$ (mean $\pm$ fitting error).

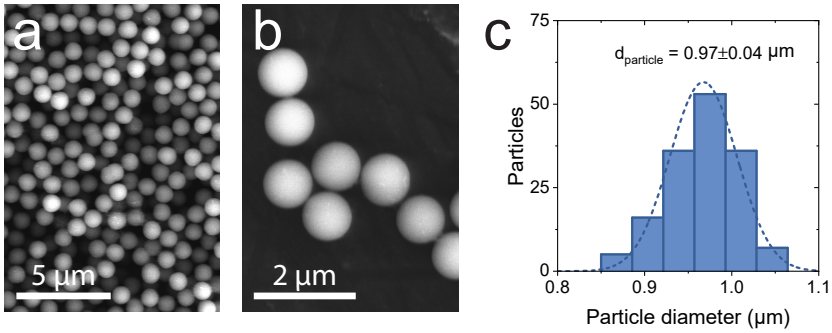

Figure 3.13: size dispersion quantification of silica particles using scanning electron microscopy (SEM). (a) Overview SEM image with multiple silica particles. Scale bar indicates 5 µm. (b) Magnified SEM image of individual particles. Scale bar indicates 2 µm. (c) Histogram of the measured particle diameter. The mean diameter was found to be 0.97 ± 0.04 µm (mean ± standard deviation) which results in a coefficient of variation of $3.9 \pm 0.5\%$ (mean ± fitting error).

The size dispersion of silica particles is also estimated from DNA-PAINT images (see Figure 3.14). In Figure 3.14a, all DNA-PAINT localizations are visualized for a single field-of-view in a DNA-PAINT experiment where the particles are clearly visible as high-density localization clouds. The area of each localization cloud was determined by a convex hull, from which the diameter was calculated, which was found to be 1.09 ± 0.05 µm (mean $\pm$ standard deviation). A CV_{size} of $4.9 \pm 0.7\%$ (mean $\pm$ fitting error) was calculated, which largely matches with the results presented in Figure 3.13c. The slightly larger diameter can be explained by the additional NeutrAvidin layer, the localization imprecision in DNA-PAINT measurements, and possible inclusion of nonspecific events close to the particle.

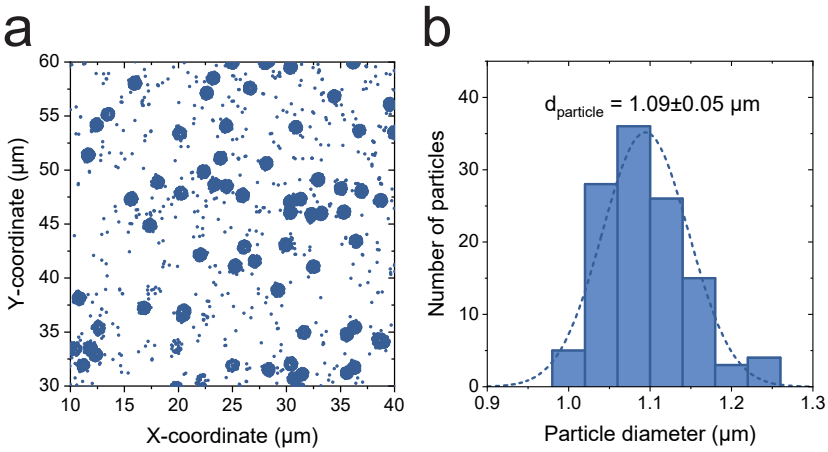

FIGURE 3.14: SIZE DISPERSION QUANTIFICATION OF SILICA PARTICLES USING DNA-PAINT LOCALIZATIONS. (a) x- and y-coordinates of all DNA-PAINT localizations in a single measurement. (b) The mean diameter of the localization cloud is assumed to represent the particle diameter $d_{\text{particle}} = 1.09 \pm 0.05$ µm (mean ± standard deviation) which results in a coefficient of variation of $4.9 \pm 0.7\%$ (mean ± fitting error).

3.6.5 *Clark-Evans test*

The Clark-Evans (CE) test is used to compare the mean observed nearest-neighbor (NN) distance between two targeting moiety positions to the expected mean NN-distance based on the targeting moiety density.[20] Based on this test, the targeting moiety positions can be significantly dispersed, where the mean NN-distance is larger than expected (*i.e.*, ordered positions), significantly clustered, where the mean NN-distance is shorter than expected, or randomly positioned, where the mean NN-distance is comparable to what is expected under the complete spatial randomness (CSR) hypothesis. The CSR hypothesis was tested using a standardized sample mean z_m which is a measure for the degree of clustering (negative z_m) or dispersion (positive z_m):

$$z_m = \frac{\overline{d}_m - \widehat{\mu}}{\widehat{\sigma}} \tag{3.5}$$

with $\overline{d}_m = \frac{1}{m}\sum_{i=1}^{m} D_i$ being the observed mean NN-distance of m targeting moiety positions, $\widehat{\mu} = \frac{1}{2\sqrt{\rho}}$ the expected mean NN-distance based on a targeting moiety density ρ and $\widehat{\sigma}^2 = \frac{4-\pi}{m(4\rho\pi)}$ the expected variance of the NN-distance. In order to use this method to accept or reject the CSR hypothesis, three requirements have to be met:

1. The total number of DNA-PAINT localizations N_L per particle should be high enough to accurately accept or reject the CSR

hypothesis, *i. e.*, the number of targeting moieties falsely classified as clustered (false positives) should be low.

2. The number of reflexive nearest-neighbors and edge effects should be minimized, to prevent including double nearest-neighbors and to prevent increased nearest-neighbor distances respectively.

3. The chance that a binder is observed multiple times should be minimized, *i. e.*, mean number of localizations per binder λ is low.

In Figure 3.15, the results of the optimization of the CE-method have been visualized, where the aforementioned requirements are considered. Random positions of targeting moieties were simulated on a particle hemisphere for a total of 50 particles with $N_L = 150$, $m = 30$ and 10% edge removal (see black arrows on x-axes). For panels a and b, the number of targeting moiety locations per particle equals the number of localizations per particle, *i. e.*, no stochastic binding of imager strand was simulated. However, for panel c, stochastic binding was included.

Figure 3.15a shows the dependency of z_m on the number of localizations per particle N_L. The error with which z_m can be calculated depends on N_L due to statistics, since the error scales according to $\sigma \propto N_L^{-0.5}$. In Figure 3.15b (top) the number of reflexive NNs is reduced by taking 10^3 random subsamples of size m from all localizations and calculate z_m for all subsamples; the mean z_m was reported as the z_m value of that particular particle. By increasing the subsample size m, z_m shows no change in its mean value while the variance increases, where the error of z_m scales with $\sigma_{z_m} \propto \sqrt{m}$. However, since the estimated variance of the NN-distances scales with $\widehat{\sigma} \propto m^{-0.5}$ (see Equation 3.5), a balance has to be found between reducing the effect of reflexive neighbors and a reasonable error of the estimated mean NN-distance. In Figure 3.15b (bottom) the dependency of z_m on the edge localizations removal is visualized. Here the x-axis resembles the percentage of the z-coordinate span which is removed from analysis. Using this approach, the highest z-coordinates (at the edge of the hemisphere) are removed from analysis. By including all localizations, the z_m value increases since the mean NN-distance for localizations at the edge is larger, compared to localizations in the middle of the hemisphere. By removing 10% of the edge, no bias was observed in the calculated z_m value. In conclusion, a number of localizations $N_L = 150$ and subsample size $m = 30$ yields approximately 0.1% false positives in rejecting the CSR hypothesis (one-tailed test with $\alpha = 0.05$).

In Figure 3.15c the stochastic sampling of the targeting moieties was

simulated for nonclustered targeting moieties (blue), and 25% clustered targeting moieties (red, equal to the 25% clustered simulation in Figure 3.3b), where the calculated z_m value is given as a function of the mean number of localizations per targeting moiety λ. λ can be tuned by the imager strand concentration and the duration of the measurement and was approximately equal for all ssDNA coverages given in Figure 3.3c. The simulations for no clustering show induced clustering by oversampling, since the targeting moieties could be observed more than once in a DNA-PAINT experiment. It was found that for $0.05 \geq \lambda \geq 0.15$ (shaded area) induced clustering is minimized, while the difference between no clustering and clustering is observable. Larger values for λ would result in a percentage of targeting moieties that are imaged more than once of $> 1\%$.

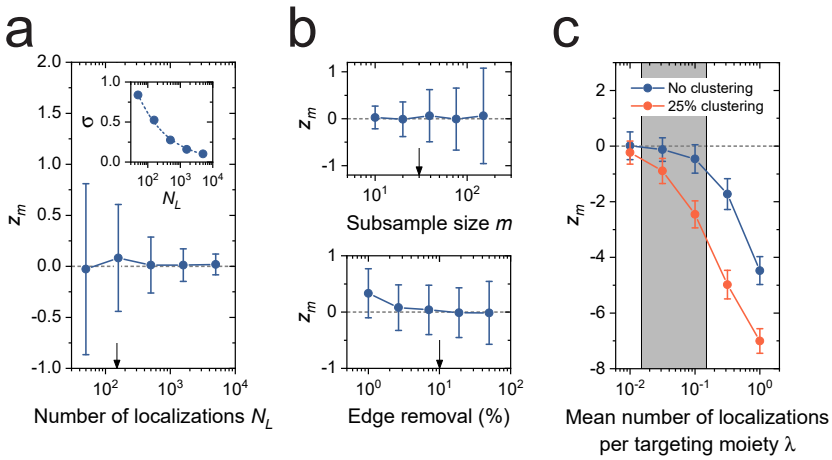

FIGURE 3.15: OPTIMIZING THE CE-TEST TO ACCEPT OR REJECT THE COMPLETE SPATIAL RANDOMNESS (CSR) HYPOTHESIS. (a) Dependency of the z_m value and its error on the number of localizations per particle N_L. $N_L = 150$ (black arrow) is chosen to accurately reject the CSR hypothesis (one-tailed test with $\alpha = 0.05 \rightarrow$ false positives ~0.1%). The following parameters were used: $m = 30$, edge removal = 10%, $R_p = 500$ nm, and no Poisson sampling process. The error of z_m is shown in the inset which scales with the number of localizations according to $\sigma \propto N_L^{-1/2}$ as would be expected with Poisson statistics. (b) Top: the effect of reflexive NNs. Including reflexive NNs causes an increase of the variance of the mean z_m value. Bottom: dependency of z_m on the edge localizations removal; including particle probe positions at the edge increases the mean z_m. $m = 150$ and edge removal = 10% (black arrows) were chosen required to accurately reject the CSR hypothesis (one-tailed test with $\alpha = 0.05 \rightarrow$ false positives ~0.1%). The following parameters were used: $N_L = 150$, $m = 30$ (bottom) or edge removal = 10% (top), $R_p = 500$ nm, and no Poisson sampling process. (c) Stochastic sampling of the targeting moieties for nonclustered targeting moieties (blue), and 25% clustered targeting moieties (red, see Figure 3.3b), with z_m as a function of the mean number of localizations per targeting moiety λ. Both curves show a decreasing z_m for an increasing λ due to oversampling and therefore induced clustering. The shaded area indicates the range in which the oversampling is minimized, while the difference between nonclustered and clustered targeting moieties could be distinguished. The following parameters were used: $N_L = 150$, $m = 30$, edge removal = 10%, $R_p = 500$ nm, and a Poisson sampling process. For all simulations each data point consists of 50 particles of which the means and standard deviations are visualized.

3.6.6 *Scaling of intraparticle targeting moiety variability with interaction area*

The contribution of intraparticle variability due to clustered functionalization on a particle to the reactivity variability for a given interaction area can be defined by:

$$\begin{aligned} \sigma^2_{\text{moiety}} &= \sigma^2_{\text{intraparticle}} + \sigma^2_{\text{stochastic}} \\ \sigma^2_{\text{intraparticle}} &= \sigma^2_{\text{moiety}} - N_{\text{moiety}} \end{aligned} \tag{3.6}$$

with σ_{moiety} being the variation in the number of targeting moieties for a given interaction area, $\sigma_{\text{intraparticle}}$ the intraparticle variation for a given interaction area, $\sigma_{\text{stochastic}}$ the variability caused by stochastic functionalization of targeting moiety, and N_{moiety} the mean number of targeting moieties in a given interaction area. All parameters are a function of the interaction area a_i.

In Figure 3.16a the variation in the number of targeting moieties is given as a function of a_i using the simulations presented in Figure 3.3b. It was found that both the random, nonclustered particles (blue) and clustered particles (red) show $CV_{\text{moiety}} \propto a_i^{-1/2}$ (dashed blue and red lines). This relation changes at the outer limits (dashed gray lines) due to simulation artifacts. For small interaction areas, the distribution changes from a normal distribution to a Poisson distribution causing an underestimation of σ_{moiety}. For large interaction areas, σ_{moiety} approaches zero since a fixed number of targeting moieties was used for each simulated particle to exclude interparticle variation effects. Figure 3.16b shows $\sigma_{\text{intraparticle}}$ as a function of the interaction area using Equation 3.6. Similar to the variation in the number of targeting moieties, the intraparticle variation scales with $CV \propto a_i^{-1/2}$ (dashed red line).

3.6.7 *Correlation between inter- and intraparticle targeting moiety variabilities*

The correlation between the interparticle variability quantified by qPAINT experiments, and the intraparticle variability quantified by DNA-PAINT experiments, is shown in Figure 3.17. Here, the calculated z_m value is indicated on the x-axis, and the number of targeting moieties per particle measured using qPAINT on the y-axis. Each dot represents a single particle, and the red cross the mean value of the z_m value and the number of targeting moieties per particle. This figure shows that (1) there is no correlation between intraparticle variabil-

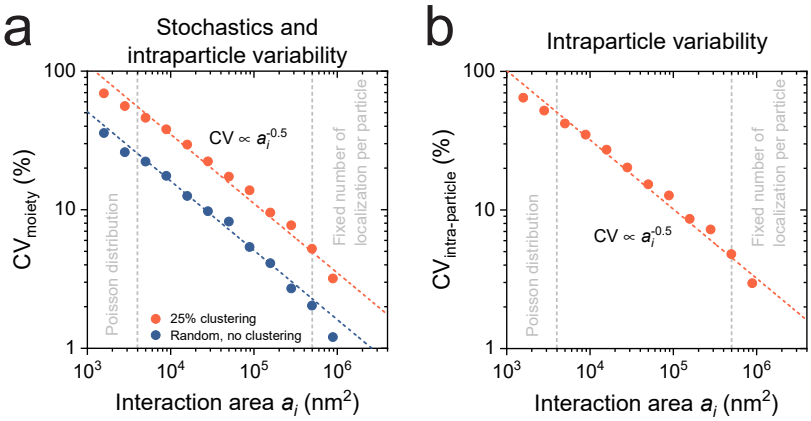

FIGURE 3.16: SCALING OF THE INTRAPARTICLE VARIABILITY WITH THE INTERACTION AREA DUE TO CLUSTERED TARGETING MOIETY FUNCTIONALIZATION. (a) Variation in the number of targeting moieties as a function of the interaction area, where both stochastic and the intraparticle variability are taken into account, for particles with a random placement of targeting moieties (blue) and a superposition of 25% clustered and 75% random placement of targeting moieties (red). The dashed blue and red lines indicate $CV \propto a_i^{-1/2}$. The gray dashed lines indicate the area between which no simulation artifacts occur. (b) Variation in the number of targeting moieties as a function of the interaction area, where only the intraparticle variability was considered using Equation 3.6. The dashed red line indicates $CV \propto a_i^{-1/2}$.

ity and number of targeting moieties on a single particle, and (2) the spread (*i. e.*, the variation) in the distribution of the number of targeting moieties per particle does not depend on the z_m value. Both observations are in agreement with the fact that the intrinsic length scales of inter- and intraparticle heterogeneity are very different, so that these heterogeneities can be treated as independent terms.

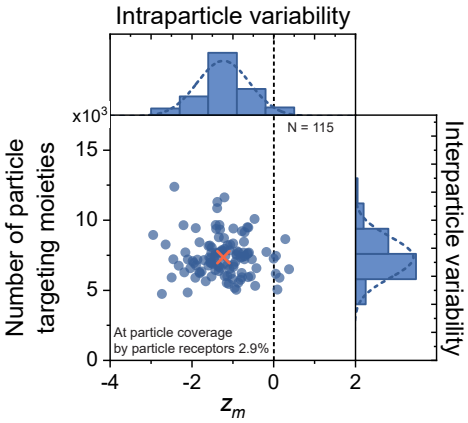

FIGURE 3.17: CORRELATION BETWEEN INTER- AND INTRAPARTICLE VARIABILITIES. On the x-axis, z_m is given (see Figure 3.3c), and on the y-axis the number of targeting moieties (see Figure 3.2a) for a particle coverage of 2.9%. Each blue dot represents a single particle for which the number of targeting moieties was determined using qPAINT and for which z_m was calculated using DNA-PAINT data. The red cross indicates the mean number of targeting moieties and mean z_m. The dashed blue lines indicate a normal distribution.

3.6.8 *Biosensing by particle mobility*

Assay principle

In this chapter the concept and consequences of superpositional heterogeneity for the variability in reactivity of biofunctionalized particles, are illustrated using BPM, a biosensing method with both single-particle and single-molecule resolution.[17–19] The molecular design and measurement principle are sketched in Figure 3.18, illustrated with a sandwich assay format. Figure 3.18a shows a particle that is tethered to a substrate by a molecular nanoswitch system comprising three functional components:[19] (1) a dsDNA stem which tethers the particle to the substrate; (2) a ssDNA targeting moiety coupled to the stem; and (3) multiple ssDNA targeting moieties coupled to the particle surface. Figure 3.18b illustrates the sensing functionality of the BPM system. The targeting moiety on the stem can transiently bind to target molecules captured from solution by the targeting moieties on the particle. The transient binding affects the mobility of the particle, because an unbound particle has a larger in-plane motional freedom than a bound particle. Two mobility time traces are sketched in Figure 3.18c, at a high (left) and low (right) target concentration. The switching frequency of the particle depends on the target concentration, because the unbound state lifetime of a particle decreases when the number of captured target molecules increases.

Interaction area

Here, the interaction area a_i is calculated for two BPM designs, namely, the BPM sensor with single stem targeting moiety[19] and the BPM sensor having the substrate coated with multiple targeting moieties,[17,18] see Figure 3.19. The interaction area can be calculated using the area formula for a spherical cap:

$$a_i = 2\pi R_p^2 \cdot (1 - \cos\alpha) \tag{3.7}$$

with R_p being the particle radius, and α the angle between the rays from the center of the sphere to the apex of the cap and the edge of the cap. The angle α can be calculated using $d = R_p\alpha$ where d is the great-circle distance from the center to the edge of the cap of the interaction area.

Figure 3.19 shows the BPM geometries for a small[19] and large interaction area.[17,18] The interaction areas are $a_i = 6.4 \cdot 10^3$ nm² (*i. e.*, ~0.2% of the total particle area, see Figure 3.19a) and $a_i = 6.1 \cdot 10^4$ nm² (*i. e.*,

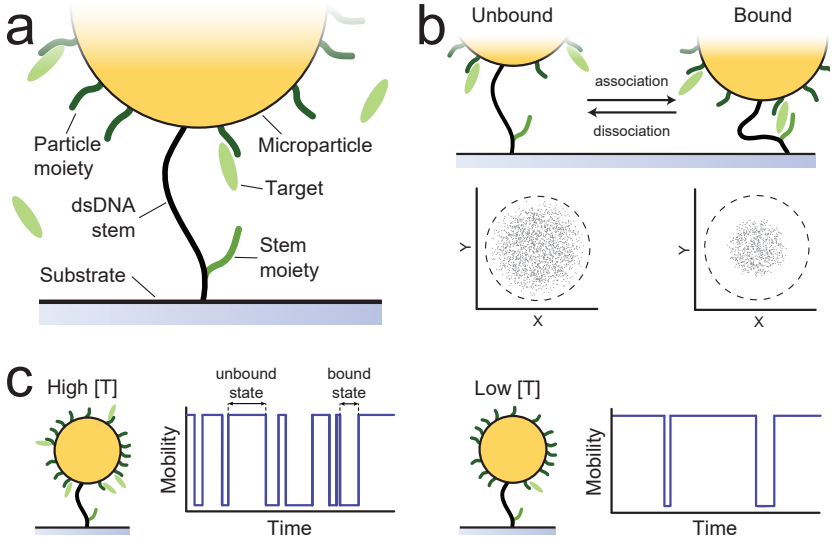

FIGURE 3.18: MOLECULAR DESIGN AND MEASUREMENT PRINCIPLE OF BIOSENSING BY PARTICLE MOBILITY (BPM) USING A SINGLE TARGETING MOIETY ON THE STEM. (a) Micrometer-sized particles (yellow) are tethered to a substrate using a dsDNA stem (black). The particle is functionalized with targeting moieties (dark green) and a single stem targeting moiety (green). Both targeting moiety types can bind reversibly to single target molecules (light green) present in solution. (b) Target molecules binding to the targeting moieties on the particle and subsequently the targeting moiety on the stem cause the particle to exhibit either of two concentric Brownian motion patterns, *i.e.*, the projection of the center if the particle onto the *xy*-plane, corresponding to the unbound (high mobility) and bound state (low mobility). (c) Digital binding and unbinding events are identified by following the mobility of the particles over time. The time between two events corresponds to either the unbound state lifetime, or the bound state lifetime. For a high or low target concentration in solution, the microparticle shows a high or a low switching frequency respectively.

~2% of the total particle area, see Figure 3.19b), respectively. The BPM design with a small interaction area exhibits variabilities dominated by stochastic and intraparticle heterogeneity. The BPM design with a large interaction area has variability due to all three components (stochastic, intraparticle, and interparticle).

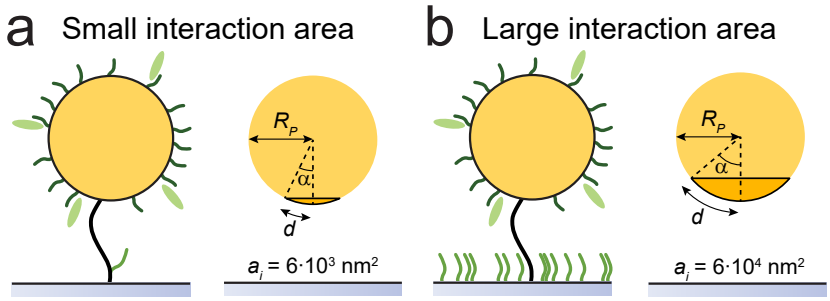

Figure 3.19: schematic visualizations of the interaction area for two BPM system designs. (a) Schematic visualization of the BPM design presented in Lubken *et al.*[19] The characteristic length of the interaction area d was estimated to be 45 nm which results in $\alpha \sim 5°$. (b) Schematic visualization of the BPM design presented in Yan *et al.*[18] The characteristic length of the interaction area d was estimated to be 140 nm which results in $\alpha \sim 16°$.

3.7 REFERENCES

1. Petros, R. A. & Desimone, J. M. Strategies in the Design of Nanoparticles for Therapeutic Applications. *Nature Reviews Drug Discovery* **9,** 615–627 (2010).
2. Howes, P. D., Chandrawati, R. & Stevens, M. M. Colloidal Nanoparticles as Advanced Biological Sensors. *Science* **346,** 1247390 (2014).
3. Bogart, L. K., Pourroy, G., Murphy, C. J., Puntes, V., Pellegrino, T., Rosenblum, D., Peer, D. & Lévy, R. Nanoparticles for Imaging, Sensing, and Therapeutic Intervention. *ACS Nano* **8,** 3107–3122 (2014).
4. Taylor, A. B. & Zijlstra, P. Single-Molecule Plasmon Sensing: Current Status and Future Prospects. *ACS Sensors* **2,** 1103–1122 (2017).
5. Wu, Y., Tilley, R. D. & Gooding, J. J. Challenges and Solutions in Developing Ultrasensitive Biosensors. *Journal of the American Chemical Society* **141,** 1162–1170 (2019).
6. Irvine, D. J. & Dane, E. L. Enhancing Cancer Immunotherapy with Nanomedicine. *Nature Reviews Immunology* **20,** 321–334 (2020).
7. Mullen, D. G. & Banaszak Holl, M. M. Heterogeneous Ligand–Nanoparticle Distributions: A Major Obstacle to Scientific Understanding and Commercial Translation. *Accounts of Chemical Research* **44,** 1135–1145 (2011).
8. Rabanel, J.-M., Adibnia, V., Tehrani, S. F., Sanche, S., Hildgen, P., Banquy, X. & Ramassamy, C. Nanoparticle Heterogeneity: an Emerging Structural Parameter Influencing Particle Fate in Biological Media? *Nanoscale* **11,** 383–406 (2019).
9. Jungmann, R., Steinhauer, C., Scheible, M., Kuzyk, A., Tinnefeld, P. & Simmel, F. C. Single-Molecule Kinetics and Super-Resolution Microscopy by Fluorescence Imaging of Transient Binding on DNA Origami. *Nano Letters* **10,** 4756–4761 (2010).
10. Jungmann, R., Avendaño, M. S., Dai, M., Woehrstein, J. B., Agasti, S. S., Feiger, Z., Rodal, A. & Yin, P. Quantitative Super-Resolution Imaging with qPAINT. *Nature Methods* **13,** 439–442 (2016).
11. Feiner-Gracia, N., Beck, M., Pujals, S., Tosi, S., Mandal, T., Buske, C., Linden, M. & Albertazzi, L. Super-Resolution Microscopy Unveils Dynamic Heterogeneities in Nanoparticle Protein Corona. *Small* **13,** 1701631 (2017).
12. Delcanale, P., Miret-Ontiveros, B., Arista-Romero, M., Pujals, S. & Albertazzi, L. Nanoscale Mapping Functional Sites on Nanoparticles by Points Accumulation for Imaging in Nanoscale Topography (PAINT). *ACS Nano* **12,** 7629–7637 (2018).
13. Patiño, T., Feiner-Gracia, N., Arqué, X., Miguel-López, A., Jannasch, A., Stumpp, T., Schäffer, E., Albertazzi, L. & Sánchez, S. Influence of Enzyme Quantity and Distribution on the Self-Propulsion of Non-Janus Urease-Powered Micromotors. *Journal of the American Chemical Society* **140,** 7896–7903 (2018).

14. Horáček, M., Armstrong, R. E. & Zijlstra, P. Heterogeneous Kinetics in the Functionalization of Single Plasmonic Nanoparticles. *Langmuir* **34,** 131–138 (2018).

15. Pujals, S., Feiner-Gracia, N., Delcanale, P., Voets, I. & Albertazzi, L. Super-Resolution Microscopy as a Powerful Tool to Study Complex Synthetic Materials. *Nature Reviews Chemistry* **3,** 68–84 (2019).

16. Horáček, M., Engels, D. J. & Zijlstra, P. Dynamic Single-Molecule Counting for the Quantification and Optimization of Nanoparticle Functionalization Protocols. *Nanoscale* **12,** 4128–4136 (2020).

17. Visser, E. W. A., Yan, J., van IJzendoorn, L. J. & Prins, M. W. J. Continuous Biomarker Monitoring by Particle Mobility Sensing with Single Molecule Resolution. *Nature Communications* **9,** 2541 (2018).

18. Yan, J., van Smeden, L., Merkx, M., Zijlstra, P. & Prins, M. W. J. Continuous Small-Molecule Monitoring with a Digital Single-Particle Switch. *ACS Sensors* **5,** 1168–1176 (2020).

19. Lubken, R. M., de Jong, A. M. & Prins, M. W. J. Multiplexed Continuous Biosensing by Single-Molecule Encoded Nanoswitches. *Nano Letters* **4,** 2296–2302 (2020).

20. Clark, P. J. & Evans, F. C. Distance to Nearest Neighbor as a Measure of Spatial Relationships in Populations. *Ecology* **35,** 445–453 (1954).

21. Atkins, P. W. & Paula, J. D. *Physical Chemistry for the Life Sciences* (Oxford University Press, 2010).

4

SENSING METHODOLOGY FOR THE RAPID MONITORING OF BIOMOLECULES AT LOW CONCENTRATIONS OVER LONG TIME SPANS

ABSTRACT: Studies on the dynamics of biological systems and biotechnological processes require measurement techniques that can reveal time-dependencies of concentrations of specific biomolecules, preferably with small time delays, short time intervals between subsequent measurements, and the possibility to record over long time spans. For low-concentration biomolecules, these requirements are very challenging since low-concentration assays are typically slow and require new reagents in every assay. Here, we present a sensing methodology that enables rapid monitoring of picomolar and sub-picomolar biomolecular concentrations, using specific high-affinity binders in a reversible assay. We demonstrate the sensing methodology using simulations and experiments, showing that low-concentration biomolecules can be monitored with small time delays, short time intervals, and in principle over an endless time span.

Parts of this chapter have been published as: Lubken, R. M. *et al.* Sensing Methodology for the Rapid Monitoring of Biomolecules at Low Concentrations over Long Time Spans. *ACS Sensors.* Accepted for publication (2021).

4.1 INTRODUCTION

Biological systems and biotechnological processes exhibit time-dependencies that are at the most basic level regulated by the dynamics of constituting biomolecules, such as small molecules, hormones, proteins, and nucleic acids. This calls for measurement technologies that allow the monitoring of biomolecular concentrations, for instance to serve fundamental research on biological and biomedical dynamics,[1–6] to enable the development of patient monitoring strategies based on real time biomolecular data,[7–10] as well as to enable the development of closed loop control strategies in biotechnological applications.[11–16] Desirable characteristics of a generic monitoring technology are (1) precise and specific measurements; (2) small time delays between sampling input and data output; (3) short time intervals between successive measurements; and (4) a long total time span over which time-dependent biomolecular concentration data can be recorded.

It is a fundamental challenge to develop a sensor technology that can rapidly monitor low-concentration biomolecules over long time spans. Sensitive assays are available, such as ELISA and flow cytometry,[17–20] but in these assays new reagents are needed for every sample that is taken. The repeated consumption of reagents complicates applications where biomolecular concentrations need to be monitored over long time spans. On the other hand, sensing technologies that can operate without consuming reagents, such as surface plasmon resonance,[21] redox cycling[22] and quartz crystal microbalance,[23] have not been designed for monitoring biomolecules at low concentrations, such as in the picomolar and sub-picomolar range.

A generic principle to measure specific biomolecules at low concentrations, is by using the biochemical affinity between specific binder molecules (such as antibodies and aptamers) and the biomolecule that is to be detected (the analyte). The specificity originates from molecular interactions such as charge, hydrogen bonding, van der Waals forces, and hydrophobic and steric effects.[24] To be able to measure biomolecules at low concentrations with high precision, binder molecules are needed that have strong interactions with the analyte, which corresponds to high binding energies, low equilibrium dissociation constants K_d, and low dissociation rate constants k_{off}.[25,26] However, this conflicts with the desire to have small time delays, because low dissociation rate constants would imply a need for long incubation times to reach equilibrium.[24–26] Furthermore, low dissociation rate constants result in a slow reversibility, which conflicts with the wish to enable short time intervals between successive measurements.

In this chapter, a sensing methodology is presented that enables rapid monitoring of low-concentration biomolecules, in the picomolar and sub-picomolar range. The method is based on the use of binder molecules with a high affinity in a limited-volume assay, with a fully reversible detection principle and time-dependent sampling of the analyte of interest. The system allows optimal tradeoffs between time characteristics and precision. We present the measurement concept, time-dependencies of sensor signals, and a comprehensive analysis of the achievable time characteristics and precision as a function of sensor design parameters. We demonstrate that the sensing methodology enables precise quantification of low biomolecular concentrations, with time delays and interval times that are much shorter than the time dictated by the dissociation rate constant of the binder molecules. Furthermore, due to the reversible detection method, measurements can in principle be done over an endless time span.

4.2 BASIC CONCEPT OF THE SENSING METHODOLOGY

The basic concepts of the sensing methodology are sketched in Figures 4.1 and 4.2. The sensing system features time-dependent sampling of the analyte of interest, provided by a time-controlled analyte exchange between a biological or biotechnological system of interest and a measurement chamber (see Figure 4.1a). The measurement chamber contains specific binder molecules from which signals are recorded. The data are translated into concentration-time profiles, which should resemble as close as possible the true concentration-time profile of analyte molecules in the system of interest. During the exchange of analyte molecules, various processes occur, such as mass transport by advection and diffusion, and association and dissociation of analyte molecules to binder molecules (see Figure 4.1b). In this chapter, a rectangular measurement chamber is assumed with height H, width W, and length L. The sensor surface is provided with binder molecules, where association and dissociation of analyte molecules occurs. The rates of association and dissociation depend on the association rate constant k_{on}, the dissociation rate constant k_{off}, the density Γ_b of binder molecules, and the analyte concentration C_a at the sensor surface. These processes result in a time-dependent density γ_{ab} of analyte-binder complexes, also represented as a fractional occupancy f of binder molecules occupied by analyte molecules, where $f = \gamma_{ab}/\Gamma_b$. Variables γ_{ab} and f are changing as a function of analyte concentration and time. In an affinity-based sensor, the observed sensor signal scales with f, therefore f is used in this chapter as the sensor readout parameter to determine the analyte concentration. Analyte exchange between the system of

interest and the measurement chamber is facilitated by diffusion or a combination of diffusion and advection. A net diffusive molar flux J_a (orange gradient) is caused by concentration differences between the system of interest and the measurement chamber and by concentration differences within the measurement chamber. Advective mass transport of analyte molecules into the measurement chamber is facilitated by a developed laminar flow profile with flow rate Q and mean flow speed v_m (black arrows). Here, it is assumed that diffusive transport occurs in both the longitudinal (x-direction) and the lateral direction (y-direction) and scales with the diffusion coefficient D, while advective transport occurs only in the longitudinal direction and scales with the mean flow speed v_m.

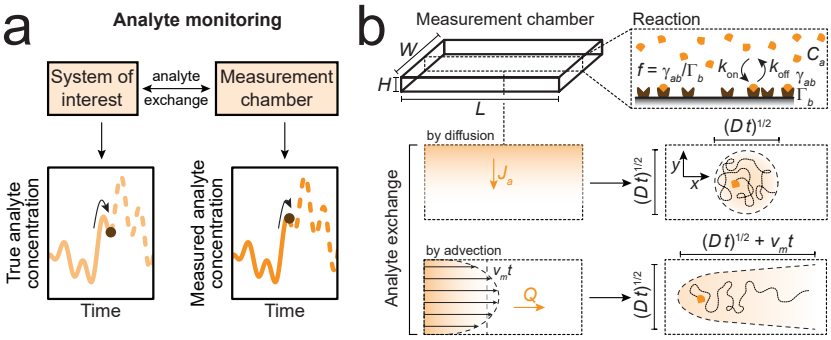

FIGURE 4.1: CONCEPT OF ANALYTE MONITORING USING DIFFUSION- AND ADVECTION-BASED SAMPLING. (a) Sensing system for biomolecular monitoring. Analyte molecules are exchanged between a biological or biotechnological system of interest and a measurement chamber. The data result in a concentration-time profile which should correspond as close as possible to the true analyte concentration in the system of interest. (b) Geometry of the measurement chamber, with height H, width W, and length L. A reaction rate at the sensor surface is caused by the association and dissociation between analyte molecules (orange) and binder molecules (brown), described by the association rate constant k_{on}, the dissociation rate constant k_{off}, the total binder density Γ_b, the analyte concentration C_a at the sensor surface, and the density of analyte-binder complexes γ_{ab}. Analyte exchange is facilitated by diffusion and advection, where diffusion occurs in both x- and y-direction with diffusion coefficient D, resulting in a net molar flux J_a, and where advection occurs in the x-direction only, with a developed flow profile with flow rate Q and a mean flow speed v_m.

Figure 4.2a sketches two different sensor designs, namely an infinite-volume assay and a limited-volume assay. The graphs visualize the fractional occupancy f of binder molecules occupied by analyte molecules as a function of time, with a corresponding characteristic time-to-equilibrium τ, defined as the time needed to attain 63% of the difference between the starting level and the equilibrium level of f (see Supplementary note 4.6.2). In an infinite-volume assay, continuous analyte exchange is enabled between the system of interest and the measurement chamber, where the system of interest is assumed to be much larger than the measurement chamber. The continuous analyte exchange could for example be facilitated by diffusive analyte transport

across a contact area between the system of interest and the measurement chamber, while another configuration may involve a continuous flow of sample fluid provided into the measurement chamber from the system of interest. When the analyte exchange is effective and gives negligible time delay, then the analyte concentration at the sensor surface (C_a) is equal to the analyte concentration in the system of interest ($C_{a,0}$). In case of low analyte concentrations ($C_{a,0} \ll K_d$), the infinite-volume assay condition leads to a characteristic time-to-equilibrium $\tau \cong 1/k_{\text{off}}$ (see Supplementary note 4.6.2). This implies that the time-to-equilibrium is determined by the dissociation rate constant k_{off}, so this time is long when the binder molecules strongly bind to the analyte molecules.

The sensor design with a limited-volume assay has very different properties. Here, analyte exchange is not enabled during the incubation, so that the binder molecules in the measurement chamber interact with only a limited sample volume and therefore with a limited amount of analyte molecules. Due to this limited volume, we can now define an effective volumetric concentration of binder molecules $C_{b,0} = \Gamma_b/H$, which is based on the number of binder molecules in the measurement chamber and the volume of the measurement chamber. When $C_{b,0}$ is high, with $C_{b,0} \gg C_{a,0}$ and $C_{b,0} \gg K_d$, then the time-to-equilibrium τ of the assay becomes dominated by the high concentration of binder molecules. When diffusional transport delays can be ignored, then the time-to-equilibrium of the assay equals $\tau \cong 1/(k_{\text{on}}C_{b,0})$ (see Table 4.1 and Supplementary notes 4.6.1 and 4.6.2). Thus, the time-to-equilibrium of the limited-volume assay is determined by the association rate constant and the effective volumetric concentration $C_{b,0}$ of binder molecules, which leads to equilibrium timescales that are much shorter than the time-to-equilibrium of the infinite-volume assay.

In monitoring applications, one would like to be able to record measurements with one and the same sensor over long time spans. To realize the limited-volume assay principle in a monitoring application, the sensor needs to be switched between two different conditions: an open condition and a closed condition. In the open condition, analyte molecules are exchanged effectively between the system of interest and the measurement chamber, as sketched in Figures 4.1a and b (see also Supplementary note 4.6.5). In the closed condition, analyte molecules are not exchanged between the system of interest and the measurement chamber, causing a limited-volume incubation in the measurement chamber, as sketched in the bottom graph of Figure 4.2a. We refer to the switching concept between the open and closed condition as 'time-controlled analyte exchange'. Figure 4.2b illustrates the operat-

ing principle for a sensor where time-controlled analyte exchange is realized by a modulated flow. Phase 1 is the exchange phase, where the measurement chamber is supplied with sample fluid, so that the starting concentration in the chamber equals $C_{a,0}$. Phase 2 is the incubation phase, where the exchange process is stopped, so that the limited-volume assay condition is provided. During incubation in the limited-volume condition, the analyte concentration C_a in the measurement chamber decreases over time (depletion) or increases over time (repletion), depending on the initial fractional occupancy f_{init} of binder molecules by analyte molecules. When f_{init} is low, the concentration of analyte molecules in the measurement chamber decreases over time, corresponding to depletion of analyte. When f_{init} is high, the concentration of analyte molecules in the chamber increases over time, corresponding to repletion of analyte. For known f_{init}, the supplied analyte concentration $C_{a,0}$ can be derived from the measured time-dependent fractional occupancy $f(t)$ during the incubation phase. At least two measurements need to be done to determine the analyte concentration $C_{a,0}$ in the system of interest, for example a measurement at the initial value f_{init} and a measurement at the final value f_{end}, as indicated in the graph.

By sequentially applying cycles with open condition and closed condition, discrete samples with a limited volume are serially measured and result in time-dependent data that relate to the different samples supplied to the sensor. Each former measurement causes a varying nonzero initial fractional occupancy f_{init} in the next measurement. The values of f_{init} and $C_{a,0}$ determine whether depletion or repletion occurs during the incubation phase. In case of depletion, a higher analyte concentration $C_{a,0}$ yields a larger, positive change of fractional occupancy $\Delta f = f_{\text{end}} - f_{\text{init}}$ since more analyte molecules are captured from solution, while for repletion a higher $C_{a,0}$ yields a smaller, negative change of fractional occupancy Δf since less analyte molecules are repleted from the sensor surface into solution. An important property of the sensor is that the interactions between binder and analyte molecules are reversible. This gives the advantage that the limited-volume assay with time-controlled analyte exchange can be used over an endless time span.

4.3 RESULTS AND DISCUSSION

4.3.1 *Timescales of the limited-volume assay*

Figure 4.3 shows simulation results of the time-to-equilibrium of the limited-volume assay, for sensor designs with different measurement

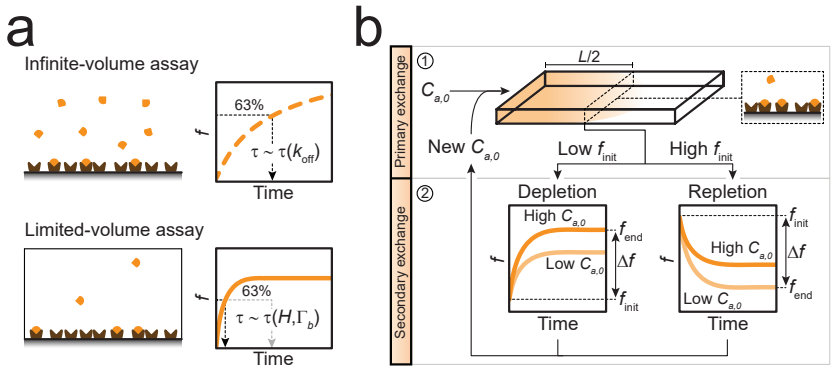

FIGURE 4.2: CONCEPT OF THE SENSING METHODOLOGY FOR THE RAPID MONITORING OF LOW ANALYTE CONCENTRATIONS. (a) Time profile of the sensor response for low analyte concentration ($C_{a,0} \ll K_d$), for two conditions: infinite-volume and limited-volume assays. Measuring in an infinite volume results in an excess of analyte molecules compared to binder molecules ($C_{a,0} \gg C_{b,0}$), causing the time-to-equilibrium τ to be determined by k_{off}. The limited-volume condition is defined as a condition where binder molecules are in excess compared to analyte molecules ($C_{b,0} \gg C_{a,0}$, with $C_{b,0} = \Gamma_b/H$) and in excess compared to the equilibrium dissociation constant ($C_{b,0} \gg K_d$). This causes τ to be determined by the effective binder concentration (*i. e.*, measurement chamber height H and binder density Γ_b), which is much shorter than $1/k_{\text{off}}$. (b) Biomolecular monitoring using a limited-volume assay involves repeated cycles with two phases. In phase 1, analyte molecules are exchanged effectively between the system of interest and the measurement chamber. In phase 2, the time-dependent signal is recorded during incubation in a limited volume (*i. e.*, in the middle of the measurement chamber at distance $L/2$ from the entrance), which reveals the analyte concentration. Inside the measurement chamber, the limited-volume condition gives a time-dependence of the analyte concentration: a decrease over time (depletion) or an increase over time (repletion), depending on the analyte concentration $C_{a,0}$ in the system of interest and the initial fractional occupancy f_{init} of binder molecules by analyte molecules. The analyte concentration $C_{a,0}$ in the system of interest is derived from the measured time-dependent fractional occupancy $f(t)$.

chamber heights, different binder densities, and different flow rates, assuming standard parameter values as listed in Table 4.1. Figure 4.3a shows how the time-to-equilibrium τ depends on the measurement chamber height H, for a sensor with instantaneous analyte exchange (see Supplementary note 4.6.6 for the influence of analyte exchange on the sensor performance). The arrow on the x-axis indicates the height as listed in Table 4.1. The data show that the time-to-equilibrium increases with the measurement chamber height. At small H, this increase is caused by a decrease of the effective volumetric binder concentration, while at large H, this increase is caused by diffusive transport limitations. The inset shows the same data, plotted as a function of the Damköhler number ($Da = \tau_D/\tau_{\text{R,LV}} = k_{\text{on}}\Gamma_b H/D$, see Table 4.1); low Da means that the kinetics are limited by the reaction, high Da means that the kinetics are limited by diffusion. To achieve a fast time-to-equilibrium, the sensor should be designed with a large $C_{b,0}$, so a small H.

Figure 4.3b shows how the time-to-equilibrium depends on the binder density Γ_b, for a sensor with instantaneous analyte exchange.

The arrow indicates the density as listed in Table 4.1. For small Γ_b, the time-to-equilibrium is long and determined by the dissociation rate constant ($\tau \cong 1/k_{\text{off}}$). For $\Gamma_b > HK_d \cong 20$ µm^{-2}, the time-to-equilibrium decreases, until it stabilizes due to diffusive transport limitations ($\tau \cong \tau_D = H^2/D$). The inset shows the same data plotted as a function of Da. To achieve a fast time-to-equilibrium, the sensor should be designed with a large $C_{b,0}$, so a large Γ_b.

TABLE 4.1: Standard parameter values used in the finite-element simulations. Details on the simulations are described in Supplementary note 4.6.4. Additional standard parameter values are given in Table 4.2 (see Supplementary note 4.6.1).

	Parameter	Value	Description
Input parameter	H	200 µm	Measurement chamber height
	D	10^{-10} m^2 s^{-1}	Diffusion coefficient of the analyte molecule
	Γ_b	10^{-9} mol m^{-2} (600 µm^{-2})	Binder density
	k_{off}	10^{-4} s^{-1}	Dissociation rate constant
	k_{on}	10^6 M^{-1} s^{-1}	Association rate constant
	$C_{a,0}$	0.1 pM	Analyte concentration
Derived parameter	$\tau_D = H^2/D$	400 s	Characteristic diffusion time
	$\tau_{R,LV} = \frac{1}{k_{\text{on}} C_{b,0}} = \frac{H}{k_{\text{on}} \Gamma_b}$	200 s	Characteristic reaction time for limited-volume assay with $C_{b,0} \gg C_{a,0}$ and $C_{b,0} \gg K_d$
	$C_{b,0} = \Gamma_b/H$	5 nM	Effective volumetric binder concentration
	$K_d = k_{\text{off}}/k_{\text{on}}$	100 pM	Equilibrium dissociation constant
	$\alpha = \frac{\Gamma_b}{HK_d} = C_{b,0}/K_d$	50	Acceleration factor: reduction factor of the time-to-equilibrium of a limited-volume assay with $\tau(H, \Gamma_b)$, compared to an infinite-volume assay with $\tau(k_{\text{off}})$.
	$Da = \tau_D/\tau_{R,LV} = k_{\text{on}} \Gamma_b H/D$	2	Damköhler number

Figure 4.3c shows how analyte exchange by advection contributes to the time-to-equilibrium per measurement cycle. The exchange phase involves a temporary flow of fluid into the measurement chamber, with flow rate Q and duration t_{exch} (see Supplementary note 4.6.6 for the influence of analyte exchange on the sensor performance). In the simulations, t_{exch} was chosen to be equal to the characteristic advection time $\tau_A = HLW/Q$ (see Table 4.1), which means that a total fluid volume equal to the volume of the measurement chamber is displaced. The time-to-equilibrium τ, which now includes a contribution t_{exch} related to the exchange, is shown as a function of flow rate, for several values of the chamber aspect ratio $\lambda = L/H$. The arrow indicates the flow rate as listed in Table 4.1. For small Q the observed τ is limited by

t_{exch}, *i. e.*, the advective transport of analyte molecules from the inlet toward the point of sensing at a distance $L/2$ from the inlet, as sketched in Figure 4.2b. For increasing λ, *i. e.*, increasing L with a fixed H, the time-to-equilibrium increases since τ_A (and thus also t_{exch}) increases. For increasing Q, the time-to-equilibrium decreases, until it stabilizes at a level where the reaction and diffusion times determine the observed τ. The inset shows the same data ($Da = 2$), supplemented with $Da = 0.2$ (reaction-limited) and $Da = 20$ (diffusion-limited), plotted as a function of the longitudinal Péclet number ($Pe_L = \tau_D/\tau_A = \frac{Q}{\lambda DW}$, see Table 4.1); low Pe_L means that the analyte exchange is limited by advection, high Pe_L means that the analyte exchange is limited by diffusion. A low Pe_L causes a long time-to-equilibrium due to slow

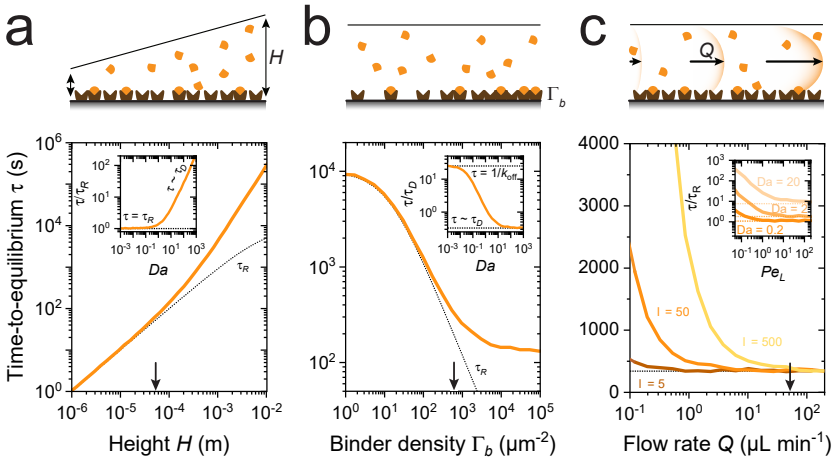

Figure 4.3: time-to-equilibrium of a limited-volume assay for a sensor design with different heights, binder densities, and flow rates of analyte exchange. (a) Time-to-equilibrium τ as a function of measurement chamber height H (orange line) for an instantaneous analyte exchange. For small H, the observed τ is reaction-dominated ($\tau \cong \tau_R = 1/(\tau_{\text{R,LV}}^{-1} + k_{\text{off}})$, black dotted line), while for increasing H the observed τ becomes diffusion-dominated. The inset shows the same data, where τ is normalized to τ_R and plotted as a function of Damköhler number Da. The sketch above the graph visualizes a measurement chamber with an increasing H. (b) Time-to-equilibrium τ as a function of the binder density Γ_b (orange line) for an instantaneous analyte exchange. For low Γ_b, the observed τ is reaction-dominated ($\tau \cong \tau_R$, black dotted line), while for increasing Γ_b the observed τ becomes diffusion-dominated. The inset shows the same data, where τ is normalized to the characteristic diffusion time τ_D and plotted as a function of Da. For low Da, τ is limited by $1/k_{\text{off}}$, while at high Da, τ is limited by τ_D. The sketch above the graph visualizes a measurement chamber with an increasing Γ_b. (c) Time-to-equilibrium τ as a function of flow rate Q for three aspect ratios $\lambda = L/H$, for time-controlled analyte exchange by advection where the flow duration t_{exch} equals the characteristic advection time τ_A. For small Q, the observed τ is limited by the advective transport of analyte molecules from the inlet toward the point of sensing at distance $L/2$ from the inlet. For increasing Q, this transport process becomes faster causing the observed τ to be dominated by reaction and/or diffusion at high flow rates. The inset shows the same data ($Da = 2$) supplemented with $Da = 0.2$ (reaction-limited) and $Da = 20$ (diffusion-limited), where τ is normalized to τ_R and plotted as a function of the longitudinal Péclet number Pe_L. The dotted lines show the τ/τ_R value at high Q and are equal to the values found in panel a. The sketch above the graph visualizes a measurement chamber with an increasing Q. In all panels, the black arrows on the x-axis indicate the standard parameter values for H, Γ_b, and Q as listed in Table 4.1.

mass transport by advection. Increasing Pe_L results in a decrease of the time-to-equilibrium due to rapid filling of the chamber, until it stabilizes at a τ value equal to the value indicated in Figures 4.3a,b for standard parameter values. In the following sections, exchange with a high Pe_L is assumed, *i. e.*, rapid filling of the measurement chamber without influence of the flow rate on the time-to-equilibrium.

4.3.2 *Limited-volume assay with time-controlled analyte exchange*

Figures 4.4 and 4.5 show simulation results for a limited-volume assay with time-controlled analyte exchange. The analyte exchange is assumed to be instantaneous and the incubation phase includes mass transport by diffusion and reaction kinetics within the measurement chamber itself, but no analyte exchange between the system of interest and the measurement chamber. Figure 4.4 shows data for repeated incubations with $C_{a,0} = 0.1$ pM. The analyte concentration C_a in the measurement chamber (brown line) and the fractional occupancy f of the binders by analyte molecules (orange line) are plotted as a function of time, for conditions of analyte depletion (left) and analyte repletion (right). The time-to-equilibrium τ of each incubation equals approximately 340 s (see Figure 4.3), having contributions from reaction ($\tau_R = 200$ s) and diffusion ($\tau_D = 400$ s). The contribution from the

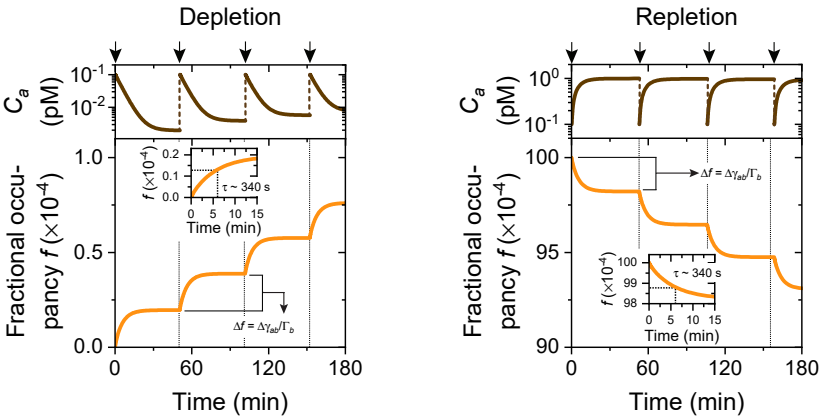

FIGURE 4.4: SIMULATED RESPONSE OF THE BIOMOLECULAR MONITORING SYSTEM USING TIME-CONTROLLED ANALYTE EXCHANGE FOR A REPEATING CONCENTRATION ADDITION. (a) Analyte concentration C_a in the measurement chamber (brown line) and the fractional occupancy f of binder molecules by analyte molecules (orange line) as a function of time, for low f_{init} and depletion of analyte in solution (left), and for high f_{init} and repletion of analyte in solution (right). The dashed lines and black arrows indicate time points where instantaneous analyte exchange occurs, where the bulk analyte concentration was set to $C_a = C_{a,0} = 0.1$ pM after each period of approximately 50 min. The insets highlight the kinetics of the first cycles, showing a time-to-equilibrium of $\tau = 340$ s. For many cycles ($n \to \infty$) both curves would approach $f_{\text{eq,IV}} = C_{a,0}/(C_{a,0} + K_d) = 10 \cdot 10^{-4}$, which equals the equilibrium value when an infinite volume is supplied (see Table 4.2).

reaction to the time-to-equilibrium is much smaller than $1/k_{\text{off}} = 10^4$ s, the value that would have been observed in case of an infinite-volume assay. In absence of diffusion limitations, the acceleration of the reaction that can be achieved with a limited-volume assay compared to an infinite-volume assay equals $\alpha = \frac{1/k_{\text{off}}}{\tau_{\text{R,LV}}} = \frac{k_{\text{on}}\Gamma_b}{Hk_{\text{off}}} = C_{b,0}/K_d$, which clarifies how the speed of the assay is directly related to the ratio between effective volumetric binder concentration and the equilibrium dissociation constant.

Figure 4.5 shows the simulated response of a limited-volume assay with time-controlled analyte exchange for an analyte concentration that varies in time. As an example, the sensor is incubated with a time series of analyte concentrations that alternate around 0.1 pM (orange line): the analyte concentration is alternatingly $C_{a,0} = 0.05$ pM or $C_{a,0} = 0.15$ pM. The infinite-volume equilibrium fractional occupancy $f_{\text{eq,IV}}$ is given for $C_{a,0} = 0.05$ pM and $C_{a,0} = 0.15$ pM by the dashed black lines. The panels on the right show zoom-ins of the sensor response at three different time periods (starting at $t = 0$ h, 12 h, and 42 h). In all cases the time-to-equilibrium is $\tau = 340$ s $\cong 5.7$ min. Incubation with

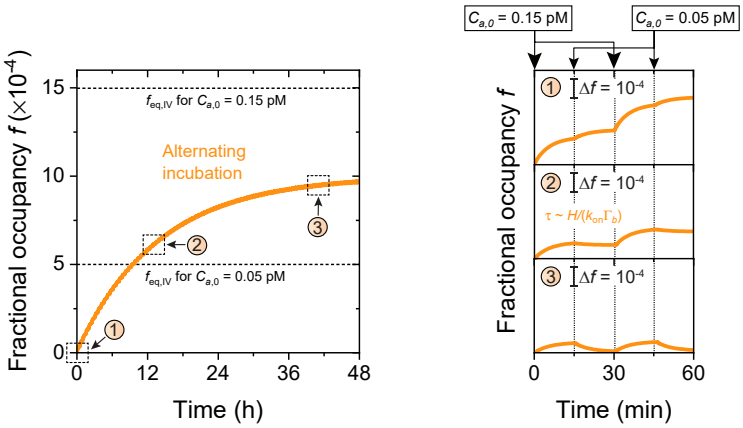

Figure 4.5: Simulated response of the biomolecular monitoring system using time-controlled analyte exchange for an alternating concentration addition. Fractional occupancy f as a function of time where cycles of analyte exchange and incubation are applied every 15 min with alternatingly $C_{a,0}$= 0.15 pM and $C_{a,0} = 0.05$ pM. The curve saturates at $f_{\text{eq,IV}} = 10 \cdot 10^{-4}$, which equals the infinite-volume equilibrium value for the average concentration value $C_{a,0} = 0.1$ pM (see Table 4.2). Dashed lines: continuous supply of $C_{a,0} = 0.05$ pM yields $f_{\text{eq,IV}} = 5 \cdot 10^{-4}$ and $C_{a,0} = 0.15$ pM yields $f_{\text{eq,IV}} = 15 \cdot 10^{-4}$ (see Table 4.2). The right panel shows zoom-ins of three sections of the solid curve, each representing four cycles of instantaneous analyte exchange and subsequent incubations of 15 minutes. In zoom-in 1 (t = 0-1 h) all curve segments show depletion behavior. In zoom-ins 2 (t = 12-13 h) and 3 (t = 42-43 h), depletion is seen for $C_{a,0} = 0.15$ pM, since $f_{\text{init}} < f_{\text{eq,IV}}$ ($C_{a,0} = 0.15$ pM), and repletion is seen for $C_{a,0} = 0.05$ pM, since $f_{\text{init}} > f_{\text{eq,IV}}$ ($C_{a,0} = 0.05$ pM). For all curve segments, the time-to-equilibrium $\tau = 340$ s. The vertical scale bars indicate $\Delta f = 10^{-4}$.

$C_{a,0} = 0.15$ pM gives depletion behavior at all times (since $f_{\text{init}} < f_{\text{eq,IV}}$, top black line); for $C_{a,0} = 0.05$ pM, depletion behavior is seen at $t < 10$ h and repletion at $t > 10$ h (when $f_{\text{init}} > f_{\text{eq,IV}}$, bottom black line).

Figures 4.6 and 4.7 shows an experimental study on how the time-to-equilibrium in a limited-volume assay depends on the total binder concentration in the measurement chamber. Here, the total binder concentration has two contributions, namely a contribution from surface-bound binders and a contribution from binders supplemented in solution. For detection we made use of biosensing by particle mobility (BPM), which is a biomolecular monitoring principle with single-molecule resolution. In the BPM sensor, the particles are transducers that record the binding of analyte molecules to specific binder molecules on the particle (see Supplementary note 4.6.7). Figure 4.6 shows a schematic representation of a measurement chamber with binder molecules present in the two forms: immobilized and nonimmobilized. Immobilized binder molecules are present with an effective volumetric concentration $C_{b,0}$. Binder molecules supplemented free in solution have concentration $C_{b,\text{suppl}}$. In absence of supplemented binder molecules (top), the total binder concentration in the measurement chamber equals $C_{b,\text{tot}} = C_{b,0} = \Gamma_b/H$. In presence of supplemented binder molecules (bottom), the total binder concentration equals $C_{b,\text{tot}} = \Gamma_b/H + C_{b,\text{suppl}}$. Since the time-to-equilibrium of the reaction scales according to $\tau_{\text{R,LV}} \propto 1/C_{b,\text{tot}}$ (see Table 4.1), an increasing supplemented binder concentration $C_{b,\text{suppl}}$ results in a smaller τ.

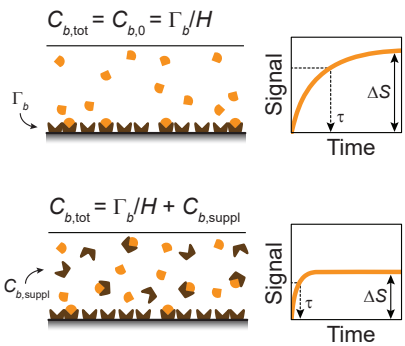

FIGURE 4.6: SKETCH OF THE EXPERIMENTAL STUDY OF A LIMITED-VOLUME ASSAY WITH VARYING BINDER CONCENTRATIONS USING BIOSENSING BY PARTICLE MOBILITY (BPM). Sketch of the measurement chamber in a BPM measurement (see Supplementary note 4.6.7) without (top) and with (bottom) supplemented binders with concentration $C_{b,\text{suppl}}$. For simplicity the particles of the BPM sensor are not shown in the sketch. In the absence of supplemented binders, the total binder concentration $C_{b,\text{tot}}$ equals $C_{b,\text{tot}} = \Gamma_b/H$; in the presence of supplemented binders, the total binder concentration $C_{b,\text{tot}}$ equals $C_{b,\text{tot}} = \Gamma_b/H + C_{b,\text{suppl}}$. Supplemented binders give a shorter time-to-equilibrium since the time-to-equilibrium scales according to $\tau_{\text{R,LV}} \propto 1/C_{b,\text{tot}}$ (see Table 4.1).

Figure 4.7 shows the measured time-to-equilibrium τ (left) and the signal change ΔS (right) as a function of $C_{b,\text{suppl}}$, for an analyte concentration of 200 pM (see Material and methods 4.5). The data show that the time-to-equilibrium decreases for increasing $C_{b,\text{suppl}}$. The measured signal change decreases with increasing supplemented binder concen-

tration because only surface-captured analyte molecules generate a measurable signal. The dashed lines in Figure 4.7 represent model fits (see the figure caption), demonstrating a good correspondence between model and experimental results. We conclude that the experimental results in Figure 4.7 prove the basic concept of the sensing methodology proposed in this chapter, namely, that a limited-volume design with time-controlled analyte exchange allows one to control the response time by tuning the concentration of binder molecules in the measurement chamber. Once the optimal binder concentration is known, the sensor can be made with binders immobilized in the measurement chamber. This will be a topic for future research.

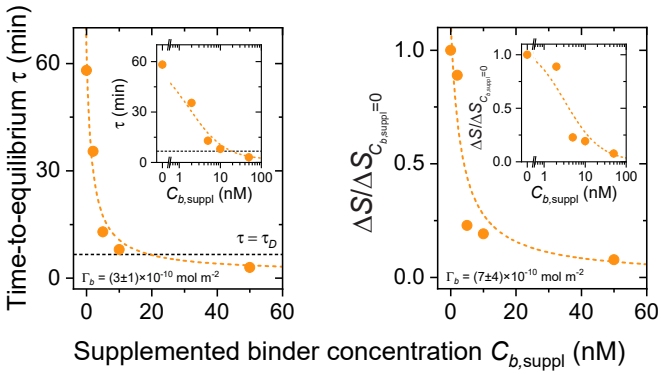

Figure 4.7: experimental study of a limited-volume assay with varying binder concentrations using biosensing by particle mobility (BPM). Experimentally observed time-to-equilibrium τ (left) and normalized signal change ΔS (right) as a function of supplemented binder concentration $C_{b,\mathrm{suppl}}$ in a BPM measurement with DNA-DNA hybridization reaction for an analyte concentration of 200 pM (see Supplementary note 4.6.7). Left: the dashed line shows the fitted curve $\tau = p_1/(p_2 + C_{b,\mathrm{suppl}}) + p_3$, where $p_1 = 1/k_{\mathrm{on}}$ (k_{on} is assumed to be equal for all binders), $p_2 = \Gamma_b/H$, and p_3 is the delay contributed by diffusion (see τ_D, dashed black line, *cf.* Figure 4.3b) and experimental handling steps (see Material and methods 4.5). Assuming $H = 200$ µm (see Table 4.1), the fit gives $\Gamma_b = (3 \pm 1) \cdot 10^{-10}$ mol m^{-2}, which is comparable to the standard parameter value as listed in Table 4.1. The fitted association rate constant is $k_{\mathrm{on}} = (1.5 \pm 0.4) \cdot 10^5$ M^{-1} s^{-1}, which is in the range of values reported in literature for comparable DNA-DNA hybridization reactions.[27,28] Right: the BPM sensor signal results from analyte molecules captured by immobilized binders. Therefore, supplementing binders in solution gives a lower signal change, because analyte molecules captured in solution do not generate signal on the sensor surface. In the depletion condition ($f_{\mathrm{init}} < f_{\mathrm{eq,IV}}$) the fractional occupancy scales according to $f \propto 1/C_{b,\mathrm{tot}} = C_{a,0}/(C_{b,0} + C_{b,\mathrm{suppl}})$. The dashed line shows the fitted curve $\Delta S = p_1/(p_2 + C_{b,\mathrm{suppl}})$, where p_1 scales the change in fractional occupancy to signal change and $p_2 = \Gamma_b/H$. For $H = 200$ µm, it was found that $\Gamma_b = (7 \pm 4) \cdot 10^{-10}$ mol m^{-2}, which is comparable to the previously found value for Γ_b and the standard parameter value as listed in Table 4.1. The insets show the same data on linear-logarithmic scales. The errors reported in the figure (smaller than the symbol size) and the caption are fitting errors based on a 68% confidence interval.

4.3.3 *Analytical performance of the limited-volume assay*

Figures 4.8-4.10 show how the analytical performance of the limited-volume assay depends on sensor design parameters. The results are based on numerical simulations with parameters as listed in Table

4.1. The analyte exchange is assumed to be instantaneous and the incubation phase includes mass transport by diffusion and reaction kinetics within the measurement chamber only. All panels show curves for different values of the initial fractional occupancy f_{init} of the binder molecules.

Figure 4.8a shows the fractional occupancy of binders by analyte molecules at the end of the incubation (f_{end}) as a function of the analyte concentration $C_{a,0}$. For $f_{\text{init}} = 0$ (dashed black line), f_{end} scales linearly with the analyte concentration, which makes the sensor suitable for analyte quantification. For larger values of f_{init} the curves start with a rather flat segment, from which one might erroneously conclude that under those conditions low analyte concentrations cannot be determined. Interestingly, the limited-volume assay has a linear dependence on concentration by focusing not on the absolute value of f_{end} but rather on the change of fractional occupancy Δf (see Supplementary note 4.6.2):

$$\Delta f = f_{\text{end}} - f_{\text{init}} \cong \frac{H}{\Gamma_b}\left(C_{a,0} - K_d f_{\text{init}}\right) \tag{4.1}$$

This equation shows that Δf depends linearly on $C_{a,0}$, independent of the value of f_{init}. This fact is also illustrated by the simulation results in Figure 4.8b. The response scales linearly with concentration $C_{a,0}$ and are down-shifted for increasing values of f_{init}, in agreement with Equation 4.1 (note that the steep increase of the curves relates to the logarithmic x-axis). Positive values of Δf relate to depletion behavior and negative values to repletion. The curves cross the x-axis ($\Delta f = 0$) when f_{init} corresponds to the equilibrium condition, *i. e.*, when there is no net association or dissociation during incubation because f_{init} is equal to the equilibrium fractional occupancy of the infinite-volume case: $f_{\text{init}} = f_{\text{eq,IV}} = \frac{C_{a,0}}{C_{a,0}+K_d} \cong \frac{C_{a,0}}{K_d}$. For example, the curve for $f_{\text{init}} = 10^{-3}$ crosses $\Delta f = 0$ at $C_{a,0} = f_{\text{init}} K_d = 0.1$ pM, as is highlighted (black arrow) in the inset of Figure 4.8b.

Figure 4.9 shows the precision of the concentration output of the sensor, *i. e.*, the precision with which the analyte concentration in an unknown sample can be determined for a signal collection area A_s of 1 mm² (see Table 4.2). The precision is calculated based on Poisson noise, which gives the fundamental limit of the precision that is achievable with a molecular biosensor due to stochastic fluctuations in the number of analyte molecules (see Supplementary notes 4.6.3 and 4.6.8).[29] To calculate the precision, a sensor with initial fractional occupancy f_{init} is provided with a sample with analyte concentration $C_{a,0}$, resulting in

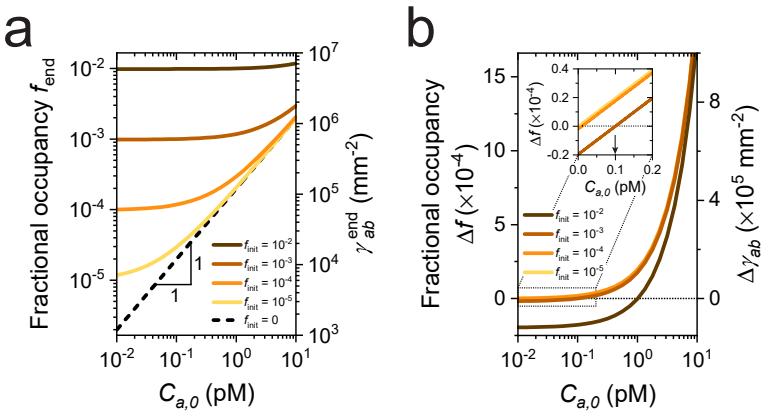

FIGURE 4.8: DOSE-RESPONSE CURVES OF THE LIMITED-VOLUME ASSAY, DERIVED FROM SIMULATIONS OF A SINGLE MEASUREMENT CYCLE. (a) Fractional occupancy at the end of the incubation f_{end} as a function of analyte concentration $C_{a,0}$ for different initial fractional occupancies f_{init}. The right y-axis indicates the number of surface-bound analyte molecules at the end of the cycle γ_{ab}^{end}. (b) Absolute change of fractional occupancy Δf as a function of $C_{a,0}$ for various f_{init}. The right y-axis indicates $\Delta\gamma_{ab}$. A positive Δf and $\Delta\gamma_{ab}$ indicate depletion; negative values indicate repletion. The inset shows the same data on a linear-linear scale.

a Δf with variability $\sigma_{\Delta f}$, which *via* the slope of the calibration curve, given in Figure 4.8b, leads to a variability σ_C in the concentration output of the sensor (see Supplementary note 4.6.3). The precision is indicated as the concentration-based coefficient of variation $CV_C = \sigma_C/\mu_C$, with σ_C the variability and μ_C the mean of the concentration output. Figure 4.9 shows how the concentration precision depends on the analyte concentration and the initial fractional occupancy f_{init}. For $f_{\text{init}} = 0$ (dashed line), the CV_C scales as $1/\sqrt{C_{a,0}}$, in agreement with number fluctuations in a Poisson process (see Supplementary note 4.6.3). For higher f_{init}, a stronger dependency is observed ($CV_C \propto 1/C_{a,0}$) caused by the smaller relative change of the fractional occupancy (see Supplementary note 4.6.3). The graph indicates the 10% precision level that is used to define the limit of quantification (LoQ) of the sensor. The results show that analyte concentrations in the sub-picomolar range can be measured with a precision better than 10%, even for high initial fractional occupancies.

Figure 4.10a shows the precision of the concentration output of the sensor as a function of two design parameters, namely the measurement chamber height H (top panel) and the binder density Γ_b (bottom panel), at an analyte concentration $C_{a,0} = 0.1$ pM, for an initial fractional occupancy f_{init} between 0 and 0.01. The arrows indicate the height and density as listed in Table 4.1. For an increasing H, a decrease of CV_C is observed, caused by an increase in the number of analyte molecules present in the measurement chamber. The CV_C is smallest for $f_{\text{init}} = 0$

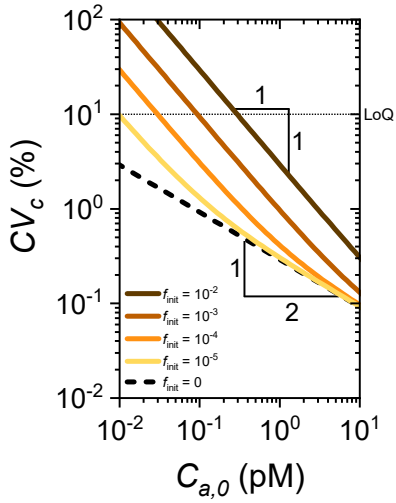

FIGURE 4.9: ANALYTICAL PERFORMANCE OF THE LIMITED-VOLUME ASSAY AS A FUNCTION OF CONCENTRATION, DERIVED FROM SIMULATIONS OF A SINGLE MEASUREMENT CYCLE. The coefficient of variation CV_C with which the analyte concentration $C_{a,0}$ can be determined as a function of analyte concentration $C_{a,0}$ for various initial fractional occupancies f_{init}. CV_C scales as $1/\sqrt{C_{a,0}}$ for low f_{init} and high $C_{a,0}$; CV_C scales as $1/C_{a,0}$ for high f_{init} and low $C_{a,0}$.

and increases for increasing f_{init} since the absolute change of fractional occupancy decreases. The CV_C decreases for increasing Γ_b caused by an increase in the number of analyte molecules captured from solution. The CV_C reaches a plateau for $f_{\text{init}} = 0$ due to a limited number of analyte molecules in the measurement chamber. For larger f_{init}, the absolute change of fractional occupancy decreases and causes a less precise concentration determination; this effect is in particular visible at high Γ_b where the absolute number of analyte-binder complexes increases due to f_{init}.

The tradeoff between precision and time-to-equilibrium is illustrated in Figure 4.10b, for sensors with different heights of the measurement chamber (left) and different binder densities (right). The arrows indicate the time-to-equilibrium that results from the height and density as listed in Table 4.1. The left panel shows that an increase of H gives on the one hand a slower sensor response (due to a larger diffusion distance) but on the other hand a lower CV_C due to a larger number of analyte molecules present in the measurement chamber. At low H, the CV_C strongly depends on f_{init} due to the low number of analyte molecules in the solution. The right panel shows again that the CV_C decreases for a slower sensor response, now controlled by decreasing the binder density Γ_b. At high Γ_b the time-to-equilibrium is diffusion-limited (resulting in $\tau = 130$ s, *cf.* Figure 4.3b). At low Γ_b the time-to-equilibrium is reaction-limited with $\tau = 1/k_{\text{off}} = 10^4$. At high Γ_b, the CV_C increases for increasing f_{init} due to the larger amount of analyte molecules on the sensor surface. At low Γ_b, the CV_C strongly

increases due to the low number of captured molecules caused by analyte dissociation over the long incubation timescale.

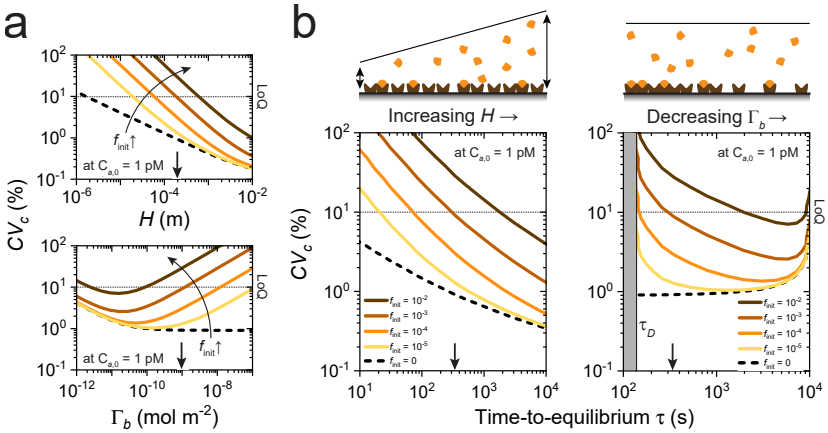

Figure 4.10: analytical performance of the limited-volume assay as a function of design parameters, derived from simulations of a single measurement cycle. (a) CV_C as a function of measurement chamber height H (top) and binder density Γ_b (bottom) for various initial fractional occupancies f_{init} and $C_{a,0} = 0.1$ pM. The arrows on the x-axes indicate the standard parameter values for H and Γ_b which as listed in Table 4.1. (b) CV_C as a function of the observed time-to-equilibrium τ when varying the measurement chamber height H (left) or binder density Γ_b (right) for various initial fractional occupancies f_{init} and $C_{a,0} = 0.1$ pM. The sketches above the graphs visualize a measurement chamber with an increasing height or a decreasing binder density. The arrows on the x-axes indicate the obtained time-to-equilibrium using the standard parameter values for H and Γ_b as listed in Table 4.1.

4.4 Conclusion

We have presented a sensing methodology suitable for monitoring low-concentration biomolecules with high precision, with small time delays and short time intervals, over an endless time span. The sensing methodology is based on a limited-volume assay, using high-affinity binders, a fully reversible detection principle, and time-controlled analyte exchange. We studied by simulations how the kinetics of the sensor depend on mass transport and on the surface reaction in the measurement chamber, and how time-controlled analyte exchange determines the system response and enables precise measurements of analyte concentration. Experimental results show the ability to control the sensor response time by tuning the total binder concentration in the measurement chamber. Finally, simulations show that the sensing principle allows picomolar and sub-picomolar concentrations to be monitored with a high precision over long time spans.

Approaches described in literature for measuring low-concentration biomolecules have focused primarily on assays in which every concen-

tration determination involves consumption of reagents.[17–20,30,31] When numbers of assays become high, due to frequent measurements over long time spans, then reagent consuming approaches are complex and costly. The sensing methodology described in this chapter is based on a fully reversible assay principle, without consuming reagents with each newly recorded concentration datapoint, enabling measurements with high frequency over an endless time span. The described assay principle can be implemented on several sensing platforms, *e. g.*, based on optical, electrical, or acoustical transduction methods, where especially sensing platforms with single-molecule resolution seem suitable since these allow digital measurements with very high precision, limited only by the number of observed molecular interactions. The sensing method is suited for the monitoring of a wide variety of analytes, including small molecules, proteins, and viral particles (see Supplementary note 4.6.9). Furthermore, the sensing methodology can be combined with various sampling methods, including remote advection-based sampling through a sampling line or a catheter, and proximal diffusion-based sampling methods for on-body and in-body monitoring devices. The presented sensing principle warrants further experimental studies, *e. g.*, to investigate tradeoffs between time characteristics and precision, for various transduction methods, sampling methods, measurement chamber geometries, binder types and the influence of complex biological matrices. Due to its generalizability and unique and tunable sensing performance, we believe that the limited-volume assay with time-controlled analyte exchange will enable research on time-dependencies of low-concentration biomolecules and novel applications in the fields of dynamic biological systems, patient monitoring, and biotechnological process control.

4.5 MATERIAL AND METHODS

FINITE-ELEMENT ANALYSIS: Finite-element simulations were performed by solving diffusion, advection and reaction equations simultaneously using COMSOL (COMSOL Multiphysics 5.5) and MATLAB (MATLAB R2019a, COMSOL Multiphysics LiveLink for MATLAB) (see Supplementary note 4.6.4). From the simulations, the time-to-equilibrium τ was determined by calculating the time at which the analyte-binder complex density γ_{ab} is at 63% of the difference between the starting level and the equilibrium level of γ_{ab}. The time-controlled analyte exchange (see Figures 4.4 and 4.5) was simulated by instantaneously increasing/decreasing the analyte concentration throughout the measurement chamber C_a to $C_{a,0}$, with which a new measurement cycle starts. The density of analyte-binder complexes $\gamma_{ab}^{\text{start}}$ at the start of a cycle was set to be equal to the density of analyte-binder complexes

γ_{ab}^{end} at the end of the preceding cycle. Sensor signals are reported at distance $L/2$ in the measurement chamber (see Figure 4.2b). Precisions are reported at a distance $L/2$ in the measurement chamber, where the signal is collected over a signal collection area A_s of 1 mm² (Figures 4.9 and 4.10).

FLUID CELL ASSEMBLY: Glass slides (25 x 75 mm, #5, Menzel-Gläser) were cleaned by 40 minutes sonication in isopropanol (VWR, absolute) and twice by 10 minutes sonication in Milli-Q (Thermo Fisher Scientific, Pacific AFT 20). Subsequently, the glass slides were dried under nitrogen flow. A polymer mixture of PLL(20)-g[3.5]-PEG(2) (SuSoS) and PLL(15)-g[3.5]-PEG(2)-N_3 (Nanosoft Polymers) was prepared at a final concentration of 0.45 mg mL^{-1} and 0.05 mg mL^{-1} in Milli-Q respectively. The glass slides were treated by oxygen plasma (Plasmatreat GmbH) for 1 minute. A custom-made fluid cell sticker (Grace Biolabs), with an approximate volume of 20 µL, was attached to the glass slide and immediately filled with the polymer mixture. After 2 hour incubation, the polymer mixture was removed and the fluid cell was immediately filled with 0.5 nM dsDNA tether solution (221 bp, with DBCO at one end and biotin at the other end) in 0.5 M NaCl in PBS.[32] After overnight incubation, the solution in the fluid cell was exchanged by 2 µM DBCO-functionalized dsDNA solution[32] in 0.5 M NaCl in PBS and incubated for several days until use.

PARTICLE FUNCTIONALIZATION: 2 µL streptavidin-functionalized particles (10 mg mL^{-1}, Dynabeads MyOne Streptavidin C1, Thermo Fisher Scientific) were incubated with 1 µL biotinylated ssDNA binder molecules (10 µM, IDT, HPLC purification) and 4 µL PBS for 70 minutes. The particles were magnetically washed in 0.05 vol.-% Tween-20 (Sigma-Aldrich) in PBS and resuspended in 0.5 M NaCl in PBS to a final concentration of 0.1 mg mL^{-1} and sonicated using an ultrasonic probe (Hielscher).

BPM ASSAY: 25 µL particle solution was added to the fluid cell and incubated for 10 minutes. After incubation, the fluid cell was reversed causing unbound particles to sediment. After washing with 40 µL 0.5 M NaCl in PBS, 40 µL mPEG-biotin (500 µM, PG1-BN-1k, Nanocs) in 0.5 M NaCl in PBS was added to the fluid cell. After 15 minutes incubation, the fluid cell was washed twice with 40 µL PBS. A mixture of ssDNA analyte molecules (IDT, standard desalting) and free binder molecules in PBS was added to the flow cell at the required concentration, immediately after preparation. The sample was observed under a white light source using a microscope (Leica DMI5000M) with a dark field illumination setup at a total magnification

of 10× (Leica objective, N plan EPI 10×/0.25 BD). A field of view of approximately 1100 × 700 µm² with a few thousand particles was imaged using a CMOS camera (FLIR, Grasshopper3, GS3-U3-23S6M-C) with an integration time of 5 ms and a sampling frequency of 30 Hz. The particles were tracked by applying a phasor-based localization method.[33] The particle activity was determined from the x- and y-trajectories of all particles, by applying a maximum-likelihood multiple-windows change point detection algorithm.[34] The particle activity at equilibrium and the time-to-equilibrium were extracted by fitting the measured particle activity over time using the equation given in Box 4.1.

4.6 SUPPLEMENTARY NOTES

4.6.1 *Standard parameter values*

Standard parameter values used throughout the chapter are listed in Table 4.2.

4.6.2 *Analytical expression of the dose-response curve*

In a limited-volume sensor with time-controlled analyte exchange, a limited number of analyte molecules interact with binder molecules present in a measurement volume. The analyte concentration $C_{a,0}$ can be derived from the time-evolution of the density of surface-bound analyte-binder complexes γ_{ab}. It is assumed that all binder molecules are immobilized on a surface, with effective volumetric concentration $C_{b,0} = \Gamma_b / H$ where Γ_b is the density of surface binders and H the height of the measurement chamber. It is assumed that binder molecules are in excess compared to analyte molecules ($C_{b,0} \gg C_{a,0}$) and are in excess compared to the equilibrium dissociation constant ($C_{b,0} \gg K_d$). Furthermore, it is assumed that no significant mass transport through the chamber inlet or outlet occurs during incubation, *i. e.*, the inlet and outlet areas are smaller than the total sensor area. Assuming first-order Langmuir kinetics, with reversible 1:1 interactions between binder molecules and analyte molecules, the change in effective volumetric analyte-binder complex concentration per unit time can be described by:

$$\frac{dC_{ab}(t)}{dt} = k_{\text{on}} \left(C_{a,0} - C_{ab}(t) + f_{\text{init}} C_{b,0} \right) C_{b,0} - k_{\text{off}} C_{ab}(t) \tag{4.2}$$

with $\frac{dC_{ab}(t)}{dt}$ being the time-derivative of the (spatial-dependent) effective volumetric analyte-binder complex concentration C_{ab}, k_{on} the

TABLE 4.2: Standard parameter values used in the finite-element simulations. Details about the simulations are described in Supplementary note 4.6.4.

	Parameter	Value	Description
Input parameter	H	200 µm	Measurement chamber height
	L	1 cm	Measurement chamber length
	W	2 mm	Measurement chamber width
	D	10^{-10} m^2 s^{-1}	Diffusion coefficient of the analyte molecule
	Q	100 µL min^{-1}	Flow rate during analyte exchange
	Γ_b	10^{-9} mol m^{-2} (600 µm^{-2})	Binder surface density
	k_{off}	10^{-4} s^{-1}	Dissociation rate constant
	k_{on}	10^{6} M^{-1} s^{-1}	Association rate constant
	$C_{a,0}$	0.1 pM	Analyte concentration
	A_s	1 mm^2	Signal collection area
Derived parameter	$\lambda = L/H$	50	Aspect ratio of measurement chamber
	$\tau_D = H^2/D$	400 s	Characteristic diffusion time
	$\tau_A = HLW/Q$	2.4 s	Characteristic advection time
	$\tau_{R,LV} = \frac{H}{k_{\text{on}}\Gamma_b}$	200 s	Characteristic reaction time for limited-volume assay with $C_{b,0} \gg C_{a,0}$ and $C_{b,0} \gg K_d$
	$C_{b,0} = \Gamma_b/H$	5 nM	Effective volumetric binder concentration
	$K_d = k_{\text{off}}/k_{\text{on}}$	0.1 nM	Equilibrium dissociation constant
	$\alpha = \frac{\Gamma_b}{HK_d} = C_{b,0}/K_d$	50	Acceleration factor: reduction factor of the time-to-equilibrium of a limited-volume biosensor (with $\tau(H,\Gamma_b)$) compared to an infinite-volume biosensor (with $\tau(k_{\text{off}})$).
	$Da = \tau_D/\tau_{R,LV} = k_{\text{on}}\Gamma_b H/D$	2	Damköhler number
	$Pe_L = \frac{\tau_D}{\tau_A} = \frac{Q}{\lambda DW}$	167	Longitudinal Péclet number
	$f_{eq,IV} = \frac{C_{a,0}}{C_{a,0} + K_d}$	10^{-3}	Equilibrium value of the fractional occupancy in an infinite-volume assay

association rate constant, $C_{a,0}$ the analyte concentration, f_{init} the initial fractional occupancy of the binder by an analyte molecule, $C_{b,0}$ the total effective binder concentration, and k_{off} the dissociation rate constant. Using $C_{ab}(t) = \gamma_{ab}(t)/H$, where γ_{ab} is the density of analyte-binder complexes, Equation 4.2 can be rewritten as a surface reaction rate:

$$\frac{d\gamma_{ab}(t)}{dt} = k_{\text{on}}\left(C_{a,0} + f_{\text{init}}\frac{\Gamma_b}{H}\right)\Gamma_b - k_{\text{on}}\left(\frac{\Gamma_b}{H} + K_d\right)\gamma_{ab}(t) \quad (4.3)$$

with $\frac{d\gamma_{ab}(t)}{dt}$ being the time-derivative of the density γ_{ab} of analyte-binder complexes, Γ_b the binder density, and K_d the equilibrium disso-

ciation constant. To calculate the time-dependent response of the sensor, we solve in Box 4.1 the differential equation given in Equation 4.3 and obtain the general solution for the time-evolution of the density γ_{ab} of analyte-binder complexes after instantaneous analyte exchange when no mass transport effects are considered.

BOX 4.1: Derivation of the analytical expression for the time-evolution of the density of analyte-binder complexes after instantaneous analyte exchange.

$$\frac{d\gamma_a b(t)}{dt} = k_{\text{on}}\left(C_{a,0} + f_{\text{init}}\frac{\Gamma_b}{H}\right)\Gamma_b - A\gamma_{ab}(t) \text{ with } A = k_{\text{on}}\left(\frac{\Gamma_b}{H} + K_d\right)$$

$$\frac{d\gamma_a b(t)}{dt} + C_1\gamma_{ab}(t) = C_2 \rightarrow \gamma_{ab}(t) = \frac{C_2}{C_1} + C_3\exp(-At)$$

$$\gamma_{ab}(t=0) = f_{\text{init}}\Gamma_b = \frac{\Gamma_b}{\Gamma_b/H+K_d}\left(C_{a,0} + f_{\text{init}}\frac{\Gamma_b}{H}\right) + C_3$$

$$\rightarrow C_3 = f_{\text{init}}\Gamma_b - \frac{\Gamma_b}{\Gamma_b/H+K_d}\left(C_{a,0} + f_{\text{init}}\frac{\Gamma_b}{H}\right)$$

$$\boxed{\gamma_{ab}(t) = \frac{\alpha}{\alpha+1}\left(HC_{a,0} + f_{\text{init}}\Gamma_b\right) + \beta\exp(-t/\tau_R)}$$

with $\alpha = \Gamma_b/(HK_d)$ being the acceleration factor (see Table 4.2), $\beta = f_{\text{init}}\Gamma_b - \frac{\alpha}{\alpha+1}(HC_{a,0} + f_{\text{init}}\Gamma_b)$, and $\tau_R = \left(k_{\text{on}}\left(\frac{\Gamma_b}{H} + K_d\right)\right)^{-1}$ the characteristic time-to-equilibrium of the reaction. When the γ_{ab} reaches equilibrium (*i.e.*, $t \rightarrow \infty$), then $\gamma_{ab} = \gamma_{ab}^{\text{end}} = \frac{\alpha}{\alpha+1}(HC_{a,0} + f_{\text{init}}\Gamma_b)$. For a limited-volume sensor with $C_{b,0} \gg C_{a,0}$ and $C_{b,0} \gg K_d$ in the equilibrium condition, nearly all analyte molecules are bound ($f_{\text{bound}} = \frac{\alpha}{\alpha+1} \cong 1$) and only a small fraction of analyte molecules is unbound ($f_{\text{unbound}} = \frac{1}{\alpha+1}$). Therefore τ_R can be simplified to $\tau_R = H/(k_{\text{on}}\Gamma_b)$. In the equation of the time-evolution of the density of analyte-binder complexes in Box 4.1, the depletion and repletion regimes can be recognized. When $f_{\text{init}} < C_{a,0}/K_d$, then $\beta < 0$, so the sensor shows depletion behavior. Conversely, if $f_{\text{init}} > C_{a,0}/K_d$, then $\beta > 0$ and the sensor shows repletion behavior. Rewriting the time-evolution of the density of analyte-binder complexes using the fractional occupancy $f = \gamma_{ab}/\Gamma_b$ and $t \rightarrow \infty$, yields the dose-response relationship as visualized in Figure 4.8a:

$$f_{\text{end}} = \frac{\alpha}{\alpha+1}\left(\frac{H}{\Gamma_b}C_{a,0} + f_{\text{init}}\right) \cong \frac{H}{\Gamma_b}C_{a,0} + f_{\text{init}} \tag{4.4}$$

Therefore, f_{end} depends linearly on $C_{a,0}$, independent of the value of f_{init}. The change of fractional occupancy Δf yields the dose-response relation as visualized in Figure 4.8b:

$$\begin{aligned}\Delta f = f_{\text{end}} - f_{\text{init}} &= \frac{\alpha}{\alpha+1}\left(\frac{H}{\Gamma_b}C_{a,0} + f_{\text{init}}\right) - f_{\text{init}} \\ &= \frac{1}{\alpha+1}\left(\frac{C_{a,0}}{K_d} - f_{\text{init}}\right) \cong \frac{H}{\Gamma_b}\left(C_{a,0} - K_d f_{\text{init}}\right)\end{aligned} \tag{4.5}$$

where Δf depends linearly on $C_{a,0}$, independent of the value of f_{init}.

4.6.3 *Precision of the concentration output*

The precision of the concentration output of the sensor, is the precision with which the analyte concentration in an unknown sample can be determined using the limited-volume assay. Under the assumption that the measured signal change $\Delta S = S_{\text{init}} - S_{\text{end}}$ scales linearly with the change in fractional occupancy Δf, *i.e.*, $\Delta S \propto \Delta f$, the precision of $C_{a,0}$ is calculated using the precision with which S_{init} and S_{end} can be determined. Therefore, no accumulation of errors from previously performed measurements occurs. We assume a measurement with variabilities which are dominated by Poisson noise in the number of bound analyte molecules. Other factors contributing to variability are not taken into account, but are discussed in another publication[29] and in Chapter 3. An analytical expression is derived for the precision of the analyte concentration $C_{a,0}$ in Box 4.2 of which the results are given in Figures 4.9 and 4.10.

BOX 4.2: Derivation of the analytical expression for the precision of the analyte concentration based on Poisson noise only.

The error of the signal change $\sigma_{\Delta S}$ can be estimated by:

$$\sigma_{N_{ab}^{\text{end}}} = \sqrt{N_{ab}^{\text{end}}} \text{ and } \sigma_{N_{ab}^{\text{init}}} = \sqrt{N_{ab}^{\text{init}}}$$

where N_{ab}^{end} and N_{ab}^{init} are the total number of analyte molecules bound to binder molecules that contribute to the signal of the sensor, at the end and start of a measurement respectively.

The measurement signal change equals $\Delta S = S_{\text{end}} - S_{\text{init}}$. Thus the squared signal change error is equal to the sum of the squared errors of the two terms:

$$\sigma_{\Delta S}^2 = \sigma_{S_{\text{end}}}^2 + \sigma_{S_{\text{init}}}^2 = \left(\frac{S_{\text{end}}}{\sqrt{N_{ab}^{\text{end}}}}\right)^2 + \left(\frac{S_{\text{init}}}{\sqrt{N_{ab}^{\text{init}}}}\right)^2$$

The concentration of the analyte is the output of the sensor. The output precision can be determined using the signal change error and the slope of the calibration curve, *i. e.*, the slope of the dose-response curve: $\sigma_C = \frac{\delta C_{a,0}}{\delta \Delta S}\sigma_{\Delta S}$ with $\frac{\delta \Delta S}{\delta C_{a,0}}$ the concentration-derivative of the signal change. This gives the following expression for the error of the concentration determination using a sensor with Poisson-limited precision:

$$\boxed{\sigma_C = \frac{\delta C_{a,0}}{\delta \Delta S}\sqrt{\left(\frac{S_{\text{end}}}{\sqrt{N_{ab}^{\text{end}}}}\right)^2 + \left(\frac{S_{\text{init}}}{\sqrt{N_{ab}^{\text{init}}}}\right)^2}}$$

The derivation in Box 4.2 gives the following analytical expression for the precision of the sensor output, *i. e.*, the error of the concentration σ_C:

$$\sigma_C = \frac{\delta C_{a,0}}{\delta \Delta S}\sqrt{\left(\frac{S_{\text{end}}}{\sqrt{N_{ab}^{\text{end}}}}\right)^2 \left(\frac{S_{\text{init}}}{\sqrt{N_{ab}^{\text{init}}}}\right)^2} \tag{4.6}$$

Equation 4.6 shows that σ_C decreases (*i. e.*, the precision increases) for an increasing number of analyte molecules N_{ab}^{end} for a given signal collection area (see Table 4.2), for instance by increasing the height of the measurement chamber or the binder density (see Box 4.1). Since

S_{end} and thus N_{ab}^{end} scale linearly with the analyte concentration (see Equation 4.4), we can derive:

$$\sigma_C \propto \sqrt{C_{a,0}} \rightarrow CV_C = \frac{\sigma_C}{C_{a,0}} \propto \frac{\sqrt{C_{a,0}}}{C_{a,0}} = \frac{1}{\sqrt{C_{a,0}}} \tag{4.7}$$

which results in a 1:2 slope ($CV_C : C_{a,0}$) in Figure 4.9 for low f_{init}. However, if f_{init} is close to or higher than $HC_{a,0}/\Gamma_b$, then the contribution of f_{init} to the fractional occupancy f_{end} at the end of a measurement cycle is relatively large, which results in a rather flat region in the f_{end}-$C_{a,0}$ curve as visualized in Figure 4.8a. Since $f_{\text{end}} \sim f_{\text{init}}$, σ_C is largely determined by f_{init}, then Equation 4.7 converts to $CV_C = \sigma_C/C_{a,0} \propto 1/C_{a,0}$, resulting in a 1:1 slope ($CV_C : C_{a,0}$) in Figure 4.9 for high f_{init}.

4.6.4 *Nondimensionalization*

The simulation study of the time-dependent behavior of the biochemical assay was performed using dimensionless parameters for all mass transport processes and reaction rates.[35] The nondimensionalized parameters for mass transport by diffusion and advection are given in Table 4.3.

TABLE 4.3: Dimensionless parameters used in the finite-element analysis for modeling mass transport by diffusion and advection.

Dimensionless parameter	Symbol	Expression
Analyte concentration	$\tilde{c}$	$\tilde{c} = C_a/C_{a,0}$
Longitudinal distance	$\tilde{x}$	$\tilde{x} = x/L$
Transversal distance	$\tilde{y}$	$\tilde{y} = y/H$
Time	$\tilde{t}$	$t = H^2/D \rightarrow \tilde{t} = t\,D/H^2$

For all finite-element analyses, the time was nondimensionalized using the diffusion time τ_D (*e.g.*, Figure 4.3b) and thereafter recalculated to normalize with respect to other time scales (*e.g.*, τ_R in Figures 4.3a and c). When advective flow is included, the used analytical expression of the advective flow is given by:

$$\vec{v}\,(y) = \frac{6Q}{WH^3} y\,(H-y)\,\vec{e_x} \tag{4.8}$$

with $\vec{v}(y)$ being the flow speed as a function of the height y inside the measurement chamber, Q the flow rate, W the width of the measurement chamber, and H the height of the measurement chamber. The

general equation used in the simulation to describe mass transport by advection and diffusion is given by:

$$\frac{\delta C_a}{\delta t} = D\nabla^2 C_a - \vec{v}(y) \cdot \nabla C_a \tag{4.9}$$

with $\frac{\delta C_a}{\delta t}$ being the time-derivative of the (spatial-dependent) analyte concentration C_a and D the diffusion coefficient. The dimensionless form of Equation 4.9 is derived in Box 4.3.

BOX 4.3: Derivation of the dimensionless advection-diffusion equation.

$$\frac{\delta(\tilde{c}C_{a,0})}{\delta\left(\frac{\tilde{t}H^2}{D}\right)} = D\frac{\delta^2(\tilde{c}C_{a,0})}{\delta(\tilde{x}L)^2} + D\frac{\delta^2(\tilde{c}C_{a,0})}{\delta(\tilde{y}H)^2} - \frac{6Q}{WH^3}\tilde{y}H\left(H - \tilde{y}H\right)\frac{\delta(\tilde{c}C_{a,0})}{\delta(\tilde{x}L)}$$

$$\frac{\delta\tilde{c}}{\delta\tilde{t}} = \frac{H^2}{D}\frac{1}{L^2}D\frac{\delta^2\tilde{c}}{\delta\tilde{x}^2} + \frac{H^2}{D}\frac{1}{H^2}D\frac{\delta^2\tilde{c}}{\delta\tilde{y}^2} - \frac{H^2}{D}\frac{6Q}{WH^3}\frac{1}{L}\tilde{y}H^2\left(1-\tilde{y}\right)\frac{\delta\tilde{c}}{\delta\tilde{x}}$$

$$\boxed{\frac{\delta\tilde{c}}{\delta\tilde{t}} = \frac{H^2}{L^2}\frac{\delta^2\tilde{c}}{\delta\tilde{x}^2} + \frac{\delta^2\tilde{c}}{\delta\tilde{y}^2} - \frac{6QH}{LDW}\tilde{y}\left(1-\tilde{y}\right)\frac{\delta\tilde{c}}{\delta\tilde{x}}}$$

Using the derivation given in Box 4.3, measurement chamber aspect ratio $\lambda = L/H$, and longitudinal Péclet number $Pe_L = \frac{Q}{\lambda DW}$ (see Table 4.2), the simplified dimensionless advection-diffusion equation is given by:

$$\frac{\delta\tilde{c}}{\delta\tilde{t}} = \frac{1}{\lambda^2}\frac{\delta^2\tilde{c}}{\delta\tilde{x}^2} + \frac{\delta^2\tilde{c}}{\delta\tilde{y}^2} - 6Pe_L\tilde{y}\left(1-\tilde{y}\right)\frac{\delta\tilde{c}}{\delta\tilde{x}} \tag{4.10}$$

The nondimensionalized parameters for the reaction rate are given in Table 4.4.

TABLE 4.4: Dimensionless parameters used in the finite-element analysis for modeling the reaction at the sensor surface.

Dimensionless parameter	Symbol	Expression
Analyte concentration at the sensor surface	$\tilde{c}^*$	$\tilde{c}^* = C_a^*/C_{a,0}$
Density of analyte-binder complexes	$\tilde{\gamma}$	$\tilde{\gamma} = \gamma_{ab}/(C_{a,0}H)$
Time	$\tilde{t}$	$\tilde{t} = t\,D/H^2$

The general equation used in the simulation to model the reaction at the sensor surface is given by:

$$\frac{\delta\gamma_{ab}(t)}{\delta t} = k_{\text{on}}C_a^*\left(\Gamma_b - \gamma_{ab}(t)\right) - k_{\text{off}}\gamma_{ab}(t) \tag{4.11}$$

with $\frac{\delta \gamma_{ab}}{\delta t}$ being the time-derivative of the (spatial-dependent) density γ_{ab} of analyte-binder complexes and C_a^* the analyte concentration at the sensor surface, which is known by solving Equation 4.10. The dimensionless form of Equation 4.11 is derived in Box 4.4.

BOX 4.4: Derivation of the dimensionless reaction rate equation

$$\frac{\delta(\widetilde{\gamma} C_{a,0} H)}{\delta\left(\frac{tH^2}{D}\right)} = k_{\text{on}} \widetilde{c}^* C_{a,0} \left(\Gamma_b - \widetilde{\gamma} C_{a,0} H\right) - k_{\text{off}} \widetilde{\gamma} C_{a,0} H$$

$$\frac{\delta \widetilde{\gamma}}{\delta \widetilde{t}} = \frac{H^2}{D} \frac{k_{\text{on}} \widetilde{c}^*}{H} \left(\Gamma_b - \widetilde{\gamma} C_{a,0} H\right) - \frac{H^2}{D} k_{\text{off}} \widetilde{\gamma}$$

$$\frac{\delta \widetilde{\gamma}}{\delta \widetilde{t}} = \frac{k_{\text{on}} \Gamma_b H}{D} \widetilde{c}^* - \frac{k_{\text{on}} H}{D} \widetilde{c}^* \widetilde{\gamma} C_{a,0} H - \frac{H^2}{D} k_{\text{off}} \widetilde{\gamma}$$

$$\boxed{\frac{\delta \widetilde{\gamma}}{\delta \widetilde{t}} = \frac{C_{a,0} H}{\Gamma_b} \frac{k_{on} \Gamma_b H}{D} \left[\widetilde{c}^* \left(\frac{\Gamma_b}{C_{a,0} H} - \widetilde{\gamma}\right) - \frac{K_d}{C_{a,0}} \widetilde{\gamma}\right]}$$

Using the derivation given in Box 4.4 and Damköhler number $Da = \frac{k_{\text{on}} \Gamma_b H}{D}$ (see Table 4.2), the simplified dimensionless reaction rate equation is given by:

$$\frac{\delta \widetilde{\gamma}}{\delta \widetilde{t}} = \frac{C_{a,0} H}{\Gamma_b} Da \left[\widetilde{c}^* \left(\frac{\Gamma_b}{C_{a,0} H} - \widetilde{\gamma}\right) - \frac{K_d}{C_{a,0}} \widetilde{\gamma}\right] \tag{4.12}$$

4.6.5 *Time-controlled analyte exchange*

Time-controlled analyte exchange in a limited-volume assay refers to the switching between the exchange phase and the incubation phase (see Figure 4.2b). In the analyte exchange phase, mass transport exists between the system of interest and the measurement chamber, *e. g.*, by diffusion and/or advection. In the incubation phase, mass transport between the system of interest and the measurement chamber is limited, *e. g.*, by stopping flow and/or diffusion.

Figures 4.11 and 4.12 show how time-controlled analyte exchange influences the performance of the sensor, for two analyte exchange principles, namely remote advection-based sampling and proximal diffusion-based sampling (see Figure 4.11). In Supplementary note 4.6.6, the influence of time-controlled analyte exchange on the performance of the sensor is quantified by simulating the time-to-equilibrium τ and the coefficient of variation of the concentration CV_C as a function of the duration of analyte exchange.

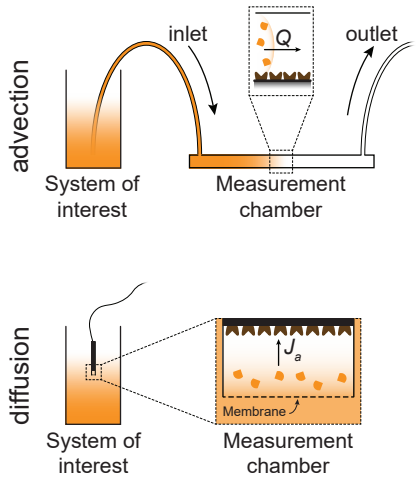

FIGURE 4.11: TIME-CONTROLLED ANALYTE EXCHANGE BY ADVECTION- AND DIFFUSION-BASED SAMPLING. Concepts of analyte exchange by advection (top) and by diffusion (bottom) between a system of interest and a measurement chamber, using flow rate Q and molar flux J_a through a semi-permeable membrane respectively.

Figure 4.11 schematically visualizes time-controlled analyte exchange by advection (top) and by diffusion (bottom), where the analyte exchange process has a characteristic time τ_{exch} and a duration t_{exch} (see Figure 4.12). The duration of the analyte exchange is controlled by adjusting the flow rate Q or the molar flux J_a (by controlling the membrane permeability P)[36] in time. For advection-based sampling, τ_{exch} equals the characteristic advection time τ_A, while for diffusion-based sampling, τ_{exch} equals the characteristic diffusion time τ_D (see Table 4.2). In t_{exch}, analyte molecules are transported over a characteristic length $L_A = t_{\text{exch}}Q/(HW)$ by advection and $L_D = \sqrt{t_{\text{exch}}D}$ by diffusion.

Three regimes can be identified regarding the analyte exchange. First, $t_{\text{exch}} < \tau_{\text{exch}}$ implies that L_A or L_D is shorter than the length L of the measurement chamber or the height H of the measurement chamber for advection-based sampling and diffusion-based sampling respectively. Second, if t_{exch} equals τ_{exch}, the transport distance equals L or H for advection-based sampling and diffusion-based sampling respectively; this condition is used in Figure 4.3c for analyte exchange by advection, since here the exchanged volume equals the volume of the measurement chamber. Third, $t_{\text{exch}} > \tau_{\text{exch}}$ implies that L_A or L_D is longer than L or H for advection-based sampling and diffusion-based sampling respectively.

In the simulations presented in this work, we made the following assumptions. First, analyte exchange between the system of interest and the measurement chamber only occurs during the analyte exchange

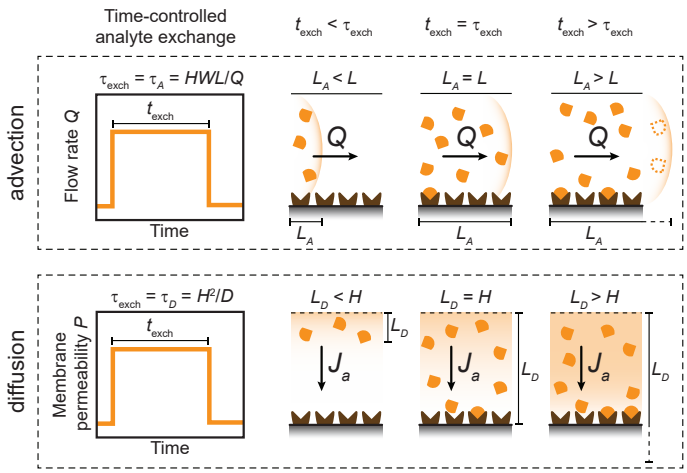

FIGURE 4.12: TIME-CONTROLLED ANALYTE EXCHANGE BY ADVECTION AND DIFFUSION. Schematic visualizations of time-controlled analyte exchange by controlling the flow rate Q (top) and the molar flux J_a (by controlling the membrane permeability P, bottom) in time. The time-controlled analyte exchange process has a characteristic time τ_{exch}, which equals τ_A for advection-based analyte exchange, and τ_D for diffusion-based analyte exchange, and a duration of t_{exch} in which analyte molecules travel characteristic length L_A or L_D. Three regimes are identified: (1) $t_{exch} < \tau_{exch}$ where $L_A < L$ or $L_D < H$; (2) $t_{exch} = \tau_{exch}$ where $L_A = L$ or $L_D = H$; and (3) $t_{exch} > \tau_{exch}$ where $L_A > L$ or $L_D > H$.

phase. For advection-based analyte exchange, this implies that the flow rate Q is high in phase 1 (the analyte exchange phase) and zero in phase 2 (the incubation phase). For diffusion-based analyte exchange, the membrane permeability P is high in phase 1, and zero in phase 2. The second assumption is that diffusive mass transport within the measurement chamber itself is always present.

Analyte exchange can be controlled by controlling the characteristic analyte exchange time τ_{exch} (by design parameters Q and P) and by controlling the analyte exchange duration t_{exch}. In Supplementary note 4.6.6 we study the performance as a function of Q and t_{exch} for advection-based exchange. For diffusion-based exchange, we study the performance as a function of t_{exch}, assuming $P \to \infty$.

4.6.6 *The influence of time-controlled analyte exchange on the sensor performance*

The influence of flow rate Q on the observed time-to-equilibrium τ and the precision of the concentration determination CV_C is quantified in Figure 4.13 for a sensor with diffusion-based sampling and with standard parameter values as listed in Table 4.2. Figure 4.13a shows the time-to-equilibrium τ as a function of longitudinal Péclet number Pe_L, by varying the flow rate Q, for three values of $t_{exch}/\ \tau_A$. For small

Pe_L, mass transport by advection is slow compared to mass transport by diffusion, and thus τ is advection-limited and scales according to $\tau \propto 1/Q$ (see Box 4.5). Besides, increasing the analyte exchange duration t_{exch} causes the observed time-to-equilibrium τ to be longer. The plateau value (dashed line) is reached when mass transport by advection is fast compared to mass transport by diffusion, *i.e.*, at high flow rates, which corresponds to the τ found in Figure 4.3c for an equal sensor height. In this regime, the sensor can be assumed to be incubated with a concentration $C_{a,0}$ instantaneously. For $Pe_L \to \infty$, a τ is observed equal to τ found for instantaneous analyte exchange (see Figures 4.13a,b).

BOX 4.5: The influence of analyte exchange by advection on the time-to-equilibrium.

When the time-to-equilibrium is advection-limited, this results in $\tau = t_{\text{exch}}$:

$$\tau = t_{\text{exch}} \to \tau = \frac{HLW}{Q}\frac{t_{\text{exch}}}{\tau_A} = \frac{\lambda DW}{Q}\frac{HL}{\lambda D}\frac{t_{\text{exch}}}{\tau_A} = \frac{1}{Pe_L}\frac{H^2}{D}\frac{t_{\text{exch}}}{\tau_A}$$

$$\tau \propto \frac{1}{Pe_L} \to \tau : Pe_L = 1 : 1$$

Figure 4.13b shows the precision of the concentration determination as a function of the longitudinal Péclet number Pe_L and flow rate Q on the secondary x-axis. Again, roughly two regimes can be identified: for small Pe_L, CV_C depends on Pe_L since the analyte molecules entering the measurement chamber bind to the binders on the surface, which results in longitudinal depletion. This results in a positional dependency of the density γ_{ab} of analyte-binder complexes and thus the precision. For large Pe_L, the analyte exchange by advection is much faster than analyte exchange by diffusion causing almost instantaneous exchange of material, which results in lateral depletion, making the precision independent of Pe_L. For $Pe_L \to \infty$, a CV_C is observed equal to the CV_C found for instantaneous analyte exchange (see Figure 4.10).

Figure 4.14 shows the influence of diffusion-based analyte exchange on the observed time-to-equilibrium, by comparing instantaneous analyte exchange to diffusion-based analyte exchange, where $t_{\text{exch}}/\tau_D = 1$. Figure 4.14a shows the time-to-equilibrium τ as a function of Damköhler number Da by varying the height H of the measurement chamber, for diffusion-based analyte exchange (dark orange) and for instantaneous analyte exchange (light orange, same data as Figure 4.3a). At low Da (*i.e.*, at small measurement chamber height H), for both exchange methods, the observed time-to-equilibrium is reaction-limited since

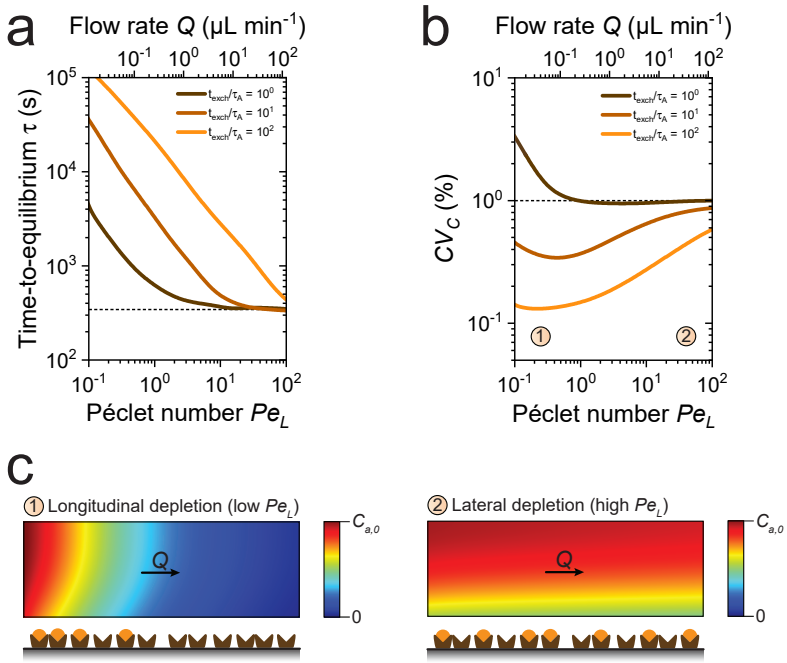

FIGURE 4.13: INFLUENCE OF ADVECTION-BASED ANALYTE EXCHANGE ON THE PERFORMANCE OF THE BIOMOLECULAR MONITORING SYSTEM USING TIME-CONTROLLED ANALYTE EXCHANGE BY ADVECTION. (a) Time-to-equilibrium τ as a function of the longitudinal Péclet number Pe_L, with the flow rate Q on the secondary x-axis (see Table 4.2), for three values of t_{exch}/τ_A (see Figure 4.12). For small Pe_L, τ depends on Pe_L where $\tau \propto 1/Pe_L$ (see Box 4.5). τ decreases for increasing Pe_L since the analyte exchange process is faster (higher flow rate Q), but τ increases for increasing t_{exch}/τ_A since the duration of the analyte exchange process is longer. For large Pe_L, τ is independent of Pe_L; the Pe_L value where τ becomes independent of Pe_L, depends on t_{exch}/τ_A. (b) Precision of the measured concentration CV_C as a function of the longitudinal Péclet number Pe_L at an analyte concentration $C_{a,0} = 0.1$ pM, with the flow rate Q on the secondary x-axis (see Table 4.2), for three values of t_{exch}/τ_A. For small Pe_L, a longitudinal depletion zone appears where (almost) all analyte molecules are captured from solution by binder molecules directly after entering the measurement chamber, causing a positional dependency of the density of analyte-binder complexes, and a lower CV_C (*i.e.*, a higher precision) at the point of sensing. For $t_{\text{exch}}/\tau_A = 100$ this effect is largest since analyte exchange has a short duration. By increasing t_{exch}/τ_A, the CV_C decreases since more analyte molecules are exchanged. For large Pe_L, a lateral depletion zone appears where the analyte exchange can be assumed to be instantaneous (see Figure 4.3); here CV_C is independent of Pe_L and no positional dependency of the density of analyte-binder complexes exists. (c) Schematic visualizations of the measurement chamber cross-section show the spatial distribution of the concentration C_a, where red equals high C_a ($C_a = C_{a,0}$) and blue equals low C_a ($C_a = 0$).

the diffusion time scale is fast compared to the reaction time scale. However, for increasing Da, the time-to-equilibrium increases faster for diffusion-based exchange since the characteristic length scale L_D over which the molecules have to diffuse is larger ($L_D = H$) as compared to instantaneous analyte exchange (on average $L_D \cong H/2$).

Figure 4.14b shows the time-to-equilibrium τ as a function of Da by varying the binder density Γ_b, for diffusion-based analyte exchange

(dark orange) and for instantaneous analyte exchange (light orange, same data as Figure 4.3b). At low Da (*i. e.*, at low surface binder density Γ_b), for both exchange methods, the observed time-to-equilibrium is reaction-limited since the reaction time scale is short ($\tau_R = 1/k_{\text{off}}$) compared to the diffusion time scale. However, at high Da where the time-to-equilibrium τ is determined by the diffusion time scale, τ is larger for diffusion-based exchange since the characteristic length scale L_D over which the molecules have to diffuse is larger.

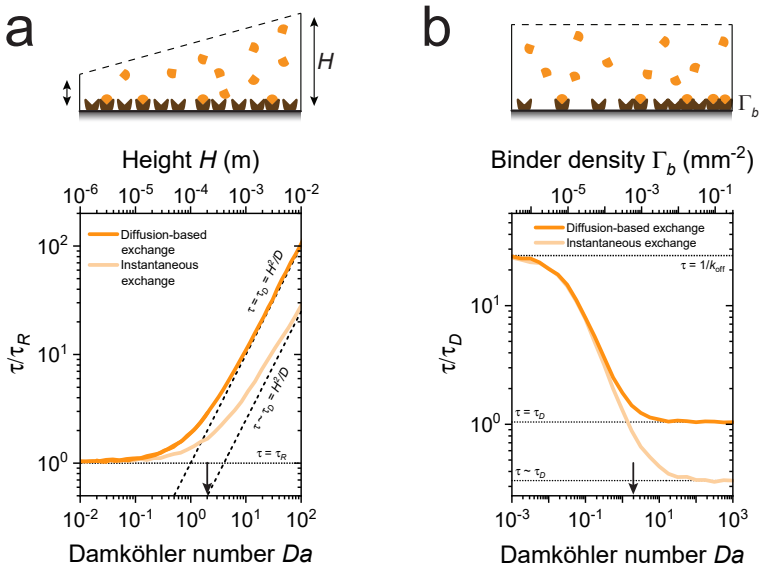

FIGURE 4.14: INFLUENCE OF DIFFUSION-BASED ANALYTE EXCHANGE ON THE OBSERVED TIME-TO-EQUILIBRIUM. (a) Time-to-equilibrium τ, normalized to the characteristic reaction time τ_R as a function of Damköhler number Da, with the measurement chamber height H on the secondary y-axis, for diffusion-based (orange) and instantaneous analyte exchange (light orange). For small Da, no difference in τ/τ_R exists since the observed reaction is reaction-limited. For large Da, diffusion-based analyte exchange results in a slower observed reaction since the characteristic distance L_D is larger. (b) Time-to-equilibrium τ normalized to the characteristic diffusion time τ_D as a function of Damköhler number Da, with the binder density Γ_b on the secondary y-axis. A difference in τ/τ_D exists caused by a longer L_D. For large Da, the observed reaction is diffusion-limited. In these simulations it was assumed that $t_{\text{exch}}/\tau_D = 1$. In both panels, the black arrows on the x-axis indicate the standard parameter value for Da (using H and Γ_b) which is given in Table 4.2.

Figure 4.15 shows the influence of the time-controlled analyte exchange process on the time-to-equilibrium and the precision of the sensor for two monitoring geometries as presented in Figure 4.12 and using the standard parameter values given in Table 4.2. Figure 4.15a sketches the time-evolution of the fractional occupancy (solid orange line) and the analyte exchange process (dashed light orange line) of advection (by controlling flow rate Q) or diffusion (by controlling membrane permeability P). Three regimes are given here: (1) $\tau > t_{\text{exch}}$,

where τ is determined by the mass transport by diffusion within the measurement chamber; (2) $\tau \sim t_{\text{exch}}$, where τ is determined by the duration of the analyte exchange process; and (3) $\tau < t_{\text{exch}}$, where τ is determined by the dissociation rate constant k_{off}. Note that for a short t_{exch}, the fractional occupancy when equilibrium is reached, is lower, since less molecules have been exchanged between the measurement chamber and the system of interest.

Figure 4.15b shows the simulated results of the time-to-equilibrium τ normalized to the diffusion time scale τ_D as a function of the duration of analyte exchange t_{exch} normalized to the diffusion time scale τ_D (left) and the coefficient of variation of the concentration CV_C as a function of t_{exch}/τ_D (right). The three regimes shown in panel a are observed in both graphs. For a small t_{exch}/τ_D, the observed time-to-equilibrium τ is diffusion-limited, since t_{exch} is much smaller than τ_D. However, CV_C is high (*i. e.*, precision is low) since the number of exchanged analyte molecules is small. Here, CV_C scales according to $CV_C \propto 1/\sqrt[4]{t_{\text{exch}}/\tau_D}$ (see Box 4.6). For a large t_{exch}/τ_D, the observed time-to-equilibrium τ is reaction-limited, since the assay converts into an infinite-volume assay. However, CV_C is low (*i. e.*, precision is high) since the number of exchanged analyte molecules is large (*i. e.*, there is an infinite supply of analyte molecules). Now the precision is independent of the analyte-exchange process, since the reaction reaches an equilibrium under infinite supply of analyte molecules. When $\tau \sim t_{\text{exch}}$, the time-to-equilibrium is mainly determined by the duration of the analyte-exchange process since the assay can be regarded as neither a limited-volume assay nor an infinite-volume assay; here, CV_C scales roughly according to $CV_C \propto 1/\sqrt{t_{\text{exch}}/\tau_D}$ (see Box 4.6).

BOX 4.6: The mathematical derivation of the dependency of precision on analyte exchange by diffusion.

Fick's First Law gives $J_a^D = -D\nabla C_a$, where J_a^D is the diffusion flux of analyte molecules, which translates into $J_a^D = -D\frac{\delta C_a}{\delta y}$ assuming one-dimensional transversal diffusion. The maximum density $\gamma_{ab}^{\max}$ of analyte-binder complexes that can be reached, is calculated by $\gamma_{ab}^{\max} = J_a^D t_{\text{exch}}$. The mean length L_D over which analyte molecules diffuse during t_{exch} equals $\delta y = L_D = \sqrt{H^2 \frac{t_{\text{exch}}}{\tau_D}}$ for $L_D < H$ and $\delta y = H$ for $L_D \geq H$.

$L_D < H$, gives $\gamma_{ab}^{\max} = HC_a\sqrt{\frac{t_{\text{exch}}}{\tau_D}}$ and $L_D \geq H$, gives $\gamma_{ab}^{\max} = HC_a\frac{t_{\text{exch}}}{\tau_D}$. The maximum coefficient of variation can be calculated by $CV_C = \frac{1}{\sqrt{\gamma_{ab}^{\max} A_s}}$, where A_s is the signal collection area.

For $L_D < H$, $CV_C \propto \frac{1}{\sqrt[4]{\frac{t_{\text{exch}}}{\tau_D}}}$ and for $L_D \geq H$, $CV_C \propto \frac{1}{\sqrt{\frac{t_{\text{exch}}}{\tau_D}}}$.

Figure 4.15c shows the simulated results of the time-to-equilibrium τ, normalized to the advection time scale τ_A, as a function of the duration of analyte exchange t_{exch}, normalized to the advection time scale τ_A (left), and the coefficient of variation of the concentration CV_C as a function of t_{exch}/τ_A (right). Again, the three regimes in panel a are observed in both graphs. The behavior is similar to panel b: for a small t_{exch}/τ_A, the observed time-to-equilibrium τ is diffusion-limited, but CV_C is high (*i. e.*, precision is low) since the number of exchanged analyte molecules is small. No values are shown for $t_{\text{exch}}/\tau_A < 1$ due to the development of positional dependency of γ_{ab} when the volume of the measurement chamber is not fully exchanged (see Figure 4.13b). At low t_{exch}/τ_A, the precision is roughly independent of t_{exch}/τ_A due to the development of a lateral depletion zone (see Figure 4.13b). For a large t_{exch}/τ_A, the observed time-to-equilibrium τ is reaction-limited and CV_C is low (*i. e.*, precision is high) since the number of exchanged analyte molecules is large (*i. e.*, there is an infinite supply of analyte molecules). When $\tau \sim t_{\text{exch}}$, the time-to-equilibrium is mainly determined by the duration of the analyte exchange and CV_C scales roughly as $CV_C \propto 1/\sqrt{t_{\text{exch}}/\tau_A}$ (see Box 4.7). However, this CV_C derived from the number of analyte molecules (see black dashed line, left bottom corner), is lower than the observed CV_C (see also panel b), since in the case of analyte exchange by advection, analyte molecules can be lost through the outlet without

contributing to the precision of the sensor. Therefore the maximum density $\gamma_{ab}^{\max}$ can only be reached in diffusion-based analyte exchange.

BOX 4.7: The mathematical derivation of the dependency of precision on analyte exchange by advection.

The advective flux of analyte molecules J_a^A can be described by $J_a^A = QC_{a,0}$. The maximum analyte-binder surface density $\gamma_{ab}^{\max}$ can be calculated by $\gamma_{ab}^{\max} = \frac{J_a^A}{WL} t_{\text{exch}} \rightarrow \gamma_{ab}^{\max} = HC_{a,0} \frac{t_{\text{exch}}}{\tau_A}$, assuming $L_A \geq L$ with lateral depletion. The maximum coefficient of variation can be calculated by $CV_C = \frac{1}{\sqrt{\gamma_{ab}^{\max} A_s}}$, where A_s is the signal collection area. For $L_A \geq L$, $CV_C \propto \frac{1}{\sqrt{\frac{t_{\text{exch}}}{\tau_A}}}$.

4.6.7 *Biosensing by particle mobility*

In this chapter, the concept of rapid monitoring of low-concentration biomolecules by time-controlled analyte exchange is experimentally demonstrated using biosensing by particle mobility (BPM), a biosensing method with both single-particle and single-molecule resolution.[37–39] The molecular design and measurement principle are sketched in Figure 4.16, illustrated with a sandwich assay format. Figure 4.16a shows a particle that is tethered to a substrate by a dsDNA tether and functionalized with ssDNA binder molecules, and a surface that is functionalized with secondary binder molecules.

Figure 4.16b illustrates the sensing functionality of the BPM system. The secondary binder molecules can transiently bind to analyte molecules captured from solution by the binder molecules on the particle. The transient binding affects the mobility of the particle, because an unbound particle has a larger in-plane motional freedom than a bound particle. Two mobility time traces are sketched in Figure 4.16c, at a high (left) and low (right) analyte concentration. The switching frequency of the particle, *i. e.*, the activity, depends on the analyte concentration, because the unbound state lifetime of a particle decreases when the number of captured analyte molecules increases.

To demonstrate the rapid monitoring methodology for low-concentration biomolecules using BPM, we used ssDNA analyte molecules that bind with a 20nt interaction to the ssDNA binder molecules on the particle. The particles are functionalized with a high binder density[29] and have a high-affinity interaction with the analyte (characteristic life-

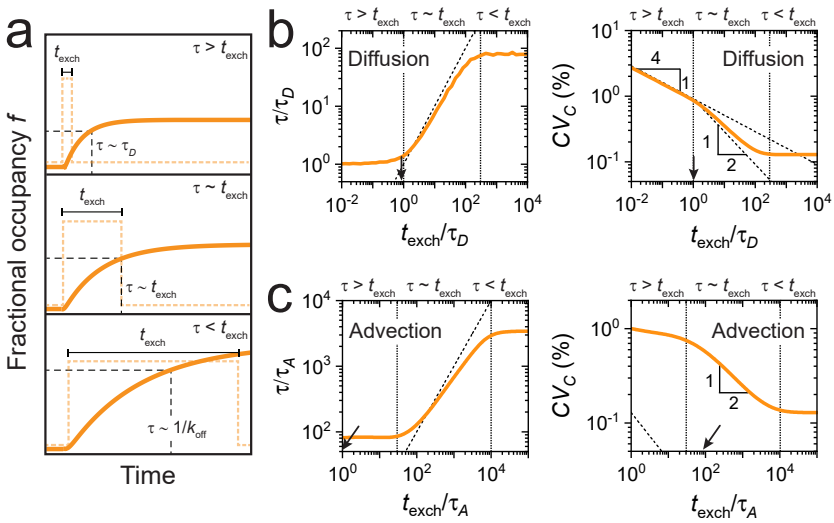

FIGURE 4.15: INFLUENCE OF THE ANALYTE EXCHANGE PROCESS ON THE PERFORMANCE OF THE BIOMOLECULAR MONITORING SYSTEM USING TIME-CONTROLLED ANALYTE EXCHANGE. (a) Sketches of the time-evolution of the fractional occupancy upon analyte exchange by advection (by controlling flow rate Q) or diffusion (by controlling membrane permeability P). Three regimes are identified: (1) $\tau > t_{\text{exch}}$ where τ is determined by the mass transport by diffusion within the measurement chamber itself; (2) $\tau \sim \tau_{\text{exch}}$ where τ is determined by the duration of the analyte exchange process; and (3) $\tau < \tau_{\text{exch}}$ where τ is determined by the dissociation rate constant k_{off}. (b) Performance using time-controlled analyte exchange by diffusion for a sensor with parameters described in Table 4.2. Left: τ/τ_D as a function of t_{exch}/τ_D. For small t_{exch}/τ_D (where $\tau > t_{\text{exch}}$), τ is independent of the exchange time since τ is limited by the mass transport after analyte exchange within the measurement chamber (reaction and diffusion, see Figures 4.13a,b and Figure 4.14). For large t_{exch}/τ_D (where $\tau < t_{\text{exch}}$), τ is independent of the exchange time since the assay can be considered as an infinite-volume assay. When $\tau \sim t_{\text{exch}}$, τ is strongly determined by the duration of the analyte exchange t_{exch}. The dashed black line represents $\tau = t_{\text{exch}}$. Right: CV_C as a function of t_{exch}/τ_D. For small t_{exch}/τ_D (where $\tau > t_{\text{exch}}$), CV_C depends on the amount of exchanged analyte molecules where an increasing t_{exch} results in a decreasing CV_C where $CV_C \propto \sqrt[4]{t_{\text{exch}}}$ (dashed black line, see Box 4.6). For large t_{exch}/τ_D (where $\tau < t_{\text{exch}}$), CV_C is independent of t_{exch} since the assay can be considered as an infinite-volume assay. When $\tau \sim t_{\text{exch}}$, CV_C depends more strongly on t_{exch} due to an increased molar flux J_a, where $CV_C \propto \sqrt{t_{\text{exch}}}$ (dashed black line, see Box 4.6). The black arrows on the x-axis indicate the value for $t_{\text{exch}}/\tau_D = 1$ used in Figure 4.14. (c) Performance using time-controlled analyte exchange by advection with τ/τ_A and CV_C as a function of t_{exch}/τ_A. Left: τ/τ_A as a function of t_{exch}/τ_A. The shape of the graph is similar to panel b, left, though shifted to higher values of t_{exch}/τ_A which depends on the flow rate used for analyte exchange. Besides, small t_{exch}/τ_A yield $\tau/\tau_A \neq 1$ due to an additional diffusion time penalty caused by the mass transport within the measurement chamber, during and after analyte exchange. The dashed black line represents $\tau = t_{\text{exch}}$. Right: For small t_{exch}/τ_A (where $\tau > t_{\text{exch}}$), CV_C is roughly independent of t_{exch} since the analyte exchange by advection includes an outlet where analyte molecules are lost, in contrast to analyte exchange by diffusion. Therefore the minimum CV_C which can be reached theoretically by analyte exchange by advection (dashed black line, see Box 4.7) is much lower than the observed CV_C. For large t_{exch}/τ_A (where $\tau < t_{\text{exch}}$), CV_C is independent of t_{exch} since the assay can be considered as an infinite-volume assay. No values for $t_{\text{exch}}/\tau_A < 0$ are shown for analyte exchange by advection, since in this regime positional dependency strongly influences τ and CV_C. The black arrows on the x-axis indicate the value for $t_{\text{exch}}/\tau_A = 1$ used in Figure 4.13 and Figure 4.3c

time of several hours[27,28]), which implies that $C_{b,0} > C_{a,0}$ and $C_{b,0} > K_d$, and therefore the effective volumetric binder concentration dominates the time-to-equilibrium of the reaction.

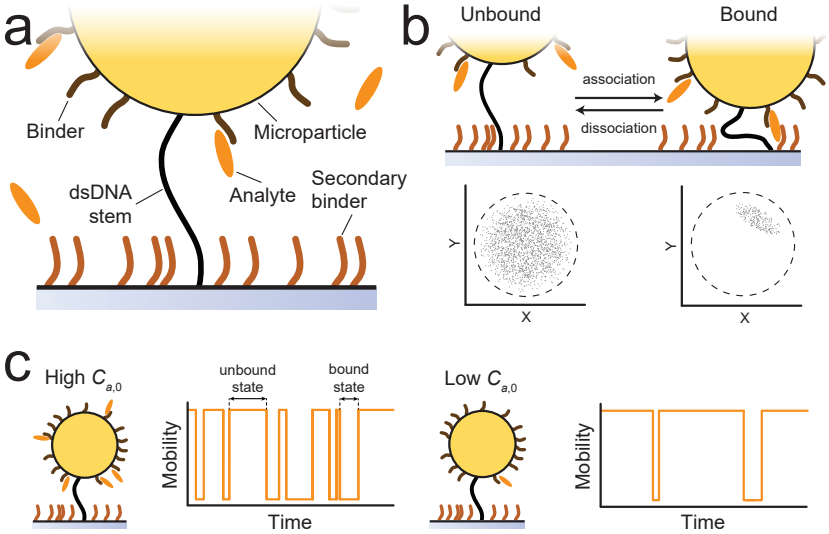

Figure 4.16: measurement principle of biosensing by particle mobility (bpm). (a) Micrometer-sized particles (yellow) are tethered to a substrate using a dsDNA stem (black). The particle is functionalized with ssDNA binder molecules (brown) and the planar surface with ssDNA secondary binder molecules (light brown). Both binders can reversibly bind to single ssDNA analyte molecules (orange) present in solution. (b) Analyte molecules binding to the binder molecules on the particle and subsequently the secondary binder molecules on the planar surface cause the particle to exhibit distinct Brownian motion patterns, *i.e.*, the projection of the center of the particle onto the xy-plane, corresponding to an unbound state (high mobility) or a bound state (low mobility). (c) Digital binding and unbinding events are identified by following the mobility of the particles over time. The time between two events corresponds to either the unbound state lifetime, or the bound state lifetime. For a high or low target concentration in solution, the microparticle shows a high or a low switching frequency respectively.

4.6.8 *Precision of biosensing by particle mobility with time-controlled analyte exchange*

The results of BPM measurements with time-controlled analyte exchange are given in Figure 4.17. Figure 4.17a shows the measured activity per measurement block of 5 minutes as a function of time for multiple consecutive measurement cycles (bottom). At the start of each cycle (see vertical gray lines), the measurement chamber was filled with a solution containing analyte concentration $C_{a,0} = 200$ pM (middle) and a varying supplemented binder concentration $C_{b,\text{suppl}}$ (top). The data show that the time-to-equilibrium is shorter in a condition with high supplemented binder concentration. Values for the time-to-equilibrium τ and for the signal change ΔS were obtained from fits to the data in Figure 4.17a. The fitted values for τ and ΔS are plotted in Figure 4.7b and discussed in this chapter.

In the remainder of this section we focus on the question to what extent the precision of the BPM sensor is limited by Poisson statistics

(*cf.* Figures 4.9-4.10). We quantify the total variation observed in a measurement and calculate the variation induced by the measurement itself. Using this approach, we can estimate the variation caused by other sources than the measurement and compare this to the variation caused by the discrete number of analyte-binder complexes on the particles, *i. e.*, the Poisson-limited variation.

Figure 4.17b shows a zoom-in of the measurement cycle where $C_{b,\text{suppl}} = 10$ nM (top) and the distribution of the observed activity when the reaction is in equilibrium (bottom). The activity as a function of time is shown with a moving average, with a time window T_w of 1 s, of which the observed variation of the activity equals $\sigma_{\text{obs}} = 3$ mHz. The activity as a function of time is fitted by a single exponential of the form given in Box 4.1 (top, dashed line), from which the time-to-equilibrium τ and ΔS were extracted (see Figure 4.7b). The distribution of the observed activity is fitted with a normal distribution from which the mean activity μ_A and σ_{obs} are extracted.

Figure 4.17c shows σ_{obs} as a function of T_w for the first cycle ($C_{b,\text{suppl}} =$ 50 nM, brown) and the second cycle ($C_{b,\text{suppl}} = 10$ nM, orange). Increasing the time window T_w, results in a smaller σ_{obs} since the calculated activity is averaged over more time data points. The observed variation in the activity depends on the variation induced by the measurement and by other sources of variation:

$$\sigma_{\text{obs}}^2 = \sigma_{\text{meas}}^2 + \sigma_{\text{other}}^2 \tag{4.13}$$

where $\sigma_{\text{meas}}^2 = \sigma_{\text{ref}}/\sqrt{T_w}$, with σ_{meas} being the measurement induced variation, σ_{ref} a reference variation which is taken as the measurement induced variation at $T_w = 1$ s, T_w the time window of the moving average of the activity as a function of time, and σ_{other} the variation from a different source than the measurement itself, *e. g.*, a discrete number of analyte-binder complexes or variations in surface chemistry. If the precision of a sensor is Poisson-limited, σ_{other} equals σ_{Poisson}, where σ_{Poisson} is the variation caused by the discrete number of observed analyte-binder complexes within the signal collection area. For a BPM measurement, the number of observed analyte-binder complexes can be calculated by:

$$N_{ab}^{\text{obs}} = \gamma_{ab}^{\text{eff}} A_s \epsilon_p^{\text{obs}} \tag{4.14}$$

with γ_{ab}^{eff} being the effective analyte-binder complex density, A_s the

signal collection area and ϵ_p^{obs} the observed fraction of the particle area. In a BPM measurement with 1 µm particles, only approximately 2% of the particle surface contributes to the observed signal,[29] which results in $\epsilon_p^{\text{obs}} = 0.02$. γ_{ab}^{eff} can be calculated by:

$$\gamma_{ab}^{\text{eff}} = f_a^{\text{eff}} f_{\text{end}} \Gamma_b \tag{4.15}$$

with $f_a^{\text{eff}} = \Gamma_b / (HC_{b,\text{suppl}} + \Gamma_b)$ being the effective fraction of the total analyte molecules captured by the binders on the surface, and f_{end} the fractional occupancy of all binder molecules by analyte molecules at the end of a measurement cycle for a given analyte concentration $C_{a,0}$. Note that f_a^{eff} can be larger than 1 when multiple consecutive cycles have been measured: for the first cycle, $f_a^{\text{eff}} = \Gamma_b / (HC_{b,\text{suppl},1} + \Gamma_b)$, while for the second cycle, $f_a^{\text{eff}} = \Gamma_b / (HC_{b,\text{suppl},1} + \Gamma_b) + \Gamma_b / (HC_{b,\text{suppl},2} + \Gamma_b)$. Using standard parameter values from Table 4.2, $f_{\text{end}} = 10^{-2}$ (extrapolated from Figure 4.8a at $C_{a,0} = 200$ pM), and a signal collection area of $A_s = 1$ mm², it can be found that $\sigma^*_{\text{Poisson}} = \sqrt{N_{ab}^{\text{obs}}} = 1.0 \cdot 10^2$ for the first cycle (where $C_{b,\text{suppl}} = 50$ nM) and that $\sigma^*_{\text{Poisson}} = 2.3 \cdot 10^2$ for the second cycle (where $C_{b,\text{suppl}} = 10$ nM). Assuming a Poisson-limited sensor, the variation in the observed activity equals $\sigma_{\text{Poisson}} = CV_{\text{Poisson}} \mu_A$ where $CV_{\text{Poisson}} = \sigma^*_{\text{Poisson}} / N_{ab}^{\text{obs}}$ is the coefficient of variation in the observed number of analyte-binder complexes and μ_A the mean observed activity at equilibrium (see panel a). This gives $CV_{\text{Poisson}} = 9.6 \cdot 10^{-3}$ and therefore $\sigma_{\text{Poisson}} = 0.18$ mHz for the first incubation cycle (where $C_{b,\text{suppl}} = 50$ nM), and $CV_{\text{Poisson}} = 4.4 \cdot 10^{-3}$ and therefore $\sigma_{\text{Poisson}} = 0.18$ mHz for the second incubation cycle (where $C_{b,\text{suppl}} = 10$ nM).

The dashed lines in Figure 4.17c represent fits according to Equation 4.13. By taking the limit $T_w \to \infty$, σ_{obs} equals σ_{other}. At the first cycle with $C_{b,\text{suppl}} = 50$ nM, σ_{other} was found to be equal to $\sigma_{\text{other}} = 0.09 \pm 0.02$ mHz, while at the second cycle with $C_{b,\text{suppl}} = 10$ nM, $\sigma_{\text{other}} = 0.21 \pm 0.03$ mHz. Comparing these values to the previously quantified σ_{Poisson}, one can conclude that $\sigma_{\text{other}} \cong \sigma_{\text{Poisson}}$, which indicates that the precision in the BPM measurement is Poisson-limited. Therefore, the precision of the BPM measurements is determined by the fundamental limit of stochastic fluctuations in the number of analyte-binder complexes, and can be compared to the results given in Figures 4.8-4.10.

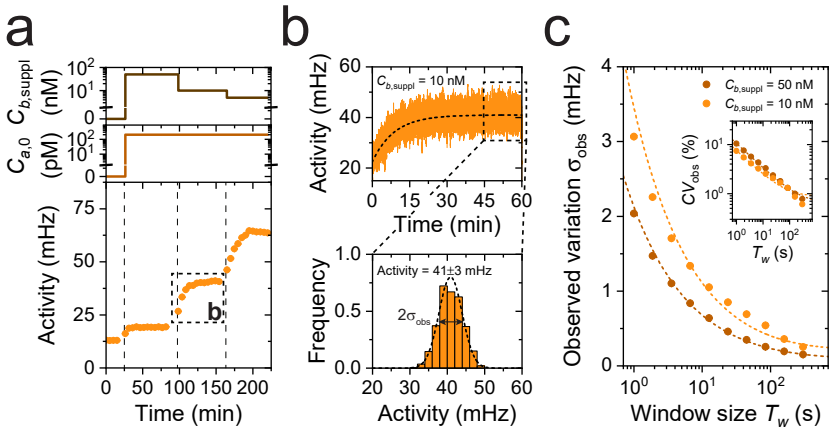

FIGURE 4.17: PRECISION OF BIOSENSING BY PARTICLE MOBILITY (BPM) MEASUREMENTS WITH TIME-CONTROLLED ANALYTE EXCHANGE. (a) Response of a BPM sensor with time-controlled analyte exchange. Activity per measurement of 5 minutes as a function of time for multiple consecutive measurement cycles (orange). At the start of each cycle (vertical lines), $C_{a,0}$ was set to 200 pM (light brown) and a varying supplemented binder concentration $C_{b,\text{suppl}}$ was added (dark brown). (b) Top: zoom-in of the activity as a function of time calculated by a moving average with time window $T_w = 1$ s, for $C_{b,\text{suppl}} = 10$ nM (see panel a). The dashed line shows a single-exponential fit ($S_{\text{init}} + \Delta S \cdot \exp(-t/\tau)$, see Supplementary note 4.6.2), from which the time-to-equilibrium $\tau = 474 \pm 2$ s and the signal change $\Delta S = 19.02 \pm 0.05$ mHz could be determined (see Figure 4.7). Bottom: distribution of the observed activity at equilibrium ($t > 45$ min). The dashed line is a fitted normal distribution with a mean activity μ_A and an observed variation σ_{obs}. (c) Observed variation σ_{obs} as a function of T_w for the first cycle ($C_{b,\text{suppl}} = 50$ nM, brown) and second cycle ($C_{b,\text{suppl}} = 10$ nM, orange). The dashed lines give the fit of the data according to Equation 4.13. For $T_w \to \infty$, the observed variation σ_{obs} approaches the variation induced by other sources than the measurement itself σ_{other}, which equals $\sigma_{\text{other}} = 0.09 \pm 0.02$ mHz for $C_{b,\text{suppl}} = 50$ nM and $\sigma_{\text{obs}} = 0.21 \pm 0.03$ mHz for $C_{b,\text{suppl}} = 10$ nM. The inset shows the same data, with the coefficient of variation CV_{obs} as a function of T_w. For $T_w \to \infty$, it was found that $CV_{\text{obs}} = (7 \pm 2) \cdot 10^{-3}$ for $C_{b,\text{suppl}} = 50$ nM and $CV_{\text{obs}} = (9 \pm 1) \cdot 10^{-3}$ for $C_{b,\text{suppl}} = 10$ nM. The errors reported in panel a are stochastic errors (smaller than the symbol size). The reported errors in panel c and the caption of panel c, are fitting errors based on a 68% confidence interval (smaller than the symbol size).

4.6.9 *The influence of the analyte size on the sensor performance*

Consider a sensor with standard parameter values given in Table 4.2, then $\frac{C_{b,0}}{C_{a,0}} = \Gamma_b/(HC_{a,0}) = 5 \cdot 10^4$, indicating a condition of binder-excess. Here, we consider three analyte exchange methods: instantaneous exchange, analyte exchange by longitudinal advection, analyte exchange by transverse diffusion. We compare two analyte sizes: small analyte molecules, such as ions and small molecules (~0.1-1 nm, MW up to ~1 kDa) and large analyte molecules, such as antibodies and virions (~10-100 nm, MW between 100 kDa and 100 MDa).

Instantaneous analyte exchange (as in Figures 4.3a,b):

For small analyte molecules with $D = 10^{-9}$ m² s⁻¹, $Da = 0.2$, the kinetics are reaction-limited ($\tau/\tau_R \sim 1$) and the time-to-equilibrium

equals $\tau = 200$ s (3 min). For large analyte molecules with $D = 10^{-11}$ m² s⁻¹, $Da = 20$, the kinetics are diffusion-limited ($\tau/\tau_R \sim 8$) and the time-to-equilibrium equals $\tau = 1,600$ s (30 min).

Analyte exchange by longitudinal advection (as in Figure 4.3c):

Preferably the sensor is designed with an analyte exchange process that hardly contributes to the time-to-equilibrium. For small analyte molecules with $Da = 0.2$, no influence is observed at $Pe_L > 10^0 \rightarrow Q >$ 10 µL min⁻¹. For large analyte molecules with $Da = 20$, no influence is observed at $Pe_L > 10^1 \rightarrow Q > 1$ µL min⁻¹.

Analyte exchange by transverse diffusion (as in Figure 4.14):

According to Figure 4.14, for small analyte molecules the analyte exchange process does not influence the time-to-equilibrium for $\tau/\tau_R \sim 1 \rightarrow \tau = 200$ s (3 min) while for large molecular complexes $\tau/\tau_R \sim 20 \rightarrow \tau = 4,000$ s (60 min). Large analyte molecules cause a longer time-to-equilibrium due to diffusion limitations (see Figures 4.3a,b and 4.14). The kinetics can be improved by decreasing the measurement chamber height (see Figure 4.3a). With $H = 20$ µm, large analyte molecules give $\tau_D = 40$ s, achieving a 100 times improvement in kinetics.

Precision of the concentration reading using instantaneous analyte exchange (as in Figure 4.10):

Assume a sensor with a small height $H = 20$ µm. The height decrease from 200 µm to 20 µm gives an improvement in kinetics, but also a decrease in precision (Figure 4.10a and Figure 4.10b, left). For small analyte molecules, the sensor with small height would result in $CV_C =$ 1% and for large analyte molecules $CV_C = 3\%$ where the precision strongly depends on f_{init}. For $f_{\text{init}} = 10^{-3}$, $CV_C = 10\%$ and $CV_C =$ 100% for small and large analyte molecules respectively. The precision can be improved by decreasing the binder density Γ_b (see Figure 4.10b, right), but this will also cause an increase in the time-to-equilibrium.

4.7 REFERENCES

1. Buszko, M., Nita-Lazar, A., Park, J.-H., Schwartzberg, P. L., Verthelyi, D., Young, H. A. & Rosenberg, A. S. Lessons Learned: New Insights on the Role of Cytokines in COVID-19. *Nature Immunology* **22,** 404–411 (2021).
2. Fajgenbaum, D. C. & June, C. H. Cytokine Storm. *New England Journal of Medicine* **383,** 2255–2273 (2020).
3. Duffy, D. Standardized Immunomonitoring: Separating the Signals from the Noise. *Trends in Biotechnology* **36,** 1107–1115 (2018).
4. Chen, P., Huang, N.-T., Chung, M.-T., Cornell, T. T. & Kurabayashi, K. Label-Free Cytokine Micro- and Nano-Biosensing towards Personalized Medicine of Systemic Inflammatory Disorders. *Advanced Drug Delivery Reviews* **95,** 90–103 (2015).
5. Young, A. T., Rivera, K. R., Erb, P. D. & Daniele, M. A. Monitoring of Microphysiological Systems: Integrating Sensors and Real-Time Data Analysis toward Autonomous Decision-Making. *ACS Sensors* **4,** 1454–1464 (2019).
6. Zhang, Y. S. *et al.* Multisensor-Integrated Organs-on-Chips Platform for Automated and Continual in situ Monitoring of Organoid Behaviors. *Proceedings of the National Academy of Sciences* **114,** E2293–E2302 (2017).
7. Heikenfeld, J., Jajack, A., Feldman, B., Granger, S. W., Gaitonde, S., Begtrup, G. & Katchman, B. A. Accessing Analytes in Biofluids for Peripheral Biochemical Monitoring. *Nature Biotechnology* **37,** 407–419 (2019).
8. Kim, J., Campbell, A. S., Esteban-Fernández de Ávila, B. & Wang, J. Wearable Biosensors for Healthcare Monitoring. *Nature Biotechnology* **37,** 389–406 (2019).
9. Heikenfeld, J., Jajack, A., Rogers, J., Gutruf, P., Tian, L., Pan, T., Li, R., Khine, M., Kim, J. & Wang, J. Wearable Sensors: Modalities, Challenges, and Prospects. *Lab on a Chip* **18,** 217–248 (2018).
10. Rodbard, D. Continuous Glucose Monitoring: A Review of Successes, Challenges, and Opportunities. *Diabetes Technology & Therapeutics* **18,** S3–S13 (2016).
11. Li, J., Liang, J. Y., Laken, S. J., Langer, R. & Traverso, G. Clinical Opportunities for Continuous Biosensing and Closed-Loop Therapies. *Trends in Chemistry* **2,** 319–340 (2020).
12. Rawson, T. M. *et al.* Delivering Precision Antimicrobial Therapy through Closed-Loop Control Systems. *Journal of Antimicrobial Chemotherapy* **73,** 835–843 (2018).
13. Mage, P. L., Ferguson, B. S., Maliniak, D., Ploense, K. L, Kippin, T. E. & Soh, H. T. Closed-Loop Control of Circulating Drug Levels in Live Animals. *Nature Biomedical Engineering* **1,** 0070 (2017).
14. Chemmalil, L. *et al.* Online/At-Line Measurement, Analysis and Control of Product Titer and Critical Product Quality Attributes (CQAs) during Process Development. *Biotechnology and Bioengineering* **117,** 3757–3765 (2020).

15. Wasalathanthri, D. P. *et al.* Technology Outlook for Real-Time Quality Attribute and Process Parameter Monitoring in Biopharmaceutical Development — A Review. *Biotechnology and Bioengineering* **117,** 3182–3198 (2020).

16. Randek, J. & Mandenius, C.-F. On-Line Soft Sensing in Upstream Bioprocessing. *Critical Reviews in Biotechnology* **38,** 106–121 (2018).

17. Todd, J., Freese, B., Lu, A., Held, D., Morey, J., Livingston, R. & Goix, P. Ultrasensitive Flow-Based Immunoassays Using Single-Molecule Counting. *Clinical Chemistry* **53,** 1990–1995 (2007).

18. Rissin, D. M. *et al.* Single-Molecule Enzyme-Linked Immunosorbent Assay Detects Serum Proteins at Subfemtomolar Concentrations. *Nature Biotechnology* **28,** 595–599 (2010).

19. Dunbar, S. A. Applications of Luminex® xMAP™ Technology for Rapid, High-Throughput Multiplexed Nucleic Acid Detection. *Clinica Chimica Acta* **363,** 71–82 (2006).

20. Pinheiro, L. B., Coleman, V. A., Hindson, C. M., Herrmann, J., Hindson, B. J., Bhat, S. & Emslie, K. R. Evaluation of a Droplet Digital Polymerase Chain Reaction Format for DNA Copy Number Quantification. *Analytical Chemistry* **84,** 1003–1011 (2012).

21. Schasfoort, R. B. M. *et al. Handbook of Surface Plasmon Resonance: 2nd Edition* (Royal Society of Chemistry., 2017).

22. Schoukroun-Barnes, L. R., Macazo, F. C., Gutierrez, B., Lottermoser, J., Liu, J. & White, R. J. Reagentless, Structure-Switching, Electrochemical Aptamer-Based Sensors. *Annual Review of Analytical Chemistry* **9,** 163–181 (2016).

23. Durmuş, N. G., Lin, R. L., Kozberg, M., Dermici, D., Khademhosseini, A. & Demirci, U. in *Encyclopedia of Microfluidics and Nanofluidics* chap. Acoustic-Based Biosensors (Springer, 2015).

24. Atkins, P. W. & Paula, J. D. *Physical Chemistry for the Life Sciences* (Oxford University Press, 2010).

25. Kamat, V., Rafique, A., Huang, T., Olsen, O. & Olson, W. The Impact of Different Juman IgG Capture Molecules on the Kinetics Analysis of Antibody-Antigen Interaction. *Analytical Biochemistry* **593,** 113580 (2020).

26. Yang, D., Singh, A., Wu, H. & Kroe-Barrett, R. Dataset of the Binding Kinetic Rate Constants of Anti-PCSK9 Antibodies Obtained Using the Biacore T100, ProteOn XPR36, Octet RED384, and IBIS MX96 Biosensor Platforms. *Data in Brief* **8,** 1173–1183 (2016).

27. Bielec, K., Sozanski, K., Seynen, M., Dziekan, Z., Wolde, P. R. T. & Holyst, R. Kinetics and Equilibrium Constants of Oligonucleotides at Low Concentrations. Hybridization and Melting Study. *Physical Chemistry Chemical Physics* **21,** 10798–10807 (2019).

28. Wetmur, J. G. & Davidson, N. Kinetics of Renaturation of DNA. *Journal of Molecular Biology* **31,** 349–370 (1968).

29. Lubken, R. M., de Jong, A. M. & Prins, M. W. J. How Reactivity Variability of Biofunctionalized Particles Is Determined by Superpositional Heterogeneities. *ACS Nano* **15,** 1331–1341 (2021).

30. Poudineh, M. *et al.* A Fluorescence Sandwich Immunoassay for the Real-Time Continuous Detection of Glucose and Insulin in Live Animals. *Nature Biomedical Engineering* **5,** 53–63 (2021).

31. Wilson, B. D. & Soh, H. T. Re-Evaluating the Conventional Wisdom about Binding Assays. *Trends in Biochemical Sciences* **45,** 639–649 (2020).

32. Lin, Y.-T., Vermaas, R., Yan, J., de Jong, A. M. & Prins, M. W. J. Click-Coupling to Electrostatically Grafted Polymers Greatly Improves the Stability of a Continuous Monitoring Sensor with Single-Molecule Resolution. *ACS Sensors* **6,** 1980–1986 (2021).

33. Martens, K. J. A., Bader, A. N., Baas, S., Rieger, B. & Hohlbein, J. Phasor based Single-Molecule Localization Microscopy in 3D (pSMLM-3D): An Algorithm for MHz Localization Rates Using Standard CPUs. *The Journal of Chemical Physics* **148,** 123311 (2018).

34. Bergkamp, M. H., van IJzendoorn, L. J. & Prins, M. W. J. Real-Time Detection of State Transitions in Stochastic Signals from Biological Systems. *ACS Omega* **6,** 17726–17733 (2021).

35. Squires, T. M., Messinger, R. J. & Manalis, S. R. Making It Stick: Convection, Reaction and Diffusion in Surface-Based Biosensors. *Nature Biotechnology* **26,** 417–426 (2008).

36. Kwon, T. & Chun, J. ON/OFF Switchable Nanocomposite Membranes for Separations. *Polymers* **12,** 2415 (2020).

37. Visser, E. W. A., Yan, J., van IJzendoorn, L. J. & Prins, M. W. J. Continuous Biomarker Monitoring by Particle Mobility Sensing with Single Molecule Resolution. *Nature Communications* **9,** 2541 (2018).

38. Yan, J., van Smeden, L., Merkx, M., Zijlstra, P. & Prins, M. W. J. Continuous Small-Molecule Monitoring with a Digital Single-Particle Switch. *ACS Sensors* **5,** 1168–1176 (2020).

39. Lubken, R. M., de Jong, A. M. & Prins, M. W. J. Multiplexed Continuous Biosensing by Single-Molecule Encoded Nanoswitches. *Nano Letters* **4,** 2296–2302 (2020).

5

REAL TIME MONITORING OF BIOMOLECULES: DYNAMIC RESPONSE LIMITS OF AFFINITY-BASED SENSORS

ABSTRACT: Sensors for the monitoring of biomolecular dynamics in biological systems and biotechnological processes in real time, need to accurately and precisely reconstruct concentration-time profiles. This requirement becomes challenging when transport processes and biochemical kinetics are important, as is typically the case for biomarkers at low concentrations. Here, we present a comprehensive methodology to study the concentration-time profiles generated by affinity-based sensors that continuously interact with a biological system of interest. Simulations are performed for sensors with diffusion-based sampling (*e. g.*, a sensor patch on the skin) and advection-based sampling (*e. g.*, a sensor connected to a catheter). The simulations clarify how transport processes and molecular binding kinetics result in concentration gradients and time delays in the sensor system. Using these simulations, measured and true concentration-time profiles of insulin were compared as a function of sensor design parameters. The results lead to guidelines how biomolecular monitoring sensors can be designed for optimal bioanalytical performance in terms of concentration and time properties.

Parts of this chapter have been published as: Lubken, R. M. *et al.* Real Time Monitoring of Biomolecules: Dynamic Response Limits of Affinity-Based Sensors. *ACS Sensors.* Accepted for publication (2021).

5.1 INTRODUCTION

Biological systems and biotechnological processes exhibit time-dependencies that are imposed by dynamic changes of constituting biomolecules, such as nutrients, hormones, proteins, and nucleic acids. To study dynamic processes in real time, monitoring sensors that can reveal biomolecular concentration-time profiles are needed, in order to support fundamental research,[1–7] patient monitoring,[8–14] and closed-loop control applications.[15–21] Such monitoring sensors should be able to reconstruct concentration-time profiles accurately and precisely, both in concentration and in time, and the sensors should be suitable for measuring a wide variety of molecular markers.

The developments in biomolecular monitoring have mainly been focused on measuring high-concentration metabolites, such as glucose and lactate.[8,12,13] Due to their small size and high concentrations, the transport and detection of these biomolecules is fast. However, in case of biomolecular markers at lower concentrations, less molecules are available and transport limitations become important.[22] Furthermore, biochemical reactions are slow at low concentrations,[23] generating time delays in the sensors and time-related errors in the concentration results.

To understand and predict how real time monitoring of biomolecules is limited by dynamic processes, we present a comprehensive methodology for studying affinity-based sensors that continuously interact with a time-dependent system of interest. Here, concentration changes, which are present in a system of interest, propagate into a monitoring sensor by diffusion-based sampling or advection-based sampling. We focus on sensing by biochemical affinity between binder molecules and analyte molecules, since this is a very generic molecular mechanism for achieving specific and sensitive measurements. Frequency-dependent simulations are presented in order to clarify how concentration gradients and time delays are caused by mass transport processes and molecular binding kinetics. The results lead to relationships between on the one hand sensor design parameters and on the other hand measurable concentration change rates, time delays and concentration errors. This will help researchers to design biomolecular sensors for optimal bioanalytical performance in terms of concentration and time properties.

5.2 BIOMOLECULAR MONITORING WITH CONTINUOUS ANALYTE EXCHANGE

The conceptual layout of the monitoring arrangement is sketched in Figure 5.1 with continuous analyte exchange between a biological or biotechnological system of interest and a measurement chamber. The system of interest exhibits dynamic changes of analyte concentration where the sensing aim is to achieve minimal differences between the true concentration-time profile $C_{a,0}(t)$ and the measured concentration-time profile $C^m_{a,0}(t)$. The basic modelling approach is to study analyte concentrations that vary with a sinusoidal time dependence around a mean concentration value:

$$C(t) = C + \frac{\Delta C}{2} \sin(2\pi f t + \phi) \tag{5.1}$$

with $C(t)$ being the oscillating concentration-time profile, C the mean concentration, ΔC the top-to-top amplitude of concentration change, f the oscillation frequency, and ϕ the phase. In the analysis, the concentration change ΔC is a small perturbation on the mean value C (a few percent). The advantage of studying sinusoidal functions is that concentration-time profiles of arbitrary shape can be reconstructed by frequency decomposition, as will be discussed later in this chapter. Concentration symbols with subscript 'a' refer to analyte concentrations: the analyte concentration-time profile in the system of interest is denoted by $C_{a,0}(t)$, at the sensor surface by $C_a(t)$, and the measured analyte concentration-time profile by $C^m_{a,0}(t)$. From the simulations in this chapter, it will become apparent that the response of the monitoring system resembles a low-pass filter: at low frequencies, the measured and true concentration-time profiles are close to each other; however, at frequencies higher than a cutoff frequency f_c, the measured concentration-time profile deviates from the true concentration-time profile, visible in the concentration change ΔC and in the lag time Δt that follows from to the phase lag ϕ.

The measurement chamber is assumed to be rectangular with height H, width W, and length L (see Figure 5.2a). The bottom surface of the measurement chamber is a sensor surface with affinity binder molecules (brown), where association and dissociation of the analyte molecules (orange) occur. The association and dissociation rates depend on the association rate constant k_{on}, the dissociation rate constant k_{off}, the binder surface density Γ_b, the analyte concentration-time profile $C_a(t)$ at the sensor surface, and the surface density of analyte-binder complexes γ_{ab}. Analyte molecules binding to binder molecules on the

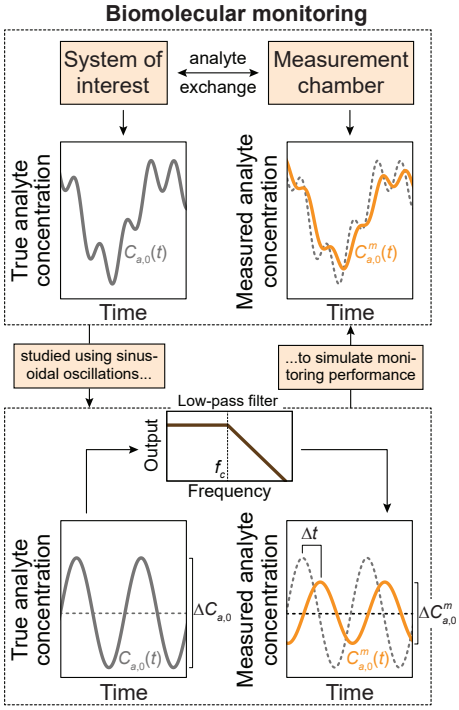

FIGURE 5.1: CONCEPTUAL LAYOUT OF A BIOMOLECULAR MONITORING SYSTEM WITH CONTINUOUS ANALYTE EXCHANGE. Biomolecular monitoring system with continuous analyte exchange between a system of interest and a measurement chamber, where the system of interest exhibits a dynamic concentration-time profile $C_{a,0}(t)$ (gray line) which results in a measured concentration-time profile $C^m_{a,0}(t)$ (orange line). Ideally, the measured concentration-time profile closely resembles the true concentration-time profile (dashed line vs. solid line). The monitoring system can be mimicked by a low-pass filter with a cutoff frequency f_c. The system of interest supplies an oscillating concentration-time profile $C_{a,0}(t)$ with concentration change $\Delta C_{a,0}$, which leads to a measured concentration $C^m_{a,0}(t)$ with concentration change $\Delta C^m_{a,0}$. A comparison of the true and measured concentration-time profiles (dashed line vs. solid line) gives the system response in terms of the concentration change ratios and lag time Δt.

sensor surface, cause γ_{ab} to change as a function of time, resulting in a time-dependent signal which relates to the oscillating analyte concentration $C_{a,0}(t)$ in the system of interest (see Supplementary note 5.6.1).

We study two modes of continuous analyte exchange, namely, analyte exchange by diffusion only (top sketch) and analyte exchange by advection as well as diffusion (bottom sketch). Diffusion-based sampling applies to a sensor that is worn on the skin or that is fully embedded in a bioreactor, for example.[8–10] Advection-based sampling applies to a sensor that is connected to a patient via a catheter or that is connected to a bioreactor via a sampling line.[19–21] In case of diffusion-based sampling, a net molecular flux J_a is caused by a concentration difference (orange gradient), facilitating mass transport between the system of interest and the measurement chamber. In case of advection-based sampling, a laminar flow with flow rate Q facilitates mass transport between the system of interest and the measurement chamber. In the simulations, it is assumed that diffusion occurs in both the longitudinal (x-direction) and the lateral direction (y-direction) and scales with the diffusion coefficient D. In case of advective exchange, the diffusive transport is superposed onto the advective transport caused

by a flow, of which the transport scales with the mean flow velocity v_m, and thus the flow rate Q. In this chapter, different design parameters will be studied which lead to different monitoring performances, as exemplified in Figure 5.2b.

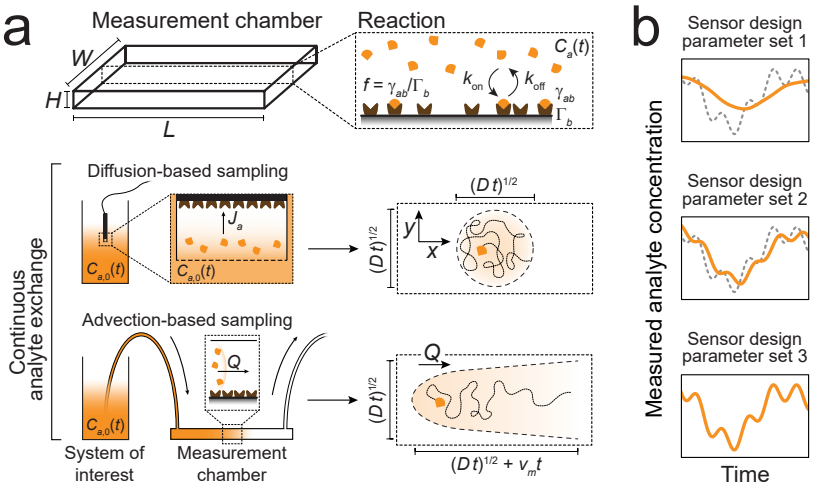

Figure 5.2: Transport and reaction processes influencing monitoring performance of a biomolecular monitoring system. (a) Geometry of the measurement chamber with height H, width W, and length L. The signal of the sensor is generated by an affinity reaction at the sensor surface, where analyte molecules (orange) associate with and dissociate from binder molecules (brown), of which the reaction rates are described by the association rate constant k_{on}, the dissociation rate constant k_{off}, the binder density Γ_b, the concentration-time profile $C_a(t)$ at the sensor surface, and the analyte-binder complex density γ_{ab}. Two modes of continuous analyte exchange are studied: analyte exchange by diffusion (top) and by advection (bottom). In the measurement chamber, mass transport by diffusion occurs in both x- and y-direction, caused by a concentration gradient (orange gradient) that results in a net molecular flux J_a which scales with the diffusion coefficient D. Mass transport by advection occurs in the x-direction only, caused by a flow with mean flow velocity v_m and flow rate Q. (b) Examples of how the monitoring performance can differ for different sensor design parameter sets.

Biomolecular monitoring applications differ widely in the analyte molecules that need to be measured, their concentrations, and their concentration change rates. Figure 5.3 sketches an overview of analyte concentrations in blood (in M) and typical concentration change rates (CCRs, in M h^{-1}) for biomedical monitoring applications such as diabetes (glucose and insulin),[12,13] organ failure (*e. g.*, creatinine)[24,25] and inflammation (*e. g.*, CRP, PCT, cytokines).[1–3,26,27] The CCRs were calculated by estimating characteristic concentration changes $\Delta C_{a,0}$ and typical fluctuation times t_{fluc} (see Supplementary note 5.6.2). For example, blood glucose concentrations vary between 4 and 8 mM in healthy persons, while for diabetic patients the glucose level can increase to 10-15 mM and higher within a period of $t_{\text{fluc}} \sim 30$ min. This results in a typical maximum CCR of about 20 mM h^{-1}. At the low end of the

concentration scale, cytokine biomarker interleukin-6 (IL-6) is indicated. Physiological IL-6 concentrations are below 0.5 pM, while for patients with acute inflammatory stress, *e. g.*, due to sepsis or due to cytokine release syndrome, the IL-6 concentration can increase to 10-100 pM and higher within a period of a few hours (t_{fluc} ~ 2 hours). This results in a typical maximum CCR of about 30 pM h^{-1}.

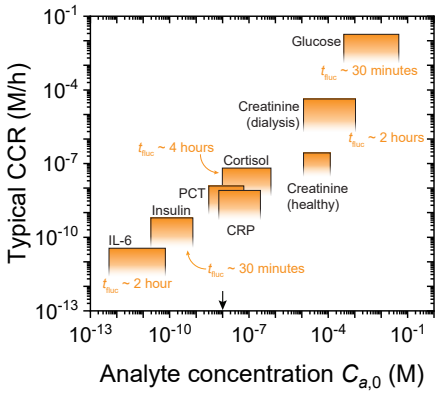

FIGURE 5.3: TYPICAL CONCENTRATION CHANGE RATES (CCRS) AND MEAN ANALYTE CONCENTRATIONS $C_{a,0}$ FOR VARIOUS ANALYTE MOLECULES IN BLOOD PLASMA. CCRs were calculated by estimating a characteristic concentration change $\Delta C_{a,0}$ and a corresponding characteristic fluctuation time t_{fluc} (see Supplementary note 5.6.2), based on reported concentration-time profiles in blood plasma. Abbreviations: IL-6 (interleukin-6), PCT (procalcitonin), and CRP (C-reactive protein). The black arrow indicates the standard parameter value for the mean analyte concentration $C_{a,0}$ as listed in Table 5.1.

In this chapter, the dynamic response of sensors with different designs is characterized by two parameters: first, the lag time Δt of the sensor signal with respect to the input concentration (see Figure 5.1), and second, the rate sensitivity, *i. e.*, the minimum CCR that can be measured with an error of 10% (see Supplementary note 5.6.5). We refer to this minimum CCR as the limit of quantification of CCR (LoCCR). In the next sections, we study how design parameters influence the lag time and rate sensitivity using standard parameter values as listed in Table 5.1. The sensor signal and its time characteristics are quantified by finite-element simulations in order to investigate the consequences of mass transport and reactions at the sensor surface. The rate sensitivity is quantified by calculating the stochastic variabilities in the number of analyte-binder complexes, for concentration-time profiles with varying concentration levels and CCRs.

5.3 RESULTS AND DISCUSSION

5.3.1 *Response of a monitoring system with diffusion-based sampling*

First we consider the case where the transport of analyte molecules between a system of interest and a sensor measurement chamber is governed by diffusion only. Figures 5.4 and 5.5 show how the analyte concentration at the sensor surface and the analyte-binder complex

TABLE 5.1: Standard parameter values used in the finite-element simulations. Details on the simulations are described in Supplementary note 5.6.1.

	Parameter	Value	Description
Input parameter	H	100 µm	Measurement chamber height
	L	1 cm	Measurement chamber length
	W	2 mm	Measurement chamber width
	D	10^{-10} m^2 s^{-1}	Diffusion coefficient of the analyte molecule
	Q	120 µL min^{-1}	Flow rate
	k_{off}	10^{-2} s^{-1}	Dissociation rate constant
	k_{on}	10^6 M^{-1} s^{-1}	Association rate constant
	$C_{a,0}$	10 nM	Mean analyte concentration in the system of interest
Derived parameter	$\lambda = L/H$	100	Aspect ratio of measurement chamber
	$\tau_D = H^2/D$	100 s	Characteristic diffusion time
	$\tau_A = HLW/Q$	1 s	Characteristic advection time
	$\tau_R = (k_{\text{on}} C_{a,0} + k_{\text{off}})^{-1}$	50 s	Characteristic reaction time
	$K_d = k_{\text{off}}/k_{\text{on}}$	10 nM	Equilibrium dissociation constant
	$\Delta C_{a,0}/K_d$	0.05 (5%)	Concentration change
	$Da = \frac{\tau_D}{\tau_R} = \frac{(k_{\text{on}} C_{a,0} + k_{\text{off}})H^2}{D}$	2	Damköhler number
	$Pe_L = \frac{\tau_D}{\tau_A} = \frac{Q}{\lambda DW}$	100	Longitudinal Péclet number

density respond to an oscillating concentration $C_{a,0}(t)$ in the system of interest with concentration change $\Delta C_{a,0}$, for various oscillation frequencies. Figure 5.4a shows how diffusive mass transport influences the concentration profile $C_a(t)$ at the sensor surface, by quantifying the concentration change ΔC_a at the sensor surface (top, orange line, normalized to $\Delta C_{a,0}$), and the lag time Δt (bottom, orange line, normalized to the diffusion time τ_D), given as a function of f (normalized to the diffusion time τ_D). In the top graph, for small f, the concentration change ratio $\Delta C_a/\Delta C_{a,0}$ is close to unity indicating that the concentration change at the sensor surface is approximately equal to the concentration change in the system of interest. Since the oscillation time $1/f$ is larger than τ_D, the analyte molecules are evenly distributed throughout the measurement chamber, *i. e.*, there is no concentration gradient. For large f, $\Delta C_a/\Delta C_{a,0}$ decreases for increasing f, which means that the concentration change at the sensor surface is smaller than the concentration change in the system of interest. Since $1/f$ is now smaller than τ_D, a concentration gradient is present in the measurement chamber in the direction of H (see top sketch). This gradient results

in dispersion of analyte molecules, which effectively reduces ΔC_a. A characteristic parameter to describe this decrease in $\Delta C_a/\Delta C_{a,0}$ is the cutoff frequency f_c, which is the frequency at which $\Delta C_a/\Delta C_{a,0} = 0.5$ (horizontal dotted black line). In this case the diffusion-induced cutoff frequency f_c^D is equal to $f_c^D \tau_D \cong 0.65$ (vertical dotted black line). The bottom graph shows that for f smaller than f_c^D, the observed lag time Δt is independent of f, since within a period of $1/f$ analyte molecules can be transported throughout the measurement chamber by diffusion. This results in a homogeneous analyte concentration in the measurement chamber where Δt is only determined by diffusion ($\Delta t \sim \tau_D$). For f larger than f_c^D, a concentration gradient is present in the measurement chamber in the direction of H (see top sketch). Now Δt decreases according to $\Delta t \propto 1/\sqrt{f}$ (dashed black line, see Supplementary note 5.6.3), concomitant with a reduction in ΔC_a (top graph). The inset shows the phase lag $\Delta\phi$ as a function of f. For increasing f, the absolute phase lag increases ($\Delta\phi$ becomes more negative) due to the time needed for transport of analyte molecules from the top of the measurement chamber to the sensor surface. For large f, the concentration at the sensor surface can lag multiple cycles ($\Delta\phi > 2\pi$) with respect to the concentration in the system of interest (not shown here).

Figure 5.4b shows how association and dissociation of analyte molecules to binder molecules influence the measured signal. Mass transport effects are neglected and the concentration profile $C_a(t)$ at the sensor surface oscillates with a frequency f. The top graph shows the change in analyte-binder complex density $\Delta\gamma_{ab}$, normalized to the expected analyte-binder complex density change $\Delta\gamma_{ab}^{\text{exp}}$ based on the concentration profile $C_a(t)$ at the sensor surface (see Supplementary note 5.6.4). The bottom graph shows the lag time Δt as a function of the frequency f (normalized to the reaction time τ_R). For small f, $\Delta\gamma_{ab}/\Delta\gamma_{ab}^{\text{exp}}$ is close to unity, indicating that the affinity reaction reaches equilibrium, since the oscillation time $1/f$ is larger than the reaction time τ_R (see Table 5.1). For large f, $\Delta\gamma_{ab}/\Delta\gamma_{ab}^{\text{exp}}$ decreases indicating that less analyte molecules bind to binder molecules on the sensor surface than expected based on $C_a(t)$ under equilibrium conditions. This results in a reaction-induced cutoff frequency f_c^R, at $f_c^R \tau_R \cong 0.27$ (vertical dotted black line). For f smaller than f_c^R, Δt is largely independent of f. Now equilibrium is reached, causing the lag time to be determined by the time to equilibrium, *i. e.*, Δt is reaction-limited ($\Delta t \sim \tau_R$). For f larger than f_c^R, Δt depends on f as $\Delta t \propto 1/f$ (dashed black line, see Supplementary note 5.6.3). The inset shows the phase lag $\Delta\phi$ as a function of f. For increasing f, the absolute phase lag increases ($\Delta\phi$ becomes more negative) since less analyte-binder complexes are formed within

a time $1/f$. For large f, the phase lag reaches a minimum value of $\Delta\phi = -\pi/2$ (horizontal black dotted line) with respect to γ_{ab}^{exp} since the reaction rates are directly related to the analyte concentration C_a at the sensor surface and therefore the phase lag cannot be more negative (see Supplementary note 5.6.3).

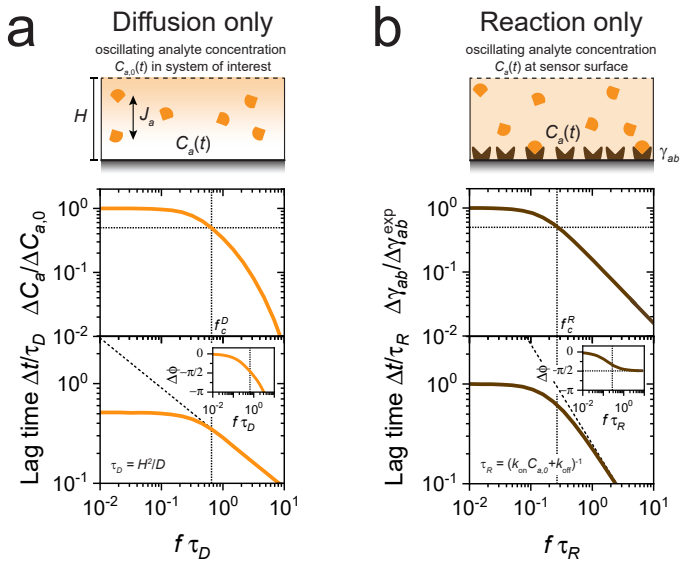

Figure 5.4: Frequency response of a biomolecular monitoring system with continuous analyte exchange by diffusion-based sampling. (a) Frequency response when only diffusion is considered. Top graph: concentration change ΔC_a at the sensor surface (normalized to the concentration change $\Delta C_{a,0}$ in the system of interest) as a function of the frequency f (normalized to the diffusion time τ_D). The diffusion-induced cutoff frequency f_c^D (horizontal dotted black line), is $f_c^D \tau_D \cong 0.65$ (vertical dotted black line). Bottom graph: lag time Δt (normalized to the diffusion time τ_D) as a function of f (normalized to the diffusion time τ_D). For large f, Δt scales as $\Delta t \propto 1/\sqrt{f}$ (dashed black line, see Supplementary note 5.6.3). The inset shows the phase lag $\Delta\phi$ as a function of f. The sketch above the graphs visualizes a measurement chamber with a concentration flux J_a caused by a concentration gradient (orange gradient). (b) Frequency response when only the surface reaction is considered. Top graph: analyte-binder complex density change $\Delta\gamma_{ab}$ (normalized to the expected analyte-binder complex density change $\Delta\gamma_{ab}^{\text{exp}}$, see Supplementary note 5.6.4), as a function of f (normalized to the reaction time τ_R). The reaction-induced cutoff frequency f_c^R is $f_c^R \tau_D \cong 0.27$ (vertical dotted black line). Bottom graph: lag time Δt (normalized to the reaction time τ_R) as a function of f (normalized to the reaction time τ_R). For large f, Δt scales according to $\Delta t \propto 1/f$ (dashed black line, see Supplementary note 5.6.3). The inset shows the phase lag $\Delta\phi$ as a function of f, where $\Delta\phi$ reaches a maximum negative value (see Supplementary note 5.6.3). The sketch above the graphs visualizes a measurement chamber with an oscillating concentration $C_a(t)$ at the sensor surface and a resulting oscillating analyte-binder complex density γ_{ab}.

Figure 5.5 shows the cutoff frequency f_c as a function of the measurement chamber height H (panel a) and the mean analyte concentration $C_{a,0}$ in the system of interest (panel b, normalized to the equilibrium dissociation constant K_d) when both diffusion and reaction processes are considered. Standard values for the chamber height H and mean concentration $C_{a,0}$ are indicated by the black arrows (see Table 5.1). For small H, the diffusion time τ_D is short since analyte molecules

only need to travel a short distance from the top of the measurement chamber to the sensor surface. This causes the observed cutoff frequency f_c to be reaction-limited where $f_c = f_c^R \sim 1/\tau_R$. For large H, analyte molecules need to travel a long distance which causes f_c to be diffusion-limited where $f_c = f_c^D \sim 1/\tau_D$. For small $C_{a,0}$, the reaction is slow since the reaction time τ_R is determined by the dissociation rate, causing f_c to be reaction-limited. For large $C_{a,0}$, τ_R is short since the reaction time τ_R is determined by the association rate, causing f_c to be diffusion-limited. The insets show f_c (normalized to the reaction time τ_R) as a function of the Damköhler number Da (see Table 5.1). Da is a dimensionless parameter describing the relative contribution of reaction and diffusion to the observed time scale (for $Da \gg 1$ diffusion is slow relative to reaction, for $Da \ll 1$ reaction is slow relative to diffusion). For high Da, the cutoff frequency is diffusion-limited, while for low Da, the cutoff frequency is reaction-limited.

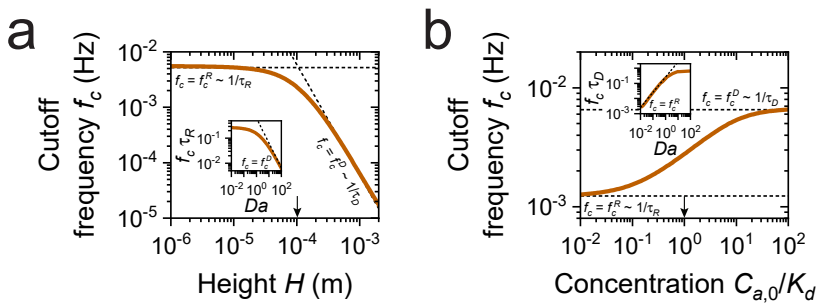

FIGURE 5.5: CUTOFF FREQUENCY OF A BIOMOLECULAR MONITORING SYSTEM WITH CONTINUOUS ANALYTE EXCHANGE BY DIFFUSION-BASED SAMPLING. Cutoff frequency f_c as a function of measurement chamber height H and mean analyte concentration $C_{a,0}$ in the system of interest. (a) For small H, f_c is reaction-limited where $f_c = f_c^R \sim 1/\tau_R$, while for large H, f_c is diffusion-limited with $f_c = f_c^D \sim 1/\tau_D$. The inset shows f_c, normalized to the reaction time τ_R, as a function of Damköhler number Da, with $f_c = f_c^D = \alpha_1/\tau_D$ and $\alpha_1 \cong 0.65$ (dashed black line, *cf.* panel Figure 5.4a). (b) For low $C_{a,0}$, f_c is reaction-limited and $f_c = f_c^R \sim 1/\tau_R$, while for high $C_{a,0}$, f_c is diffusion-limited with $f_c = f_c^D \sim 1/\tau_D$. The inset shows f_c, normalized to the diffusion time τ_D, as a function of Da with $f_c = f_c^R = \alpha_2/\tau_D$ and $\alpha_2 \cong 0.27$ (dashed black line, *cf.* panel Figure 5.4b). Note that using standard parameter values as listed in Table 5.1, the full range of Da cannot be reached by only changing $C_{a,0}$ because τ_R becomes dissociation rate-limited when $C_{a,0} \ll K_d$; therefore k_{off} was varied instead. The black arrows indicate standard parameter values as listed in Table 5.1.

5.3.2 *Response of a monitoring system with advection-based sampling*

Figures 5.6 and 5.7 show how dynamic concentration changes generate signals in a monitoring sensor based on advective sampling, *i. e.*, sampling dominated by flow. Figure 5.6a visualizes how diffusion and advection jointly influence the concentration profile $C_a(t)$ at the sensor surface. The concentration change ΔC_a at the sensor surface (top, orange line, normalized to concentration change $\Delta C_{a,0}$ in the system of

interest) and the lag time Δt (bottom, orange line, normalized to the advection time τ_A) are given as a function of the oscillation frequency f (normalized to τ_A) of the analyte concentration $C_{a,0}$ in the system of interest. Here, a longitudinal Péclet number $Pe_L = \tau_D/\tau_A = 100$ was assumed (see Table 5.1), where Pe_L describes the relative contribution of diffusion and advection to the transport process (for $Pe_L \gg 1$ diffusion is slow relative to advection, for $Pe_L \ll 1$ advection is slow relative to diffusion). In the top graph, for small f, $\Delta C_a/\Delta C_{a,0}$ equals unity indicating that the concentration is evenly distributed throughout the measurement chamber. For large f, $\Delta C_a/\Delta C_{a,0}$ decreases which indicates for a concentration gradient in the measurement chamber perpendicular to the velocity profile. This results in an advection-induced cutoff frequency f_c^A (horizontal dotted black line) which can be found at $f_c^A \tau_A \cong 0.39$ (vertical dotted black line). Note that the advection-induced cutoff frequency roughly equals $f_c^A = 100 \cdot f_c^D$ since $Pe_L = 100$, where f_c^D is the cutoff frequency for a monitoring system with diffusion-based sampling (*cf.* Figure 5.5). In the bottom graph, for small f, the observed lag time Δt of the concentration at the sensor surface compared to the concentration in the system of interest, is largely independent of f since the analyte concentration is homogeneous in the measurement chamber, causing the lag time to be advection-limited ($\Delta t \sim \tau_A$). For f larger than f_c^A, a concentration gradient is present in the measurement chamber, causing a loss in ΔC_a due to dispersion of the analyte molecules. Here, Δt depends less on the frequency f ($\Delta t \propto 1/\sqrt[3]{f}$, dashed black line) compared to Figure 5.4, since the observed time lag is caused by both advection and diffusion, where the contribution of advection is independent of f (see Supplementary note 5.6.3). Furthermore, diffusion occurs on a length scale smaller than H, reducing its contribution to the frequency-dependency. The inset shows the same data visualized as the phase lag $\Delta\phi$ as a function of f. For increasing f, the absolute phase lag increases ($\Delta\phi$ becomes more negative) due to the time needed to transport analyte molecules from the bulk of the measurement chamber to the sensor surface. For large f, $C_a(t)$ can lag for multiple cycles with respect to $C_{a,0}(t)$ (not shown here), though ΔC_a decreases sharply due to dispersion for $f > f_c^A$ (see top graph).

Figure 5.6b visualizes the cutoff frequency f_c as a function of the flow rate Q measured at two positions, namely in the bulk of the measurement chamber (position 1, dark brown line) and at the surface of the measurement chamber (position 2, orange line). The black arrow indicates the standard parameter value for Q as listed in Table 5.1. The inset shows the same data with f_c (normalized to τ_A) as a function of Pe_L. For small Q, there is a concentration gradient in the longitudinal

direction since the distance over which molecules need to diffuse to the sensor surface is smaller compared to the situation in Figures 5.4 and 5.5. This results in an advection-limiting process at $Pe_L < 1$ with a constant f_c. For increasing Q, the observed f_c becomes different when measuring in the bulk or at the sensor surface. For measuring in the bulk, an increased Q results in a change of the shape of the concentration gradient, namely perpendicular to the velocity profile (top sketch, dashed black profile) instead of in the longitudinal direction. The flow rate where f_c becomes advection-limited depends on the measurement chamber geometry: for a small L, f_c is advection-limited at small flow rates since the distance over which molecules need to be transported is small. For measuring at the sensor surface, the stationary layer becomes smaller for increasing Q effectively decreasing the distance over which the molecules need to diffuse to the sensor surface. This effect results in f_c scaling with the advection time less than $1/\tau_A$ (see main graph, dashed black lines) and that the normalized cutoff frequency f_c decreases (see inset).

Figure 5.7 visualizes the cutoff frequency f_c as a function of the flow rate Q (panel a) and the mean analyte concentration $C_{a,0}$ in the system of interest (panel b), where diffusion, advection and reaction are included. Standard values for the flow rate Q and mean concentration $C_{a,0}$ are indicated by the black arrows (see Table 5.1). In the top graph, for a low Q, the cutoff frequency is advection-limited, where $f_c = f_c^A \sim 1/\tau_A$. For large Q, the cutoff frequency is limited by a combination of diffusion and reaction. The inset shows the same data with f_c (normalized to the advection time τ_A) as a function of Pe_L. In the bottom graph, for low $C_{a,0}$, the reaction is slow which causes the observed cutoff frequency f_c to be dissociation rate-limited where $f_c = f_c^R \sim k_{\text{off}}$. For large $C_{a,0}$, the reaction is association rate-limited where $f_c = f_c^R \sim k_{\text{on}} C_{a,0}$. The inset shows the same data with f_c (normalized to the diffusion time τ_D) as a function of Damköhler number Da. For small Da, the cutoff frequency is reaction-limited (dashed black line). For large Da, the cutoff frequency becomes diffusion-limited.

5.3.3 *Continuous biomolecular monitoring for arbitrary concentration profiles*

The measured concentration profile of a monitoring sensor should resemble as closely as possible the true concentration profile of the analyte. While Figures 5.4-5.7 discussed the effects of diffusion, advection and reaction on the cutoff frequency and lag time, the question remains how these processes influence an actual concentration profile and the differences between the measured and the true concentration

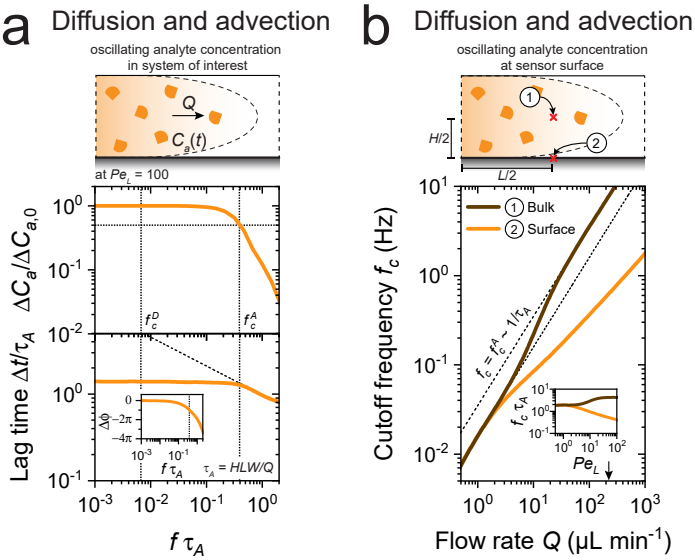

FIGURE 5.6: FREQUENCY RESPONSE OF A BIOMOLECULAR MONITORING SYSTEM WITH CONTINUOUS ANALYTE EXCHANGE BY ADVECTION-BASED SAMPLING. (a) Frequency response when only diffusion and advection are considered, for an advection dominated sensor geometry with $Pe_L = 100$ (see Table 5.1). Top graph: concentration change ΔC_a at the sensor surface, normalized to the concentration change $\Delta C_{a,0}$ in the system of interest, as a function of the frequency f (normalized to the advection time τ_A), measured at the sensor surface at distance $L/2$ from the inlet (see also the sketch in panel b). The diffusion-induced cutoff frequency f_c^D is taken from Figure 5.4a, and the advection-induced cutoff frequency f_c^A is found to be $f_c^A \tau_A \cong 0.39$ (vertical dotted black line) and roughly equals $f_c^A = 100 \cdot f_c^D$. Bottom graph: lag time Δt, normalized to τ_A, as a function of the frequency f, normalized to τ_A. For large f, Δt scales according to $\Delta t \propto 1/\sqrt[3]{f}$ (black dashed line). (b) Cutoff frequency as a function of flow rate Q when only diffusion and advection are taken into account, measuring in the middle in the bulk of the measurement chamber at height $H/2$ (dark brown line) and at the sensor surface of the measurement chamber (orange line) both at distance $L/2$ from the inlet. For increasing Q, measuring in the bulk results in an advection-limited cutoff frequency (dashed black lines). The inset shows the same data with the observed cutoff frequency f_c, normalized to the advection time τ_A, as a function of the longitudinal Péclet number Pe_L. For small Pe_L, f_c for both bulk and surface measurements are comparable with $= f_c^D$. For increasing Pe_L, f_c increases due to a higher flow rate, until the system becomes advection-limited. Measuring at the sensor surface results in a weaker dependency on τ_A than $1/\tau_A$.

profiles. Here, we study an insulin concentration profile with standard parameter values listed in Table 5.1 as an example (see Supplementary note 5.6.6). In this chapter, the rate sensitivity is quantified as the Limit of quantification of CCR (LoCCR), *i. e.*, the smallest CCR that can be measured with an error of 10% (see Supplementary note 5.6.5). The LoCCR is calculated assuming a sensor with noise that is dominated by Poisson statistics, with a signal collection area $A_s = 1$ mm², and a binder density $\Gamma_b = 10^{-9}$ mol m^{-2}. Poisson noise represents the fundamental limit of the precision that can be achieved in a biosensor due to stochastic fluctuations in the number of detected analyte molecules.[28,29]

Figures 5.8-5.10 show the collective influence of diffusion, advection, and reaction on the LoCCR and the measured concentration profile, for

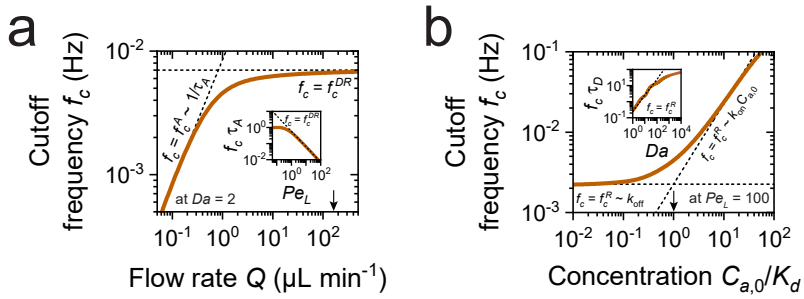

FIGURE 5.7: CUTOFF FREQUENCY OF A BIOMOLECULAR MONITORING SYSTEM WITH CONTINUOUS ANALYTE EXCHANGE BY ADVECTION-BASED SAMPLING. Cutoff frequency f_c as a function of the chamber height H with a fixed chamber length L and mean analyte concentration $C_{a,0}$ in the system of interest for a sensor when diffusion, advection and reaction are taken into account. (a) For small H, f_c is reaction-limited where $f_c = f_c^R \sim 1/\tau_R$, while for large H, f_c is diffusion-limited with $f_c = f_c^D \sim 1/\tau_D$. The inset shows the same data with the cutoff frequency f_c, normalized to the reaction time τ_R, as a function of Damköhler number. (b) For $H = 100$ µm (see Table 5.1), the cutoff frequency is reaction-limited. Therefore, for low $C_{a,0}$, f_c is dissociation rate-limited and $f_c = f_c^R \sim k_{\text{off}}$, while for high $C_{a,0}$, f_c is association rate-limited with $f_c = f_c^R \sim k_{\text{on}} C_{a,0}$. The inset shows the same data with the cutoff frequency f_c, normalized to the diffusion time τ_D, as a function of Damköhler number. f_c becomes diffusion limited at $Da \gg 1$ and reaches a plateau level larger than $f_c \tau_D = 1$ (*cf.* Figure 5.5) since $\tau_D = H^2/D$, while actual distance over which molecules decreases for increasing Q. Note that using the standard parameter values in Table 5.1 the full range of Da cannot be reached by only changing $C_{a,0}$ because τ_R becomes dissociation rate-limited when $C_{a,0} \ll K_d$; therefore the k_{off} was varied instead. The black arrows indicate standard parameter values as listed in Table 5.1.

different measurement chamber heights H (in case of diffusion-based analyte exchange) and for different flow rates Q (in case of advection-based analyte exchange). Figure 5.8 shows the LoCCR as a function of frequency f using standard parameter values as listen in Table 5.1, for diffusion-based sampling (panel a) and advection-based sampling (panel b). Figure 5.8a shows results for measurement chamber heights $H = 200$ µm (dark brown) and $H = 800$ µm (orange). For low f, the LoCCR equals the value found for Poisson noise only (dashed black line, see also Supplementary note 5.6.5), which is due to the fact that the sensor reaches equilibrium and no dispersion occurs (*cf.* Figures 5.4 and 5.5). For increasing f, the results depend on the measurement chamber height because a small H gives a larger cutoff frequency (*cf.* Figure 5.5). Here, both lines deviate from the Poisson-limit, since equilibrium is not reached within a time equal to $1/f$, resulting in fewer analyte-binder complexes. The inset shows the same data with the minimum concentration change $\Delta C_{a,0}$ that can be quantified with an error of less than 10% as a function of frequency f. Figure 5.8b shows advection-based sampling with flow rates $Q = 10$ µL min^{-1} (dark brown) and $Q = 0.1$ µL min^{-1} (orange).[30–32] Here, the lines deviate from the Poisson-limit at higher frequencies compared to diffusion-based sampling, since the cutoff frequency is higher in advection-based sampling compared to diffusion-based sampling (see Figures 5.5 and 5.7). The inset shows the same data with the minimum concentration

change $\Delta C_{a,0}$ that can be quantified with an error of less than 10% as a function of frequency f.

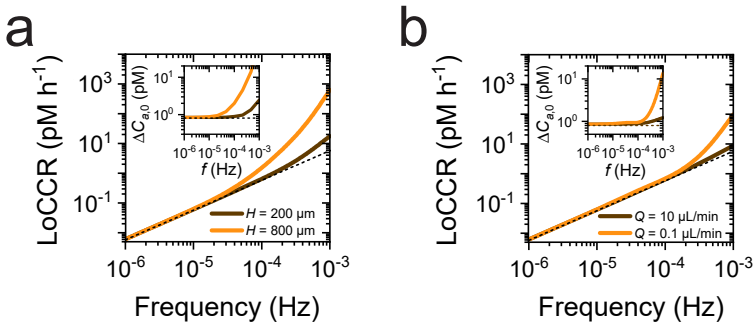

Figure 5.8: limit of quantification of ccr (loccr) of the monitoring system using two modes of continuous analyte exchange. LoCCR as a function of frequency f in a monitoring system with continuous analyte exchange by diffusion-based sampling (panel a) and by advection-based sampling (panel b). The insets show the same data with the concentration change $\Delta C_{a,0}$ as a function of f. For low f, the precision of the CCR is limited by Poisson noise (dashed black line). For increasing f, the lines start to deviate since the frequencies become higher than the corresponding cutoff frequencies.

Figure 5.9a shows a typical insulin profile (dotted black line) and corresponding measured insulin profiles, using diffusion-based analyte exchange and the standard parameter values listed in Table 5.1. The bottom graphs show the frequency spectrum of the true and measured insulin profiles plotted as CCR components (see Supplementary note 5.6.2). For $H = 200$ µm (brown line), the measured concentration profile is almost identical to the true concentration profile, since the cutoff frequency $f_c = 9 \cdot 10^{-4}$ Hz (see Figure 5.5a) is higher than the frequencies present in the true insulin profile (see bottom graphs, left). For $H = 800$ µm (orange line), the true concentration profile cannot be accurately reconstructed, only the general up-and-down trend at a 6-hour interval, since the cutoff frequency $f_c = 1 \cdot 10^{-4}$ Hz (see Figure 5.5a) is close to the frequencies in the insulin profile (see bottom graphs, right). Also, the average lag time Δt of the measured signal is smaller for $H = 200$ µm than for $H = 800$ µm, since a smaller distance requires less time for diffusion.

Figure 5.9b shows the results for advection-based analyte exchange, for flow rates $Q = 10$ µL min^{-1} (dark brown) and $Q = 0.1$ µL min^{-1} (orange). In both cases the measured insulin profile is similar to the true insulin profile, since the cutoff frequencies are $f_c = 7 \cdot 10^{-3}$ Hz and $f_c = 8 \cdot 10^{-4}$ Hz respectively (see Figure 5.7a). The strong similarities are also visible in the frequency spectrum (bottom panel).

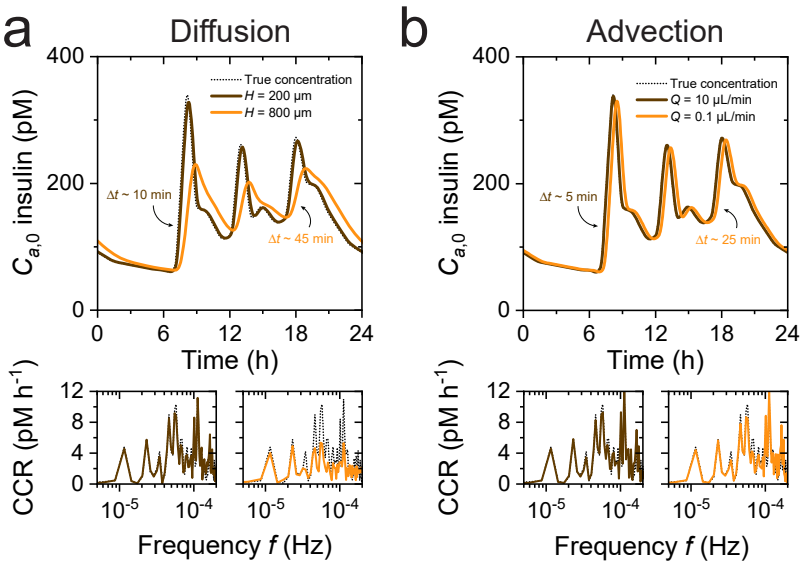

FIGURE 5.9: MEASURING CONCENTRATION-TIME PROFILES USING TWO MODES OF CONTINUOUS ANALYTE EXCHANGE. (a) Concentration-time profiles for a measurement chamber height $H = 200$ µm (brown line) and $H = 800$ µm (orange line), and the true analyte concentration (black dotted line), for diffusion-based analyte exchange. The bottom graphs show the frequency spectrum with the CCR component as a function of frequency. For small H, the concentration profile closely resembles the true concentration profile. However, for large H, the similarity is only visible at low frequencies; at high frequencies, the measured CCR is close to 0, indicating that sinusoidal components with these frequencies are not present in the measured signal. (b) Concentration-time profiles for a measurement chamber with flow rate $Q = 10$ µL min^{-1} (brown line) and $Q = 0.1$ µL min^{-1} (orange line), and the true analyte concentration (black dotted line, behind the brown line), for advection-based analyte exchange. The bottom shows the frequency spectrum. For both flow rates, the concentration profile closely resembles the true concentration profile.

Figure 5.10 investigates the limits of dynamic monitoring when affinity binders with very high affinity are used, *i. e.*, binders with a very low dissociation rate constant ($k_{\text{off}} = 10^{-3}$ s^{-1}), which is relevant to study when low-concentration analytes need to be measured. Figure 5.10a shows simulation results for diffusion-based sampling. The data show that the lower dissociation rate constant causes a lower cutoff frequency, a longer lag time, and a higher LoCCR (see Supplementary note 5.6.5). The reversibility of the sensor is worse, particularly for a large measurement chamber height ($H = 800$ µm) because the large volume of the measurement chamber contains many analyte molecules. Figure 5.10b shows results for advection-based sampling. The flow rate increases the rate of exchange of the large volume above the sensor surface. A flow rate as low as 0.1 µL min^{-1} already significantly improves the dynamic performance of the sensor. A flow rate of 10 µL min^{-1} gives small differences between the measured and real concentrations with a lag time that is very close to $1/k_{\text{off}} = 1/(10^{-3}\ \text{s}^{-1}) = 17$ min.

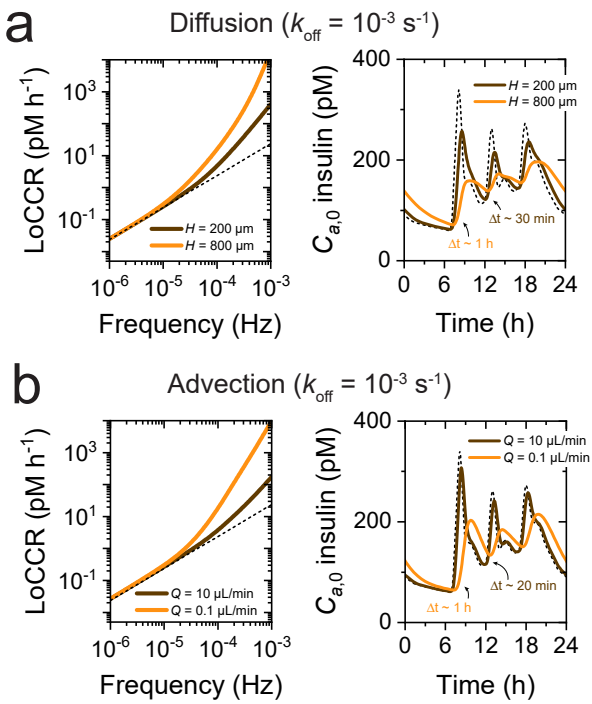

Figure 5.10: measuring concentration profiles with high-affinity binders using two modes of continuous analyte exchange. LoCCR as a function of f and corresponding concentration profiles for diffusion-based analyte exchange (panel a) and advection-based analyte exchange (panel b), where $k_{off} = 10^{-3}$ s^{-1} (compared to $k_{off} = 10^{-2}$ s^{-1}. Due to higher cutoff frequencies, the similarity of the measured concentration profiles is less compared to Figure 5.9.

5.4 conclusion

To measure in real time the dynamic changes of biomolecular concentrations in biological systems or biotechnological processes, monitoring sensors are required that reveal reliable concentration-time profiles. We have studied the influence of sensor design parameters on the differences between the true and the measured concentration-time profile, focusing on the lag time of the sensor signal with respect to the input concentration, and on the rate sensitivity. To quantify a rate sensitivity, we introduced the concept of concentration change rate (CCR), which is expressed in the units molar per second. The CCR that needs to be resolved differs strongly between different biomolecular monitoring applications, due to their respective concentration changes and fluctuation times (see Figure 5.3). The limit of the measurable CCR was evaluated as the limit of quantification of the CCR (LoCCR), *i.e.*, the lowest CCR that can be quantified with a precision of 10%.

In this chapter, we have presented a comprehensive methodology to

study the properties and limitations of dynamic measurements using affinity-based sensors, as these represent a very generic and broad class of bioanalytical measurement techniques. Analyte exchange was considered between the system of interest and the sensor by diffusive as well as advective sampling. Finite-element simulations were used to describe the spatial and temporal dependency of analyte concentration within the measurement chamber. Sinusoidal concentration-time profiles were studied as well as arbitrary concentration-time profiles by frequency decomposition. Using this approach, the effects were studied of mass transport and biochemical kinetics on the speed of concentration change, time delays, and concentration errors in the sensing system.

The study of sensor performance was exemplified for insulin monitoring. The results show that diffusion-based sampling performs equal to advection-based sampling in reconstructing the concentration-time profile for small heights of the measurement chamber (< 200 µm). However, for larger heights, diffusion-based sampling causes an increased lag time and decreased rate sensitivity. A monitoring system with advection-based sampling performs similarly with respect to the rate sensitivity for flow rates down to ~0.1 µL min^{-1}, while the lag time is larger for low flow rates.

For low-concentration biomolecules, less molecules are available for detection and therefore continuous monitoring sensors with a single-molecule resolution are useful, because these sensors can have Poisson-limited noise levels and therefore a high detection sensitivity. In case of binder molecules with a high affinity ($k_{off} = 10^{-3}$ s^{-1}), the analytical performance deteriorates for diffusion-based sampling, but not for advection-based sampling with flow rates of 10 µL min^{-1} and higher, allowing the measurement of all CCR components present in an insulin concentration-time profile.

The results and learnings presented in this chapter can assist researchers to identify the most important processes influencing the performance of continuous monitoring sensors. Insight in the individual and combined influence of analyte diffusivity, analyte concentration, binder affinity, sampling method, measurement chamber geometry, and flow speed on the observed lag time and rate sensitivity of the measured concentration-time profile, will help researchers to develop monitoring systems with desirable sensor characteristics for a diverse range of biomarkers and applications.

5.5 METHODS

FINITE-ELEMENT ANALYSIS: Finite-element simulations were performed by solving diffusion, advection and reaction equations simultaneously using COMSOL (COMSOL Multiphysics 5.5) and MATLAB (MATLAB R2019a, COMSOL Multiphysics LiveLink for MATLAB) (see Supplementary note 5.6.1). The LoCCRs were reported at a distance $L/2$ in the measurement chamber (Figure 5.2a), where the signal was collected over a signal collection area $A_s = 1$ mm² with a binder molecule density $\Gamma_b = 10^{-9}$ mol m^{-2} (see Supplementary note 5.6.5).

FREQUENCY ANALYSIS: The amplitude and the phase lag of the concentration at the sensor surface (Figures 5.4a and 5.6a) and analyte-binder complex density (Figures 5.4b, 5.5 and 5.7) were calculated using the Fourier transform of its density profile. The calculated values were compared to the amplitude and the phase (*i.e.*, $\phi = 0$) of the input concentration profile. The cutoff frequency was determined at the frequency where the observed amplitude was 50% of the input amplitude. The LoCCR was determined according to Supplementary notes 5.6.2 and 5.6.5.

5.6 SUPPLEMENTARY NOTES

5.6.1 *Finite-element simulations*

The simulation study of the time-dependent behavior of the biochemical assay was performed using dimensionless parameters for all mass transport processes and reaction rates.[22,29] The nondimensionalized parameters for mass transport by diffusion and advection are given in Table 5.2.

TABLE 5.2: Dimensionless parameters used in the finite-element analysis for modeling mass transport by diffusion and advection.

Dimensionless parameter	Symbol	Expression
Analyte concentration	$\tilde{c}$	$\tilde{c} = C_a/C_{a,0}$
Longitudinal distance	$\tilde{x}$	$\tilde{x} = x/L$
Transversal distance	$\tilde{y}$	$\tilde{y} = y/H$
Time	$\tilde{t}$	$t = H^2/D \rightarrow \tilde{t} = t\,D/H^2$

For all finite-element analyses, the time was nondimensionalized using the diffusion time τ_D (*e.g.*, Figures 5.4a and 5.5) and thereafter recalculated to normalize with respect to other time scales (*e.g.*, τ_R

in Figures 5.4b and 5.5a). When advective flow is included, the used analytical expression of the advective flow is given by:

$$\vec{v}\,(y) = \frac{6Q}{WH^3} y\,(H-y)\,\vec{e_x} \tag{5.2}$$

with $\vec{v}(y)$ being the flow speed as a function of the height y inside the measurement chamber, Q the flow rate, W the width of the measurement chamber, and H the height of the measurement chamber. The general equation used in the simulation to describe mass transport by advection and diffusion is given by:

$$\frac{\delta C_a}{\delta t} = D\nabla^2 C_a - \vec{v}(y)\cdot\nabla C_a \tag{5.3}$$

with $\frac{\delta C_a}{\delta t}$ being the time-derivative of the (spatial-dependent) analyte concentration C_a and D the diffusion coefficient. The dimensionless form of Equation 5.3 is derived in Box 5.1.

BOX 5.1: Derivation of the dimensionless advection-diffusion equation.

$$\frac{\delta(\tilde{c}C_{a,0})}{\delta\left(\frac{\tilde{t}H^2}{D}\right)} = D\frac{\delta^2(\tilde{c}C_{a,0})}{\delta(\tilde{x}L)^2} + D\frac{\delta^2(\tilde{c}C_{a,0})}{\delta(\tilde{y}H)^2} - \frac{6Q}{WH^3}\tilde{y}H\,(H-\tilde{y}H)\,\frac{\delta(\tilde{c}C_{a,0})}{\delta(\tilde{x}L)}$$

$$\frac{\delta\tilde{c}}{\delta\tilde{t}} = \frac{H^2}{D}\frac{1}{L^2}\,D\frac{\delta^2\tilde{c}}{\delta\tilde{x}^2} + \frac{H^2}{D}\frac{1}{H^2}D\frac{\delta^2\tilde{c}}{\delta\tilde{y}^2} - \frac{H^2}{D}\frac{6Q}{WH^3}\frac{1}{L}\tilde{y}H^2\,(1-\tilde{y})\,\frac{\delta\tilde{c}}{\delta\tilde{x}}$$

$$\boxed{\frac{\delta\tilde{c}}{\delta\tilde{t}} = \frac{H^2}{L^2}\frac{\delta^2\tilde{c}}{\delta\tilde{x}^2} + \frac{\delta^2\tilde{c}}{\delta\tilde{y}^2} - \frac{6QH}{LDW}\tilde{y}\,(1-\tilde{y})\,\frac{\delta\tilde{c}}{\delta\tilde{x}}}$$

Using the derivation given in Box 5.1, measurement chamber aspect ratio $\lambda = L/H$, and longitudinal Péclet number $Pe_L = \frac{Q}{\lambda DW}$ (see Table 5.1), the simplified dimensionless advection-diffusion equation is given by:

$$\frac{\delta\tilde{c}}{\delta\tilde{t}} = \frac{1}{\lambda^2}\frac{\delta^2\tilde{c}}{\delta\tilde{x}^2} + \frac{\delta^2\tilde{c}}{\delta\tilde{y}^2} - 6Pe_L\tilde{y}\,(1-\tilde{y})\,\frac{\delta\tilde{c}}{\delta\tilde{x}} \tag{5.4}$$

The nondimensionalized parameters for the reaction rate are given in Table 5.3.

The general equation used in the simulation to model the reaction at the sensor surface is given by:

TABLE 5.3: Dimensionless parameters used in the finite-element analysis for modeling the reaction at the sensor surface.

Dimensionless parameter	Symbol	Expression
Analyte concentration at the sensor surface	$\tilde{c}^*$	$\tilde{c}^* = C_a^*/C_{a,0}$
Density of analyte-binder complexes	$\tilde{\gamma}$	$\tilde{\gamma} = \gamma_{ab}/(C_{a,0}H)$
Time	$\tilde{t}$	$\tilde{t} = t\,D/H^2$

$$\frac{\delta\gamma_{ab}}{\delta t} = k_{\text{on}}C_a^*\left(\Gamma_b - \gamma_{ab}\right) - k_{\text{off}}\gamma_{ab} \tag{5.5}$$

with $\frac{\delta\gamma_{ab}}{\delta t}$ being the time-derivative of the (spatial-dependent) density γ_{ab} of analyte-binder complexes and C_a^* the analyte concentration at the sensor surface, which is known by solving Equation 5.3. The dimensionless form of Equation 5.5 is derived in Box 5.2.

BOX 5.2: Derivation of the dimensionless reaction rate equation.

$$\frac{\delta(\tilde{\gamma}C_{a,0}H)}{\delta\left(\frac{\tilde{t}H^2}{D}\right)} = k_{\text{on}}\tilde{c}^*C_{a,0}\left(\Gamma_b - \tilde{\gamma}C_{a,0}H\right) - k_{\text{off}}\tilde{\gamma}C_{a,0}H$$

$$\frac{\delta\tilde{\gamma}}{\delta\tilde{t}} = \frac{H^2}{D}\frac{k_{\text{on}}\tilde{c}^*}{H}\left(\Gamma_b - \tilde{\gamma}C_{a,0}H\right) - \frac{H^2}{D}k_{\text{off}}\tilde{\gamma}$$

$$\frac{\delta\tilde{\gamma}}{\delta\tilde{t}} = \frac{k_{\text{on}}\Gamma_b H}{D}\tilde{c}^* - \frac{k_{\text{on}}H}{D}\tilde{c}^*\tilde{\gamma}C_{a,0}H - \frac{H^2}{D}k_{\text{off}}\tilde{\gamma}$$

$$\boxed{\frac{\delta\tilde{\gamma}}{\delta\tilde{t}} = \frac{C_{a,0}H}{\Gamma_b}\frac{k_{on}\Gamma_b H}{D}\left[\tilde{c}^*\left(\frac{\Gamma_b}{C_{a,0}H} - \tilde{\gamma}\right) - \frac{K_d}{C_{a,0}}\tilde{\gamma}\right]}$$

Using the derivation given in Box 5.2 and Damköhler number $Da = \frac{k_{\text{on}}\Gamma_b H}{D}$ (see Table 5.1), the simplified dimensionless reaction rate equation is given by:

$$\frac{\delta\tilde{\gamma}}{\delta\tilde{t}} = \frac{C_{a,0}H}{\Gamma_b}Da\left[\tilde{c}^*\left(\frac{\Gamma_b}{C_{a,0}H} - \tilde{\gamma}\right) - \frac{K_d}{C_{a,0}}\tilde{\gamma}\right] \tag{5.6}$$

The nondimensionalized parameters for the oscillating concentration are given in Table 5.4.

The general equation used in the simulation to describe the oscillating concentration in the system of interest $C_{a,0}$ is given by:

$$C_{a,0}\left(t\right) = C_{a,0} + \frac{\Delta C_{a,0}}{2}\sin\left(2\pi f t + \phi\right) \tag{5.7}$$

TABLE 5.4: Dimensionless parameters used in the finite-element analysis for modeling the oscillating concentration input.

Dimensionless parameter	Symbol	Expression
Analyte concentration in the system of interest	$\tilde{c}_{a,0}$	$\tilde{c}_{a,0} = C_{a,0}(t)/C_{a,0}$
Mean analyte concentration in the system of interest	–	$1 = C_{a,0}/C_{a,0}$
Concentration change	$\Delta\tilde{C}_{a,0}$	$\Delta\tilde{C}_{a,0} = \Delta C_{a,0}/C_{a,0}$
Time	$\tilde{t}$	$\tilde{t} = t\,D/H^2$
Frequency	$\tilde{f}$	$\tilde{f} = fH^2/D$

with $C_{a,0}$ being the mean concentration in the system of interest, $\Delta C_{a,0}$ the concentration change, f the frequency, and ϕ the phase. The outcome of Equation 5.7 forms the boundary condition at the inlet of the measurement chamber when solving Equations 5.4 and 5.6 simultaneously. The dimensionless form of Equation 5.7 is derived in Box 5.3.

BOX 5.3: Derivation of the dimensionless oscillating concentration input.

$$\tilde{c}_{a,0}C_{a,0} = C_{a,0} + \frac{\Delta\tilde{C}_{a,0}C_{a,0}}{2}\sin\left(2\pi\tilde{f}\frac{D}{H^2}\tilde{t}\frac{H^2}{D} + \phi\right)$$

$$\tilde{c}_{a,0} = 1 + \frac{\Delta\tilde{C}_{a,0}}{2}\sin\left(2\pi\tilde{f}\tilde{t} + \phi\right)$$

$$\boxed{\tilde{c}_{a,0} = 1 + \frac{\Delta\tilde{C}_{a,0}}{2}\sin\left(2\pi\tilde{f}\tilde{t} + \phi\right)}$$

5.6.2 *Concentration change rate*

The concentration change rate (CCR) is the change (increase or decrease) in concentration per unit time. From a concentration profile, the CCR can be estimated using a characteristic concentration change $\Delta C_{a,0}$, *i. e.*, the difference between a minimum and a maximum concentration value, and a characteristic fluctuation time t_{fluc}, *i. e.*, the time required to increase from the minimum and maximum concentration value or vice versa (see Figure 5.11):

$$\text{CCR} = \frac{\Delta C_{a,0}}{t_{\text{fluc}}} \tag{5.8}$$

From a sinusoidal concentration profile with amplitude $\Delta C_{a,0}/2$ and

frequency f, the CCR can be calculated using the concentration change $\Delta C_{a,0}$ and the frequency f, where $f = 1/(2 \cdot t_{\text{fluc}})$ (see Figure 5.11b):

$$\text{CCR} = 4\frac{\Delta C_{a,0}}{2} f = 2\Delta C_{a,0} f \tag{5.9}$$

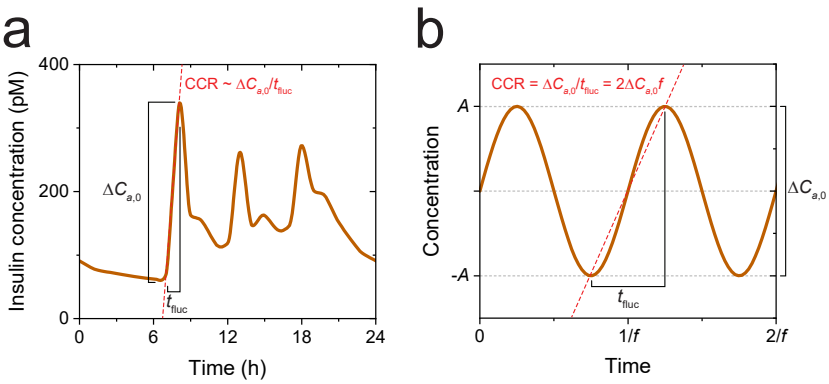

Figure 5.11: Insulin concentration profile and a sinusoidal function with a typical concentration change and a typical fluctuation time. (a) Insulin concentration profile (brown) with a typical concentration change $\Delta C_{a,0}$ and a typical fluctuation time t_{fluc}. The concentration change rate (CCR) can be estimated by CCR ~ $\Delta C_{a,0}/t_{\text{fluc}}$ (red dashed line). (b) Sinusoidal concentration profile with amplitude $\Delta C_{a,0}/2$ and frequency f. The CCR can be calculated by CCR $= \Delta C_{a,0}/t_{\text{fluc}} = 2\Delta C_{a,0} f$ (red dashed line).

The typical CCR for insulin as visualized in Figure 5.3 is higher than can be found in the Fourier spectra in Figure 5.9. The difference here can be explained by the fact that in Figure 5.9, the observed CCR comprises multiple sinusoidal components, which results in a summed observed CCR, and thus a smaller CCR per sinusoidal concentration profile.

5.6.3 *Frequency-dominated lag time*

In Box 5.4 a mathematical derivation is given for the observed lag time Δt of the concentration $C_a(t)$ at the sensor surface using diffusion-based sampling, when Δt is frequency-dominated, for a given oscillating concentration $C_{a,0}(t)$ in the system of interest. For $f > f_c^D$, a concentration gradient in the lateral direction develops with a concentration wavelength λ_C^D.

BOX 5.4: Mathematical derivation of the frequency-dominated lag time Δt for the concentration $C_a(t)$ at the sensor surface using diffusion-based sampling.

When the observed lag time Δt is frequency-dominated, a concentration gradient in the lateral direction exists with a characteristic length scale equal to the concentration wavelength λ_C^D due to diffusion: $\lambda_C^D = \sqrt{D/f}$, where D is the diffusion coefficient and f the frequency. The phase lag $\Delta\phi^D$ of the observed concentration at the sensor surface compared to the concentration at the inlet of the measurement chamber, can be calculated by $\Delta\phi^D = 2\pi H/\lambda_c^D$, while the corresponding lag time $\Delta\tau$ can be calculated by $\Delta t_D = \frac{\Delta\phi^D}{2\pi f} = \frac{H}{f\lambda_C^D}$. This yields $\Delta t_D = H/\sqrt{Df}$. By normalizing Δt and f using the diffusion time scale $\tau_D = H^2/D$, we obtain $\Delta t_D/\tau_D = 1/\sqrt{f\tau_D}$, which results in $\Delta t_D \propto 1/\sqrt{f}$ (see Figure 5.4a).

In Box 5.5 a mathematical derivation is given for the observed lag time Δt of the density γ_{ab} of analyte-binder complexes, when Δt is frequency-dominated, for a given concentration $C_a(t)$ at the sensor surface. For $f > f_c^R$, no equilibrium can be reached resulting in a quasi-equilibrium that is determined by f. When a concentration $C_a(t)$ at the sensor surface is supplied with a high frequency, the observed phase lag $\Delta\phi$ equals $-\pi/2$ (see Figure 5.4b). The density γ_{ab} of analyte-binder complexes cannot lag more than this with respect to the expected density γ_{ab}^{exp} since the association and dissociation rates directly depend on the concentration $C_a(t)$ at the sensor surface and $\gamma_{ab}(t)$:

$$r_a = k_{\text{on}} C_a(t)\,(\Gamma_b - \gamma_{ab}) \text{ and } r_d = k_{\text{on}}\gamma_{ab}(t) \tag{5.10}$$

with r_a being the association rate, k_{on} the association rate constant, Γ_b the binder density, r_d the dissociation rate, and k_{off} the dissociation rate constant. From Equation 5.10 can be concluded that r_a directly responds to a change in $C_a(t)$, while r_d only responds after analyte-binder complexes are formed in the association reaction.

BOX 5.5: Mathematical derivation of the frequency-dominated lag time Δt for the density γ_{ab} of analyte-binder complexes.

In contrast to diffusion, the phase lag $\Delta\phi^R$ of the observed density γ_{ab} of analyte-binder complexes with respect to the expected density γ_{ab}^{exp} of analyte-binder complexes, is independent of frequency for $f > f_C^R$ since $\Delta\phi^R = -\frac{\pi}{2}$ since the association and the dissociation rates depend on the concentration $C_a(t)$ at the sensor surface. The lag time can be calculated by $\Delta t_R = \frac{\Delta\phi^R}{2\pi f}$. This yields $\Delta t_R = \frac{1}{4f}$. By normalizing Δt and f using the reaction time $\tau_R = \frac{1}{k_{\text{on}}C_a + k_{\text{off}}}$, we obtain $\Delta t_R/\tau_R = \frac{1}{4f\tau_R}$, which results in $\Delta t_R \propto 1/f$ (see Figure 5.4b).

In Box 5.6 a mathematical derivation is given for the observed lag time Δt of the concentration $C_a(t)$ at the sensor surface using advection-based sampling, when Δt is frequency-dominated, for a given concentration $C_{a,0}(t)$ in the system of interest. For $f > f_c^A$, a concentration gradient perpendicular to the velocity profile with a concentration wavelength λ_C^A.

BOX 5.6: Mathematical derivation of the frequency-dominated lag time Δt for the concentration $C_a(t)$ at the sensor surface using advection-base sampling.

When the observed lag time Δt is frequency-dominated, an oscillating concentration gradient exists with a characteristic length scale equal to the concentration wavelength λ_C^A due to advection: $\lambda_C^A = \frac{Q}{HWf}$, where D is the diffusion coefficient and f the frequency.

The phase lag $\Delta\phi^A$ of the observed concentration at the sensor surface compared to the concentration at the inlet of the measurement chamber, can be calculated by $\Delta\phi^A = 2\pi L/\lambda_C^A$, while the corresponding lag time $\Delta\tau$ can be calculated by $\Delta t_A = \frac{\Delta\phi^A}{2\pi f} = \frac{HLW}{f\lambda_C^D}$. This yields $\Delta t_A = \frac{HLW}{Q}$ which equals the characteristic advection time. The frequency-dependency is caused by diffusion to the sensor surface, where the characteristic diffusion length is much smaller than measurement chamber height H which results in a less strong dependency of the lag time Δt on the frequency f (compare Figure 5.4a and Figure 5.6a).

5.6.4 *Expected analyte-binder complex density change*

The expected analyte-binder complex density γ_{ab}^{exp} can be calculated for a given analyte concentration $C_a(t)$ at the sensor surface. For this we use the following equation:

$$\gamma_{ab}^{\text{exp}} = \Gamma_b \frac{C_a(t)}{C_a(t) + K_d} \tag{5.11}$$

with Γ_b being the total binder density (assumed to be 10^{-9} mol m^{-2}, *i. e.*, 600 µm^{-2}), $C_a(t)$ the analyte concentration at the sensor surface, and K_d the dissociation constant. When $C_a(t)$ oscillates with a concentration change ΔC_a around a mean concentration C_a, this will result in an oscillating γ_{ab}^{exp} with a density change $\Delta\gamma_{ab}^{\text{exp}}$. For this we use the following equation:

$$\Delta\gamma_{ab}^{\text{exp}} = \Gamma_b \frac{C_a + \Delta C_a/2}{C_a + \Delta C_a/2 + K_d} - \Gamma_b \frac{C_a - \Delta C_a/2}{C_a - \Delta C_a/2 + K_d} \tag{5.12}$$

Under the assumption that $C_a \ll K_d$, $\Delta\gamma_{ab}^{\text{exp}}$ can be calculated by:

$$\Delta\gamma_{ab}^{\text{exp}} \cong \Gamma_b \frac{\Delta C_a}{K_d} \tag{5.13}$$

5.6.5 *Precision of concentration change rate*

To calculate the precision of the monitoring system, we defined a rate sensitivity which is the smallest CCR that can be quantified with an error of 10%. We refer to this minimum CCR as the limit of quantification of CCR (LoCCR). In this chapter, we assume that two concentrations need to be distinguished from each other within a given time span based on a sinusoidal oscillating concentration $C_{a,0}(t)$ with mean concentration $C_{a,0}$, concentration change $\Delta C_{a,0}$, and frequency f. A mathematical derivation of the LoCCR is given in Box 5.7.

BOX 5.7: Mathematical derivation of the sensitivity of the concentration change rate in a biomolecular monitoring system.

The CCR can be calculated by CCR$= 2\Delta C_{a,0} f$ assuming an oscillating concentration with concentration change $\Delta C_{a,0}$ and frequency f. For a given frequency f, the minimum CCR that can be determined precisely is when the coefficient of variation CV_{CCR} of the concentration change rate is smaller than or equal to 10%, *i. e.*, $CV_{\text{CCR}} = CV_{\Delta C_{a,0}} = \frac{\sigma_{\Delta C_{a,0}}}{\Delta C_{a,0}} \leq 10\%$. The error of the concentration change $\sigma_{\Delta C_{a,0}}$ can be calculated by:

$$\sigma^2_{\Delta C_{a,0}} = \left(\sigma_C^{\max}\right)^2 + \left(\sigma_C^{\min}\right)^2 \rightarrow \sigma_{\Delta C_{a,0}} \cong \sqrt{2}\sigma_C$$

with $\sigma_C^{\max}$ and $\sigma_C^{\min}$ being the errors of the maximum and minimum of the oscillating concentration profile respectively. For simplicity, we assume that $\sigma_C^{\max} \cong \sigma_C^{\min} = \sigma_C$ which is true if the precision of the sensor is Poisson-limited and $\Delta C_{a,0}$ is small. The error of the concentration σ_C can be determined using the error of the signal σ_S and the slope of the dose-response curve: $\sigma_C = \frac{\delta C_{a,0}}{\delta S}\sigma_S$ with $\frac{\delta S}{\delta C_{a,0}}$ the concentration-derivative of the signal. The error of the signal σ_S can be determined using the statistical variation $\sigma_{N_{ab}}$ in the number of analyte-binder complexes:

$$\sigma_{N_{ab}} = \sqrt{N_{ab}} \rightarrow \sigma_S = \frac{S}{\sqrt{N_{ab}}}$$

with N_{ab} being the total number of analyte molecules bound to binder molecules that contribute to the signal of the sensor and S is the measured signal. Combining all derivations given above, gives the following expression for the minimum concentration change that can be determined precisely:

$$\Delta C_{a,0} \geq 10 \cdot \sigma_{\Delta C_{a,0}} \rightarrow \Delta C_{a,0} \geq 10\sqrt{2}\,\frac{\delta C_{a,0}}{\delta S}\frac{S}{\sqrt{N_{ab}}}$$

and the LoCCR for a given frequency f using Equation 5.9:

$$\boxed{\text{LoCCR} = 20 f \sqrt{2}\frac{\delta C_{a,0}}{\delta S}\frac{S}{\sqrt{N_{ab}}}}$$

The results of the mathematical derivation of the LoCCR given in Box 5.7, are visualized in Figures 5.12 and 5.13, where the monitoring system was assumed to be in equilibrium ($f \rightarrow 0$), and limited by Poisson noise only.[28] Figure 5.12a shows the normalized signal S as a function of concentration $C_{a,0}$, which directly scales with the fractional

occupancy f of binder molecules by analyte molecules. The normalized signal can be calculated using the following equation, assuming first-order Langmuir kinetics:

$$S = A_B + (1 - A_B)\frac{C_{a,0}}{C_{a,0} + K_d} \tag{5.14}$$

with S being the measured signal, A_B the background signal, $C_{a,0}$ the concentration in the system of interest, and K_d the dissociation constant. Here it was assumed that there is no background signal. The error of the signal is determined by the number of observed analyte-binder complexes on the sensor surface within a signal collection area of $A_s = 1$ mm² with a binder molecule density $\Gamma_b = 10^{-9}$ mol m⁻² (600 µm⁻²). This error of the signal σ_S is determined by the number of observed analyte-binder complexes (see Box 5.7) and therefore increases with an increasing $C_{a,0}$ until saturation is reached where no more surface binders are available for binding analyte molecules (see inset, top). However, the relative error, indicated by the coefficient of variation of the measured signal $CV_S = \sigma_S / S$ (see inset, bottom), decreases for increasing $C_{a,0}$ which results in a more precise signal measurement when high concentrations are supplied to the sensor.

Figure 5.12b shows the coefficient of variation of the measured concentration $CV_C = \sigma_C / C_{a,0}$ as a function of $C_{a,0}$. The inset shows the precision of the concentration σ_C that can be calculated from σ_S (see Box

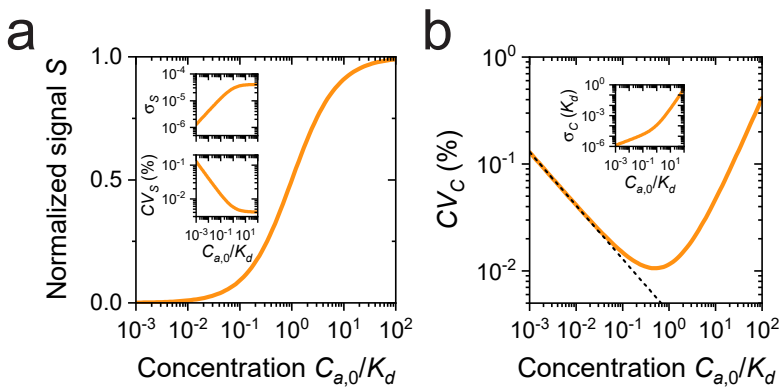

FIGURE 5.12: PRECISION OF THE SIGNAL AND CONCENTRATION IN A MONITORING SYSTEM. (a) Normalized signal S as function of concentration $C_{a,0}$. The insets show the signal error σ_S (top) and the coefficient of variation of the signal CV_S (bottom) as a function of concentration $C_{a,0}$. For low $C_{a,0}$, the signal error is limited by the number of analyte-binder complexes. For high $C_{a,0}$ the signal error is limited by the number of binder molecules. (b) Coefficient of variation of the concentration CV_C as a function of mean concentration $C_{a,0}$. The inset shows the concentration error σ_C as a function of concentration. For low C_a, CV_C is determined Poisson noise (black dashed line). For high $C_{a,0}$, the precision of the concentration is decreasing by saturation of binder molecules by analyte molecules.

5.7). For low concentrations, the precision is Poisson-limited (dashed black line). However, for increasing concentrations, the precision starts to deviate with an increasing CV_C. This effect is caused by saturation effects of the binder molecules on the sensor surface decreasing the precision (*i. e.*, increasing CV_C) of the concentration determination.

Figure 5.13 shows the minimum concentration change $\Delta C_{a,0}$ that can be determined as a function of concentration $C_{a,0}$. The inset shows the corresponding LoCCR (using Equation 5.9) as a function of frequency f, for a given concentration $C_{a,0} = K_d$. The dashed black arrow indicates the concentration as listed in Table 5.1. Here it can be seen that a small $\Delta C_{a,0}$ can be measured at low concentrations since here the absolute σ_C is small. At high concentrations, $\Delta C_{a,0}$ starts to increase steeply due to saturation effects (*cf.* Figure 5.12b). A small CCR can be measured at low frequencies since CCR scales according to CCR $= 2f\Delta C_{a,0}$.

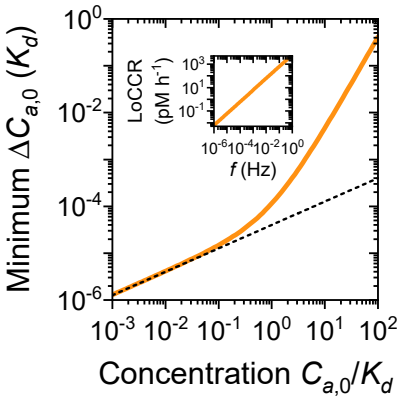

FIGURE 5.13: PRECISION OF THE CCR IN A MONITORING SYSTEM. Minimum concentration change $\Delta C_{a,0}$ that can be determined as a function of mean concentration $C_{a,0}$. For low $C_{a,0}$, the minimum $\Delta C_{a,0}$ is determined by Poisson noise (black dashed line). At high $C_{a,0}$, the minimum $\Delta C_{a,0}$ is increasing by the saturation of binder molecules by analyte molecules. The inset shows the LoCCR as a function of frequency f at a given concentration $C_{a,0} = K_d$.

From simulated data we obtain surface densities, which directly scale with signal, instead of measured concentrations. Therefore, in Figure 5.14 the minimum observed signal change ΔS is visualized as a function of the mean concentration $C_{a,0}$ with three signal changes $\Delta C_{a,0}/K_d = 50\%$, 5%, and 0.5%. The minimum ΔS that can be measured assuming a Poisson-limited sensor, can be estimated by the following equation (*cf.* Box 5.7):

$$\Delta S \geq 10\sqrt{2}\frac{S}{\sqrt{N_{ab}}} \tag{5.15}$$

By determining the intersection (black arrows) of the dashed black line (Poisson-limit) and the orange curves that show the observed signal

change ΔS as a function of the mean concentration $C_{a,0}$ of the oscillating concentration $C_{a,0}(t)$ for a given concentration change $\Delta C_{a,0}$, we can estimate the minimum concentration change that can be determined at a given $C_{a,0}$. When the frequencies are low (f ~ hours, left) the minimum concentration change $\Delta C_{a,0}$ is small at low concentration, but for high frequencies (f ~ minutes, right), only a higher $\Delta C_{a,0}$ can be determined precisely at that same concentration. This results in the LoCCR as visualized in Figures 5.8 and 5.10 using Equation 5.9.

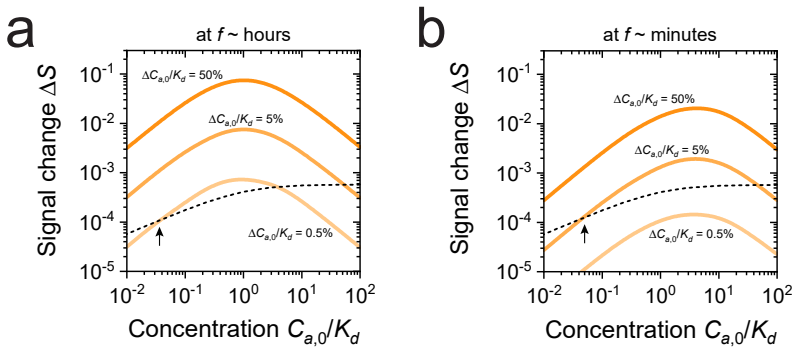

FIGURE 5.14: MINIMUM QUANTIFIABLE CONCENTRATION CHANGE AT A GIVEN FREQUENCY AND MEAN CONCENTRATION OF THE OSCILLATING INPUT CONCENTRATION. Signal change ΔS as a function the mean concentration $C_{a,0}$ of an concentration profile $C_{a,0}(t)$ at a low frequency f (f ~ hours, panel a) and at a high f (f ~ minutes, panel b), for an example monitoring system with three concentration changes $\Delta C_{a,0}$ (orange). The dashed black lines shows the minimum signal change ΔS as determined by Equation 5.15. The intersection (black arrows) gives the minimum concentration change $\Delta C_{a,0}$ which can be determined for a given frequency f and mean concentration $C_{a,0}$.

5.6.6 *Example calculations of insulin monitoring*

Continuous glucose monitoring devices help diabetes patients to control their blood glucose levels.[12,13] Advanced closed-loop systems are available that automatically regulate insulin delivery based on glucose monitoring data.[15] Even better regulations may be enabled by also including continuous monitoring data of blood insulin levels. A typical CCR for insulin is CCR ~ 600 pM h^{-1} with an insulin concentration ranging from 20 to 800 pM (see Figure 5.3). To reconstruct insulin concentration profiles as closely as possible, the LoCCR should be much smaller than 600 pM h^{-1}. Ideally, a monitoring system can measure CCRs over a range of a few decades, for instance CCR ~ 0.6-600 pM h^{-1}. Assuming a sinusoidal concentration profile, CCR $= 2\Delta C_{a,0} f$ and $f = 1/(2 \cdot t_{\text{fluc}})$ ~ $2.8 \cdot 10^{-4}$ mHz (see Supplementary note 5.6.2), typical concentration changes $\Delta C_{a,0}$ that need to be distinguished are 0.3-300 pM, which corresponds to concentration changes of a few percent of the mean insulin concentration.

We consider the standard parameter values as listed in Table 5.1 with a mean insulin concentration of 100 pM. Here we estimate the fastest fluctuation of insulin concentration profile for which the measured concentration profile still closely resembles the true concentration profile.

DIFFUSION-BASED SAMPLING (SEE FIGURES 5.4 AND 5.5): We consider a small measurement chamber height $H = 200$ µm and a large measurement chamber height $H = 800$ µm. The diffusion coefficient of insulin is approximately $D = 10^{-10}$ m² s⁻¹. For small H (200 µm), $\tau_D = 100$ s and $Da \sim 1$ (neither reaction-limited nor diffusion-limited). From Figure 5.5 we obtain a cutoff frequency of $f_c = 2 \cdot 10^{-3}$ Hz. Therefore for $H = 200$ µm, insulin monitoring is reliable for a frequency $f < f_c$, resulting in $t_{\text{fluc}} > 5$ min. For large H (800 µm), $\tau_D = 6400$ s and $Da \sim 64$ (diffusion-limited). From Figure 5.5 we obtain a cutoff frequency of $f_c = 1 \cdot 10^{-4}$ Hz. In this case, insulin monitoring is reliable if $t_{\text{fluc}} > 80$ min.

ADVECTION-BASED SAMPLING (SEE FIGURES 5.6 AND 5.7): Here we consider a high flow rate $Q = 120$ µL min⁻¹ and a low flow rate $Q = 0.1$ µL min⁻¹. For high Q (120 µL min⁻¹), $\tau_A = 1$ s and $Pe_L = 100$ (mass transport process is diffusion-limited). From Figure 5.7 we obtain a cutoff frequency $f_c = 1 \cdot 10^{-2}$ Hz. Accurate insulin monitoring is reliable for $f < f_c$, which results in $t_{\text{fluc}} > 1$ min. For low Q (0.1 µL min⁻¹), $\tau_A = 1200$ s and $Pe_L = 0.08$ (mass transport process is advection-limited). From Figure 5.7 we obtain a cutoff frequency $f_c = 8 \cdot 10^{-4}$ Hz. Now accurate insulin monitoring is reliable for $f < f_c$, which corresponds to $t_{\text{fluc}} > 10$ min.

5.7 REFERENCES

1. Buszko, M., Nita-Lazar, A., Park, J.-H., Schwartzberg, P. L., Verthelyi, D., Young, H. A. & Rosenberg, A. S. Lessons Learned: New Insights on the Role of Cytokines in COVID-19. *Nature Immunology* **22,** 404–411 (2021).
2. Fajgenbaum, D. C. & June, C. H. Cytokine Storm. *New England Journal of Medicine* **383,** 2255–2273 (2020).
3. Yiu, H. H., Graham, A. L. & Stengel, R. F. Dynamics of a Cytokine Storm. *PLOS ONE* **7,** 1–15 (2012).
4. Duffy, D. Standardized Immunomonitoring: Separating the Signals from the Noise. *Trends in Biotechnology* **36,** 1107–1115 (2018).
5. Chen, P., Huang, N.-T., Chung, M.-T., Cornell, T. T. & Kurabayashi, K. Label-Free Cytokine Micro- and Nano-Biosensing towards Personalized Medicine of Systemic Inflammatory Disorders. *Advanced Drug Delivery Reviews* **95,** 90–103 (2015).
6. Young, A. T., Rivera, K. R., Erb, P. D. & Daniele, M. A. Monitoring of Microphysiological Systems: Integrating Sensors and Real-Time Data Analysis toward Autonomous Decision-Making. *ACS Sensors* **4,** 1454–1464 (2019).
7. Zhang, Y. S. *et al.* Multisensor-Integrated Organs-on-Chips Platform for Automated and Continual in situ Monitoring of Organoid Behaviors. *Proceedings of the National Academy of Sciences* **114,** E2293–E2302 (2017).
8. Heikenfeld, J., Jajack, A., Feldman, B., Granger, S. W., Gaitonde, S., Begtrup, G. & Katchman, B. A. Accessing Analytes in Biofluids for Peripheral Biochemical Monitoring. *Nature Biotechnology* **37,** 407–419 (2019).
9. Kim, J., Campbell, A. S., Esteban-Fernández de Ávila, B. & Wang, J. Wearable Biosensors for Healthcare Monitoring. *Nature Biotechnology* **37,** 389–406 (2019).
10. Heikenfeld, J., Jajack, A., Rogers, J., Gutruf, P., Tian, L., Pan, T., Li, R., Khine, M., Kim, J. & Wang, J. Wearable Sensors: Modalities, Challenges, and Prospects. *Lab on a Chip* **18,** 217–248 (2018).
11. Ates, H. C., Brunauer, A., Stetten, F., Urban, G. A., Güder, F., Merkoçi, A., Früh, S. M. & Dincer, C. Integrated Devices for Non-Invasive Diagnostics. *Advanced Functional Materials* **31,** 2010388 (2021).
12. Rodbard, D. Continuous Glucose Monitoring: A Review of Successes, Challenges, and Opportunities. *Diabetes Technology & Therapeutics* **18,** S3–S13 (2016).
13. Klonoff, D. C., Ahn, D. & Drincic, A. Continuous Glucose Monitoring: A Review of the Technology and Clinical Use. *Diabetes Research and Clinical Practice* **133,** 178–192 (2017).
14. Christodouleas, D. C., Kaur, B. & Chorti, P. From Point-of-Care Testing to eHealth Diagnostic Devices (eDiagnostics). *ACS Central Science* **4,** 1600–1616 (2018).

15. Boughton, C. K. & Hovorka, R. New Closed-Loop Insulin Systems. *Diabetologia* **64,** 1007–1015 (2021).

16. Li, J., Liang, J. Y., Laken, S. J., Langer, R. & Traverso, G. Clinical Opportunities for Continuous Biosensing and Closed-Loop Therapies. *Trends in Chemistry* **2,** 319–340 (2020).

17. Rawson, T. M. *et al.* Delivering Precision Antimicrobial Therapy through Closed-Loop Control Systems. *Journal of Antimicrobial Chemotherapy* **73,** 835–843 (2018).

18. Mage, P. L., Ferguson, B. S., Maliniak, D., Ploense, K. L, Kippin, T. E. & Soh, H. T. Closed-Loop Control of Circulating Drug Levels in Live Animals. *Nature Biomedical Engineering* **1,** 0070 (2017).

19. Chemmalil, L. *et al.* Online/At-Line Measurement, Analysis and Control of Product Titer and Critical Product Quality Attributes (CQAs) during Process Development. *Biotechnology and Bioengineering* **117,** 3757–3765 (2020).

20. Wasalathanthri, D. P. *et al.* Technology Outlook for Real-Time Quality Attribute and Process Parameter Monitoring in Biopharmaceutical Development — A Review. *Biotechnology and Bioengineering* **117,** 3182–3198 (2020).

21. Randek, J. & Mandenius, C.-F. On-Line Soft Sensing in Upstream Bioprocessing. *Critical Reviews in Biotechnology* **38,** 106–121 (2018).

22. Squires, T. M., Messinger, R. J. & Manalis, S. R. Making It Stick: Convection, Reaction and Diffusion in Surface-Based Biosensors. *Nature Biotechnology* **26,** 417–426 (2008).

23. Atkins, P. W. & Paula, J. D. *Physical Chemistry for the Life Sciences* (Oxford University Press, 2010).

24. Pundir, C., Kumar, P. & Jaiwal, R. Biosensing Methods for Determination of Creatinine: A Review. *Biosensors and Bioelectronics* **126,** 707–724 (2019).

25. Yeh, H.-C., Lo, Y.-C., Ting, I.-W., Chu, P.-L., Chang, S.-N., Chiang, H.-Y. & Kuo, C.-C. 24-hour Serum Creatinine Variation Associates with Short- and Long-Term All-Cause Mortality: A Real-World Insight into Early Detection of Acute Kidney Injury. *Scientific Reports* **10,** 6552 (2020).

26. Meisner, M. Update on Procalcitonin Measurements. *Annals of Laboratory Medicine* **34,** 263–273 (2014).

27. Teachey, D. T. *et al.* Identification of Predictive Biomarkers for Cytokine Release Syndrome after Chimeric Antigen Receptor T-cell Therapy for Acute Lymphoblastic Leukemia. *Cancer Discovery* **6,** 664–679 (2016).

28. Lubken, R. M., de Jong, A. M. & Prins, M. W. J. How Reactivity Variability of Biofunctionalized Particles Is Determined by Superpositional Heterogeneities. *ACS Nano* **15,** 1331–1341 (2021).

29. Lubken, R. M., Bergkamp, M. H., de Jong, A. M. & Prins, M. W. J. Sensing Methodology for the Rapid Monitoring of Biomolecules at Low Concentrations over Long Time Spans. *ACS Sensors.* Accepted for publication (2021).

30. Nightingale, A. M., Leong, C. L., Burnish, R. A., Hassan, S.-U., Zhang, Y., Clough, G. F., Boutelle, M. G., Voegeli, D. & Niu, X. Monitoring Biomolecule Concentrations in Tissue Using a Wearable Droplet Microfluidic-Based Sensor. *Nature Communications* **10,** 2741 (2019).

31. Gowers, S. A. N. *et al.* Clinical Translation of Microfluidic Sensor Devices: Focus on Calibration and Analytical Robustness. *Lab on a Chip* **19,** 2537–2548 (2019).

32. Nandi, P. & Lunte, S. M. Recent Trends in Microdialysis Sampling Integrated with Conventional and Microanalytical Systems for Monitoring Biological Events: A Review. *Analytica Chimica Acta* **651,** 1–14 (2009).

6 CONCLUSION

The goal of this thesis was to study bioanalytical functionalities that can be achieved with continuous affinity-based biomolecular sensors using single-molecule resolution. For this, the thesis focused on two main topics, namely, (1) new applications of single-molecule resolution in continuous monitoring sensors, and (2) speed, sensitivity, and precision functionalities of continuous biosensing with single-molecule resolution. The first topic was discussed in chapters two and three, and the second topic was discussed in chapters four and five. In this chapter, the main conclusions of this thesis are summarized and discussed, and an outlook is presented.

6.1 SUMMARY OF MAIN RESULTS

In Chapter 2 we demonstrated a new application of single-molecule detection in continuous monitoring applications, namely, multiplexing by means of single-molecule kinetic identification of single particles. We presented a sensor design with an encoded binary nanoswitch, which enabled continuous sensing of multiple target molecules simultaneously, at picomolar concentrations in human blood plasma. Multiplexing by single-molecule kinetic encoding is interesting for real time biomolecular monitoring applications, since it does not require any reagents in contrast to other multiplexing solutions. Moreover, kinetic encoding can be supplemented with orthogonal identification approaches, such as optical identification and identification by surface area imaging, enabling a high degree of multiplexing. The sensors open the perspective to gain accurate real time insights into live biological systems by continuous monitoring of biomolecules with a high level of multiplexing, high sensitivity, and high specificity using single-molecule information.

In Chapter 3 we presented a framework to study the influence of heterogeneities on the reactivity variability of biofunctionalized particles for targeted nanomedicine and particle-based biosensing applications. To quantify the reactivity variability, we have studied three variability contributors, namely stochastic heterogeneity, interparticle heterogeneity, and intraparticle heterogeneity, jointly referred to as superpositional heterogeneities. These three types of heterogeneity cause biofunctionalized particles to have variable reactivities, where reactivity was defined as the number of particle-coupled targeting moieties that are available for interaction toward a countersurface. We have experimentally quantified targeting moiety number variabilities using microscopy methods with single-molecule resolution, namely, qPAINT and DNA-PAINT, using DNA-functionalized silica particles as a model system. We found that the interparticle heterogeneity originates from particle size dispersion and targeting moiety density fluctuations, and intraparticle heterogeneity is caused by nonuniform functionalization. The reactivity variability was studied by experiments and simulations for a particle-based biosensing technique with single-particle and single-molecule resolution (biosensing by particle mobility, BPM). The results show that the reactivity variability strongly depends on the size of the interaction area, which dictates the relative contributions of stochastic and inter- and intraparticle heterogeneity to the observed reactivity variability. By extrapolating the results toward the fields of targeted nanomedicine and particle-based biosensing in general, it was shown that large fluctuations (tens of percent) in the reactivity can be expected when targeting

effects at a biological site of interest or at a sensor surface are determined by interactions from small particles, low targeting moiety density, small interaction area, and a limited number of particles. The use of the developed framework to quantify and model the influence of superpositional heterogeneities on the reactivity variability will enable researchers to engineer particles for biomedical applications with high precision, guided by a thorough understanding of heterogeneities and their collective consequences.

In Chapter 4 we presented a sensing methodology that enables rapid monitoring of low-concentration biomolecules with high precision, with small time delays and short time intervals, over an endless time span. The sensing methodology is based on a limited-volume assay, using high-affinity binders, a fully reversible detection principle, and time-controlled analyte exchange. Using simulations, we studied how the kinetics of the sensor depend on mass transport and on the surface reaction in the measurement chamber, and how time-controlled analyte exchange determines the system response and enables precise measurements of analyte concentration. Experimental results show the ability to control the sensor response time by tuning the total binder concentration in the measurement chamber. Finally, simulations show that the sensing principle allows picomolar and sub-picomolar concentrations to be monitored with a high precision over long time spans. Approaches described in literature for measuring low-concentration biomolecules have focused primarily on assays in which every concentration determination involves consumption of reagents, which is complex and costly for monitoring applications. In contrast, the sensing methodology described in this chapter is based on a fully reversible assay principle, without consuming reagents with each newly recorded concentration datapoint, enabling measurements with high frequency over an endless time span. Due to its generalizability and unique and tunable sensing performance, we believe that the limited-volume assay with time-controlled analyte exchange will enable studies on time-dependencies of low-concentration biomolecules, for novel applications in the fields of dynamic biological systems, patient monitoring, and biotechnological process control.

In Chapter 5 we investigated continuous biomolecular analyte exchange between a dynamic system of interest and the measurement chamber of a monitoring sensor. We have studied the influence of sensor design parameters on the differences between the true and the measured concentration-time profile, focusing particularly on the lag time of the sensor signal with respect to the input concentration, and the sensitivity to concentration changes over time. To quantify the latter,

we introduced the concentration change rate (CCR) parameter, which is expressed in unit molar per second. The limit of the measurable CCR was evaluated as the limit of quantification of CCR (LoCCR). In this chapter, we have presented a comprehensive methodology to study the properties and limitations of dynamic measurements using affinity-based sensors with diffusive as well as advective sampling. Finite-element simulations were used to study the spatial and temporal dependence of analyte concentration within the measurement chamber. The analyte was supplied into the measurement chamber with sinusoidal concentration-time profiles, which later allowed the study of arbitrary concentration-time profiles by frequency decomposition. Using this approach, we could study how mass transport and biochemical kinetics determine the speed of concentration change, time delays, and concentration errors in the sensing system. The study is especially relevant for low-concentration biomolecules, which are most suitably measured using sensors with single-molecule resolution and Poisson-limited noise levels. The results and learnings presented in this chapter can assist researchers to identify the most important processes influencing the performance of continuous monitoring sensors. Insight in the individual and combined influence of analyte diffusivity, analyte concentration, binder affinity, sampling method, measurement chamber geometry, and flow speed on the observed lag time and rate sensitivity of the measured concentration-time profile, will help researchers to develop monitoring systems with desirable sensor characteristics for a diverse range of biomarkers and applications.

6.2 DISCUSSION AND OUTLOOK

This thesis has explored bioanalytical functionalities of continuous monitoring sensors with single-molecule resolution, with the specific focus on a new sensing methodology called biosensing by particle mobility (BPM). Single-molecule resolution allows detection with low noise levels (Poisson-limited) and allows one to resolve heterogeneities that are averaged out in ensemble-based approaches.

The ability to measure heterogeneities and distributions based on single-molecule information provides insights in time-dependent processes, such as the lifetimes of association and dissociation events that continuously occur at the molecular level. However, the use of kinetic identification for multiplexing functionality (Chapter 2) requires narrow lifetime distributions, which can be achieved by a sensor with single stem probe, but that design comes at a cost of sensitivity due to the limited surface area (Chapter 3). We think that the sensor with single stem probe is suited for detailed characterizations of single-molecule

affinity interactions and for studies to deepen the understanding of specific and nonspecific interactions.

The work in this thesis showed the benefits of single-molecule characterization techniques for comparing sources of variability, by quantifying individual contributions as well as their collective effect. However, this work merely lays a groundwork for future experimental research; many conditions can be investigated that influence the particle reactivity variability such as biofunctionalization strategies, particle materials, sizes, and geometries of particles, different targeting moiety types, and the influence of complex biological matrices (*e. g.*, protein corona). The measured distributions and heterogeneity simulations can then be related to the precision of particle-based targeting effects. Moreover, heterogeneities should also be studied as a function of time to understand sensor stability, which is required for long-term monitoring applications.

For the monitoring of low-concentration biomarkers where only a limited number of molecules are present for detection, counting single molecules becomes important. The sensor simulations in this thesis (Chapters 4 and 5) assumed that the noise on the signal was dominated by Poisson statistics. Future experiments should focus on the effect of other variability contributors as well, such as background, variability in receptor functionality, nonspecific interactions, and time-dependent sensor degradation. In addition, the ability to precisely quantify time-dependent concentration profiles depends on tradeoffs between the speed of the concentration determination and the number of observed molecules that generate the signal. Preliminary experimental work on this topic (Chapter 4) showed the control over the speed. Further studies could focus on gains of speed *versus* loss of sensitivity, on implementations in a variety of sensing platforms, and on sensor performance in complex biological systems.

We believe that the learnings of this thesis will expand monitoring functionalities into previously inaccessible classes of low-concentration biomolecules. This creates the potential to open a broad range of applications, such as the monitoring of dynamic processes in lab-on-a-chip and organ-on-a-chip devices, the monitoring of patients for health care applications, the monitoring and control of industrial processes, *e. g.*, food production in bioreactors and fermentors, and the monitoring of environmental conditions, *e. g.*, water quality control.

PUBLICATIONS

ARTICLES

. **Lubken, R. M.**, de Jong, A. M. & Prins, M. W. J. Multiplexed Continuous Biosensing by Single-Molecule Encoded Nanoswitches. *Nano Letters* **4,** 2296–2302 (2020).

. **Lubken, R. M.**, de Jong, A. M. & Prins, M. W. J. How Reactivity Variability of Biofunctionalized Particles Is Determined by Superpositional Heterogeneities. *ACS Nano* **15,** 1331–1341 (2021).

. **Lubken, R. M.**, Bergkamp, M. H., de Jong, A. M. & Prins, M. W. J. Sensing Methodology for the Rapid Monitoring of Biomolecules at Low Concentrations over Long Time Spans. *ACS Sensors.* Accepted for publication (2021).

. **Lubken, R. M.**, de Jong, A. M. & Prins, M. W. J. Real Time Monitoring of Biomolecules: Dynamic Response Limits of Affinity-Based Sensors. *ACS Sensors.* Accepted for publication (2021).

ORAL PRESENTATIONS

. **Lubken, R. M.**, Visser, E. W. A., Yan, J., van IJzendoorn, L. J. & Prins, M. W. J. *Biomarker Monitoring by Particle Mobility Sensing.* EUROPT(R)ODE XIV, 25–28 March 2018, Naples, Italy.

. **Lubken, R. M.**, Visser, E. W. A., Yan, J., van IJzendoorn, L. J. & Prins, M. W. J. *Single-Molecule Kinetic Fingerprinting in a Biosensor Based on Particle Mobility.* World Congress on Biosensors 2018, 12–15 June 2018, Miami, USA.

. **Lubken, R. M.**, de Jong, A. M. & Prins, M. W. J. *Single-Molecule Kinetic Fingerprinting for Continuous Biosensing.* CHAINS, 3–5 December 2018, Eindhoven, the Netherlands.

CURRICULUM VITÆ

Rafiq Lubken was born on the 3rd of July 1994 in Son en Breugel, the Netherlands. After graduating from his secondary education at Lyceum Bisschop Bekkers in Eindhoven, he started his study of Medicine at Radboud University in Nijmegen, in 2012. Due to a lack of a technology-centered education, he started a new study of Biomedical Engineering at Eindhoven University of Technology in Eindhoven, in 2013.

During his Biomedical Engineering study, he participated in several extracurricular activities, such as the iGEM competition in 2014 and the SensUs competition in 2016. During his master project, he studied the feasibility of a two-state molecular switch for continuous single-molecule biosensing. As part of his master education, he performed an internship at Single Technologies in Stockholm, Sweden, where he designed a surface patterning method suitable for thin flexible substrates for high-density distribution of DNA amplicons for DNA sequencing. He graduated with honors in 2017.

In November 2017, he started working as a PhD student in the Molecular Biosensing for Medical Diagnostics group (MBx) at the Biomedical Engineering and Applied Physics departments of Eindhoven University of Technology. Under the supervision of prof.dr.ir. Menno Prins and dr.ir. Arthur de Jong, he conducted research in the area of biomolecular monitoring techniques with a single-molecule resolution, specifically focusing on the quantification of sensor properties using single-molecule techniques. The main results of the research performed during his PhD are summarized in this thesis.

DANKWOORD

Vier jaar geleden had ik me al levendig voorgesteld hoe ik de pagina's van het dankwoord van mijn thesis zou vullen. Benen omhoog na het harde werken, een Westvleteren 12 of iets dergelijks om de afronding van mijn thesis te vieren, en een zonnetje dat mij vanuit buiten lachend toeschijnt. Alleen het eerste is me een soort van gelukt; de zon kan helaas niet altijd schijnen en het werkende leven gaat ook gewoon door — of het werkende leven is nu pas begonnen, zo kan je het natuurlijk ook zien. Maar goed, die zon die komt wel een keer terug en de Westvleteren is al lang op, op het moment dat iemand ook maar één woord op deze pagina heeft gelezen.

Het zijn onbevangen, leerzame en verhelderende jaren geweest. Ik vergelijk het nu misschien geheel onterecht als een speeltuin waarin je kon doen wat je wilde, maar zo voelde het soms wel. Alleen waren je schepjes en emmertjes, waarmee je een zandkasteel moest bouwen, diep in het zand verstopt en had je werkelijk geen idee waar en op welke diepte je zoeken moest. Eigenlijk had je ook geen idee of het wel de bedoeling was een zandkasteel te bouwen. Gelukkig heb ik in dit avontuur van vele mensen hulp gehad in de zoektocht naar de juiste richting; ontwikkeling en vooruitgang gaan nu eenmaal sneller wanneer je de mogelijkheid hebt om te leren van andere mensen. Voor deze hulp, die zich per persoon in een unieke vorm heeft gemanifesteerd, en in meer of mindere mate terug te vinden is in mijn thesis, ben ik dan ook erg dankbaar.

De personen die ik natuurlijk als eerste wil bedanken, zijn de personen die mij het meest direct hebben geholpen bij het tot stand brengen van de "zelfstandig onderzoeker" die ik nu ben/moet zijn: Menno en Arthur. Zoals al halverwege mijn promotieonderzoek was gebleken, academisch onderzoek is niet helemaal mijn ding. Desondanks wisten jullie het op zo'n manier samen met mij vorm te geven, dat het uiteindelijk een leertraject geworden is dat ik nooit van mijn leven zou hebben willen missen. Menno, ik waardeer enorm je gevoel van vertrouwen dat je naar mij uitstraalt en de mogelijkheid die je me hebt gegeven, en mij nog steeds geeft, om mijn ideeën, gedachten en inzichten zelf vorm te geven en te onderzoeken. En dat afgetopt met een forse dosis van jouw enthousiasme. Bovendien heb ik het één en ander bij je kunnen afkijken voor wat betreft de kunst in het scheiden van aandacht, het overzien van het grotere doel: een PhD als een moestuin, waarin oog voor het

noodzakelijke dagelijkse onderhoud, zoals het geven van water en het wieden van onkruid, de sleutel is tot een uiteindelijk succes. Arthur, ik heb door jou geleerd dat het kritisch nadenken en het stellen van kritische vragen toch altijd nog naar een niveau hoger kan worden getild. Vaak had ik een goed doordacht idee of verklaring die door een welgerichte vraag van je volledig overhoop geschoten kon worden. Daarmee denk ik dat deze thesis scherper en relevanter is geworden dan hij zonder jou ooit zou zijn geweest.

Ik heb altijd de toegankelijke en gelijkwaardige sfeer gewaardeerd die onze onderzoeksgroep zo erg typeert. Ideeën, plannen, problemen, zij het nu werkgerelateerd of niet, het bespreken hiervan was altijd mogelijk en met iedereen. Collega's heb je dus niet alleen om mee samen te werken, maar ook om samen mee te leren. In het bijzonder Max, mijn ex-achterbuurman in het kantoor: onze onderlinge gesprekken die we voerden in het kantoor of in het lab moesten vaak onderbroken worden doordat er iemand binnenkwam. Zoals je zelf al eerder hebt beschreven; de reden van onze onderbrekingen kan beter onder ons blijven.

Dan zijn er nog drie personen waarvan ik niet zozeer weet of ik er nu daadwerkelijk iets nuttigs van heb geleerd: Boris, Leroy en Jasper. Als vier musketiers zijn wij zo goed als onze volledige studie met elkaar opgetrokken, achterlijke en onverstandige dingen gedaan, maar uiteindelijk hebben we wel op zo goed als hetzelfde moment onze diploma's gehaald. We bleken het achteraf toch wel te kunnen. Na onze studie zijn we ieder onze eigen weg gegaan, maar als we nu weer bij elkaar komen, blijkt er gelukkig met de dynamiek niks veranderd te zijn: die achterlijke en onverstandige dingen komen dan vanzelf weer terug.

Ik heb besloten mijn thesis op te dragen aan mijn familie. Familie is vanaf het eerste moment één van de belangrijkste dingen in het leven voor mij geweest. In het bijzonder, pap en mam, jullie houden het nu al zo lang vol met mij. Maar ook Indra, iets anders geformuleerd, we houden het nu al zo lang met elkaar vol. Om precies te zijn sinds dat ik werd geboren, vanaf dat moment waren jullie er altijd voor me, een basis waarop ik terug kan vallen. De waarde van zo'n basis besef je vaak, helaas, in tijden zoals het afgelopen jaar. Een tijd waarin we elkaar als familie meer dan anders nodig hebben gehad. Ik denk dat wij dit als geen ander voor elkaar en met elkaar hebben gedaan. Als ik voor ons allen mag spreken, denk ik dat we van geluk mogen spreken dat we zoveel aan elkaar hebben gehad, maar bovenal, op welke manier dan ook, nog altijd zoveel aan elkaar zullen hebben.

Mijn laaste woorden van dit dankwoord richt ik aan Vera, mijn liefde, mijn maatje, de persoon bij wie ik mezelf kan zijn. Ik kan veel benoemen wat ik de afgelopen jaren van je heb geleerd, maar ik durf met zekerheid zeggen dat helemaal niets daarvan in mijn thesis terecht gekomen is. Op één ding na dan: lees maar eens de zin aan het einde van dit dankwoord. Een zin die komt uit *De la Terre à la Lune* van Jules Verne, de man die de toekomst uitvond. Het is praktisch om rationeel onze reis door ons leven te observeren, op te reflecteren en richting te geven. Maar tot op de dag van vandaag, heb je me laten zien dat het leven een stuk verrassender en uitdagender kan worden als ik zo nu en dan deze rationalisatie als academische bijwerking eens loslaat. En zo vinden wij samen onze eigen toekomst uit.

Rafiq Lutken

Que de choses niées la veille
dont le lendemain a fait des réalités!

How many things have been denied one day
only to become realities the next!

— Jules Verne
DE LA TERRE À LA LUNE (1865)